UNIVERSITY OF CALIFORNIA SAN DIEGO

Evolution, Atmospheres and Chemistry of Ancient Stellar Populations

A dissertation submitted in partial satisfaction of the
requirements for the degree
Doctor of Philosophy

in

Physics

by

Roman Gerasimov

Committee in charge:

Professor Adam J. Burgasser, Chair
Professor Quinn M. Konopacky
Professor Michael L. Norman
Professor Mark H. Thiemens
Professor Frank Würthwein

2023

The dissertation of Roman Gerasimov is approved, and it is acceptable in quality and form for publication on microfilm and electronically.

University of California San Diego

2023

DEDICATION

In memory of my first advisor, Andrew Samuel Friedman.

EPIGRAPH

A model is a lie

that helps you see the truth.

— Howard Skipper

TABLE OF CONTENTS

LIST OF FIGURES

LIST OF TABLES

ACKNOWLEDGEMENTS

I would like to thank my advisor Professor Adam Burgasser not only for his unconditional guidance and support, but also for creating a community where I always felt welcome and appreciated. For the last five years, the Cool Star laboratory truly was my home away from home. I would like to extend my gratitude to all former and current members of the lab I had the pleasure of sharing the workspace with, especially Doctor Jon Rees, Doctor Chris Theissen, Doctor Dino Chih-Chun Hsu, Doctor Christian Aganze, Emma Softich and Preethi Karpoor. This dissertation was inspired by their suggestions and insightful feedback.

I am thankful to all undergraduate students who attended my classes, participated in the summer research experience programs and collaborated with me on research projects. Their unique perspectives on the subject have transformed my understanding of the field more times than I can count, making me a far better astronomer than I could otherwise be. I am especially grateful to Mikaela Larkin, Praneet Bhoj, Tianxing Zhou and Angelica Whisnant, who chose me as their research advisor. Mikaela Larkin in particular has led a year-long investigation into the atmospheres of Population III stars that resulted in Chapter 2 of this dissertation.

I express my sincere gratitude to Professor Brian Keating, Professor Raphael Flauger and all members of the UCSD Cosmology Research Group, who encouraged and supported my extremely broad research interests during the first half of my graduate career. While my research in the field of cosmology may not be the centerpiece of this dissertation, the skills and knowledge I obtained from that memorable experience will be apparent in every chapter.

I would like to thank Doctor Andrew Friedman: my first graduate advisor, a brilliant mentor and the most passionate science communicator I ever had the privilege of knowing. Although Andy passed away in my second year, his impact on my academic and personal development will last indefinitely. This dissertation is dedicated to his memory. The experience I gained from working with Andy allowed me to conclude his study of quantum gravity with continuous support from our collaborator at the University of New Hampshire, Professor Fabian

Kislat. In those difficult times, Fabian assumed the role of my de facto advisor and supervised the publication of my very first lead-author paper in a peer-reviewed journal.

I am thankful to my dissertation committee for their ongoing support, especially Professor Quinn Konopacky and all members of her lab for our weekly "supergroup" meetings that filled the upper floors of SERF with the much-needed collaborative spirit and friendly atmosphere. I would like to thank Professor Shelley Wright who trusted me to serve as a teaching assistant and a planetarium presenter in her courses and outreach engagements. While providing insightful guidance, she gave me complete freedom to experiment with my delivery style that helped me grow as an educator. I am deeply grateful to my undergraduate mentor at University College London, Professor Steve Fossey, whose passion for education turned me from someone with mere interest in astronomy into a professional astronomer, and made this dissertation possible.

Lastly, I would like to thank the California Department of Parks and Recreation, the U.S. Department of Agriculture and the U.S. Department of the Interior for protecting the natural beauty of the Golden State and the dark skies above it. The opportunity to escape into the wild during the hardest of times was essential to maintaining my mental health and served as an important reminder that my work extends beyond my laptop towards the stars.

I acknowledge the funding support from Hubble Space Telescope (HST) Program GO-15096, provided by NASA through a grant from the Space Telescope Science Institute, which is operated by the Association of Universities for Research in Astronomy, Incorporated, under NASA contract NAS5-26555. The computational demand of this dissertation was met by the Extreme Science and Engineering Discovery Environment (XSEDE), supported by NSF grant ACI-1548562. This work was conducted at UCSD, which was built on the unceded territory of the Kumeyaay Nation. Today, the Kumeyaay people continue to maintain their political sovereignty and cultural traditions as vital members of the San Diego community. I acknowledge their tremendous contributions to our region and thank them for their stewardship.

Chapter 2, in full, was submitted with minor alterations and accepted for publication

in the Astronomical Journal Series 2023. An edited version of this chapter is now available in print in Volume 165, Issue 1, authored by Mikaela M. Larkin, Roman Gerasimov, and Adam J. Burgasser. The dissertation author provided the evolutionary models used in the study and made a significant contribution to the detailed analysis of the properties of Population III stars and the required literature research.

Chapter 3, in full, was submitted with minor alterations and accepted for publication in the Astrophysical Journal Series 2022. An edited version of this chapter is now available in print in Volume 930, Issue 1, authored by Roman Gerasimov, Adam J. Burgasser, Derek Homeier, Luigi R. Bedin, Jon M. Rees, Michele Scalco, Jay Anderson, and Maurizio Salaris. The dissertation author was the primary investigator of this study.

Chapter 4, in full, is being prepared for submission to the Astrophysical Journal Series 2023, authored by Roman Gerasimov, Adam J. Burgasser, Ilaria Caiazzo, Derek Homeier, Harvey Richer, Matteo Correnti and Jeremy Heyl. The dissertation author is the primary investigator of this study.

VITA

2018	Bachelor of Science in Astrophysics, University College London
2021	Doctor of Philosophy Candidate in Physics, University of California San Diego
2023	Doctor of Philosophy in Physics, University of California San Diego

PUBLICATIONS

F. J. Pozuelos, M. Timmermans, B. V. Rackham, L. J. Garcia, A. J. Burgasser, S. R. Kane, M. N. Günther, K. G. Stassun, V. Van Grootel, M. Dévora-Pajares, R. Luque, B. Edwards, P. Niraula, N. Schanche, R. D. Wells, E. Ducrot, S. Howell, D. Sebastian, K. Barkaoui, W. Waalkes, C. Cadieux, R. Doyon, R. P. Boyle, J. Dietrich, A. Burdanov, L. Delrez, B. -O. Demory, J. de Wit, G. Dransfield, M. Gillon, Y. Gómez Maqueo Chew, M. J. Hooton, E. Jehin, C. A. Murray, P. P. Pedersen, D. Queloz, S. J. Thompson, A. H. M. J. Triaud, S. Zúñiga-Fernández, K. A. Collins, M. M. Fausnaugh, C. Hedges, K. M. Hesse, J. M. Jenkins, M. Kunimoto, D. W. Latham, A. Shporer, E. B. Ting, G. Torres, P. Amado, J. R. Rodón, C. Rodríguez-López, J. C. Suárez, R. Alonso, Z. Benkhaldoun, Z. K. Berta-Thompson, P. Chinchilla, M. Ghachoui, M. A. Gómez-Muñoz, R. Rebolo, L. Sabin, U. Schroffenegger, E. Furlan, C. Gnilka, K. Lester, N. Scott, C. Aganze, **R. Gerasimov**, C. Hsu, C. Theissen, D. Apai, W. P. Chen, P. Gabor, T. Henning, and L. Mancini. *A super-Earth and a mini-Neptune near the 2:1 MMR straddling the radius valley around the nearby mid-M dwarf TOI-2096* in *Astronomy and Astrophysics*, vol. 672, 2023. [ADS]

L. R. Bedin, M. Salaris, J. Anderson, M. Scalco, D. Nardiello, E. Vesperini, H. Richer, A. Burgasser, M. Griggio, **R. Gerasimov**, D. Apai, A. Bellini, M. Libralato, P. Bergeron, R. M. Rich, and A. Grazian. *The HST large programme on NGC 6752 - IV. The White Dwarf sequence* in *Monthly Notices of the Royal Astronomical Society*, vol. 518, no. 3, 2023. [ADS]

M. M. Larkin, **R. Gerasimov**, and A. J. Burgasser. *Characterization of Population III Stars with Stellar Atmosphere and Evolutionary Modeling and Predictions of their Observability with the JWST* in *The Astronomical Journal*, vol. 165, no. 1, 2023. [ADS]

T. Zhou, A. Whisnant, **R. Gerasimov**, and A. J. Burgasser. *Synthetic Color-Magnitude Diagrams for the Globular Cluster 47 Tucanae* in *Research Notes of the American Astronomical Society*, vol. 6, no. 10, 2022. [ADS]

R. Gerasimov, A. J. Burgasser, D. Homeier, L. R. Bedin, J. M. Rees, M. Scalco, J. Anderson, and M. Salaris. *The HST Large Program on ω Centauri. V. Exploring the Ultracool Dwarf Population with Stellar Atmosphere and Evolutionary Modeling* in *The Astrophysical Journal*, vol. 930, no. 1, 2022. [ADS]

B. S. Hensley, S. E. Clark, V. Fanfani, N. Krachmalnicoff, G. Fabbian, D. Poletti, G. Puglisi, G. Coppi, J. Nibauer, **R. Gerasimov**, N. Galitzki, S. K. Choi, P. C. Ashton, C. Baccigalupi, E. Baxter, B. Burkhart, E. Calabrese, J. Chluba, J. Errard, A. V. Frolov, C. Hervías-Caimapo, K. M. Huffenberger, B. R. Johnson, B. Jost, B. Keating, H. McCarrick, F. Nati, M. Sathyanarayana Rao, A. van Engelen, S. Walker, K. Wolz, Z. Xu, N. Zhu, and A. Zonca. *The Simons Observatory: Galactic Science Goals and Forecasts* in *The Astrophysical Journal*, vol. 929, no. 2, 2022. [ADS]

A. Gagliano, L. Izzo, C. D. Kilpatrick, B. Mockler, W. V. Jacobson-Galán, G. Terreran, G. Dimitriadis, Y. Zenati, K. Auchettl, M. R. Drout, G. Narayan, R. J. Foley, R. Margutti, A. Rest, D. O. Jones, C. Aganze, P. D. Aleo, A. J. Burgasser, D. A. Coulter, **R. Gerasimov**, C. Gall, J. Hjorth, C. Hsu, E. A. Magnier, K. S. Mandel, A. L. Piro, C. Rojas-Bravo, M. R. Siebert, H. Stacey, M. C. Stroh, J. J. Swift, K. Taggart, S. Tinyanont, and S. Tinyanont. *An Early-time Optical and Ultraviolet Excess in the Type-Ic SN 2020oi* in *The Astrophysical Journal*, vol. 924, no. 2, 2022. [ADS]

J. K. Faherty, J. Gagné, M. Popinchalk, J. M. Vos, A. J. Burgasser, J. Schümann, A. C. Schneider, J. D. Kirkpatrick, A. M. Meisner, M. J. Kuchner, D. C. Bardalez Gagliuffi, F. Marocco, D. Caselden, E. C. Gonzales, A. Rothermich, S. L. Casewell, J. H. Debes, C. Aganze, A. Ayala, C. Hsu, W. J. Cooper, R. L. Smart, **R. Gerasimov**, C. A. Theissen, and Backyard Worlds: Planet 9 Collaboration. *A Wide Planetary Mass Companion Discovered through the Citizen Science Project Backyard Worlds: Planet 9* in *The Astrophysical Journal*, vol. 923, no. 1, 2021. [ADS]

A. C. Schneider, A. M. Meisner, J. Gagné, J. K. Faherty, F. Marocco, A. J. Burgasser, J. D. Kirkpatrick, M. J. Kuchner, L. Gramaize, A. Rothermich, H. Brooks, F. J. Vrba, D. Bardalez Gagliuffi, D. Caselden, M. C. Cushing, C. R. Gelino, M. R. Line, S. L. Casewell, J. H. Debes, C. Aganze, A. Ayala, **R. Gerasimov**, E. C. Gonzales, C. Hsu, R. Kiman, M. Popinchalk, C. Theissen, and Backyard Worlds: Planet 9 Collaboration. *Ross 19B: An Extremely Cold Companion Discovered via the Backyard Worlds: Planet 9 Citizen Science Project* in *The Astrophysical Journal*, vol. 921, no. 2, 2021. [ADS]

M. Scalco, A. Bellini, L. R. Bedin, J. Anderson, P. Rosati, M. Libralato, M. Salaris, E. Vesperini, D. Nardiello, D. Apai, A. J. Burgasser, and **R. Gerasimov**. *The HST large programme on* ω *Centauri - IV. Catalogue of two external fields* in *Monthly Notices of the Royal Astronomical Society*, vol. 505, no. 3, 2021. [ADS]

A. M. Meisner, A. C. Schneider, A. J. Burgasser, F. Marocco, M. R. Line, J. K. Faherty, J. D. Kirkpatrick, D. Caselden, M. J. Kuchner, C. R. Gelino, J. Gagné, C. Theissen, **R. Gerasimov**, C. Aganze, C. Hsu, J. P. Wisniewski, S. L. Casewell, D. C. Bardalez Gagliuffi, S. E. Logsdon, P. R. M. Eisenhardt, K. Allers, J. H. Debes, M. B. Allen, N. Stevnbak Andersen, S. Goodman, L. Gramaize, D. W. Martin, A. Sainio, M. C. Cushing, and Backyard Worlds: Planet 9 Collaboration. *New Candidate Extreme T Subdwarfs from the Backyard Worlds: Planet 9 Citizen Science Project* in *The Astrophysical Journal*, vol. 915, no. 2, 2021. [ADS]

R. Gerasimov, P. Bhoj, and F. Kislat. *New Constraints on Lorentz Invariance Violation from Combined Linear and Circular Optical Polarimetry of Extragalactic Sources* in *Symmetry*, vol.

13, no. 5, 2021. [ADS]

J. D. Kirkpatrick, C. R. Gelino, J. K. Faherty, A. M. Meisner, D. Caselden, A. C. Schneider, F. Marocco, A. J. Cayago, R. L. Smart, P. R. Eisenhardt, M. J. Kuchner, E. L. Wright, M. C. Cushing, K. N. Allers, D. C. Bardalez Gagliuffi, A. J. Burgasser, J. Gagné, S. E. Logsdon, E. C. Martin, J. G. Ingalls, P. J. Lowrance, E. S. Abrahams, C. Aganze, **R. Gerasimov**, E. C. Gonzales, C. Hsu, N. Kamraj, R. Kiman, J. Rees, C. Theissen, K. Ammar, N. S. Andersen, P. Beaulieu, G. Colin, C. A. Elachi, S. J. Goodman, L. Gramaize, L. K. Hamlet, J. Hong, A. Jonkeren, M. Khalil, D. W. Martin, W. Pendrill, B. Pumphrey, A. Rothermich, A. Sainio, A. Stenner, C. Tanner, M. Thévenot, N. V. Voloshin, J. Walla, Z. Wędracki, and Backyard Worlds: Planet 9 Collaboration. *The Field Substellar Mass Function Based on the Full-sky 20 pc Census of 525 L* in *The Astrophysical Journal Supplement*, vol. 253, no. 1, 2021. [ADS]

R. Low, A. J. Burgasser, C. Reylé, **R. Gerasimov**, C. Hsu, and C. A. Theissen. *Spectroscopic Confirmation of an M6 Dwarf Companion to the Nearby Star BD-08 2582* in *Research Notes of the American Astronomical Society*, vol. 5, no. 2, 2021. [ADS]

R. Gerasimov, D. Homeier, A. Burgasser, and L. R. Bedin. *A New Grid of Model Atmospheres for Metal-poor Ultracool Brown Dwarfs* in *Research Notes of the American Astronomical Society*, vol. 4, no. 12, 2020. [ADS]

A. S. Friedman, **R. Gerasimov**, D. Leon, W. Stevens, D. Tytler, B. G. Keating, and F. Kislat. *Improved constraints on anisotropic birefringent Lorentz invariance and C P T violation from broadband optical polarimetry of high redshift galaxies* in *Physical Review D*, vol. 102, no. 4, 2020. [ADS]

A. M. Meisner, J. K. Faherty, J. D. Kirkpatrick, A. C. Schneider, D. Caselden, J. Gagné, M. J. Kuchner, A. J. Burgasser, S. L. Casewell, J. H. Debes, É. Artigau, D. C. Bardalez Gagliuffi, S. E. Logsdon, R. Kiman, K. Allers, C. Hsu, J. P. Wisniewski, M. B. Allen, P. Beaulieu, G. Colin, H. A. Durantini Luca, S. Goodman, L. Gramaize, L. K. Hamlet, K. Hinckley, F. Kiwy, D. W. Martin, W. Pendrill, A. Rothermich, A. Sainio, J. Schümann, N. S. Andersen, C. Tanner, V. Thakur, M. Thévenot, J. Walla, Z. Wędracki, C. Aganze, **R. Gerasimov**, C. Theissen, and Backyard Worlds: Planet 9 Collaboration. *Spitzer Follow-up of Extremely Cold Brown Dwarfs Discovered by the Backyard Worlds: Planet 9 Citizen Science Project* in *The Astrophysical Journal*, vol. 899, no. 2, 2020. [ADS]

A. C. Schneider, A. J. Burgasser, **R. Gerasimov**, F. Marocco, J. Gagné, S. Goodman, P. Beaulieu, W. Pendrill, A. Rothermich, A. Sainio, M. J. Kuchner, D. Caselden, A. M. Meisner, J. K. Faherty, E. E. Mamajek, C. Hsu, J. J. Greco, M. C. Cushing, J. D. Kirkpatrick, D. Bardalez-Gagliuffi, S. E. Logsdon, K. Allers, J. H. Debes, and Backyard Worlds: Planet 9 Collaboration. *WISEA J041451.67-585456.7 and WISEA J181006.18-101000.5: The First Extreme T-type Subdwarfs?* in *The Astrophysical Journal*, vol. 898, no. 1, 2020. [ADS]

ABSTRACT OF THE DISSERTATION

Evolution, Atmospheres and Chemistry of Ancient Stellar Populations

by

Roman Gerasimov

Doctor of Philosophy in Physics

University of California San Diego, 2023

Professor Adam J. Burgasser, Chair

The chemical diversity of our galaxy is owed to multiple generations of stars that converted the primordial mixture of hydrogen and helium into ~ 100 elements that make up the periodic table. The first stars to form after the Big Bang (Population III) were nearly metal-free and are believed to have been far more massive, luminous and short-lived than their later descendants. It is therefore expected that none of the Population III stars in the Milky Way survived to present day and their properties are highly debated. By contrast, the oldest metal-poor (Population II) stars that formed during or shortly after the era of Population III dominance may still be found in the galactic halo. Large numbers of those ancient stars are contained within the Milky Way globular clusters that are of particular interest to studies of stellar populations due to their coeval

nature. Recent observations have confirmed that globular clusters undergo complex evolution and host multiple chemically distinct stellar populations. The physical origin of this unique feature remains largely unexplained, in part, because detailed composition measurements are only available for the most massive, spectroscopically accessible members.

In order to study the early chemical evolution of the universe, I developed a method to extract the fundamental properties of chemically peculiar stellar populations from multiband photometry. My approach uniquely incorporates the calculation of new evolutionary stellar models and model atmospheres for every considered chemical composition, thereby capturing the exact relationships between individual atomic abundances and photometric colors. The computational efficiency of the fitting process is attained by identifying the components of the stellar models that are most sensitive to particular elements, and recalculating them only when the abundances of those elements are updated.

In this dissertation, I describe applications of my modelling framework to the oldest stars in the universe from the elusive Population III to the ancient members of the nearby globular clusters ω Centauri and 47 Tucanae. I present predicted colors of metal-free stars at high redshift as they may be observed by the recently launched James Webb Space Telescope (JWST) under favourable gravitational lensing. These future observations or lack of thereof will provide strict constraints on the mass function, formation and supernova yields of the first stars. My models reproduce the entire color distribution of the main sequence stars in the globular cluster 47 Tucanae and provide a theoretical baseline for the ongoing observing campaigns with JWST that are expected to uncover the substellar cooling sequence of the cluster. The new theoretical isochrones, tailored to the chemical composition of 47 Tucanae, allow the first detailed analysis of the variation in chemical abundances with stellar mass, which is essential to determine the origin of multiple populations in globular clusters.

Chapter 1

Introduction

1.1 Populations I, II and III

Of the ~ 9000 stars discernible with an unaided eye, fewer than 10% may be described as "blue" (spectral types $\lesssim$ B9, $B-V \lesssim -0.1$); yet, they contribute half of the total luminosity [ESA, 1997; Reed, 1998]. This fact is not surprising on its own, since bluer stars are hotter and, in general, more luminous by the Stefan-Boltzmann law. It was, however, unexpected when the opposite pattern was observed in the Milky Way globular clusters (e.g. M3, M13 and M68, [ten Bruggencate, 1927]; M92, [Hachenberg, 1939]; M4, [Greenstein, 1939]) with red giants outshining the brightest blue stars (presently known to be helium-burning members of the horizontal branch) by nearly 3 visual magnitudes. The first observations of an equivalent phenomenon in the nearby dwarf galaxies [Baade, 1944] led Walter Baade to conclude that stars exist in two distinct populations: the "ordinary" Population I, dominated by blue stars, and the globular cluster-like Population II, dominated by red stars. Figure 1.1 contains a reproduction of Baade's original sketch that illustrates the difference between the two populations in a color-magnitude diagram (CMD), as well as my recreation of the sketch based on theoretical stellar models (Chapters 2, 3 and 4) and modern photometric measurements [ESA, 1997; Gaia Collaboration et al., 2021].

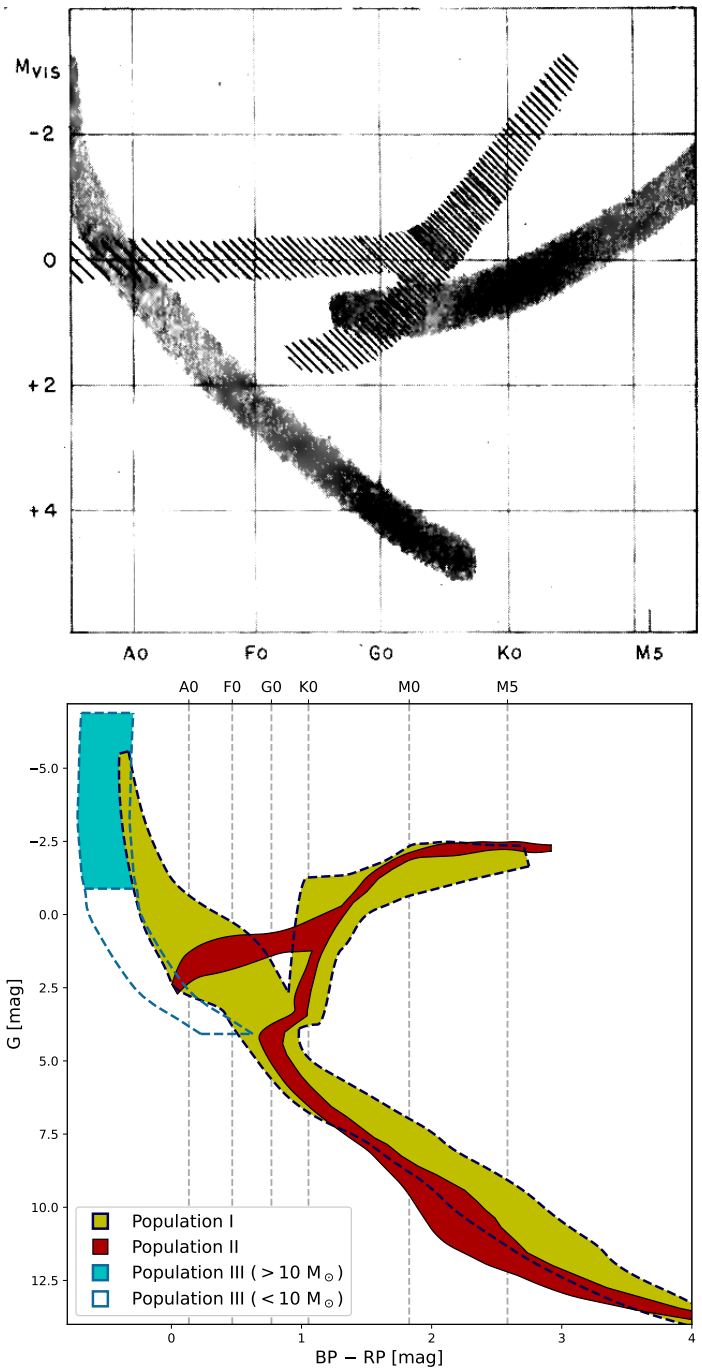

Figure 1.1. *Top:* reproduction of Figure 1 from Baade [1944] that shows the CMD morphology of field stars (shaded) and globular clusters (hatched). *Bottom:* modern recreation of the figure by the author. The CMD of Population I was estimated from Gaia [Gaia Collaboration et al., 2021] and HIPPARCOS [ESA, 1997] photometry. The CMD of Population II is based on the Gaia photometry of ω Centauri and 47 Tucanae above the turn-off point, and stellar models from Chapter 4 below it. The CMD of Population III was derived from the models in Chapter 2.

Baade [1944] also recognized that Population II was not confined to globular clusters and dwarf satellites, but present throughout the galaxy in the form of high-velocity stars, identified by Oort [1926] nearly twenty years prior, that were also characterized by the apparent deficit of the blue spectral types O and B. The nearly uniform absolute magnitude distribution of Population II stars, followed by an abrupt cut-off at a clearly delineated maximum luminosity, hints at a period of rapid formation of these objects during the early stages of galactic evolution [Gamow, 1951; Russell, 1948; Sandage, 1953]. In turn, the high velocities of Population II stars suggest that our galaxy had a "violent" past, characterized by pronounced gas turbulence [Spitzer and Schwarzschild, 1951].

The discrepancy in stellar ages alone is insufficient to explain the observed differences between the two populations. Even before the concept of stellar populations was introduced, high-velocity stars were known to "*cause serious trouble in using the method of spectroscopic parallaxes*" [Morgan et al., 1943] due to their aberrant mass-luminosity relation. A similar property was also attributed to the so-called "*Russell-Moore discordant stars*" [Russell and Moore, 1940] that were noticeably over-luminous for their spectral types[1] [Hynek, 1948a,b], yet lacked the distinct kinematic properties of Population II stars, suggesting the existence of another fundamental parameter that differentiates them from Population I stars [Gamow, 1948]. This parameter is, of course, presently known to be the abundances of elements, directly correlated with stellar age through the chemical evolution of the galaxy.

The spectroscopic peculiarity of the high-velocity stars Arcturus, δ Leporis and κ Arietis was first noted by Morgan et al. [1943] in the form of a contradiction between the subdominant cyanogen (CN) absorption break at 421.6 nm (typically expected in dwarf stars) and the weakened iron (Fe) absorption line at 407.1 nm (typically expected in giants). Through a thorough examination of the spectroscopic evidence accumulated over the course of the decade, Schwarzschild

[1] Note that Hynek [1948a,b] concluded that the discordant stars were significantly more massive than predicted by the mass-luminosity relationship, which is at odds with later studies of Population II stars [Reddish, 1955] and our present understanding of the subject [Salaris and Cassisi, 2005, Ch. 5.5].

et al. [1951] concluded that Population I and Population II stars were indeed chemically distinct with the former presenting a somewhat higher metallicity[2]. A far larger metallicity deficit of up to an order of magnitude was subsequently identified in globular clusters [Baum, 1952] and field subdwarfs[3] [Chamberlain and Aller, 1951]. Schwarzschild and Spitzer [1953] recognized that a discrepancy of this magnitude is inconsistent with a simple rearrangement of the primordial gas in the galaxy, and must be explained in terms of the creation of metals throughout the history of the Milky Way.

Coincidentally, the metallicity of the most metal-poor stars known at the time ($[\mathrm{Fe/H}] \gtrsim -1$, [Chamberlain and Aller, 1951]) was consistent with the predicted protogalactic abundances in the steady-state cosmology [Hoyle, 1954], leading to the initial widespread assumption that Population II stars were the first stellar generation in the galaxy (e.g., [Schwarzschild and Spitzer, 1953; Taketani et al., 1956]). However, the theory of stellar nucleosynthesis [Burbidge et al., 1957], the Big Bang cosmology [Alpher et al., 1948] and the inability of the Big Bang to produce elements heavier than helium in appreciable quantities [Wagoner et al., 1967] eventually led to the mainstream expectation that stars with $[\mathrm{Fe/H}] \ll -1$ must exist in the Milky Way and that the first generation of stars must have been almost completely metal-free. Aller and Greenstein [1960] estimated $[\mathrm{Fe/H}] < -2$ for the star HD 140283 (modern estimate: $[\mathrm{Fe/H}] = -2.39$, [Casagrande et al., 2010]), which was followed by the measurement of $[\mathrm{Fe/H}] \approx -3$ in Wallerstein et al. [1963] for the star HD 122563 (modern estimate: $[\mathrm{Fe/H}] \approx -2.6$, [de Medeiros et al., 2006]). Bond [1970] carried out a dedicated search for extremely metal-poor candidates in the solar neighbourhood that lowered the metallicity floor further with HD 4306 ($[\mathrm{Fe/H}] = -2.89$, [Honda et al., 2004]). In recent years, metallicity measurements as low as $[\mathrm{Fe/H}] < -6$ have been made [Nordlander et al., 2019]; yet, no star has ever been definitively identified as a member of the original generation.

[2] Schwarzschild et al. [1951] attributed this observation to preferential accumulation of dust grains at Population I formation sites, rather than the overall chemical evolution of the galaxy.

[3] Subdwarfs (discovered by Adams and Joy [1922], historically known as "*intermediate white dwarfs*" [Adams et al., 1935]) occupy the region of the CMD between conventional white dwarfs and main sequence stars.

The classic explanation (see the discussion in Chapter 2 for alternative suggestions) for the lack of observable metal-free stars proceeds as follows. As stars form in molecular clouds, the initial masses are primarily determined by two factors: the Jeans mass at the time of fragmentation and the accretion efficiency of the circumstellar material onto the protostar [Bromm et al., 2009]. In metal-rich clouds, the Jeans mass is reduced through efficient radiative cooling by metal atoms and molecules [Omukai et al., 2005]. Of particular importance are species with low excitation energies, including C, C^+ and O due to their low-energy fine-structure lines, and CO due to its significant dipole moment. In the absence of metals, cooling is severely limited since the ground states of H and He lack fine-structure splitting, while the quadrupole energy levels of H_2 are effectively inaccessible at low temperatures ($\lesssim 200$ K). For this reason, primordial molecular clouds are expected to collapse into dense cores of order 1000 $M_\odot$ [Schneider et al., 2002], a significant fraction of which is expected to end up in the forming star, partly due to the lack of radiation feedback on dust grains that reduces the accretion efficiency in metal-rich environments [Wolfire and Cassinelli, 1987]. In this somewhat simplistic picture (ignoring stellar feedback, turbulence, magnetism, multiple star systems, dark matter etc.), the vast majority of the first metal-free stars are expected to be supermassive, perhaps even exceeding 100 $M_\odot$. The correspondingly short lifespans (< 5 Myr, [Windhorst et al., 2018]) would then preclude their existence in the present-day Milky Way.

The stark difference between the properties of these primordial objects and even the most metal-poor Population II stars warrants the addition of a third population to the traditional two. The term "Population III" was first introduced by Woolf [1965], in reference to the evidence of pre-Population II processing of helium in globular clusters [Woolf, 1966; Green, 1966; Page, 1966]. This newly added stellar population was believed to occupy the apparent metallicity gap between the enrichment yield of the Big Bang ($\ll 10^{-9}$, [Iocco et al., 2007; Cyburt et al., 2008]) and Population II stars [Wagner, 1978], and was even considered a dark matter candidate early on [Antonov and Chernin, 1977]! The modern definition of Population III stars varies

from author to author. In many cases, a further distinction is drawn between the first stars in the universe that formed in the absence of external starlight (Population III.1 [McKee and Tan, 2008] or Population IV [Jones, 1983]) and the later (likely still pre-galactic) stars that formed from primordial gas under stellar feedback (Population III.2 [McKee and Tan, 2008] or Population II.5 [Mackey et al., 2003]). In this dissertation, I ignore this distinction and use the term loosely to describe the early generations of stars that formed from nearly metal-free gas, such that the abundance of metals had negligible impact on the star formation process. The term "metal-free" will be used as synonymous and is to be understood as allowing a small tolerance in metallicity.

While no unambiguous observations of Population III stars have been made, the observable properties of these elusive objects may be predicted with theoretical stellar modelling. Using the metal-free evolutionary models and model atmospheres presented in Chapter 2, I was able to mark the approximate CMD location of Population III candidates in Figure 1.1, thereby completing Baade's original diagram with the most recent addition to the classification system.

1.2 Multiple populations in globular clusters

Despite serving as the Population II prototype, nearly all globular clusters exhibit a pattern of chemical evolution that is distinct from the field Population II stars. This phenomenon is referred to as the issue of *multiple populations*, characterized by the apparent division of cluster members into the *primordial* population that is chemically similar to the field Population II stars of equivalent metallicities, and the chemically peculiar *enriched* population(s). In many cases, the distribution of element abundances is multi-modal, resulting in the observed discreteness of sub-populations [Norris, 1987; Norris and Freeman, 1979; Anderson, 1997; Bedin et al., 2004].

The evidence for the presence of multiple populations in globular clusters falls under three broad categories, illustrated in Figure 1.2 and described below in the historical order of discovery.

1. **Spectroscopic evidence of abundance variations** was originally discovered [Lindblad,

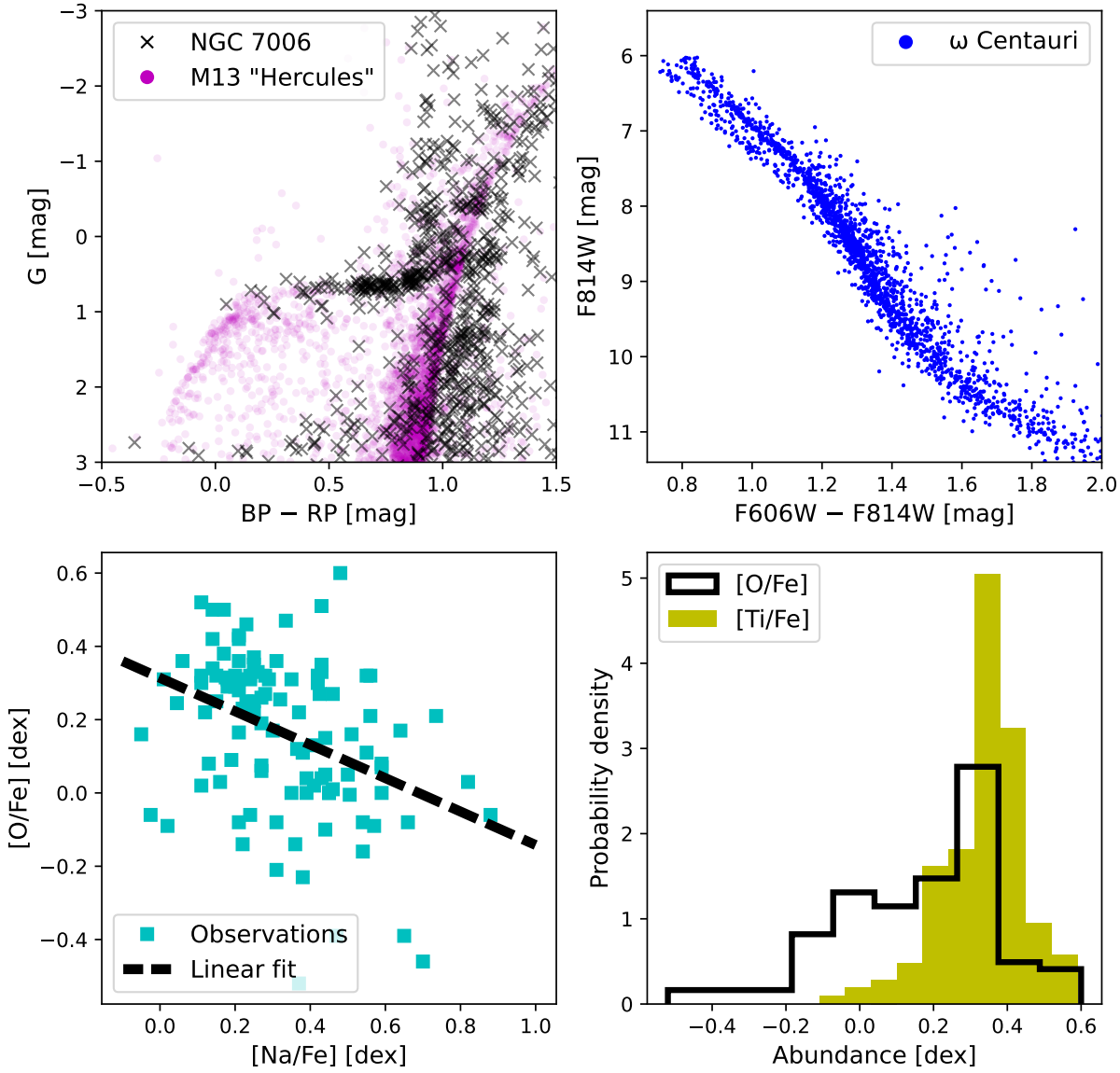

Figure 1.2. *Top left:* Gaia photometry [Gaia Collaboration et al., 2021] (uncorrected for field contamination) of the horizontal branch stars in the globular clusters M13 and NGC 7006. Despite the similar metallicities ($[\mathrm{Fe/H}] = -1.53$ and $[\mathrm{Fe/H}] = -1.52$, correspondingly, [Harris, 1996]), the two clusters have vastly different horizontal branch morphologies, examplifying the second parameter problem. *Top right:* Hubble Space Telescope photometry (see Chapter 3) of the main sequence of the globular cluster ω Centauri. The main sequence exhibits a clear bifurcation at F814W~ 8. *Bottom left:* the Na − O anti-correlation in the globular cluster 47 Tucanae, as revealed by the spectroscopic abundance measurements from Cordero et al. [2014]. *Bottom right:* the distribution of spectroscopic abundances of oxygen and titanium in 47 Tucanae based on the measurements from Cordero et al. [2014].

1922; Popper, 1947] in the form of so-called "*cyanogen discrepancy*" [Keenan and Keller, 1953], i.e. the apparent variation in the strength of CN absorption among cluster members with otherwise indistinguishable spectra. Detailed atomic abundances have since been measured for giant, subgiant and main sequence turn-off stars in the nearby globular clusters (e.g., [Sneden et al., 1992; Thygesen et al., 2014; Cordero et al., 2014; Marino et al., 2012; Yong et al., 2008]). In most cases, multiple populations are evident in the anti-correlation of [C/Fe] and [N/Fe]; and [O/Fe] and [Na/Fe] (Figure 1.2, *lower left*). The abundances of heavier elements, on the other hand, do not generally vary from star to star (Figure 1.2, *lower right*) with the exception of a few "*anomalous clusters*" [Gratton, 1982; Johnson and Pilachowski, 2010; Marino, 2013].

2. **Second parameter problem** refers to the disparity in horizontal branch morphologies (Figure 1.2, *upper left*), exhibited by the CMDs of globular clusters with similar metallicities [Sandage and Wildey, 1967; van den Bergh, 1967], suggesting that some other parameter is necessary to classify globular clusters in addition to [Fe/H]. It has been shown that the color distribution of horizontal branch stars is strongly associated with the abundance spread of multiple populations [Marino et al., 2011].

3. **CMD bifurcation**. The advent of high-precision space-based photometry with Hubble Space Telescope (HST) allowed for the discovery of split main sequences (Figure 1.2, *upper right*) in some globular clusters (e.g., [Anderson, 1997; Bedin et al., 2004]), occasionally extending into later evolutionary stages [Cassisi et al., 2008; Piotto et al., 2012]. Earlier evidence of widened color distributions (e.g., [Rodgers and Harding, 1983]) may also belong to this category.

It must be noted that the peculiar abundance patterns of the enriched population (e.g., the Na − O anti-correlation) have not been observed in open clusters [MacLean et al., 2015] and are extremely rare among field stars [Gratton et al., 2000], such that the occasional exceptions are

generally considered to be a result of globular cluster evaporation [Ramírez et al., 2012; Lind et al., 2015]. We may therefore conclude that the chemical evolution of Population II stars is strongly affected by the scale of the underlying gravitational structure.

Despite many decades of research, the origin of multiple populations remains largely unknown. A detailed summary of existing evidence and proposed theories may be found in numerous reviews of the subject [Bastian and Lardo, 2018; Gratton et al., 2004, 2015; Smith, 1987; Gratton et al., 2019; Milone and Marino, 2022; Dotter, 2013]. Here, I only give an executive summary of the problem in order to provide the necessary context for the later chapters of this dissertation.

We must first establish whether the observed spread in chemistry can be attributed to evolutionary effects (the "*mixing hypothesis*", [Smith, 1987]), such as convective delivery of internally processed material to the surface of the star, e.g., by means of meridional circulation [Sweigart and Mengel, 1979]. Since the original observations were limited to the variations in CNO abundances [Lindblad, 1922; Popper, 1947; Harding, 1962; Wing and Stock, 1973] at a narrow range of evolutionary stages, this interpretation was widely accepted early on [Zinn, 1973; Norris and Bessell, 1975; Dickens and Bell, 1976]. However, it is presently known that the abundance variations extend to heavier elements, including Na and Al [Cottrell and Da Costa, 1981; Norris et al., 1981], and can be observed in stars of all initial masses. Therefore, the mixing hypothesis is considered to be largely ruled out, although more involved versions of this model that attempt to explain the abundances of heavier elements exist in the literature (e.g., [Messenger and Lattanzio, 2002]).

We must also briefly consider the possibility that multiple populations arise from a simple redistribution of metals in the protostellar molecular cloud, which naturally arises in models where different types of dust grains display distinct reactions to the gas turbulence. A variant of this "*turbulent separation*" mechanism was first invoked to explain the observed differences between Population I and II stars [Schwarzschild et al., 1951] and may be operating in globular

clusters to some extent [Hopkins, 2014]. However, this theory cannot reproduce the asymmetry in the distribution of atomic abundances [Bastian and Lardo, 2018], previously observed in spectroscopic surveys (e.g., [Thygesen et al., 2014; Cordero et al., 2014]) and in the photometry of the lower main sequence, as I will demonstrate in Chapter 4.

The last remaining possibility is the presently mainstream "*enrichment hypothesis*" [Smith, 1987], where the enriched material is produced in dying stars and released back into the interstellar medium, analogously to the overall chemical evolution of the Milky Way. The hypothesized sites of nuclear processing include asymptotic giant branch stars [Cottrell and Da Costa, 1981; D'Ercole et al., 2016], fast-rotating massive (> 20 $M_{\odot}$) stars [Decressin et al., 2007a,b], massive close binary stars [de Mink et al., 2009], supermassive stars ($> 10^3$ $M_{\odot}$, [Denissenkov and Hartwick, 2014]) or even the accretion disks around stellar mass black holes [Breen, 2018]. In all scenarios, the release of the enriched material into the interstellar medium must be in the form of low-velocity ejecta such as stellar winds. By contrast, the high-velocity ejecta of supernova explosions are believed to escape the gravitational well of the cluster, which explains the lack of heavy element variations (under this assumption anomalous clusters are required to have a distinct formation mechanism, such as through accretion and tidal stripping of dwarf galaxies, [Hughes and Wallerstein, 2000; Johnson et al., 2020]). It is also advantageous for a proposed processing site to release the enriched material early on ($\ll 20$ Myr) to allow mixing with pristine gas in the cluster in order to reproduce the observed $\mathrm{Na}-\mathrm{O}$ anti-correlation, [D'Ercole et al., 2011]. Since the onset of supernovae is expected to evacuate the cluster of its pristine gas, a later release ($\gtrsim 20$ Myr) of the enriched material would require re-accretion of the ejected gas in most models, which may or may not be efficient enough [D'Ercole et al., 2016].

Once the enriched material becomes available in the interstellar medium, the soon-to-be enriched population of stars must inherit the peculiar chemistry either by forming anew from the processed medium, as is the case in *multiple generation models* (e.g., [Cottrell and Da Costa, 1981; Decressin et al., 2007a; de Mink et al., 2009]), or by acquiring the material through

pollution, as envisioned by *concurrent formation models* (e.g., [Gieles et al., 2018; Bastian et al., 2013; Winter and Clarke, 2023]). In both mechanisms, the total mass of the processed material must be sufficient to produce the observed number of enriched stars, which exceeds the number of primordial stars in most globular clusters [Bastian and Lardo, 2015]. This requirement is challenging to satisfy, since the high-mass stars that produce the enriched material only comprise a small fraction of the overall mass budget [Kroupa, 2001]. The proposed solutions to this so-called *mass budget problem* include non-standard initial mass functions [Prantzos and Charbonnel, 2006; Karakas et al., 2006] (this solution may result in the disintegration of the cluster [Bekki and Norris, 2006]), preferential loss of primordial stars by dynamical evolution [D'Ercole et al., 2008] (this solution is at odds with the measured ejection rates from globular clusters in dwarf galaxies, [Larsen et al., 2014, 2012]) and heavy dilution of the enriched material by the pristine gas retained by the cluster or accreted from the parent galaxy [Bekki, 2023; Bekki and Norris, 2006] (this solution requires a sufficiently long gap in population ages to allow the accretion of gas, which is in tension with observations [Martocchia et al., 2018]). The concurrent formation models are, in general, less susceptible to the mass budget problem due to the large amount of pristine gas retained in the enriched population and the mass dependency of the pollution efficiency that may introduce an upper mass cut-off in the enriched population [Bastian et al., 2013]. On the other hand, a strong advantage of multiple generation models is the natural emergence of discrete populations through the regulation of the star formation rate by stellar feedback [Gerola et al., 1980; Renzini, 2008; Bekki et al., 2017]. The observational diagnostics that may allow these two scenarios to be differentiated are discussed further in Chapter 4.

1.3 Current view and unresolved problems

I would like to conclude this review of stellar populations by describing a plausible evolutionary pathway for the early universe from the beginning of time until the formation of

globular clusters.

13.8 billion years ago [Planck Collaboration et al., 2020], the universe originated in a hot, dense and expanding state. During the first $\sim$ 15 minutes [Tytler et al., 2000], the process of Big Bang Nucleosynthesis [Alpher et al., 1948] produced the primordial baryonic gas, composed of $\approx 24.5\%$ helium and $\approx 75.5\%$ hydrogen [Valerdi et al., 2021], alongside a trace quantity of lithium ($< 10^{-7}\%$, [Cyburt et al., 2008]) and even smaller amounts of other elements [Iocco et al., 2007]. Since the production of carbon and heavier metals in appreciable quantities required triple collisions of helium nuclei [Bethe, 1939], it was too slow to make a significant contribution over such short timescale.

Over the course of the next 0.1 Gyr, $\sim 3\sigma$-overdensities in matter grew into 10^6 $M_\odot$ pre-galactic "minihaloes", where the primordial gas could cool down and collapse into the first Population III stars [Tegmark et al., 1997]. The cooling of gas occurred rapidly at first by radiative emission from H_2 molecules; however, it must have slowed down considerably around 200 K once the lowest excitation states became unreachable [Omukai et al., 2005]. The center of the protostellar cloud then started a runaway collapse, producing a dense core of the size set by the local Jeans mass ($\sim 10^3$ $M_\odot$, [Schneider et al., 2002]). The protostar formed at the center of the core and began accreting the surrounding material until the process was halted by the photoevaporative stellar wind [Hollenbach et al., 1994] with the final stellar mass likely exceeding 100 $M_\odot$ [Abel et al., 2000; Bromm et al., 2002; Yoshida et al., 2006]. The newly formed star exhausted its lifespan in under 5 Myr [Windhorst et al., 2018], eventually exploding as a pair-instability supernova or collapsing directly into a black hole depending on its mass [Heger and Woosley, 2002].

The formation of Population II stars required the metallicity of the interstellar medium to surpass the critical value, $-6 \lesssim [\mathrm{Fe/H}] \lesssim -4$, [Bromm et al., 2001a; Omukai et al., 2005; Schneider et al., 2006a; Clark et al., 2008; Sharda and Krumholz, 2022], at which efficient metal cooling becomes available, allowing the collapse of low-mass cores. Since the expected nuclear

yield of even a single Population III pair-instability supernova may be sufficient to force the transition [Wise et al., 2012b], it seems likely that the metallicity of the interstellar medium reached the level of Population II stars extremely fast. However, no appreciable Population II formation in this epoch is expected due to the dissociation of H_2 (the main coolant) by the ultraviolet radiation from nearby Population III stars [Oh and Haiman, 2002] and the disruptive shocks propagating outwards from the supernova progenitors [Greif et al., 2007]. The formation of additional Population III stars could still proceed in isolated clouds of primordial gas [Whalen et al., 2008], possibly even extending into lower masses (~ 10 $M_\odot$) under special circumstances [Mackey et al., 2003].

During the next $0.2 - 0.5$ Gyr, the minihaloes merged into larger gravitational structures, gradually increasing their virial temperatures. An important transition occurred once the haloes reached $\sim 10^8$ $M_\odot$ in mass, allowing the virialized interstellar gas at $\sim 10^4$ K to cool by atomic line emission [Greif et al., 2008]. These newly formed "atomic cooling haloes" became the sites of first protogalaxies due to their ability to suppress the feedback of ionizing radiation [Dijkstra et al., 2004], thereby allowing widespread star formation to resume. The fast timescale of chemical enrichment probably allowed formation of Population II stars right away; however, Population III stars could coexist in metal-free pockets [Johnson et al., 2008], especially if a significant fraction of the enriched material ended up locked in black holes [Madau and Rees, 2001].

The large-scale hierarchical merging of the first galaxies in combination with the rapid release of gravitational potential through efficient cooling induced extensive turbulence in the interstellar gas [Wise and Abel, 2007]. The reionization of the universe occurring in the same epoch [Ricotti and Ostriker, 2004] may have further contributed to the rapid gas compression through shocks, generated by the inward-propagating ionization fronts [Cen, 2001]. Therefore, the protogalaxies in atomic cooling halos were prime formation sites for the oldest globular clusters, some of which may exceed 13.5 Gyr in age [Bromm and Clarke, 2002] and, in fact, be

older than the Milky Way itself.

The subsequent galactic evolution proceeded in the form of further growth of protogalaxies and mergers between adjacent haloes [Moore et al., 2006; Frebel et al., 2010; Kirby et al., 2008]. The Milky Way in particular was likely assembled from $100-200$ satellites [Bullock and Johnston, 2005], aggregating some 50% of its mass and attaining the Population I metallicity ($[\mathrm{Fe/H}] \sim 0$) over the course of ~ 4 Gyr [Kruijssen et al., 2019]. The accelerated star formation during this time [Madau and Dickinson, 2014; Förster Schreiber and Wuyts, 2020], in combination with additional turbulence induced by frequent merger events, provided appropriate conditions for the formation of younger globular clusters [Kim et al., 2018]. The newly forming clusters may have originated in the Milky Way or were inherited from the satellite galaxies [Forbes et al., 2018]. Eventually, the internal chemical evolution of globular clusters branched away from the rest of the galactic halo, producing the observed multiple populations (Chapter 1.2).

This dissertation is primarily concerned with two fundamental problems, stemming from the general view described above.

1. **How did the initial stellar mass function evolve during the early history of the Milky Way?** The feedback from supermassive Population III stars is responsible for both the original chemical enrichment in the universe and the delay of Population II emergence. However, the assumed top-heavy mass function of metal-free populations is inferred from purely theoretical considerations. Recent re-evaluations of early star formation with more detailed physical models have challenged this assumption by allowing formation of $\gtrsim 10\ M_\odot$ Population III stars (e.g. [Hosokawa et al., 2011; Stacy et al., 2012; Hirano et al., 2015, 2014]) or even $< 1\ M_\odot$ stars (e.g. [Stacy et al., 2016; Susa et al., 2014; Greif et al., 2011; Clark et al., 2011]). Furthermore, the chemical patterns observed in extremely metal-poor stars do not match the predicted yields of pair-instability supernovae [Umeda and Nomoto, 2002; Nomoto et al., 2005] that are considered typical for supermassive stars. Even in the case of top-heavy Population III stars, the enrichment yield depends on the

fraction of stars that evolved into black holes, which cannot be determined without a more well-defined mass function. In contrast, the mass budget problem in globular clusters may be alleviated by a more top-heavy initial mass function than commonly assumed [Prantzos and Charbonnel, 2006; Karakas et al., 2006].

2. **What mechanism is responsible for the scale-dependence of chemical evolution?** The chemical signatures of multiple populations in globular clusters, as summarized in Chapter 1.2, have not been observed in the galactic halo or open clusters. In the hierarchical assembly history of our galaxy described above, the characteristic mass scale of constituent "building blocks" has evolved by some 6 orders of magnitude from the first minihaloes to the present-day mass of the Milky Way. A better understanding of the scale-dependence of chemical enrichment is therefore imperative in studies of galactic evolution, and globular clusters provide an ideal probe of this complex process.

As will be demonstrated in subsequent chapters, considerable progress in resolving these issues can be made by taking advantage of new observables, made available by the recent launch of the James Webb Space Telescope (JWST): direct detection of Population III stars at high redshift and photometry of ultracool dwarfs (UCDs) in globular clusters. Chapter 2 of this dissertation explores how the mass function of Population III stars can be measured or constrained with JWST, depending on whether a significant fraction of metal-free stars was supermassive in origin. The properties of UCDs and, in particular, Population II UCDs in globular clusters are reviewed next.

1.4 Ultracool dwarfs

Ultracool dwarfs (UCDs) are the lowest-mass ($\lesssim 0.1$ $M_\odot$) main sequence stars (spectral types M7 $-$ L3) and brown dwarfs ($\gtrsim$ M7) that occupy the faintest reach of the Hertzsprung–Russell Diagram (see Fig. 1.3, *left*). While only a few thousand UCDs have been discovered so far

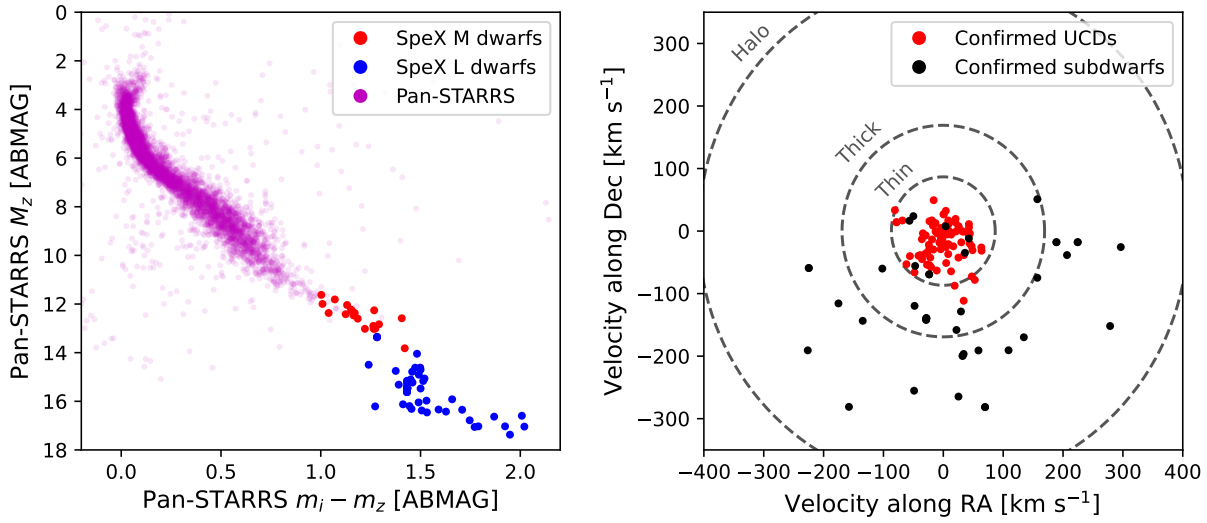

Figure 1.3. *Left:* The location of spectroscopically confirmed UCDs from the *SpeX Prism Library* [Burgasser, 2014] in the color-magnitude diagram from *Pan-STARRS* photometry [Chambers et al., 2016]. *Right*: The tangential velocity distribution of spectroscopically confirmed UCDs and ultracool subdwarfs from the *SpeX Prism Library*, transformed to the local standard of rest [Coşkunoğlu et al., 2011]. The characteristic dispersions of the thin disk, thick disk and halo are shown for comparison as adopted in Bensby et al. [2003]. Based on astrometry from *Gaia DR3* [Gaia Collaboration et al., 2021].

[Schmidt et al., 2015; Best et al., 2020], recent volume-complete surveys (e.g. [Kirkpatrick et al., 2021]) and star formation studies (e.g. [Mužić et al., 2017]) indicate that UCDs are among the most common object types in the galaxy, accounting for 20% to 50% of the stellar census.

Due to their unique properties, UCDs are excellent probes of old, chemically peculiar stellar populations, such as those found in the Milky Way globular clusters. The dominant molecular opacity in cool atmospheres makes their spectral energy distribution particularly sensitive to stellar parameters [Marley et al., 2002], allowing the determination of chemical abundances from lower resolution and lower signal-to-noise ratio spectra than those required by "warmer" stars, or even multiband photometry. Since molecular absorption mostly originates from low-energy roto-vibrational transitions, UCD spectral features are less affected by the non-equilibrium radiation field in the atmosphere [Johnson, 1994] that poses a major obstacle to reliable abundance measurements from the atomic lines of higher-temperature spectra [Bergemann, 2011]. The

interiors of UCDs are fully mixed [Chabrier and Baraffe, 1997] and undergo minimal nuclear processing, avoiding the need to correct the inferred stellar parameters for poorly constrained evolutionary effects in higher-mass stars [Messenger and Lattanzio, 2002; Salaris et al., 2020]. The lack of nuclear fusion in brown dwarfs results in long-term cooling of these objects [Baraffe et al., 2003], providing a handle on the age of the parent population that would be otherwise difficult to obtain. The lifespans of UCDs exceed the age of the universe [Laughlin et al., 1997], implying that every UCD ever formed survives to this day.

In addition to the utility of UCDs as superior chemical tracers and cosmic clocks in surveys of stellar populations, certain unresolved problems in galactic evolution and cosmology are specifically suited to cool stars. The variation in UCD kinematics as a function of spectral type may be used to differentiate between the proposed heating mechanisms that determine the present-day structure of the Milky Way [Wielen, 1977; Ryan et al., 2022]. The UCD mass function provides an important diagnostic of the scale invariance in star formation processes [Kirkpatrick et al., 2021]. Brown dwarfs with masses below ~ 70 M_J do not undergo lithium fusion [Rebolo et al., 1992] and are therefore ideal targets for measurements of the primordial lithium abundance that remains a key unresolved problem in chemical evolution [Fu et al., 2015].

Finally, I would like to note that the close separations between cool stars and their habitable zones make UCDs preferred candidates in astrobiological exoplanet searches [Becerril et al., 2010; Bolmont et al., 2017]. Our ability to reliably diagnose the surface conditions of potentially habitable worlds rests on the availability of accurate evolutionary models for their UCD hosts, as well as our understanding of the UCD magnetospheres that differ substantially from those of sun-like stars [Chabrier and Küker, 2006]. Therefore, the study of UCDs with different metallicities, such as those found in globular clusters, may have fundamental astrobiological implications.

Faint luminosities of UCDs pose a major challenge to their discovery and characterization. At present, only a few thousand candidates have been spectroscopically confirmed [Best et al., 2020; Wang et al., 2022; Schmidt et al., 2015], of which the vast majority belong to Population I

and have near-solar chemical abundances. By contrast, the much older, metal-poor and often chemically peculiar UCD members of Population II are far less explored [Burgasser et al., 2007b; Gizis, 1997]. These objects represent the earliest generations of star formation in the Milky Way, and are of paramount importance to the study of early chemical evolution. Recent dedicated searches for these so-called *ultracool subdwarfs* in the optical regime [Lodieu et al., 2012, 2017] have brought the total object count to over a hundred. In the galactic field, ultracool subdwarfs are often distinguished by their large velocities (Figure 1.3, *right*).

Modelling low-temperature atmospheres characteristic of UCDs is particularly challenging due to the highly debated cloud formation processes that vary with effective temperature [Helling et al., 2008]. Refractory species offset chemical equilibria, deplete the abundances of gaseous molecules, and introduce infrared opacity through absorption and scattering of photons off dust grains. The condensation of silicate dust at $T_{\rm eff} \lesssim 2000$ K is believed to be responsible for the observed reddening in photometric colors [Allard et al., 2001]. The effect subsides abruptly at $T_{\rm eff} \approx 1200$ K, as the grains are transported [Tsuji and Nakajima, 2003; Burgasser et al., 2002] away from the spectrum-forming region of the photosphere, giving way to more complex chloride and sulfide clouds [Morley et al., 2012]. The effect of clouds on the spectral energy distribution is often hard to separate from the chemical peculiarity [Burgasser et al., 2008; West et al., 2011], which is exacerbated for brown dwarfs with significantly non-solar abundances, such as those that belong to Population II. The diverse environments of globular clusters provide a unique opportunity to explore cloud formation at non-solar chemistry over a wide range of stellar masses.

Ongoing and future JWST campaigns will measure the colors of brown dwarfs in globular clusters over a wide range of temperatures, allowing a more rigorous evaluation of cloud models. Unlike the field brown dwarfs, for which the chemical makeup is not *a priori* known, the composition of globular cluster brown dwarfs is expected to approximately match that of the lower main sequence (at least in the primordial population, see below), since both low-mass stars and brown dwarfs are coeval and undergo minimal nuclear processing. Furthermore, the

range of brown dwarf effective temperatures covers multiple distinct cloud regimes, allowing a direct comparison of model accuracy among them. The chemical diversity of globular clusters allows characterization of clouds over a wide variety of Population II abundances, contrary to the population of field brown dwarfs that are generally much closer to the solar standard [Jurić et al., 2008].

Globular clusters are most commonly dated by comparing the main sequence turn-off point to model isochrones. This approach suffers from degeneracies between the age of the cluster and other parameters, including interstellar reddening, metallicity [Carretta et al., 2000], and the convective properties of stars [Valcin et al., 2021]. Unsurprisingly, the resulting estimates often display systematic errors in excess of 1 Gyr (e.g., Rennó et al. [2020]). Improving the accuracy of globular cluster ages is required for studies of the overall chemical evolution of the Milky Way. Observations of brown dwarfs in globular clusters provide an independent probe of globular cluster ages that may be used in conjunction with the turn-off measurements and other dating techniques to break the parameter degeneracies. The luminosity function of a globular cluster features a wide *stellar/substellar* gap between the lowest-mass stars and the highest-mass brown dwarfs. The gap increases with the age of the cluster as the brown dwarfs gradually descend their cooling curves in the absence of steady-state fusion. Refined age estimates can be obtained from this gap by fitting synthetic luminosity functions to the observed magnitude distribution.

UCDs in globular clusters provide a new test of the proposed theories of multiple populations. In multiple generation models, the compositions of brown dwarfs and lower main sequence stars are expected to match due to minimal nuclear processing in both. Brown dwarf photometry may then be used to derive more precise constraints on the chemical compositions and ages of individual sub-populations that can be directly compared to the theoretical predictions of pollution efficiency and expected nuclear yields. In concurrent formation models, the abundances of the enriched population are expected to vary between stars and brown dwarfs due to the expected dependence of pollution efficiency on stellar mass (see Chapter 4). The primordial population

will not be affected by accretion effects and can be used to differentiate between genuine physical effects and systematic errors.

1.5 Outline of the dissertation

The chapters of this dissertation are ordered by the epoch of the early chemical evolution that is explored within them. Chapter 2 presents a study of direct detectability of Population III stars at high redshifts with JWST. The properties of metal-free stars are thoroughly explored using a new set of stellar models. Chapter 3 details my exploration of the globular cluster ω Centauri that may have formed in one of the atomic cooling haloes at the earliest stages of the hierarchical assembly of our galaxy. I derive the properties of the cluster from the HST photometry of the lower main sequence and make forecasts for future observations with JWST. Finally, a study of the globular cluster 47 Tucanae is presented in Chapter 4. 47 Tucanae is considerably younger than ω Centauri ($\sim$ 11.5 Gyr as estimated in the chapter) and likely formed at a much later stage of Milky Way assembly. This dissertation is concluded in Chapter 5.

Chapter 2

Population III Stars at High Redshifts

2.1 Background

Population III stars are an elusive addition to the two traditional stellar populations identified in Baade [1944]. This yet unobserved population accommodates the earliest and nearly metal-free stars that formed shortly after the Big Bang. Nearly seven decades ago, Schwarzschild and Spitzer [1953] recognized that early stars were likely more massive, luminous and short-lived compared to their present-day Population I and II counterparts. In addition to the earliest chemical enrichment of the primordial gas, Population III stars may have contributed to the cosmic microwave background [Rowan-Robinson, 1983], the cosmic infrared background [Santos et al., 2002; Kashlinsky et al., 2005; Madau and Silk, 2005; Kashlinsky, 2005], the gravitational wave background [Suwa et al., 2007; Kowalska et al., 2012; Kinugawa et al., 2014], reionization and reheating of the universe [Haiman and Loeb, 1997; Cojazzi et al., 2000; Cen, 2003b; Wyithe and Loeb, 2003; Sokasian et al., 2004; Maio et al., 2016] and likely had a noticeable feedback effect on the formation of the first galaxies [Greif et al., 2010; Abe et al., 2021].

Recent searches for extremely metal-poor stars have revealed a sharp cut-off in the metallicity distribution around $[\mathrm{Fe/H}] \approx -4$, with fewer than 50 known objects below this cut-off

[Abohalima and Frebel, 2018]. These include the most metal-poor star known ($[\mathrm{Fe/H}] = -6.2$, [Nordlander et al., 2019]) as well as at least one object with an unmeasured iron abundance and the estimated upper limit $[\mathrm{Fe/H}] \lesssim -7$ [Keller et al., 2014]. However, the comparatively high abundances of other chemical elements (e.g. $[\mathrm{C/H}] \gg -3$ for both stars) challenge the status of these sources as true Population III representatives, unless the observed abundances are acquired from the interstellar medium through selective accretion, as proposed by Johnson [2015].

The lack of identifiable metal-free stars in surveys is consistent with the long-standing theoretical expectation of a top-heavy initial mass function (IMF) that precludes primordial stars from having sufficiently long lifespans to survive until the present day. This expectation is motivated by the lack of metals in the early universe, which leaves H_2 and HD as the only available cooling agents in molecular clouds, thereby suppressing fragmentation and producing unusually heavy stars [Larson, 1998; Maio et al., 2010]. Early numerical simulations (e.g. [Abel et al., 2000; Bromm et al., 2002; Yoshida et al., 2006]) suggested that Population III stars predominantly formed with masses in excess of 100 $M_\odot$ and collapsed into black holes, with the exception of a subset of stars with masses between 140 $M_\odot$ and 260 $M_\odot$ that produced pair-instability supernovae [Schneider et al., 2002; Heger and Woosley, 2002]. Later studies with a more detailed treatment of radiative feedback, interactions between stars, turbulence, etc., have challenged this picture by allowing formation of $\gtrsim 10\ M_\odot$ Population III stars (e.g. [Hosokawa et al., 2011; Stacy et al., 2012; Hirano et al., 2015, 2014]) or even $< 1\ M_\odot$ stars (e.g. [Stacy et al., 2016; Susa et al., 2014; Greif et al., 2011; Clark et al., 2011]) that may exist in the present-day Milky Way, likely disguised by metal-enriched mass transfer from heavier stars [Stacy and Bromm, 2014]. The existence of lower-mass primordial stars enables additional mechanisms of chemical enrichment, potentially explaining the observed inconsistency of the abundance patterns in metal-poor stars with predictions of pair-instability supernova yields [Umeda and Nomoto, 2002]. A distinct hypothetical population of supermassive primordial stars with masses in excess of $10^3 - 10^6\ M_\odot$ has also been proposed as seeds for the supermassive black holes in high-redshift quasars [Fuller

et al., 1986; Muñoz et al., 2021; Woods et al., 2021; Herrington et al., 2022].

Since the majority of Population III stars are expected to have masses between a few tens and a few hundred solar masses, the correspondingly short lifespans ($\lesssim 20$ Myr, [Windhorst et al., 2018]) necessitate direct observation of such objects at high redshifts. The first stars begin to form once the primordial molecular clouds, concentrated around growing dark matter over-densities, cool down sufficiently to become unstable against gravitational collapse. The star formation rate as a function of redshift can be traced in simulations of cosmological hydrodynamics [Xu et al., 2013; Wise et al., 2012b,a; Jaacks et al., 2019]. The first Population III stars are expected to form around $z \approx 30$ (~ 0.1 Gyr after the Big Bang) and the maximum formation rate density ($\sim 10^{-4} - 10^{-3}\ M_{\odot}\ \mathrm{yr}^{-1}\ \mathrm{Mpc}^{-3}$) is attained around $17 \lesssim z \lesssim 10$ ($\sim 0.2 - 0.5$ Gyr after the Big Bang). This result is generally consistent with early reionization optical depth measurements from the Wilkinson Microwave Anisotropy Probe (WMAP) [Spergel et al., 2003; Kogut, 2003; Cen, 2003a], although later WMAP [Bennett et al., 2013] and Planck [Planck Collaboration et al., 2016] measurements have cast doubt on the usability of this parameter as a probe of primordial star formation [Yung et al., 2020]. Population III stars give way to Population II stars once the metal mass fraction (Z) of the interstellar medium reaches a critical value, $Z_{\mathrm{cr}} \gtrsim 10^{-8} - 10^{-6}$ ($Z_{\mathrm{cr}} \gtrsim 10^{-6}\ Z_{\odot} - 10^{-4}\ Z_{\odot}$[1]; [Bromm et al., 2001a; Omukai et al., 2005; Schneider et al., 2006a; Clark et al., 2008; Sharda and Krumholz, 2022]) that allows for efficient cooling and fragmentation of collapsing molecular clouds. The lowest redshift at which Population III stars may be observed remains uncertain as isolated metal-free pockets may last for extended periods of time, producing new Population III stars at later epochs. Population III star formation is expected to continue until at least $z = 6$ (~ 1 Gyr after the Big Bang, [Trenti et al., 2009; Muratov et al., 2013]) and possibly much later under special circumstances [Liu and Bromm, 2020]. Searching for metal-free stars at redshifts as low as $z = 3$ (~ 2 Gyr after the Big Bang) is particularly important given observations of the Lynx arc – a star forming region at $z = 3.4$ with a

[1] Solar metallicity taken as $Z_{\odot} = 0.01$ to the nearest order of magnitude.

Population III-consistent ionization source [Fosbury et al., 2003]; and LLS1249 – a dense gas cloud at $z = 3.5$ with a Population III remnant metallicity [Crighton et al., 2016].

A renewed interest in direct detection of individual Population III stars has developed in anticipation of observations with the next generation of ground- and space-based facilities, in particular the recently launched James Webb Space Telescope (JWST). Using the main sequence properties of Population III stars from the evolutionary calculations in Schaerer [2002] and new metal-free model atmospheres calculated with the `TLUSTY` code [Hubeny and Lanz, 1995], Rydberg et al. [2013] estimated the observable properties of isolated primordial stars at a range of redshifts and stellar masses. Without gravitational lensing, Population III stars appear far too faint to be detected even at the lowest redshift ($z = 2$) and in extremely long exposures (100 hr). Rydberg et al. [2013] also considered the case of a favorable lensed observation through the galaxy cluster MACS J0717.5+3745 – one of the largest gravitational lenses known [Zitrin et al., 2009]. Even in the lensed case, a realistic detection was found to require either an extremely heavy Population III candidate ($\geq$ 300 $M_{\odot}$) or a primordial star formation rate, far in excess of theoretical expectation.

However, very high magnifications (μ) may be attained for brief periods of time in the event of gravitational lensing during a caustic transit. A caustic is the locus of points in the source plane where the determinant of the magnification matrix vanishes, i.e. where a true point source would experience infinite magnification [Narayan and Wallington, 1992]. A compact light source such as an individual star crossing a caustic may experience extreme magnification up to $\mu \sim 10^7$ from a lensing cluster with a continuous distribution of mass under most favorable conditions [Miralda-Escude, 1991]. In practice, microlenses within the galaxy cluster will distort the lens caustics, reducing the maximum magnification to $\mu \sim 10^4$ [Diego et al., 2018; Diego, 2019].

Since larger magnifications require more favorable and increasingly less likely configurations, the true expected magnification in any given survey will strongly depend on the redshift of interest, the number of observable targets, and the scope of the survey itself. For example,

Zackrisson et al. [2015] calculate $\mu \gtrsim 700$ as a realistic magnification estimate for detecting Population III stars in a 100 deg^2 ultra-deep survey. Extreme lensing events with $\mu \gg 10^3$ have allowed for recent discoveries of the most distant individual stars known at $z = 1.5$ ("*Icarus*", $\mu > 2000$, [Kelly et al., 2018]), $z = 2.7$ (currently unnamed, $\mu \gtrsim 10^4$, [Chen et al., 2022]) and $z = 6.2$ ("*Earendel*", $\mu > 4000$, [Welch et al., 2022a,b]). It has been suggested that the last source may in fact be a Population III star [Schauer et al., 2022].

Adopting more optimistic magnifications of $\mu \sim 10^4 - 10^5$, Windhorst et al. [2018] used new metal-free evolutionary tracks calculated with the MESA (Modules for Experiments in Stellar Astrophysics) code [Paxton et al., 2011, 2013, 2015, 2018, 2019] and assumed blackbody emergent spectra to characterize Population III stars in the context of future observations with JWST. The study estimated that a decade-long observational program monitoring up to 30 candidate lensing clusters will be required for a reliable detection.

In this chapter, we contribute to the ongoing effort of predicting future observations of Population III stars using stellar modelling. In particular, we focus on primordial stars with initial masses between 1 $M_\odot$ and $\sim 10^3$ $M_\odot$ on the zero age main sequence (ZAMS). ZAMS properties of Population III stars provide a lower bound on observability since later evolutionary stages are intrinsically more luminous and subjected to less interstellar absorption due to redder colors [Schaerer, 2002; Windhorst et al., 2018]. Additionally, the lower surface gravities of post-ZAMS stars may lead to super-Eddington luminosities in high-mass candidates, requiring detailed modelling of mechanical motion in the atmosphere that falls beyond the scope of this study (however, see [Liu et al., 2021; Yoon et al., 2012]).

We present theoretical color-magnitude diagrams of ZAMS Population III stars in JWST NIRCam filters for a broad range of redshifts based on new metal-free evolutionary models and model atmospheres. The observable properties of primordial stars are analyzed for their dependence on individual opacity sources and non-equilibrium distribution of the radiation field throughout the atmosphere. In particular, we demonstrate that even in the absence of non-

grey opacity sources, Population III atmospheres cannot be approximated as blackbodies and always require detailed modelling. The calculated metal-free physical parameters on ZAMS are compared to their metal-poor counterparts and matched to simple, physically-motivated analytic relationships. The models are also evaluated in the context of the Eddington limit, that is of particular importance at high initial masses.

In this chapter, Section 2.2 describes our modelling toolkit and presents the new atmosphere and evolutionary models calculated in this study. The key physical properties of Population III stars inferred from the models, such as the dependence of stellar evolution on the dominant energy production mechanism and the Eddington limit, are discussed in this section as well. Section 2.3 details our color-magnitude calculations at high redshift and presents the predicted color-magnitude and mass-magnitude relationships for Population III stars in the context of future JWST observations with gravitational lensing. The effect of cosmological parameters on our predictions is also estimated in Section 2.3. The key findings and important shortcomings of this investigation are summarized in Section 2.4. Population III model parameters are tabulated in Appendix A.

2.2 Modeling

2.2.1 Overview of the methodology

In this chapter of the dissertation, predictions of colors and magnitudes of Population III stars are drawn from synthetic photometry of metal-free stellar models at ZAMS. Each model is parameterized exclusively by the initial stellar mass and must account for all relevant physical processes governing the evolution of the star from its pre-main sequence (PMS) phase until steady-state hydrogen fusion. Synthetic photometry is obtained from the evolved emergent spectrum of the star, which is, in turn, calculated by solving the radiative transfer equation at every wavelength throughout the outer layers of the model comprising the stellar atmosphere.

Stellar atmospheres are particularly challenging to model due to the presence of neutral and partially ionized species, resulting in complex, wavelength-dependent opacity from significant non-grey contributions of bound-free and bound-bound sources. At high effective temperatures and extremely low metallicities considered in this work, the effect of non-grey atmospheric opacity on the structure of the stellar interior is expected to be insignificant, avoiding the need for detailed opacity calculations in the evolutionary models. However, the atmospheric opacity must be re-introduced into the model when calculating the final emergent spectrum of the star. We therefore calculate all models in multiple stages. First, evolutionary modelling was carried out from PMS to ZAMS with grey atmospheric opacity. The evolved stellar radii and luminosities were used to derive simple analytic relationships between stellar mass and the ZAMS surface parameters (effective temperature, $T_{\rm eff}$, and surface gravity, $\log_{10}(g)$). Finally, the analytic relationships were evaluated at a broad range of stellar masses (from 1 $M_{\odot}$ to 1000 $M_{\odot}$) and the resulting surface parameters were used as inputs to dedicated model atmosphere calculations with the full opacity treatment and spectral synthesis.

2.2.2 Evolutionary Modeling

We calculated all evolutionary models with the `MESA` code [Paxton et al., 2011, 2013, 2015, 2018, 2019], version 15140. Evolutionary calculations in `MESA` are carried out in adaptive time steps until the chosen termination condition is met. By default, structure equations at each step are solved using the grey atmosphere optical depth-temperature relationship as the surface boundary condition. As will be demonstrated in Chapter 3 of this dissertation, this approximation is satisfactory at effective temperatures ($T_{\rm eff}$) above 5000 K – a condition met by all models considered in this study.

In all evolutionary models, we chose to use $Y = 0.25$ as the approximation for the primordial helium mass fraction based on the Planck measurement in Planck Collaboration et al. [2020], taken to the nearest percent to match the default precision in `MESA`.

At initial masses below 90 $M_\odot$, models are initialized as PMS stars with a central temperature of 5×10^5 K (following [Choi et al., 2016]), uniform chemical composition, and a density profile that satisfies the structure equations and results in the desired stellar mass. At significantly larger initial masses, a convergent PMS solution may not exist. Instead, the 90 $M_\odot$ PMS is used as the starting point and the mass is slowly increased to the required value using the mass relaxation routine provided by `MESA`. As an example, at the initial mass of 1000 $M_\odot$, the relaxation process lasts $\approx$ 1300 yr and results in an object with the central temperature of 72.7×10^6 K.

We extract the ZAMS luminosity and stellar radius from all evolutionary models once their nuclear power output begins to exceed 90% of the total luminosity. The sensitivity of the derived ZAMS parameters on the primordial helium mass fraction (Y) as well as the adopted PMS settings was estimated by computing multiple models at the representative initial masses of 10 $M_\odot$ and 1000 $M_\odot$ for a range of Y values from 0.24 to 0.26; a range of initial central temperatures from 3×10^5 K to 7×10^5 K; and a range of maximum (pre-relaxation) PMS masses from 50 $M_\odot$ to 100 $M_\odot$ (stored in the `max_mass_to_create` variable of the `build_pre_ms_model()` subroutine). We found the effect of PMS settings to not exceed 0.002 dex in both luminosity and radius at ZAMS. The effect of the chosen Y value was slightly larger, reaching 0.02 dex at lower masses. However, neither of the aforementioned uncertainties exceeds the average accuracy of the calculated analytic mass-radius and mass-luminosity relationships (to be introduced below) that were estimated as 0.02 dex and 0.03 dex respectively. Therefore, our results are insensitive to the input parameters within the aforementioned ranges.

We calculated 428 evolutionary models with initial stellar masses ranging from 1 $M_\odot$ to 1000 $M_\odot$ and used the ZAMS radii and luminosities to derive analytical mass-radius and mass-luminosity relationships for Population III stars. Radii of main sequence stars are generally well-described by power law relations assuming that the dominant energy production and transport mechanisms do not vary significantly [Gimenez and Zamorano, 1985; Lacy, 1979; Demircan and Kahraman, 1991]. For stars with solar metallicity, the power law index changes noticeably around

$\sim 1\ M_\odot$ due to the dissipation of the outer convective zone [Kippenhahn and Weigert, 1994, Ch. 22.1] and the transition of the main hydrogen fusion mechanism from the proton-proton chain to the carbon-nitrogen-oxygen (CNO) cycle [Salaris and Cassisi, 2005, Ch. 5.2]. The latter effect is particularly important for zero-metallicity stars, as it is expected that enough carbon will be produced at sufficiently high masses to display a similar transition, thereby offsetting the power law break into the range of masses considered in this study. We therefore model the mass-radius relationship of ZAMS Population III stars as a broken power law with the break point mass ($M_{\rm bp}^{(R)}$) treated as a free parameter. The adopted relationship is

$$R \propto \begin{cases} M^{\alpha}, & \text{if } M \leq M_{\rm bp}^{(R)} \\ M^{\beta}, & \text{if } M > M_{\rm bp}^{(R)} \end{cases} \tag{2.1}$$

where M is the initial stellar mass, R is the corresponding stellar radius, and α and β are the proton-proton and CNO power indices respectively. The mass-luminosity (M–L) relationship is slightly more complicated due to the dependence on the dominant pressure support in the interior. High-mass ($M \gtrsim 10\ M_\odot$) stars behave approximately as Eddington standard models ($n = 3$ polytrope; [Eddington, 1918; Köhler et al., 2015]) with the mass-luminosity power index gradually changing from ≥ 3 at $M \lesssim 100\ M_\odot$ to the asymptotic linear relationship ($L \propto M$) in the limit of $M \to \infty$. The transition occurs as the equation of state in the interior changes from the ideal gas law to radiation pressure dominance. To accommodate this additional complexity, we allow the index of the power law to change linearly with $\log_{10}(M)$ below some break point mass ($M_{\rm bp}^{(L)}$), which is treated as a free parameter, as before. The relationship is

$$L \propto \begin{cases} M^{\delta \log_{10}(M/M_\odot)+A}, & \text{if } M \leq M_{\rm bp}^{(L)} \\ M^{\gamma}, & \text{if } M > M_{\rm bp}^{(L)} \end{cases} \tag{2.2}$$

Here, L is the luminosity, γ is the high-mass power law index, δ is the rate of change of

the index in the low-mass regime, and A is a constant, fixed by the requirement of the relationship to remain smooth around the break point,

$$A = \gamma - 2\delta \log_{10}\left(M_{\rm bp}^{(L)}/M_\odot\right) \tag{2.3}$$

The best-fit values of all six free parameters, as well as best-fit normalization factors, are given in Table 2.1. Note that the standard ZAMS mass-radius relationship for Population I (PI) stars has $\alpha_{\rm PI} \approx 0.8$ and $\beta_{\rm PI} \approx 0.57$ ([Popper, 1980], [Kippenhahn and Weigert, 1994, Ch. 22.1]). While the high-mass index matches the Population III value in Table 2.1, the low-mass index is discrepant by a factor of ~ 4. This discrepancy arises because the energy production mechanism transition in Population I stars ($\approx 1.3\ M_\odot$; [Salaris and Cassisi, 2005, Ch. 5.2]) very nearly coincides with the onset of convection in the envelope ($\sim 1\ M_\odot$), while Population III stars maintain radiative envelopes on either side of $M_{\rm bp}^{(R)}$. To compare Population III and Population I mass-luminosity relationships, we consider the average power law index in the $1 \leq M/M_\odot \leq 10$ and $1 \leq M/M_\odot \leq 40$ ranges. The standard values for Population I are 3.88 and 3.35 respectively ([Popper, 1980], [Kippenhahn and Weigert, 1994, Ch. 22.1]), while the corresponding Population III values using Eq. 2.2 and Table 2.1 are 3.87 and 3.50, suggesting that the Population III relationship is nearly identical to its Population I counterpart at low masses and marginally steeper at higher masses.

The mass-radius relationship is plotted in Fig. 2.1 alongside the direct output from selected `MESA` models. For comparison, we also calculated multiple grids of `MESA` models at non-zero metallicities, whose mass-radius relationships are overplotted in the figure as well. The expected broken power law behavior is observed at all considered metallicities; however, the break point occurs at progressively decreasing stellar masses with increasing metallicity due to the larger initial carbon abundance. The point of equality in the energy production rates of the proton-proton chain and the CNO cycle is also indicated in the figure for every mass-radius relationship shown. Note that while the equality point is strongly correlated with the power law break point, the latter

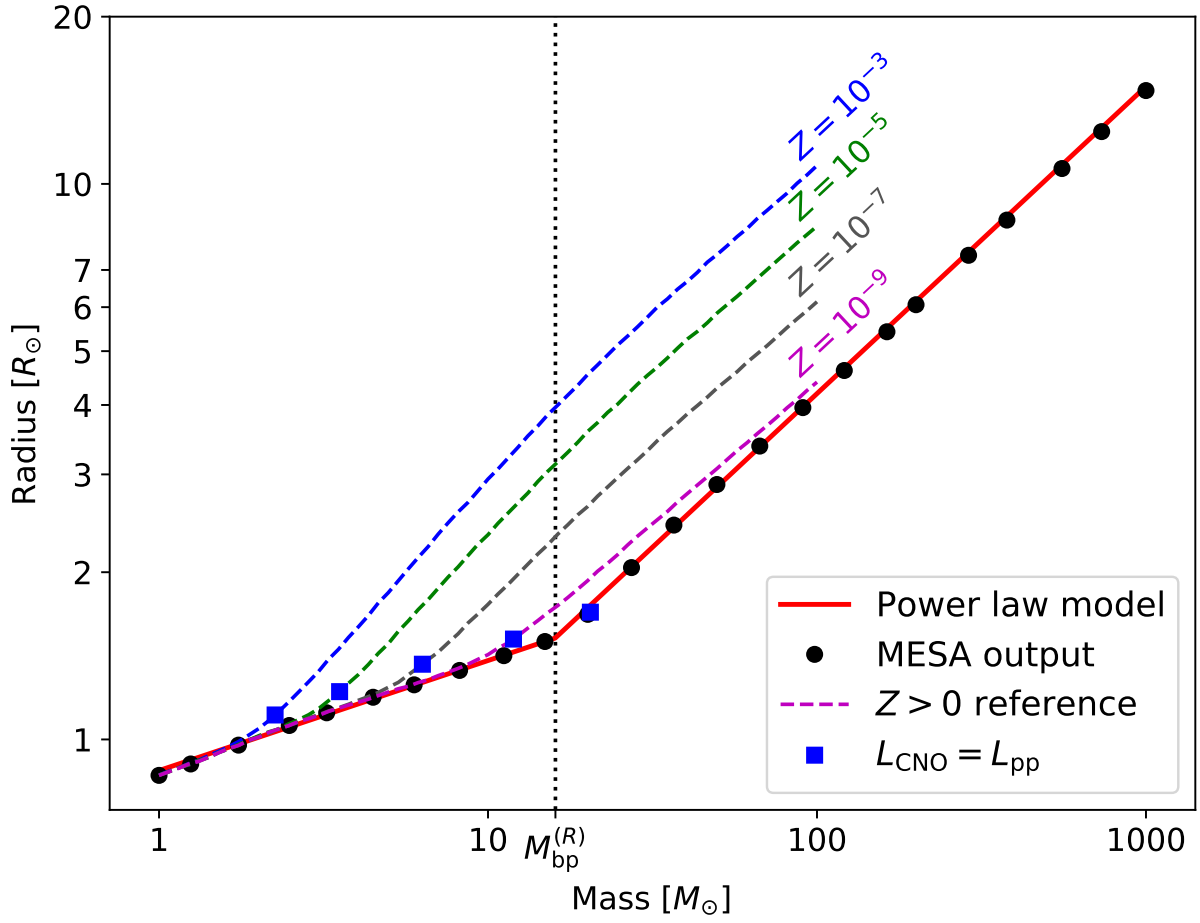

Figure 2.1. Mass-radius relationship from the metal-free evolutionary models calculated in this study alongside the best-fit power law approximation given in Eq. 2.1 and using the best-fit parameters in Table 2.1. Equivalent relationships for non-zero metallicities were calculated as well and are shown with dashed lines for comparison. Each dashed curve is parameterized by the total metal mass fraction, Z. The vertical line indicates the break in the best-fit power law relationship that originates from the onset of the CNO cycle in the core. The point where the energy production rates of the proton-proton chain ($L_{\rm pp}$) and the CNO cycle ($L_{\rm CNO}$) match is indicated with blue squares for every mass-radius relationship shown.

Table 2.1. Parameters of the analytic mass-radius and mass-luminosity relationships for Population III stars

Parameter	Value	Error	
α	0.1982	$\pm$0.0019	
β	0.5527	$\pm$0.0008	
$M_{\rm bp}^{(R)}$	16.03	$\pm$0.11	$M_\odot$
R at 1 $M_\odot$	0.8792	$\pm$0.0034	$R_\odot$
δ	$-$0.6893	$\pm$0.0030	
γ	1.3137	$\pm$0.0080	
$M_{\rm bp}^{(L)}$	153.0	$\pm$2.8	$M_\odot$
L at 1 $M_\odot$	1.850	$\pm$0.023	$L_\odot$

occurs at a lower stellar mass than the former as even a subdominant contribution from the CNO cycle is sufficient to influence the pressure structure within the star. In particular, we calculated the zero-metallicity equality point as $\approx 20.5\ M_\odot$ – over 4 $M_\odot$ higher than $M_{\rm bp}^{(R)}$.

The effective temperature ($T_{\rm eff}$) and surface gravity ($\log_{10}(g)$) are related to L, R and M according to Eqs. 2.4 (Stefan-Boltzmann law) and 2.5, where σ and G are the Stefan-Boltzmann and gravitational constants respectively.

$$T_{\rm eff} = \left(\frac{L}{4\pi\sigma R^2} \right)^{1/4} \tag{2.4}$$

$$\log_{10}(g) = \log_{10} \left(\frac{GM}{R^2\ [1\ {\rm cm\ s^{-2}}]} \right) \tag{2.5}$$

2.2.3 Atmosphere Modeling

Model atmospheres were calculated with version 9 of the ATLAS code [Kurucz, 1970; Sbordone et al., 2004; Castelli, 2005a; Kurucz, 2014]. The code attains high efficiency by sampling opacity from pre-tabulated opacity distribution functions (ODFs), described in Kurucz

et al. [1974] and Carbon [1984]. The ATLAS suite also contains the DFSYNTHE program [Castelli, 2005b] that may be used to calculate ODFs for any given set of abundances, and the SYNTHE code [Kurucz and Avrett, 1981] that computes the emergent spectrum from converged ATLAS models by sampling the opacity directly at the wavelengths of interest. All atmosphere models in this study were calculated at zero metallicity and with a more precise estimate of the primordial helium mass fraction, $Y = 0.2448$, adopted from Valerdi et al. [2021].

For this project, we developed a universal Python dispatcher that combines all three codes (originally written in Fortran) in a single user-friendly pipeline, complete with intermediate consistency checks and comprehensive documentation. Our dispatcher BasicATLAS is available online[2].

ATLAS stratifies the atmosphere into 72 plane-parallel layers spanning the range of Rosseland mean optical depths (τ) from $\tau = 10^{2}$ at the bottom to $\tau = 10^{-7}$ at the top. For all models with stellar masses below 20 $M_{\odot}$, the ODFs were calculated following the "new" format [Castelli and Kurucz, 2003] at 57 temperatures between $10^{3.3}$ K and $10^{5.3}$ K. At higher masses, the range fails to accommodate the deepest layers of the atmosphere that may exceed $10^{5.3}$ K in temperature. As such, a second set of ODFs was calculated with an extended upper temperature limit of $10^{5.85}$ K. For those calculations, the definition of the temperature grid stored in the variable TABT of the LINOP() subroutine in the ATLAS source code was modified according to the altered ODF format. Furthermore, the wavelength grid for opacity and radiation field sampling in ATLAS, that by default spans from ≈ 9 nm to 160 µm, had to be extended, first to 4 nm at stellar masses over 6 $M_{\odot}$, and then to 0.1 nm at stellar masses over 29 $M_{\odot}$. These extensions avoid errors in flux density and opacity integration due to significant contributions outside the default wavelength range. For each model, the adopted wavelength range was validated by ensuring that both the Planck function ($B_{\nu}(T)$) and its derivative (dB_{ν}/dT) drop below 0.1% of their maximum values at the wavelength range bounds in each layer of the atmosphere. The changes were applied to the

[2] https://github.com/Roman-UCSD/BasicATLAS

WBIG variable in the BLOCKR() subroutine of ATLAS.

Atmosphere calculations in ATLAS are carried out through iterative improvements of an initial guess of the temperature profile throughout the atmosphere until a new profile is found that meets both the hydrostatic equilibrium condition for the prescribed surface gravity and the energy equilibrium condition for the prescribed effective temperature. On each iteration, the hydrostatic equilibrium condition is applied first to determine the pressure profile corresponding to the current temperature profile. Energy equilibrium is then evaluated throughout the atmosphere to determine corrections for the current temperature profile as well as the current percentage error in the flux and its derivative in each layer.

Since hydrostatic equilibrium is a hard requirement in ATLAS, no models can be calculated for stars above the Eddington limit – a critical luminosity (or, equivalently, critical effective temperature) above which the radiation pressure gradient begins to exceed gravitational attraction. To determine this limit, we considered the range of gravities between $\log_{10}(g) = 4.6$ and $\log_{10}(g) = 5.2$ and searched for the maximum effective temperature ($T_{\rm eff}^{\rm max}$) at which ATLAS is able to find a solution that is both in hydrostatic equilibrium and has flux and flux derivative errors below 1% over the course of 50 iterations using the grey temperature profile [Mihalas, 1978, Ch. 3],

$$T(\tau) = T_{\rm eff}\left(\frac{3}{4}\tau + \frac{1}{2}\right)^{1/4} \tag{2.6}$$

as the initial guess, where $T(\tau)$ is the temperature at optical depth τ. The calculated values of $T_{\rm eff}^{\rm max}$ showed a nearly perfect exponential dependence on $\log_{10}(g)$ with deviations not exceeding 1% throughout the entire range of considered gravities. The functional form of the relationship is given by

$$\log_{10}(T_{\rm eff}^{\rm max}) = C_1 \log_{10}(g) + C_2 \tag{2.7}$$

where C_1 and C_2 are the best-fit parameters calculated as $C_1 = 0.2516 \pm 0.0013$ and $C_2 = 3.768 \pm 0.006$ for CGS units. Eq. 2.7 is directly comparable to the commonly adopted "classical" Eddington limit ([Mihalas, 1978, Ch. 7-2], [Rybicki and Lightman, 1986, Ch. 1], [Beznogov et al., 2020]) in CGS units, based on grey opacity dominated by Thomson scattering off electrons and local thermodynamic equilibrium (LTE):

$$\log_{10}(T_{\rm eff}^{\rm max}) = \frac{1}{4}\log_{10}(g) + \frac{1}{4}\log_{10}\left(\frac{c\rho}{\sigma n_e \sigma_T}\right) \tag{2.8}$$

Here, c is the speed of light, ρ is the mass density of the atmospheric layer, n_e is the corresponding electron number density, and σ_T is the Thomson scattering cross-section for an electron. When the layer is fully ionized, n_e/ρ only depends on the helium mass fraction:

$$\frac{n_e}{\rho} = 2\frac{Y}{m_{\rm He}} + \frac{1-Y}{m_{\rm H}} \tag{2.9}$$

where $m_{\rm He}$ and $m_{\rm H}$ are the helium and hydrogen atomic masses respectively. The "classical" equivalents of C_1 and C_2, denoted $C_1^{(T)}$ and $C_2^{(T)}$ respectively, can be evaluated numerically as $C_1^{(T)} = 0.25$ and $C_2^{(T)} = 3.795$. Since $C_1^{(T)} \approx C_1$ and $C_2^{(T)} > C_2$, the exact Eddington limit estimated with `ATLAS` is slightly lower than its "classical" counterpart at all considered surface gravities due to additional non-grey opacity sources and non-LTE effects in the atmosphere in the complete treatment.

Eq. 2.7 is plotted in Fig. 2.2 alongside the locus of surface parameters of ZAMS Population III stars derived from our analytic mass-radius and mass-luminosity relationships in Eqs. 2.1 and 2.2. The intersection between the two curves approximately represents the maximum mass of Population III stars with atmospheres in hydrostatic equilibrium, which also serves as the maximum initial stellar mass considered in this study. The maximum mass was calculated as 820.2 $M_\odot$ by gradually increasing the initial stellar mass of the model in increments of 0.1 $M_\odot$ until no convergent atmosphere solution could be found. Figure 2.2 emphasizes the importance

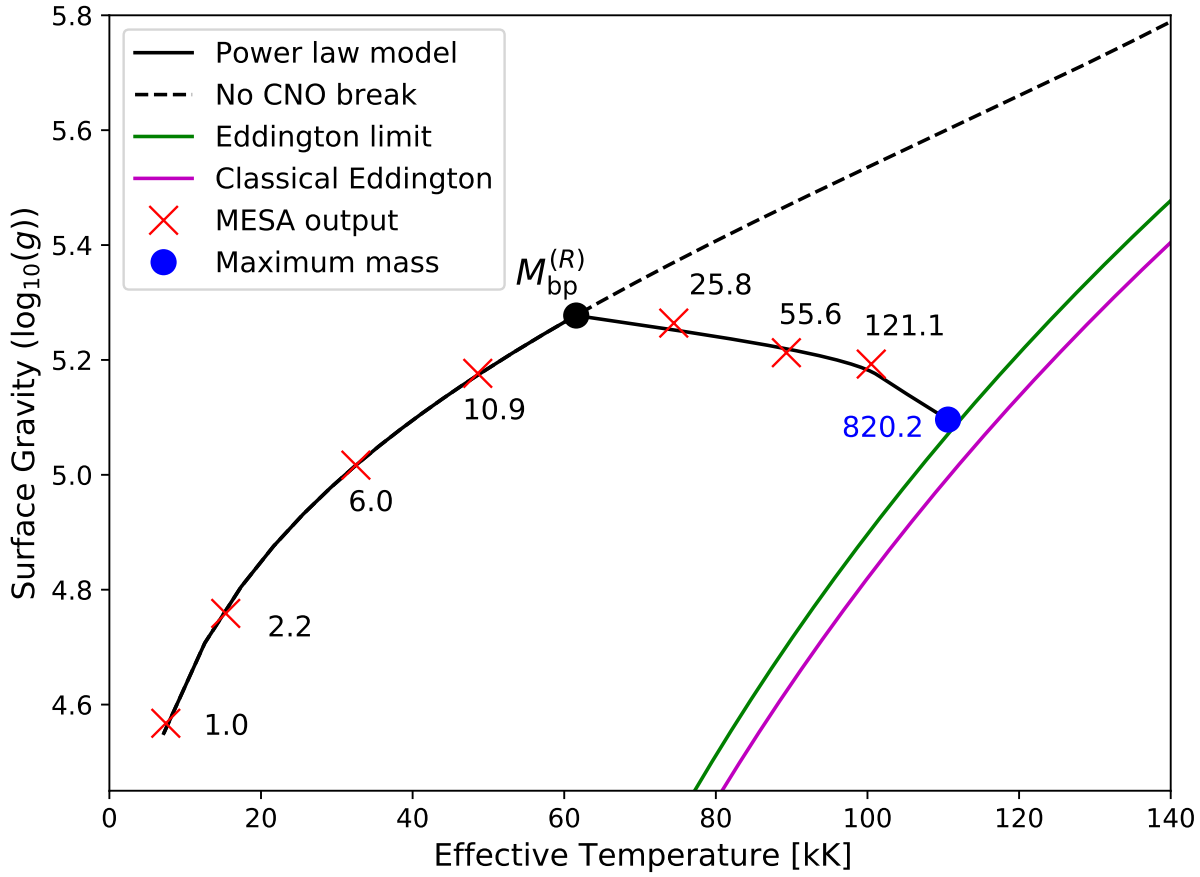

Figure 2.2. Surface parameters of ZAMS Population III stars compared to the exact calculation of the Eddington limit, including non-LTE effects and non-grey atmospheric opacity. The dashed curve traces out an alternative locus of surface parameters in the absence of the CNO break in the mass-radius relationship at $M_{\rm bp}^{(R)} \approx 16\ M_\odot$. Surface parameters extracted directly from selected `MESA` models are shown with red markers and labelled by the initial masses (in $M_\odot$). The maximum stellar mass with a convergent `ATLAS` atmosphere is shown with the blue circle at 820.2 $M_\odot$. The "classical" (grey atmosphere, LTE) Eddington limit from Eq. 2.8 is shown for reference. Note that the exact Eddington limit results in a lower maximum mass value.

of the CNO cycle in Population III stars, as the shape of the surface parameters locus is clearly dominated by the power law break in the derived mass-radius relationship at $M \approx 16\,M_{\odot}$.

Overall, we calculated 59 ATLAS atmospheres, logarithmically sampling the range of initial stellar masses between 1 $M_{\odot}$ and 820.2 $M_{\odot}$ and using the derived analytic relationships for surface parameters. For each model, the number of iterations was incremented in batches of 15 until the maximum flux error and the maximum flux derivative error dropped below the standard convergence requirements of 1% and 10% respectively ([Sbordone and Bonifacio, 2005; Mészáros et al., 2012]; see Appendix A for details). Synthetic spectra for each model were then calculated with SYNTHE between 0.5 nm and 2.6 µm at the resolution of $\lambda/\delta\lambda = 6 \times 10^5$. The chosen wavelength range ensures that the flux density falls below 1% of its maximum value at the range bounds for all calculated model atmospheres. To account for the limited buffer size in SYNTHE, the spectral synthesis for all atmospheres was carried out in three batches: between 0.5 nm and 14 nm; between 14 nm and 400 nm; and between 400 nm and 2.6 µm. The calculations were run in parallel using the *Triton Shared Computing Cluster* [San Diego Supercomputer Center, 2022]. The key properties of all models as well as their convergence parameters are tabulated in Appendix A.

A few representative synthetic spectra are shown in Fig. 2.3. The spectra of stars with $M \gtrsim 50\,M_{\odot}$ display a considerable flux excess blueward of the He II ionization break (≈ 22.8 nm) compared to their corresponding blackbody profiles. Since ultraviolet emission is heavily attenuated by the interstellar medium in the early universe, this effect results in an overall reduction of the observed brightness of Population III stars. The blue excess is primarily caused by non-LTE scattering of photons from deeper (and hotter) layers of the atmosphere. The departures from LTE in the radiation field are shown in Fig. 2.4 for the highest-mass Population III model considered in this study (820.2 $M_{\odot}$) as well as a solar atmosphere model ($T_{\rm eff} = 5770$ K, $\log_{10}(g) = 4.44$, abundances from Appendix C). The figure shows the 5$^{\rm th}$ and the 95$^{\rm th}$ percentiles of the wavelength distribution of the source function (S_{λ}) for the case of LTE ($S_{\lambda} = B_{\lambda}$, no scattering) and the

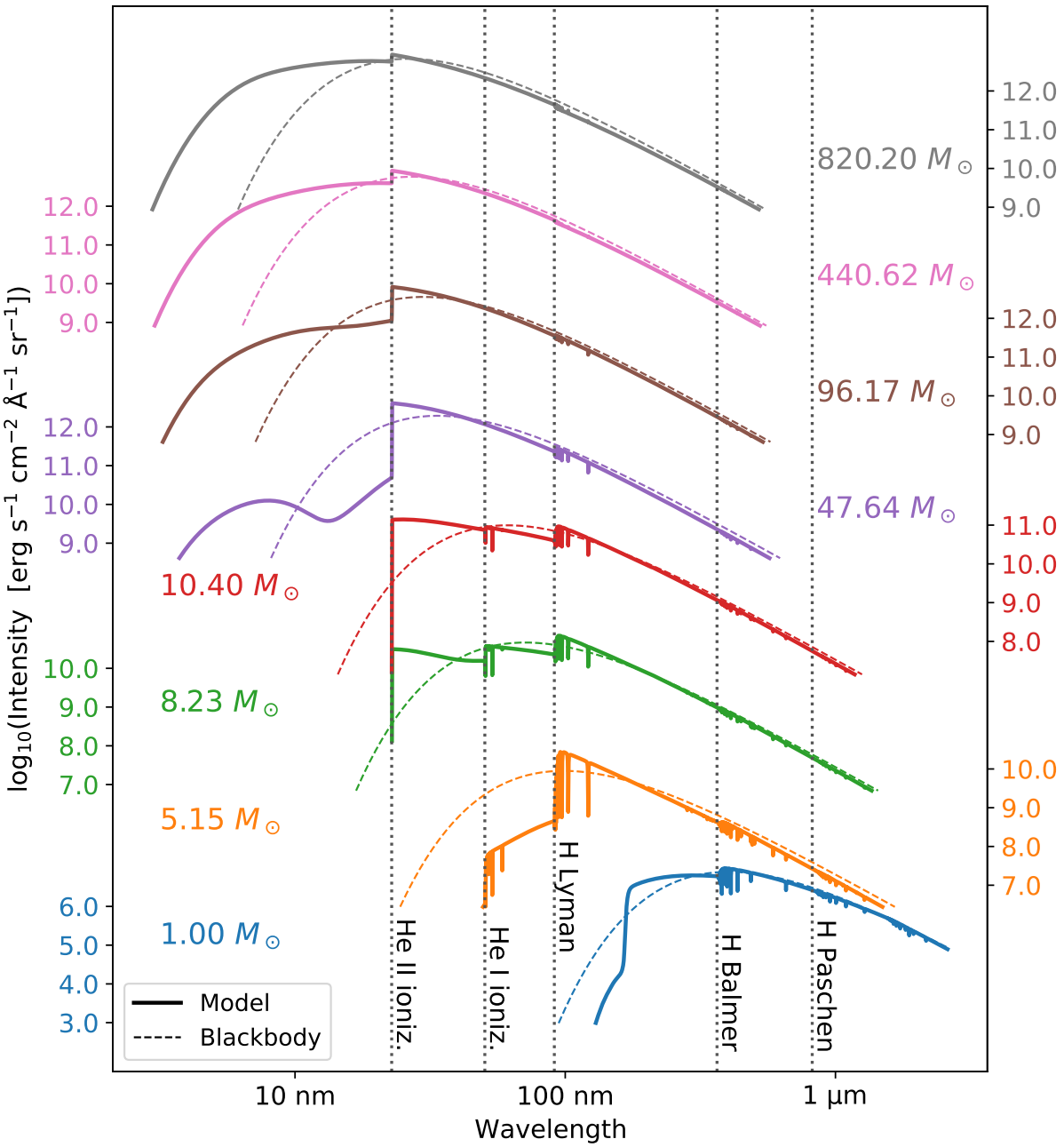

Figure 2.3. Synthetic spectra of ZAMS Population III stars for initial stellar masses between 1 $M_\odot$ and the Eddington limit (820.2 $M_\odot$). For clarity, each spectrum is shown on a separate color-coded vertical scale. The blackbody spectra at the corresponding effective temperatures are shown in dashes for reference. Important bound-free absorption breaks are highlighted with vertical lines and labelled.

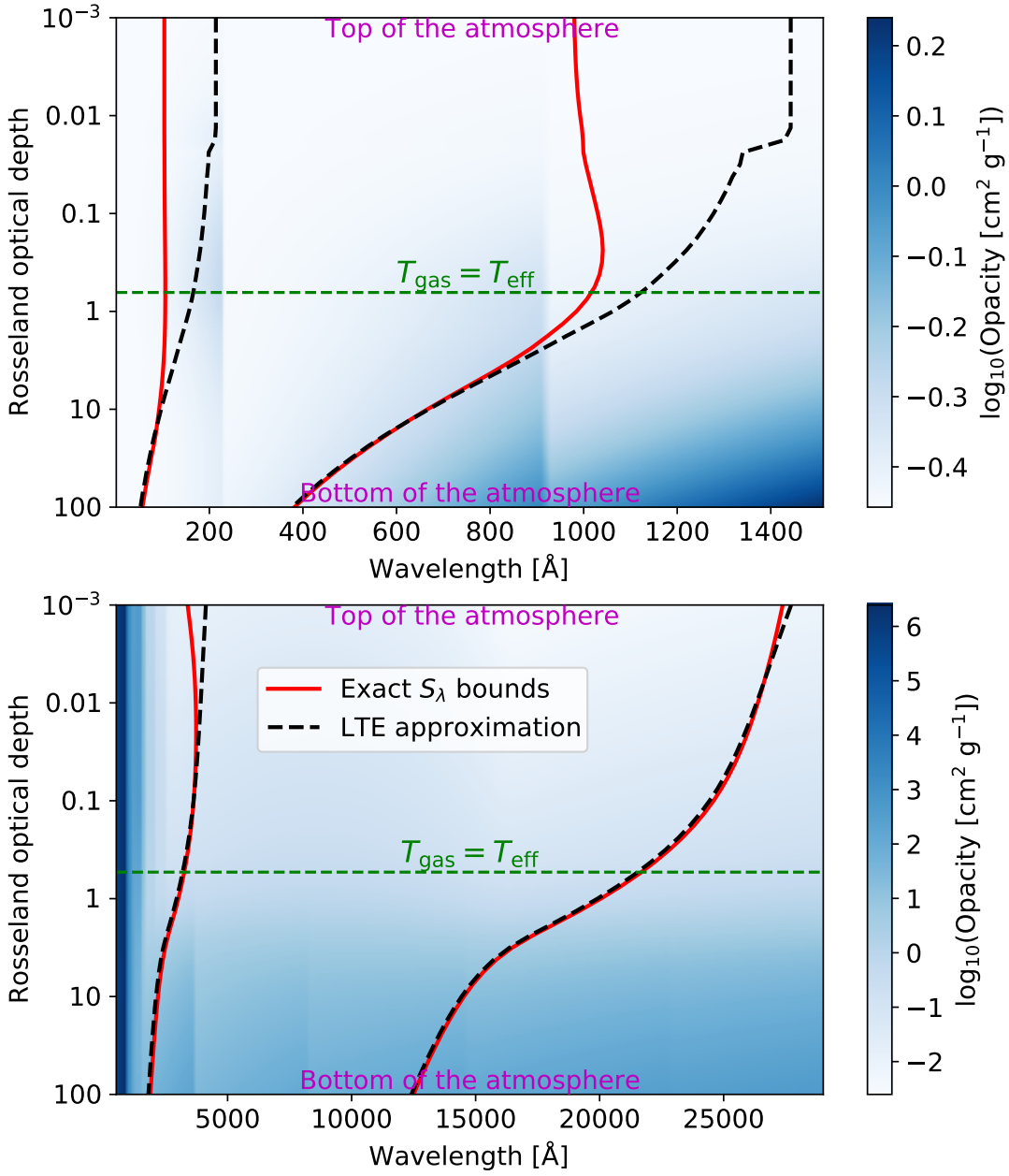

Figure 2.4. The 5$^{\rm th}$ and the 95$^{\rm th}$ percentiles of the wavelength distribution of the source function at a range of Rosseland mean optical depths for the solar atmosphere (*Bottom*) and a near-Eddington Population III atmosphere with $M = 820.2\ M_\odot$ (*Top*). The cases of the exact solution for the source function and the LTE approximation are shown in solid red and dashed black respectively. The optical depth where the gas temperature matches the effective temperature of the star is highlighted for reference. The background color scheme corresponds to the total atmospheric opacity as a function of both wavelength and Rosseland optical depth. The discontinuous changes in opacity are due to bound-free absorption breaks.

complete solution of the integral equation for S_λ [Mihalas, 1978, Ch. 6-1]. For the solar model, both cases are nearly indistinguishable in all but the outermost layers of the atmosphere that do not contribute to the emergent spectrum significantly. On the other hand, the departure from LTE is far more prominent in the Population III atmosphere, with a noticeable blue excess in the radiation field at Rosseland mean optical depths shallower than ~ 10.

The line features in Fig. 2.3 diminish at higher masses due to the reduced populations of neutral species in the atmosphere required for bound-bound absorption. Selected lines may appear stronger than shown here due to unaccounted higher-order NLTE effects (e.g. overpopulation of excited levels as described in [Auer and Mihalas, 1972]), as captured in model sets with a more detailed treatment of NLTE line profiles [Bromm et al., 2001b; Rauch et al., 2018; Rydberg et al., 2013]. However, the impact of narrow line features on broadband synthetic photometry is expected to be insignificant, especially in the JWST bands chosen in this study (see Section 2.3) that mostly occupy the comparatively line-free wavelength interval between the Lyman series of hydrogen and the Fowler series of ionized helium. To verify this claim, we recalculated our synthetic photometry (introduced in Section 2.3) with all line profiles artificially strengthened by the extreme factor of 10. We found that at stellar masses over 100 $M_\odot$, the predicted magnitudes do not deviate from their nominal values by more than 0.003 mag in the chosen JWST bands.

2.3 Observable parameters

Color-magnitude diagrams (CMDs) in Fig. 2.5 and mass-magnitude relationships in Fig. 2.6 are provided for Population III stars in the most efficient JWST transmission bands. All synthetic photometry in this study was carried out in the `ABMAG` system [Oke and Gunn, 1983] from the newly calculated synthetic spectra. For comparison, we also provide equivalent results for blackbody atmospheres at the corresponding effective temperatures.

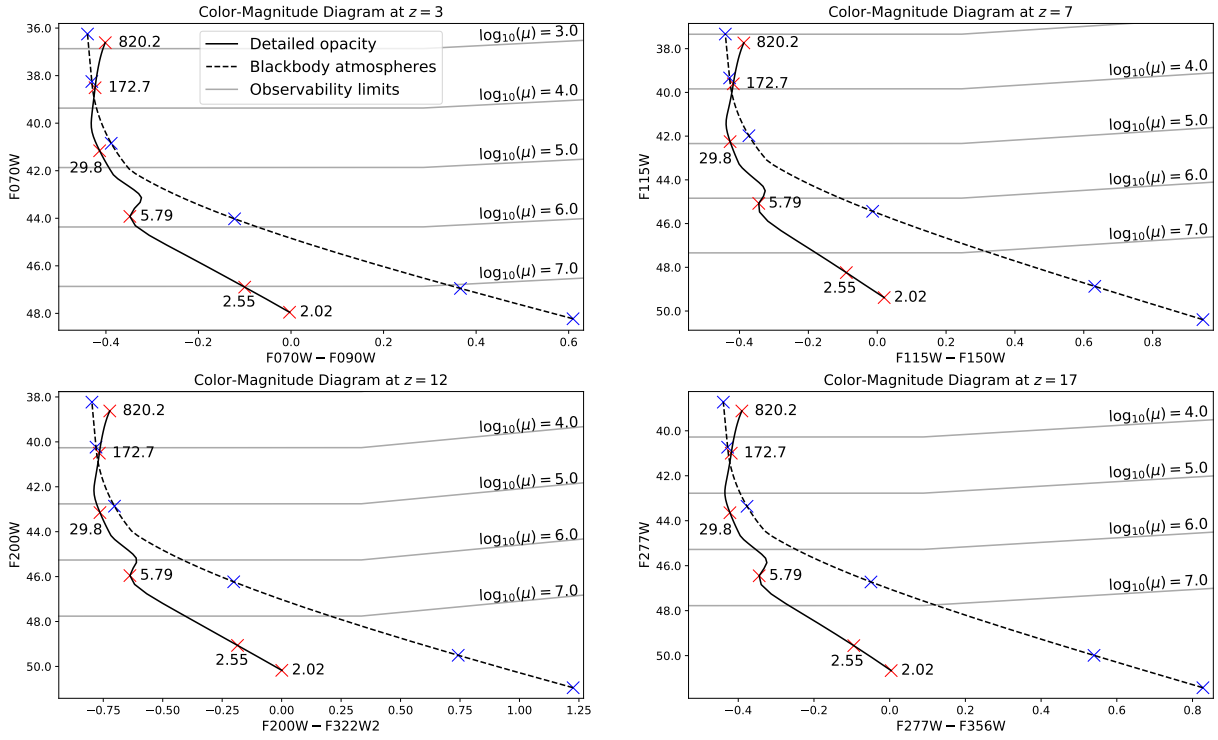

Figure 2.5. Color-magnitude diagrams of ZAMS Population III stars in the most optimal JWST bands listed in Table 2.2 at four different redshifts. Synthetic photometry is shown for both detailed opacity calculations based on model atmospheres and the corresponding blackbody profiles. Selected initial stellar masses are indicated in both cases with red and blue markers respectively. The red markers are labelled in solar masses. The blue markers correspond to the same masses as the red markers in the same order along the color-magnitude curve. Observability limits for JWST are shown in grey and labelled with the required gravitational lensing magnification, μ.

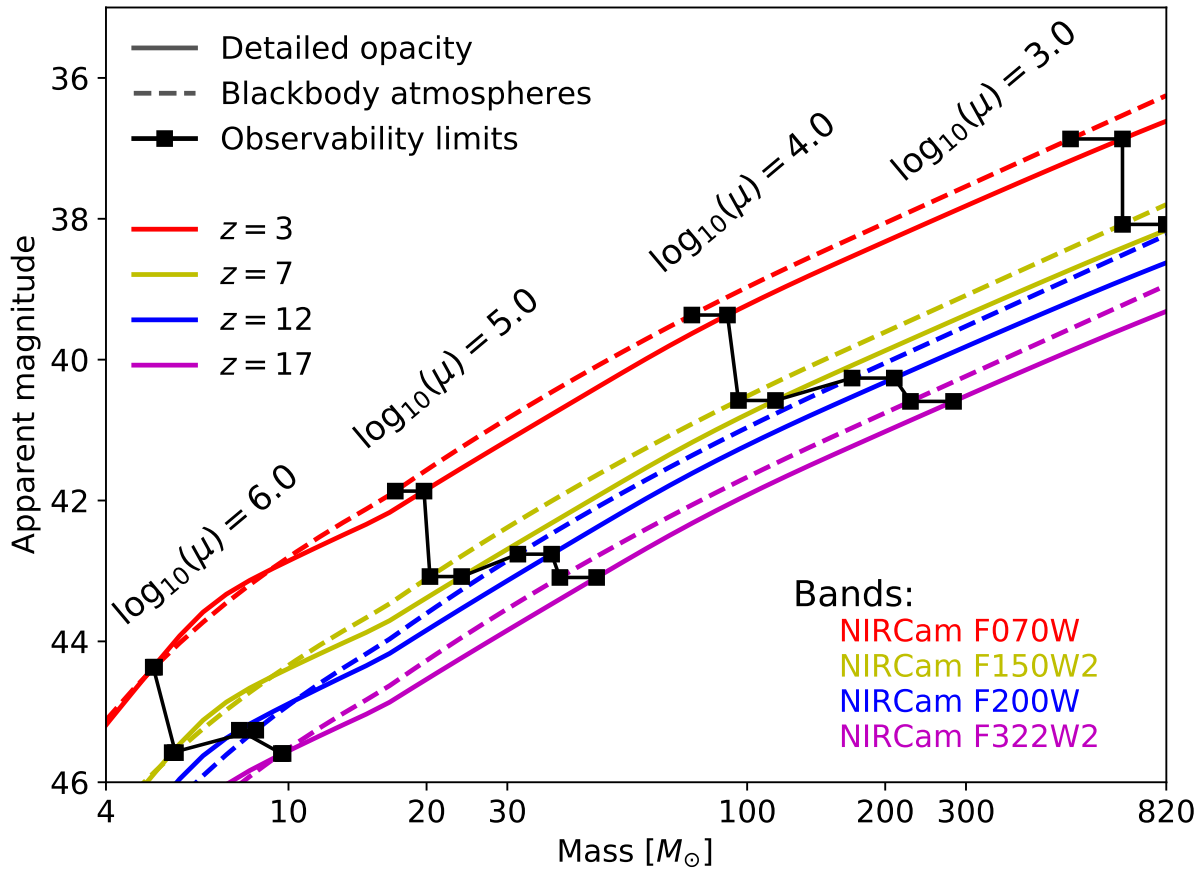

Figure 2.6. Mass-magnitude relationships for ZAMS Population III stars in the most optimal JWST bands listed in Table 2.2 at four different redshifts, color-coded. Note that a different band is used at each redshift. The equivalent relationships for the corresponding blackbody profiles are shown in dashed lines for comparison. The observability limits for JWST are indicated with black markers for each relationship shown. The displayed observability limits are grouped by the required gravitational lensing magnitification, μ.

2.3.1 High-redshift synthetic photometry

In ABMAG, the apparent magnitude, m_{AB}, is calculated from the observed spectrum as:

$$m_{AB} = -2.5\log_{10}\left(\frac{\int(\nu)^{-1} f_\nu(\nu) e(\nu) d\nu}{\int 3631\ \mathrm{Jy}\ (\nu)^{-1} e(\nu) d\nu}\right) \tag{2.10}$$

Here, $f_\nu(\nu)$ is the apparent flux density per unit frequency, $e(\nu)$ is the efficiency of the instrument, and the integrals are evaluated over all frequencies (ν) in the frame of reference of the observer. The factor of $(\nu)^{-1}$ is included to adapt the relationship to a photon-counting instrument [Bohlin et al., 2014]. Equivalently, Eq. 2.10 may be written in terms of the observed wavelength, λ, to match the output of SYNTHE:

$$m_{AB} = -2.5\log_{10}\left(\frac{\int \lambda f_\lambda(\lambda) e(\lambda) d\lambda}{\int 3631\ \mathrm{Jy}\ (\lambda)^{-1} e(\lambda) c d\lambda}\right) \tag{2.11}$$

At high redshift, the apparent flux density, f_λ, in Eq. 2.11 is derived from the modelled surface flux density, F_λ:

$$f_\lambda(\lambda) = F_\lambda(\lambda_e) T(\lambda, z) \frac{R^2}{(1+z) D_L^2} \tag{2.12}$$

(e.g. see [Blanton and Roweis, 2007]), where $\lambda_e = \lambda/(1+z)$ is the emitted wavelength at redshift z, R is the radius of the star and D_L is the luminosity distance to the star. In the equation, $T(\lambda, z)$ is the integrated transmissivity of the interstellar medium across the line of sight to the source. In the wavelength range of interest, the most significant contributions to interstellar attenuation are the bound-free and bound-bound absorption by ground state neutral hydrogen at $\lambda_e \leq 1215.67\,\text{Å}$ – the Lyman α wavelength.

The photons absorbed by the interstellar medium will be re-emitted at longer wavelengths. Depending on the dynamical evolution of the medium under radiative feedback and the spatial density of Population III stars, this reprocessed radiation may contribute significantly to the

observed spectrum of the star or have low impact on direct observations due to dilution over large surface areas (e.g. compare "type A" and "type C" environments in [Zackrisson et al., 2011]; also see [Greif et al., 2009]). In this study, we focus on the purely stellar spectra; however, see Rydberg et al. [2013]; Sibony et al. [2022]; Tumlinson et al. [2003]; Kitayama et al. [2004] for various approaches to detailed feedback modelling.

At $z \leq 7$, we adopt $T(\lambda, z)$ from the numerical simulation in Meiksin [2006]. At higher redshifts, the absorption by neutral hydrogen is sufficiently strong to be well-approximated by a hard cut-off:

$$T(\lambda, z; z > 7) \approx \begin{cases} 0, & \text{if } \lambda \leq (1+z)\ 1215.67\,\text{Å} \\ 1, & \text{otherwise} \end{cases} \tag{2.13}$$

As will be demonstrated, even at redshifts below $z = 7$ considered in this study, the most appropriate JWST bands for detecting Population III stars have blue cut-offs at $\lambda_e \gtrsim 1215.67\,\text{Å}$, thereby ensuring that Eq. 2.13 remains a good approximation at all considered redshifts.

The luminosity distance, D_L, is calculated as a function of redshift as:

$$D_L = (1+z)c \int_0^z \frac{1}{H(z')} dz' \tag{2.14}$$

[Dodelson, 2003, Ch. 2.2] where $H(z')$ is the Hubble parameter [Dodelson, 2003, Ch. 2.4]:

$$H^2(z) = H_0^2 \left(\Omega_r (1+z)^4 + \Omega_M (1+z)^3 + \Omega_\Lambda\right) \tag{2.15}$$

In Eq. 2.15, H_0 is the Hubble constant and Ω_r, Ω_M and Ω_Λ are the fractional present-day contributions of radiation (including relativistic matter), non-relativistic matter, and dark energy, respectively. We adopt the Hubble constant value of $H_0 = 67.4$ km s^{-1} Mpc^{-1} and $\Omega_M = 0.315$ in accordance with Planck Collaboration et al. [2020]. The universe is assumed to be flat ($\Omega_\Lambda = 1 - \Omega_r - \Omega_M$) and Ω_r is calculated as [Dodelson, 2003, Ch. 2.4.4]:

$$\Omega_r = \left(1 + \frac{7}{8}\left(\frac{4}{11}\right)^{\frac{4}{3}} N_{\rm eff}\right) \frac{4\sigma}{c^3} \frac{T_{\rm CMB}^4}{\rho_{\rm crit}} \tag{2.16}$$

We adopt $N_{\rm eff} = 3.04$ [Mangano et al., 2002] as the effective number of neutrino flavors, $T_{\rm CMB} = 2.725$ K [Fixsen, 2009] as the present day temperature of the cosmic microwave background, and $\rho_{\rm crit} = 3/(8\pi G)H_0^2$ as the critical density of the universe. The calculation implicitly assumes massless neutrinos. The accuracy of these cosmological assumptions is examined in Section 2.3.4.

2.3.2 Choice of bands

This study considers detecting Population III stars with JWST at $z \in (3, 7, 12, 17)$. The chosen range spans between the redshift of the predicted saturation of the Population III star formation rate in Xu et al. [2013] and the redshift of the candidate Population III ionization source in Fosbury et al. [2003]. If the aim of the experiment is a simple detection of a Population III candidate in a single band, the optimal observation band for each stellar mass and redshift may be chosen by seeking the largest value of the predicted signal-to-noise ratio. At the lowest stellar masses, this condition will be met by a wide band, situated closest to the peak wavelength of the model spectrum. Due to extensive attenuation of flux by the interstellar medium at wavelengths shorter than the Lyman α, the optimal band at higher masses remains redward of the Lyman α in the observer's frame of reference instead of following the peak wavelength. The transition occurs around $\sim 10\ M_\odot$ for $z = 3$ and at $\lesssim 3\ M_\odot$ for $z \geq 7$. Since high-mass Population III stars are overwhelmingly more likely to be observable, the same high-mass optimal band may be safely employed for all Population III candidates at a given redshift.

We calculated the limiting magnitudes in all JWST Near Infrared Camera (NIRCam) and Mid-Infrared Instrument (MIRI) bands using the JWST Exposure Time Calculator [Pontoppidan et al., 2016] as the faintest magnitudes resulting in a signal-to-noise ratio of 3 in a ~ 10 hr

Table 2.2. Optimal bands for Population III detection

z	Best single	Best pair	
3	NIRCam F070W	NIRCam F070W	NIRCam F090W
7	NIRCam F150W2	NIRCam F115W	NIRCam F150W
12	NIRCam F200W	NIRCam F200W	NIRCam F322W2
17	NIRCam F322W2	NIRCam F277W	NIRCam F356W

Table 2.3. Limiting magnitudes of JWST bands

Band	Limiting magnitude	Band	Limiting magnitude
NIRCam F070W	29.3664	NIRCam F090W	29.6480
NIRCam F150W2	30.5796	NIRCam F115W	29.8404
NIRCam F150W	30.0816	NIRCam F200W	30.2616
NIRCam F322W2	30.5926	NIRCam F277W	30.2774
NIRCam F356W	30.3625		

Note. — Calculated limiting magnitudes are listed for JWST bands in Table 2.2, assuming the detection signal-to-noise ratio of 3 in a $\sim$ 10 hr exposure (20 groups, 9 integrations, DEEP2 readout pattern) of a flat frequency continuum.

exposure (NIRCam: 20 groups, 9 integrations, DEEP2 readout pattern; MIRI: 100 groups, 132 integrations, FASTR1 readout pattern) for a flat frequency continuum. The best band for each redshift was chosen as the one corresponding to the smallest difference between the expected apparent magnitude of Population III stars in the high-mass regime and the limiting magnitude of the band. The chosen bands are listed in the "*Best single*" column of Table 2.2.

A more detailed experiment may be designed with the aim of measuring the colors of Population III candidates in addition to simple detection, requiring a choice of two filters without significant overlap in their transmission profiles. We determine the optimal pairs of JWST filters for each redshift by considering all possible non-overlapping pairs of bands and choosing the one

with the smallest *average* difference between the predicted magnitude of Population III candidates and the limiting magnitude of the band. As before, the choices are made in the high-mass regime. The resulting optimal pairs of filters are listed in the "*Best pair*" column of Table 2.2.

NIRCam bands were found to be most optimal for both simple detection and color measurements. The limiting magnitudes of all bands chosen in Table 2.2 are listed in Table 2.3.

2.3.3 Results

Predicted color-magnitude diagrams are presented in Fig. 2.5 for all four redshifts in the most optimal JWST band pairs listed in Table 2.2. Synthetic photometry for blackbody atmospheres at the same range of effective temperatures is shown in the figure as well for comparison. The overall trend of the color-magnitude relationship is nearly unchanged between redshifts, as the most efficient bands are placed in similar positions with respect to the redshifted energy density distribution predicted by the model atmospheres. At low masses ($M \lesssim 100\,M_{\odot}$), predicted colors shift blueward with increasing effective temperature, with the exception of a brief inversion of the trend around 6 $M_{\odot}$. We refer to this color-magnitude diagram feature as the "*helium loop*", as the inversion is caused by bound-free absorption of singly ionized helium in the second excited state ("Fowler break", $\lambda_e = 205.1$ nm, [Silberstein, 1922]). Once formed, the break disproportionately suppresses flux in the bluer band, resulting in the redder overall color.

In the high-mass regime ($M \gtrsim 100\,M_{\odot}$), the predicted color shifts redward with increasing temperature due to progressively decreasing contributions of free-free and bound-free opacities, both of which vary as λ^3 and, therefore, redistribute the flux towards shorter wavelengths. At high masses, Population III stars are predicted to be slightly fainter than blackbodies with identical effective temperatures due to the non-LTE distribution of the radiation field illustrated in Fig. 2.4.

Magnitude predictions for the most efficient single-band observations at each redshift are shown in Fig. 2.6 as functions of mass. Both Figs. 2.5 and 2.6 also contain the estimated JWST observability limits for different gravitational lensing magnifications, from $\mu = 10^3$ (approximate

Table 2.4. Effect of cosmological parameters on the detectability of Population III stars

	Adopted value	Range		Effect [mag]	
		Min	Max	Min	Max
H_0[a]	67.4	66.9	75.0	$+0.02$	-0.23
Ω_M	0.315	0.300	0.322	$+0.04$	-0.02
m_ν[b]	0.0	0.0	0.9	0.0	-0.15

[a]Hubble constant in km s^{-1} Mpc^{-1}

[b]Neutrino mass in eV c^{-2}, assumed identical for all neutrino species

minimum required magnification for direct observations of Population III stars) to $\mu = 10^7$ (maximum theoretical magnification from [Miralda-Escude, 1991]). The observability limits are based on the calculated limiting magnitudes in each band listed in Table 2.3.

2.3.4 Cosmological parameters

Predicted colors and magnitudes of Population III stars depend on the cosmological parameters adopted when calculating the luminosity distance, D_L (Eq. 2.14). Since D_L is independent of the physical properties of the star, the effect is identical for all initial masses. In this section, we estimate the magnitude of the effect for individual variations in the Hubble constant, H_0; the present-day matter contribution, Ω_M and the average neutrino mass, m_ν. The nominal value of each parameter adopted in this study, the considered range of variation, and the shift in the predicted magnitudes at the lower and upper bounds of the considered range are provided in Table 2.4. All tests are carried out at the largest considered redshift, $z = 17$, where the effect is expected to be most significant.

For the Hubble constant, the adopted range spans from the lower error bound of the adopted nominal value (67.4 ± 0.5 km s^{-1} Mpc^{-1}, [Planck Collaboration et al., 2020]), based on

Planck observations of the cosmic microwave background (CMB), to the upper error bound of the local Hubble constant estimate in Riess et al. [2016] (73.24 ± 1.74 km s^{-1} Mpc^{-1}), based on the updated distance calibration to type Ia supernovae.

The discrepancy between the CMB and local measurements of H_0, known as the *Hubble Tension*, depends on the adopted Ω_M prior. The two measurements have been shown to be consistent at 95% confidence for $\Omega_M \lesssim 0.3$ [Wei and Melia, 2022]. We therefore adopt $\Omega_M = 0.3$ as the lower bound on the variation range and take the error in the nominal value (0.315 ± 0.007, [Planck Collaboration et al., 2020]) as the upper bound.

To estimate the effect of massive neutrinos, we replace the relativistic neutrino density in Eq. 2.16 with the approximation for neutrinos with identical masses in Komatsu et al. [2011], implemented in `Astropy` ([Astropy Collaboration et al., 2013, 2018]). We adopted $m_\nu = 0.9$ eV c^{-2} as the maximum neutrino mass, measured in the Karlsruhe Tritium Neutrino (KATRIN) experiment [Katrin Collaboration et al., 2022].

As demonstrated in Table 2.4, H_0 and m_ν have the largest effect on the predicted photometry. Larger values for both parameters lead to shorter lookback times to a given redshift and, therefore, brighter apparent magnitudes of Population III stars. However, the gain in magnitude for both parameters was calculated to fall below 0.25 at the most extreme, which is expected to remain within the measurement uncertainty at the adopted limiting magnitude signal-to-noise ratio of 3.

2.4 Discussion

In this chapter of the dissertation, we calculated new evolutionary models and model atmospheres for ZAMS Population III stars in hydrostatic equilibrium. The new models were used to investigate the physical properties of the first stars in the universe as well as to produce predictions of their colors and magnitudes as may be observed in the near future with JWST

under strong gravitational lensing. The analysis was carried out at a broad range of plausible redshifts for Population III stars from $z = 3$ to $z = 17$. Our predictions of Population III color-magnitude diagrams and mass-magnitude relations are provided in Figs. 2.5 and 2.6 respectively. All predictions are given for the optimal JWST bands listed in Table 2.2. Our other findings are listed below:

- The mass-radius relationship of ZAMS Population III stars is well approximated by a broken power law, similar to their Population I counterparts. However, the break in the power law occurs at a much higher mass ($\approx 16\ M_\odot$ for Population III stars as opposed to $\approx 1\ M_\odot$ for Population I) due to the suppressed CNO cycle.

- Despite the initial absence of metals in Population III stars, the required amount of carbon to sustain the CNO cycle is produced at sufficiently high masses. The CNO cycle becomes the dominant energy production mechanism in Population III stars around $M \approx 20.5\ M_\odot$, in agreement with Yoon et al. [2012].

- The mass-luminosity relationship of ZAMS Population III stars may be approximated as a power law with a variable power index that decreases at higher masses. This behavior is observed in Population I stars as well and is approximately consistent with the Eddington standard model.

- The evolution of true metal-free stars is nearly indistinguishable from the evolution of extremely metal-poor stars with $Z \lesssim 10^{-9}$. This result is more conservative but consistent with the $Z = 10^{-8}$ limit derived in Windhorst et al. [2018]. Furthermore, both values agree with the lower bound of the expected threshold of the Population III / Population II transition ($Z_{\rm cr} \gtrsim 10^{-8}$; [Omukai et al., 2005; Schneider et al., 2006a; Clark et al., 2008]).

- The maximum mass of ZAMS Population III stars, at which hydrostatic equilibrium is possible in the atmosphere (the Eddington limit) was calculated as $\approx 820\ M_\odot$. This value is

well above the commonly considered range of initial masses for primordial stars, suggesting that hydrostatic equilibrium may be an adequate approximation in Population III models. The exact Eddington limit was found to be slightly lower than predicted by the classical formula (Eq. 2.8) due to non-grey opacity sources in the atmosphere as well as non-LTE effects. The influence of the CNO cycle on the internal structure of Population III stars was determined to be a key factor in setting the maximum mass.

- Atmospheres of high-mass Population III stars host strongly non-LTE radiation fields, resulting in significant excess in the UV flux compared to the corresponding blackbody profiles.

- The color-magnitude diagrams of Population III stars depend strongly on the non-grey opacity sources in the atmosphere with notable features including the "*helium loop*" at $M \sim 6\ M_{\odot}$ and the color-temperature inversion at $M \gtrsim 100\ M_{\odot}$. In general, ZAMS Population III stars are fainter than expected from blackbody profiles.

- At the lowest redshift ($z = 3$), the highest-mass Population III stars considered in this study ($M \gtrsim 700\ M_{\odot}$) are just observable with a gravitational lensing magnification of $\mu \sim 10^3$. A more plausible range of stellar masses ($M \gtrsim 100\ M_{\odot}$) would likely require $\mu \sim 10^4$. Such magnification is comparable to that inferred from previous detections of the most distant individual stars known (e.g. [Welch et al., 2022a]). At higher redshifts, the required magnification for an equivalent detection increases to $\mu \sim 10^5$.

- Our predictions of Population III observability do not depend significantly on the adopted cosmological parameters; however, the maximum calculated effect of ~ 0.25 mag is comparable to the adopted signal-to-noise ratio of JWST observations and may therefore be measurable under more generous gravitational lensing conditions than the minimum detection requirement considered in this study.

This study is limited to ZAMS Population III stars and may therefore be considered a lower limit on true JWST observability since later evolution stages are generally expected to be more luminous and less attenuated by the interstellar medium. The reduction in surface gravity during the post-main sequence evolution of Population III stars may drive the highest-mass stars considered in this study above the calculated Eddington limit, requiring a more detailed modelling approach allowing for mechanical motion in the atmosphere as well as mass loss.

In our predictions of the observational signatures of Population III stars, only radiation emitted directly from the stellar photospheres was considered. Realistic regions of Population III formation are likely to display significant flux contributions from the surrounding interstellar nebula. A follow-up study could deploy an analytic ionization model, as in Sibony et al. [2022], or a numerical simulation of radiative feedback, to derive the necessary corrections. In this context, the predictions drawn here may once again be interpreted as lower limits of the true observability of individual Population III sources.

While the detailed modelling of atmospheric opacity was shown to produce noticeably different results from the commonly adopted blackbody approximation (e.g. [Windhorst et al., 2018; Fosbury et al., 2003]), the quantitative difference in predictions of the two approaches will likely remain within the measurement uncertainty for Population III candidates at the observability threshold (e.g. at $z = 3$, the magnitude difference between the two approaches is ≈ 0.2 mag at the highest considered mass). However, the discrepancy may be detectable under marginally stronger gravitational lensing and should therefore be taken into account in more detailed observational studies of Population III stars.

Our overall result generally agrees with previous studies of Population III observability (e.g. [Windhorst et al., 2018; Rydberg et al., 2013]) that detection of the first stars in the universe may be possible with JWST under strong but realistic gravitational lensing, assuming sufficiently high stellar mass. Placing more specific constraints on the expected rate of detection remains challenging due to the highly debated initial mass function of Population III stars.

Finally, we note that Population III stars likely formed in clusters or galaxies rather than in isolation (e.g. [Jaacks et al., 2019; Zackrisson et al., 2011; Johnson, 2010; Johnson et al., 2009b; DeSouza and Basu, 2015; Visbal et al., 2017]). The combined luminosity of such objects makes them more accessible targets, requiring less extreme gravitational lensing. However, modelling the spectral energy distributions of Population III clusters is further complicated by the dependence on the highly uncertain initial mass function and the concurrent formation of Population III and Population II stars [Xu et al., 2013; Wise et al., 2012b,a; Jaacks et al., 2019] at later epochs.

Chapter 2, in full, was submitted with minor alterations and accepted for publication in the Astronomical Journal Series 2023. An edited version of this chapter is now available in print in Volume 165, Issue 1, authored by Mikaela M. Larkin, Roman Gerasimov, and Adam J. Burgasser. The dissertation author provided the evolutionary models used in the study and made a significant contribution to the detailed analysis of the properties of Population III stars and the required literature research.

Chapter 3

Population II Stars in ω Centauri

3.1 Background

Over $1/6$ [Kirkpatrick et al., 2021, 2012] of the local stellar population consists of brown dwarfs – substellar objects with masses below the threshold for sustained hydrogen fusion ($\gtrsim 0.07$ $M_\odot$ for solar composition, [Hayashi and Nakano, 1963; Kumar, 1962, 1963; Chabrier and Baraffe, 1997]). In contrast to hydrogen-burning stars, brown dwarfs do not establish energy equilibrium and begin cooling continuously shortly after formation, gradually decreasing in effective temperature and luminosity. The characteristically low effective temperatures of such objects ($T_{\rm eff} \lesssim 3000$ K) allow complex molecular chemistry to take place in their atmospheres, which evolves throughout the cooling process as compounds with lower dissociation energy form. At sufficiently low temperatures, species condense into liquid and solid forms, forming clouds of various compositions [Lunine et al., 1986; Tsuji et al., 1996; Marley et al., 2002]. The resulting sensitivity of spectra to elemental abundances and age (through cooling) imply that brown dwarfs have the potential to be used as chemical tracers for studies of galactic populations and the Milky Way at large [Burgasser, 2009; Birky et al., 2020]. Furthermore, the unusual physical conditions characteristic of brown dwarfs, including their low effective temperatures,

high densities [Hatzes and Rauer, 2015], and partially degenerate, fully convective interiors [Copeland et al., 1970; Burrows and Liebert, 1993] provide empirical tests for studies of matter in extreme conditions [Hubbard et al., 1997; Hayes et al., 2020], cloud formation in exoplanetary atmospheres [Kreidberg et al., 2014; Faherty et al., 2016], and even searches for physics beyond the Standard Model [Suliga et al., 2020].

Unfortunately, the faint luminosities and low temperatures of brown dwarfs make these objects challenging to observe, with the first reliable discoveries made only in the mid-1990s [Nakajima et al., 1995; Rebolo et al., 1995; Basri et al., 1996]. While hundreds of brown dwarfs have since been identified, the difficulty of their detection has largely limited the known population to the closest and youngest brown dwarfs in the Milky Way. This limitation poses two major problems. First, current research has been focused on sources with near-solar metallicities and chemical compositions which are not representative of the early evolutionary history of the Milky Way. Second, most of the "evolved" brown dwarfs currently known are isolated objects in the field which lack secondary indicators of their origins and physical properties, such as cluster membership or binary association. The theoretical challenges associated with modelling complex atmospheric chemistry and other low-temperature phenomena inhibits our ability to measure these physical properties accurately.

The population of brown dwarfs in globular clusters of the Milky Way addresses both of these problems. A typical globular cluster contains tens of thousands of individually observable coeval members with similar ages and chemical compositions that can be photometrically inferred from the color-magnitude diagram of the population [Beasley, 2020]. The large masses of globular clusters allow their members to withstand tidal disruptions over extended periods of time, making these clusters some of the oldest coherent populations in the Milky Way ($\gtrsim$ 10 Gyr; [Marín-Franch et al., 2009; Jimenez, 1998]). In general, the long lifespans of globular clusters allow for extensive dynamical evolution: these gravitationally bound stellar systems tend towards thermodynamic equilibrium and energy equipartition, resulting in preferential segregation of

members by mass and ejection of the lowest-mass stars and brown dwarfs [Meylan and Heggie, 1997; Fall and Rees, 1977; Gnedin and Ostriker, 1997; Fall and Zhang, 2001]. However, this effect is noticeably suppressed in the outer regions of globular clusters [Vishniac, 1978; Trenti and van der Marel, 2013], whose relaxation times often exceed the age of the cluster [Harris, 1996] due to increased distances between the stars [Spitzer, 1987, Ch. 2]. These regions therefore preserve their primordial mass function and the mixing ratio between sub-populations within the cluster [Richer et al., 1991; Vesperini et al., 2013; Bianchini et al., 2019].

Unlike field stars in the solar neighbourhood, globular cluster members display chemical abundances characteristic of the early, metal-poor phases of the Milky Way's formation. Globular clusters are thus unique laboratories for studying brown dwarfs with non-solar abundances and old ages – parameters that can be independently constrained from the overall cluster population. In turn, the abundance and cooling behavior of brown dwarfs make them potential instruments for refining the ages of host globular clusters [Caiazzo et al., 2017, 2019; Burgasser, 2004], in analogy to the use of brown dwarfs in age-dating young open clusters [Stauffer et al., 1998; Martín et al., 2018]. Brown dwarfs thus provide a link between (sub)stellar evolution, galaxy formation and evolution, and cosmology (e.g., [Valcin et al., 2020]).

The large distances to globular clusters and the faint luminosities of brown dwarfs have so far prevented the unambiguous detection of this distinct population. Existing deep photometric observations of Milky Way globular clusters, made primarily with instruments on the Hubble Space Telescope (HST), have reached the faint end of the main sequence [Bedin et al., 2001; Richer et al., 2006] and motivated dedicated searches for brown dwarfs in the nearest systems [Dieball et al., 2016, 2019], although results from the latter remain ambiguous. The upcoming generation of large ground and space-based observatories, such as the James Webb Space Telescope (JWST), the Thirty Meter Telescope (TMT), the Giant Magellan Telescope (GMT), and the Extremely Large Telescope (ELT), are expected to change this situation in the next few years [Bedin et al., 2021; Caiazzo et al., 2021]. The promise of observational data for globular

cluster brown dwarfs necessitates development of a theoretical framework for characterizing these sources, in particular evolutionary tracks and model atmospheres across the brown dwarf limit for non-solar abundances.

In this work, we evaluate current HST data and make predictions for forthcoming JWST data for one of the most well-studied globular clusters in the Milky Way: ω Centauri [Halley, 1715; Dunlop, 1828]. This system is the largest known globular cluster (4×10^6 $M_\odot$, 10^7 members; [Giersz and Heggie, 2003; D'Souza and Rix, 2013]) and its dynamics fall far short of complete energy equipartition, as confirmed by direct measurements of the velocity distribution [Anderson and van der Marel, 2010] and constraints on mass segregation [Anderson, 2002]. Our analysis is based on a sample located at 3 half-light radii away from the cluster center where the relaxation time reaches $\sim 4 \times 10^{10}$ Gyr [van de Ven et al., 2006], indicating a nearly pristine primordial population of brown dwarfs and low-mass stars.

ω Centauri possesses two distinct populations, identified in a bifurcation of its optical main sequence into "blue" and "red" sequences [Anderson, 1997; Bedin et al., 2004]. Away from the center of the cluster, the red sequence of ω Centauri is the dominant population with over twice as many members as compared to the blue sequence [Bellini et al., 2009]. Since metal-rich stars generally appear redder than their metal-poor counterparts due to heavier metal line blanketing at short wavelengths [Code, 1959], a top-heavy metallicity distribution in ω Centauri is naively expected. However, this expectation is at odds with earlier spectroscopy of individual bright stars (e.g. [Norris and Da Costa, 1995]) that indicated a bottom-heavy distribution in metallicity among cluster members. By comparing the observed bifurcation to model isochrones, Bedin et al. [2004] determined that the color-magnitude diagram is unlikely to be explained by the spread in metallicity alone, nor by a background object with different chemistry. It was further suggested that the blue sequence may have a higher metallicity than the red sequence if it is significantly helium-enhanced, with a helium mass fraction (Y) in excess of 0.3 [Bedin et al., 2004]. Higher helium content increases the mean molecular weight in stellar interiors, producing hotter and

bluer stars for identical masses and ages.

Subsequent quantitative analysis in Norris [2004] found the helium mass fraction discrepancy between the sequences to be $\Delta Y \sim 0.12$. A follow-up spectroscopic study of identified members of red and blue sequences in Piotto et al. [2005] confirmed that the metallicity of blue sequence members indeed exceeds that of red sequence members by ~ 0.3 dex, strongly favouring the helium enhancement hypothesis. Consistent with all aforementioned results, King et al. [2012] calculated the helium mass fraction of the blue sequence as $Y = 0.39 \pm 0.02$ which remains the most accurate estimate to date (an analysis in [Latour et al., 2021] based on a different selection of sequence members and a different set of evolutionary models suggests that this value may be overestimated by $\gtrsim 0.05$). The origin of such extraordinarily high helium content remains under debate [Renzini, 2008; Norris, 2004; Timmes et al., 1995]. An additional noteworthy aspect of ω Centauri members is the scatter in stellar metallicities within each of the two sequences, which is fairly wide compared to other globular clusters [Bellini et al., 2017c; Johnson et al., 2009a]. This scatter suggests that ω Centauri may be the nucleus of a nearby dwarf galaxy accreted by the Milky Way; or it may be a system intermediate in scale between a dwarf galaxy and a globular cluster [Hughes and Wallerstein, 2000; Johnson et al., 2020; Norris et al., 2014]. Indeed, recent work employing ultraviolet and infrared photometry and benefiting from the enlarged color baselines was able to show that the red and blue sequences are each composed of multiple stellar subgroups, totalling up to 15 distinct sub-populations [Bellini et al., 2017c].

In this chapter of the dissertation, we calculate new interior and atmosphere models for ages and non-solar chemical compositions appropriate for the members of ω Centauri. By comparing synthetic color-magnitude diagrams (CMDs) inferred from those models to new HST photometric observations of the low-mass main sequence ($\lesssim 0.5$ $M_\odot$), we determine best-fit physical properties of the cluster and calibrate for interstellar reddening. Finally, we extend our models into the substellar regime to make predictions of expected colors, magnitudes, and color-magnitude space densities of brown dwarfs in ω Centauri down to effective temperatures of

$T_{\rm eff} \approx 1000$ K. Section 3.2 provides an overview of our approach to modelling the ω Centauri stellar and substellar population. Section 3.3 describes how synthetic isochrones for the members of ω Centauri were calculated, including our choices of specific cluster properties such as age and metallicity. We also briefly examine the role of atmosphere-interior coupling in our evolutionary models and discuss the relation of atmospheric and core lithium abundance predicted by our framework. Section 3.4 describes our astro-photometric observations of ω Centauri with HST. Section 3.5 presents our method of comparing the isochrones against our photometry, and corresponding constraints on the best-fit physical parameters. Section 3.6 provides predictions of the observable properties of brown dwarfs in the cluster in the context of future JWST observations. Section 3.7 summarizes our results. Appendix B describes the parameters of evolutionary models calculated in this study. Appendix C lists our choices of standard solar abundances. Finally, Appendix D provides a description of the HST dataset for ω Centauri used in this study.

3.2 Overview of methodology

For the modelling purposes of this chapter, we define a stellar population as a group of stars and brown dwarfs with identical age, initial chemical composition, and distance from the Sun. While allowing for multiple co-existing populations in ω Centauri, we require all of them to be drawn from the same initial mass function (IMF). The reality of a continuous, rather than discrete, distribution of chemical abundances among the members of the cluster is partly accounted for by allowing statistical scatter in the color-magnitude space (see Section 3.5). Potential variations in age are briefly considered in Section 3.6.

Our first step was to determine the best-fitting isochrone to our optical and near infrared HST observations of ω Centauri (see Section 3.4) that capture most of the main sequence but are not sensitive enough to reach the substellar regime. The multiplicity of populations in ω Centauri necessitated an approximate categorization of the cluster as a whole due to the extreme

computational demand associated with calculating complete grids of model atmospheres and interiors for multiple sets of chemical abundances. We therefore made no attempt to model the observed blue and red sequences separately; instead, we sought to model the modal color-magnitude trend of the entire cluster. Due to the narrow color separation between the two sequences along the stellar main sequence [Milone et al., 2017], we expect the modal trend to predict the colors and magnitudes of brown dwarfs in ω Centauri for both populations.

We started with an initial estimate of chemical abundances based on photometric and spectroscopic analysis of bright members in the literature [Marino et al., 2012]. The helium abundance was set to the value corresponding to the blue sequence of the cluster from King et al. [2012]. As will be demonstrated shortly, the enhanced helium mass fraction in combination with freely varying metal abundances results in a population that provides a satisfactory approximation of the modal color-magnitude trend for *both* red and blue sequences. On the other hand, we found the mass-luminosity relation of the cluster to be far more sensitive to the helium mass fraction such that no modal population could be obtained that would adequately fit the mass-luminosity relations of both red and blue sequences (see Section 3.5). We therefore chose to adopt a distinct mass-luminosity relation for the red sequence from the literature [Dotter et al., 2008] and focus our new calculations on the helium abundance of the blue sequence. This choice was made for two reasons: first, due to the scarcity of helium-enhanced stellar models in the literature; and second, because higher helium content generally results in higher luminosities for the largest-mass brown dwarfs (e.g. compare models B and G in [Burrows et al., 1989]; see also [Burrows and Liebert, 1993; Burrows et al., 2011; Spiegel et al., 2011]). The latter effect makes helium-enriched brown dwarfs more likely to be detected in future magnitude-limited surveys.

We refer to the population based on this initial set of abundances as the *nominal population* of the cluster. A synthetic isochrone was calculated and compared to existing photometry, and the chemical abundances of the nominal population (with the exception of helium) were perturbed iteratively until a best quantitative fit to the modal color-magnitude trend of the cluster was

obtained. We refer to all perturbed populations as *secondary populations*. In line with our simplified model, we assumed that the entire CMD of the cluster could be described with one modal population, with an empirically determined scatter used to account for other sub-populations, multiple star systems, and measurement uncertainty.

Next, we sought to reproduce the observed present-day luminosity function (LF) of the cluster by combining the mass-luminosity relation of the best-fitting isochrone with the commonly used broken power law IMF (e.g. [Kroupa, 2001; Sollima et al., 2007; Hénault-Brunet et al., 2020; Conroy and van Dokkum, 2012]). As explained above, we adopted an additional solar helium mass-luminosity relation from literature [Dotter et al., 2008] and added the contributions of both populations together in the LF using a population mixing ratio optimized through fitting. As demonstrated in Section 3.5, a reasonably good match to the observed LF can be obtained with a simple two-component IMF and two stellar populations. Finally, the isochrone of the calculated best-fit population and the determined IMF were extended into the substellar regime to make predictions for the colors and magnitudes of brown dwarfs expected to be identified by JWST.

The isochrones and mass-luminosity relations for the nominal and secondary populations were calculated from corresponding grids of newly computed model atmospheres and interiors. Simultaneous coupled modelling of atmospheres and interiors is challenging, as the substantial difference in physical conditions between the two requires distinct numerical approaches typically implemented in independent software packages. In addition, atmosphere modelling tends to be orders of magnitude more computationally demanding, largely due to the complex molecular chemistry and opacity present at low temperatures. For those reasons, we followed the standard approach [Baraffe et al., 1997; Choi et al., 2016] in which a grid of model atmospheres is pre-computed, covering the regions of the parameter space the stars are expected to encounter during their evolution. To ensure that the size of the model grid was computationally feasible, we restricted the number of degrees of freedom that are allowed to vary from atmosphere to atmosphere within the same population. The atmosphere grid for each population has been calculated

Table 3.1. Properties of the nominal population of ω Centauri

Parameter			Value
Metallicity	[M/H]	−1.7	dex over solar
Carbon abundance	[C/M]	−0.65	dex over solar
Nitrogen abundance	[N/M]	1.45	dex over solar
Oxygen abundance	[O/M]	−0.1	dex over solar
Age		13.5	Gyr
Helium mass fraction	Y	0.4	
Atmospheric lithium	[Li/M]	−3.0	dex over solar

over a range of effective temperatures ($T_{\rm eff}$) and surface gravities ($\log_{10}(g)$) encompassing the evolutionary states of low-mass stars and brown dwarfs, while all other parameters were assumed fixed across the population (e.g. elemental abundances, age) or derivable from the grid parameters (e.g. stellar radius). A synthetic spectrum was calculated for each model atmosphere in the grid, which could be subsequently converted to synthetic photometry for instruments of interest.

3.3 Isochrones

3.3.1 Initial parameters

The parameters adopted for the nominal population are listed in Table 3.1. All abundances are given with respect to their standard solar values summarized in Appendix C.

The abundances of carbon ([C/M]), nitrogen ([N/M]) and oxygen ([O/M]) were selected to approximate the modes of the distributions inferred from individual spectroscopy of 77 bright ($10.3 < I < 12.7$) cluster members from Marino et al. [2012]. These distributions are shown in Figure 3.1. Contrary to carbon and nitrogen, oxygen abundance lacks a well-defined modal peak and appears to vary in the range $-0.1 \lesssim [\mathrm{O/M}] \lesssim 0.6$. For the nominal population, we chose the lower bound of the oxygen distribution in the figure since the data from Marino et al. [2012]

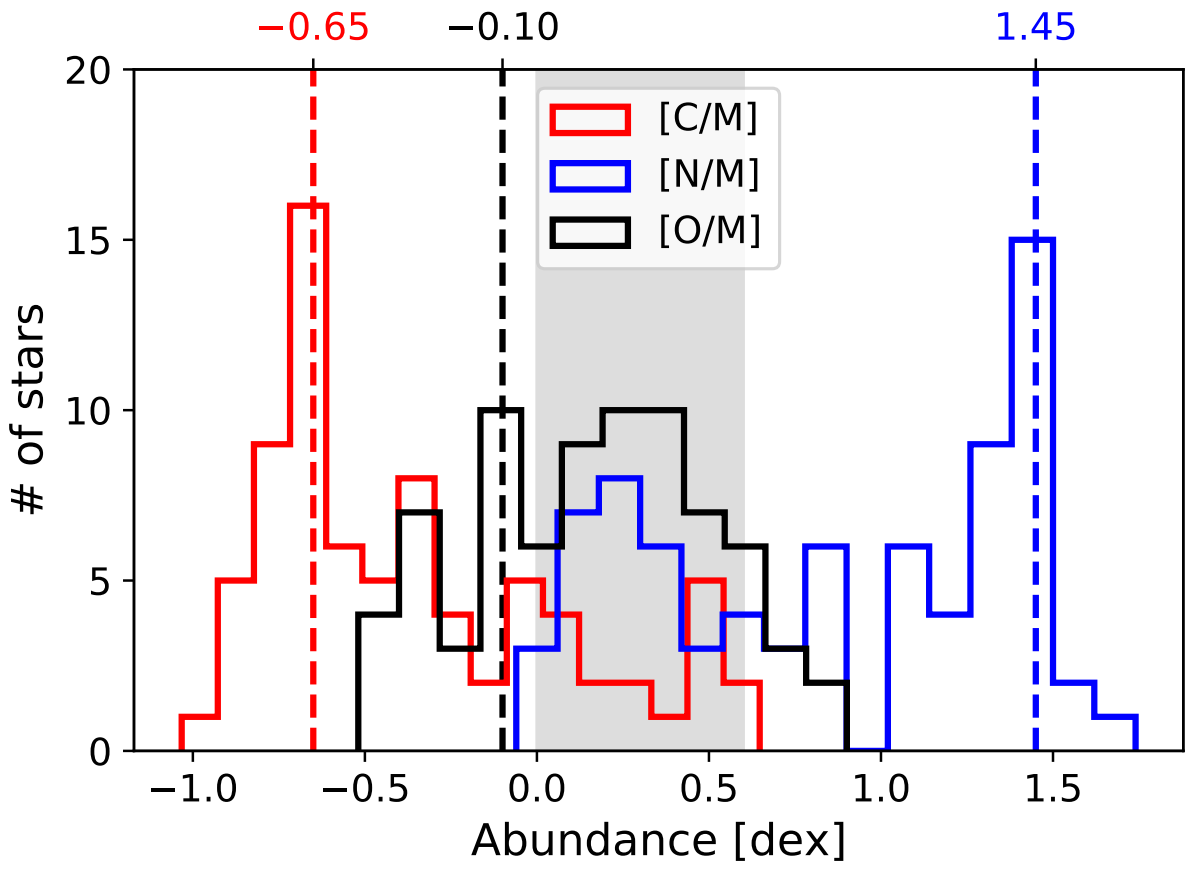

Figure 3.1. Distribution of measured elemental abundances from individual spectroscopy of 77 bright members of ω Centauri from Marino et al. [2012]. The vertical dashed lines represent the values adopted in this study for the nominal population as per Table 3.1. The shaded area represents the range of oxygen abundances considered in secondary populations as per Table 3.2.

suggest a correlation between [C/M] and [O/M], with the debiased Pearson coefficient of 0.72 ± 0.03; and an anti-correlation between [N/M] and [O/M] with the coefficient of -0.61 ± 0.04. The lower bound on [O/M] is therefore consistent with the modal peaks in [C/M] and [N/M] that appear to fall close to the low and high bounds of their corresponding distributions respectively. We note that the choices made for the nominal population are less important, as a secondary population will be used in the final analysis that best fits the data.

For every population, two sets of elemental abundances must be chosen: one for the zero age pre-main-sequence star (PMS) which will be used in evolutionary interior models; and

one for the corresponding grid of model atmospheres. Ideally, the latter set must be informed by the final stages of fully evolved stars calculated using the former set. Unfortunately, this approach is not compatible with our method, in which the grid of model atmospheres is computed before the evolutionary models, necessitating an approximate treatment. With the exception of lithium, we assumed that the final atmospheric abundances match the initial PMS abundances, since any changes in composition induced by core nuclear fusion are expected to be insignificant at low masses, while models of higher mass ($\gtrsim 0.3$ $M_\odot$) develop interior radiative zones that preserve PMS abundances in the outer layers. Our calculated evolutionary models (to be described below) affirm this choice, with changes in abundances other than Li between the PMS and the surface of the fully evolved star never exceeding ~ 0.1 dex. On the other hand, the variation in lithium abundance in both the core and the atmosphere is significant, as shown in Figure 3.2. Atmospheric lithium is almost entirely consumed through proton capture for all but the smallest mass (insufficient central temperature for Li fusion) and the largest mass (formation of a radiative zone) models. Due to the minimal effect of lithium abundance on the stellar spectrum (and, even more so, synthetic photometry), we chose to ignore the minority of masses where Li is not depleted and assumed an abundance of $[\mathrm{Li/M}] = -3.0$ for all model atmospheres (but not for PMS in evolutionary models). This choice effectively eliminates lithium from the spectra.

The overall metallicity of the nominal population was chosen following Milone et al. [2017], who fit model isochrones onto ω Centauri photometry acquired with the HST Wide Field Channel of the Advanced Camera for Surveys (ACS/WFC) [Ryon, 2019] and the Infra Red channel of the Wide Field Camera 3 (WFC3/IR) [Dressel, 2012]. While the isochrones in Milone et al. [2017] do not account for non-solar CNO abundances, they were consistent with observations and thus provide satisfactory starting parameters. Of the stellar populations identified in Milone et al. [2017], we specifically focused on the metal-poor side ($[\mathrm{Fe/H}] \approx [\mathrm{M/H}] \gtrapprox -1.7$) of the helium-rich ($Y \approx 0.4$) MS-II population that corresponds to the blue sequence in Bedin et al. [2004]. We set the lowest metallicity in the quoted range of MS-II as the initial guess for the

Table 3.2. Properties of the secondary populations of ω Centauri

Population	[O/M]	[α/M][a]	[M/H]
LMHO (Low Metal High Oxygen)	0.6	0.0	−1.7
HMET (High METal)	0.0	0.0	−1.4
HMMO (High Metal Medium Oxygen)	0.4	0.0	−1.4
HMMA (High Metal Medium Alpha)	0.0	0.4	−1.4
HMHA (High Metal High Alpha)	0.0	0.6	−1.4

[a] [α/M] refers to the enhancement of α-elements that include O, Ne, Mg, Si, S, Ar, Ca and Ti

nominal population, and allowed it to increase up to $[M/H] = -1.4$ in the secondary populations. We fixed the helium mass fraction to $Y = 0.4$ for both nominal and secondary populations in accordance with both King et al. [2012] and Milone et al. [2017].

Milone et al. [2017] chose an isochrone age of 13.5 Gyr, which we used in this investigation as well. The exact age of the cluster has little effect on the main sequence, which justifies using a single upper limit for the isochrone fitting regardless of the known variation in ages of individual members by a few Gyr [Marino et al., 2012]. In contrast, brown dwarfs continuously evolve across color-magnitude space, so our predictions were calculated for both 10 Gyr and 13.5 Gyr (Section 3.6).

Due to the multitude of populations in ω Centauri and the inevitable bias in abundances inferred by individual stellar spectroscopy, we perturbed the aforementioned parameters to generate 5 sets of models for secondary populations, whose abundances are listed in Table 3.2. The perturbations were applied iteratively until the best fit to the observed population was achieved (see Section 3.5). All properties that are not mentioned in the table are identical to the nominal population.

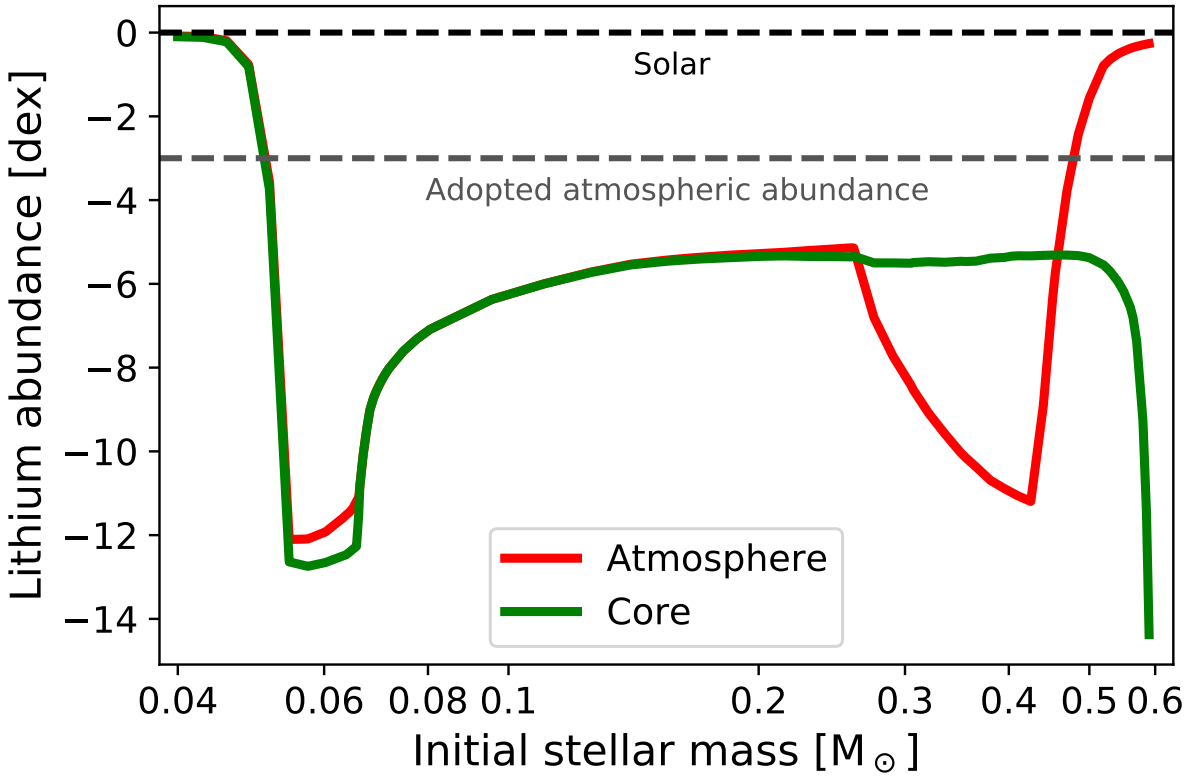

Figure 3.2. Depletion of lithium in the core and the atmosphere as a function of stellar mass for the HMMA secondary population (see Table 3.2) over 13.5 Gyr. All models are initialized with a solar lithium abundance (see Appendix C) in the PMS phase. Atmospheric lithium is not depleted at $M \lessapprox 0.055\ \mathrm{M}_\odot$ due to insufficiently high temperatures for fusion, and at $M \gtrapprox 0.5\ \mathrm{M}_\odot$ due to the early formation of a radiative zone that "freezes" the surface abundance. At intermediate masses, lithium is depleted by proton capture in the core which is propagated into the atmosphere via convective mixing. At masses above $\approx 0.07\ \mathrm{M}_\odot$, trace amounts of lithium are also produced by incomplete proton-proton chains. For masses below $\approx 0.3\ \mathrm{M}_\odot$ no radiative zone exists and lithium abundances are nearly equally depleted throughout the star. A radiative zone forms between $0.3\ \mathrm{M}_\odot$ and $0.4\ \mathrm{M}_\odot$, where the atmospheric abundance first decreases compared to core due to late formation of the radiative zone and then increases due to early formation. A late radiative zone allows lithium depletion by proton capture to propagate into the envelope but prevents diffusion of lithium enhancement from the proton-proton chain.

Table 3.3. Molecular lines included in the modelling setup

Ref	Molecules	# of lines
(1)	HOD	41.3×10^6
(2)	H_2O	505×10^6
(3)	CC, CN, CH, NH, OH, SiO, SiH, H_2	5.7×10^6
(4)	CO_2	4×10^6
(5)	NH_3	6.7×10^3
(6)	ZrO, YO	267×10^3
(7)	CO	134×10^3
(8)	C_2H_2, C_2H_4, C_2H_6, COF_2, CH_3OH, CH_3D, N_2, N_2O, NO, NO_2, NH_3, OCS, O_2, O_3, SO_2, SF_6, HI, HCN, HCOOH, HNO_3, HOCl, HOBr, HO_2, HOD, HF, HCl, HBr, H_2CO, H_2O_2, H_2O, H_2S	1.3×10^6
(9)	CO_2, OH, PH_3	31.2×10^3
(10)	CN	2.2×10^6
(11)	CH_4	34.6×10^3
(12)	H_3^+	3.1×10^6
(13)	CrH, FeH, TiH	301×10^3
(14)	MgH	53.8×10^3
(15)	CaH, TiH, VO	14.6×10^6
(16)	CH_4	31.3×10^6

Note. — (1) – AMES water [Partridge and Schwenke, 1997], (2) BT water [Barber et al., 2006], (3) – Kurucz CD-ROM #15 [Kurucz, 1995], (4) – *CDSD* (Carbon Dioxide Spectroscopic Databank) [Tashkun and Perevalov, 2011], (5) – Sharp and Burrows [2007], (6) – Ferguson et al. [2005], (7) – Goorvitch [1994], (8) – *HITRAN2004* [Rothman et al., 2005], (9) – *HITRAN2008* [Rothman et al., 2009], (10) – Jorgensen and Larsson [1990], (11) – Brown [2005], (12) – Neale and Tennyson [1995], (13) – *MoLLIST* [Bernath, 2020], (14) – Weck et al. [2003], (15) – lines inherited from `MARCS` atmospheres [Plez, 2008], (16) – methane lines generated using *STDS* (Spherical Top Data System; [Wenger and Champion, 1998]) in Homeier et al. [2003].

3.3.2 Model atmospheres

We calculate all model atmospheres with $T_{\rm eff} \leq 4000$ K using a custom setup based on a branch of version 15.5 of the PHOENIX code [Hauschildt et al., 1997]. Molecular lines considered in the calculation are listed in Table 3.3. Our modelling framework includes the formation of condensate clouds in the atmosphere and their depletion by gravitational settling according to the *Allard & Homeier* cloud formation model [Allard et al., 2012; Helling et al., 2008]. At $T_{\rm eff} < 3000$ K we used the "cloudy" mode described in Gerasimov et al. [2020]. For optimization purposes, a slightly simplified "dusty" mode is used at $T_{\rm eff} \geq 3000$ K, which differs in its coarser stratification (128 spherically symmetric layers instead of 250), disabled gravitational settling, and fewer spectral features included in the calculation. It was verified that the transition between the two modes does not introduce noticeable discontinuities in the derived bolometric corrections and the difference between "cloudy" and "dusty" spectra at the transition temperature is insignificant. All PHOENIX models were calculated at wavelengths from 1 Å to 1 mm with a median resolution of $\lambda/\Delta\lambda \approx 18250$ in the range $0.4\,\mu{\rm m} \leq \lambda \leq 2.6\,\mu{\rm m}$ and a lower resolution of ~ 8000 elsewhere.

At $T_{\rm eff} > 4000$ K, the effects of both condensates and molecular opacities become subdominant, allowing us to replace PHOENIX with the much faster and simpler ATLAS code version 9 [Kurucz, 1970; Sbordone et al., 2004; Kurucz, 2014; Castelli, 2005a].

As opposed to PHOENIX, our ATLAS setup stratifies the atmosphere into 72 plane-parallel layers covering the range of optical depths from $\tau = 100$ to $\tau \sim 10^{-7}$. Instead of direct opacity sampling, ATLAS relies on pre-computed opacity distribution functions (ODFs) [Carbon, 1984]. Convection is modelled using mixing-length theory [Böhm-Vitense, 1958; Smalley, 2005] with no overshoot. Modelled line opacities include $\sim 43 \times 10^6$ atomic transitions of various ionization stages and $\sim 123 \times 10^6$ molecular transitions including titanium oxide lines from Schwenke [1998] and water lines from Partridge and Schwenke [1997]. We use satellite utilities DFSYNTHE and SYNTHE shipped with the main ATLAS code to compute a custom set of ODFs for the abundances of interest (one set for each considered population) and derive high-resolution

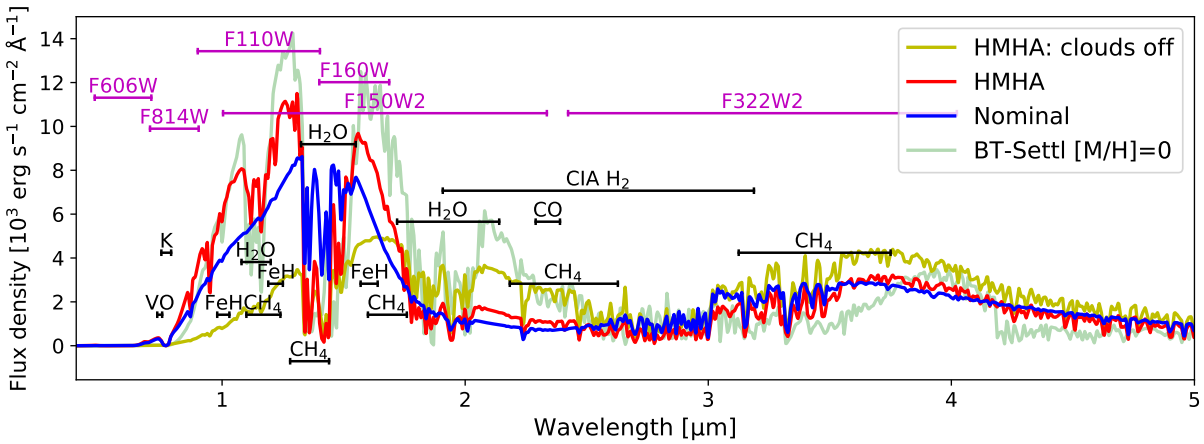

Figure 3.3. Synthetic spectra of selected low-temperature model atmospheres calculated in this study. Shown here are the $T_{\rm eff} = 1200$, $\log_{10}(g) = 5.0$ atmospheres from the nominal population (Table 3.1) and the `HMHA` population (Table 3.2). Both spectra demonstrate prominent molecular features, some of which are indicated with black bars (CIA H_2 represents the band of collision-induced absorption by molecular hydrogen). A `HMHA` spectrum with identical parameters but calculated in the "dusty" mode (no gravitational settling) is shown for comparison. The corresponding synthetic spectrum for a model of solar metallicity from the `BT-Settl` library is also shown. Magenta bars delineate 20% transmission bounds of HST ACS/WFC `F814W` and `F606W` bands; HST WFC3/IR `F110W` and `F160W` bands; and JWST NIRCam `F150W2` and `F322W2` bands. For clarity, the spectra are shown after convolution with a 3 nm-wide Gaussian kernel.

synthetic spectra from the calculated models respectively. The calculated ODFs account for flux from $\sim$ 10 nm to 160 μm to ensure correct evaluation of energy equilibrium through the atmosphere. On the other hand, our synthetic spectra span a narrower range of wavelengths from 0.1 μm to 4.2 μm, accommodating all instrument bands considered in this study. All `SYNTHE` spectra are calculated at the resolution of $\lambda/\Delta\lambda = 6 \times 10^5$.

A few examples of calculated low-temperature models are plotted in Figure 3.3. Compared to their solar metallicity counterparts, the spectra of metal-poor brown dwarfs are characterized by weaker molecular absorption (e.g., 3.5 μm methane band), more prominent collision-induced H_2 absorption originating from deeper layers of the atmosphere, and extreme pressure broadening of alkali metal lines (e.g., K I resonant line at 0.77 μm). Synthetic spectra computed under our setup have previously demonstrated good correspondence with observations of candidate metal-poor

brown dwarfs in the field [Schneider et al., 2020].

A typical PHOENIX model in the "cloudy" mode requires $\sim$ 150 CPU hours to converge on the Comet cluster at the San Diego Supercomputer Center made available to us through the *XSEDE* programme [Towns et al., 2014]. "Dusty" models were a factor of two or three faster to compute, while ATLAS models only took approximately 1 CPU hour each.

3.3.3 Atmosphere-interior coupling

We used the MESA code (Modules for Experiments in Stellar Astrophysics; [Paxton et al., 2011]) for all evolutionary calculations. At zero age, a MESA model is spawned as a PMS star with a given total mass and uniform element abundances. The initial structure is determined by assuming a fixed central temperature well below the nuclear burning limit (in our case, 5×10^5 K; [Choi et al., 2016]) and searching for a solution to the structure equations that reproduces the desired mass of the star. From here, evolution proceeds in dynamically determined time steps until the age of the model reaches the target age. On each step, the structure equations are solved using the atmospheric temperature and pressure as boundary conditions. Both can in principle be estimated from the current surface gravity and effective temperature of the model using an appropriate model atmosphere. It is those boundary conditions that establish the coupling between interiors and atmospheres. Once the interior structure of the star is known, the model can be advanced to the next time step by compounding expected changes due to diffusion, gravitational settling, nuclear reactions, mechanical expansion, and other time-dependent processes.

Our MESA configuration is derived from Choi et al. [2016] with a number of key differences outlined in detail in Appendix B. When handling atmosphere-interior coupling, MESA is able to estimate boundary conditions either by drawing them from a pre-computed table at a given optical depth or at run time using one of a variety of methods relying on simplifying assumptions such as grey atmosphere. The latter option is unlikely to be accurate at low effective temperatures where molecular opacities and clouds dominate the spectrum. The low-mass MESA setup employed by

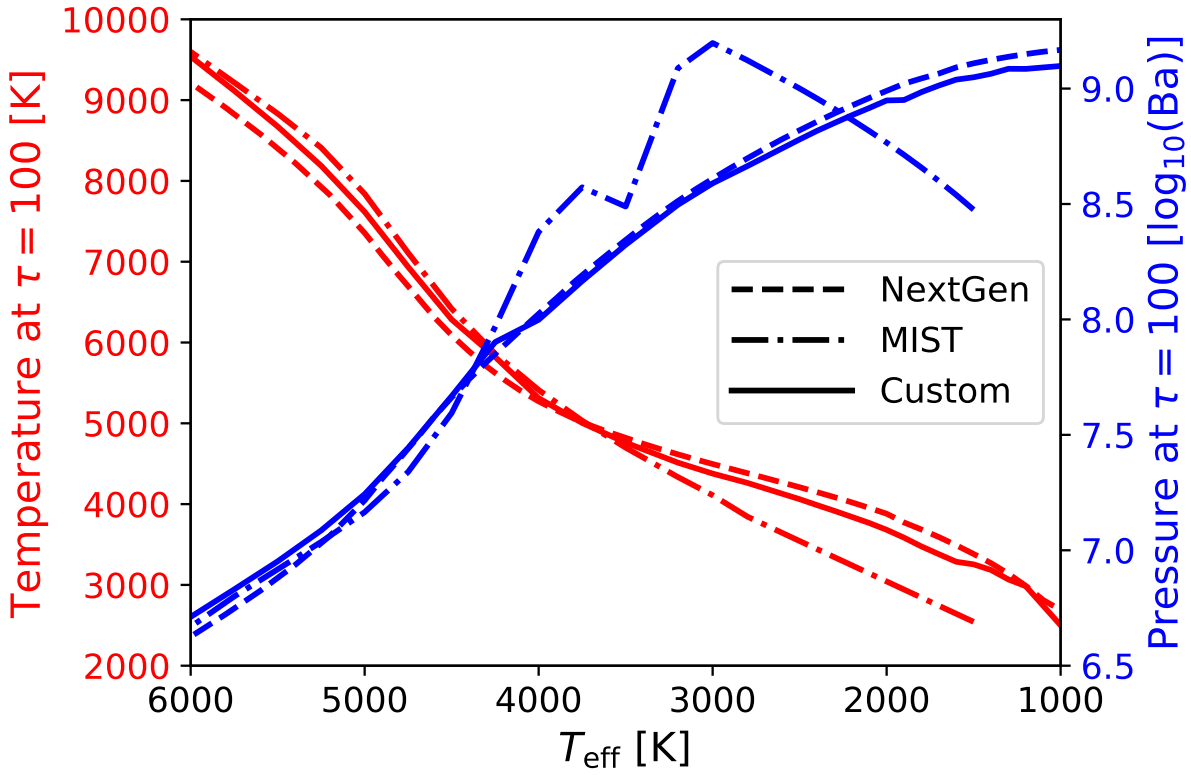

Figure 3.4. Comparison of three different sets of atmosphere-interior coupling boundary condition tables considered in this study at the surface gravity of $\log_{10}(g) = 6.0$ and metallicity of $[\mathrm{M/H}] = -1.7$. `NextGen` (dashed line) refers to the `PHOENIX` grid from Hauschildt et al. [1999]; Allard et al. [2000] that excludes gravitational settling in the atmosphere as well as enhancements of individual elements. `MIST` (dash-dotted line) refers to the `ATLAS`-derived tables used in Choi et al. [2016]. The "custom" coupling (solid line) is based on newly calculated `PHOENIX` models at low $T_{\rm eff}$ and `ATLAS` models at high $T_{\rm eff}$ and includes individual element enhancements of the nominal population (Table 3.1) in addition to the metallicity scaling as described in text. Pressure is shown in CGS units of barye ($1\ \mathrm{Ba} = 1\ \mathrm{dyn\ cm^{-2}}$).

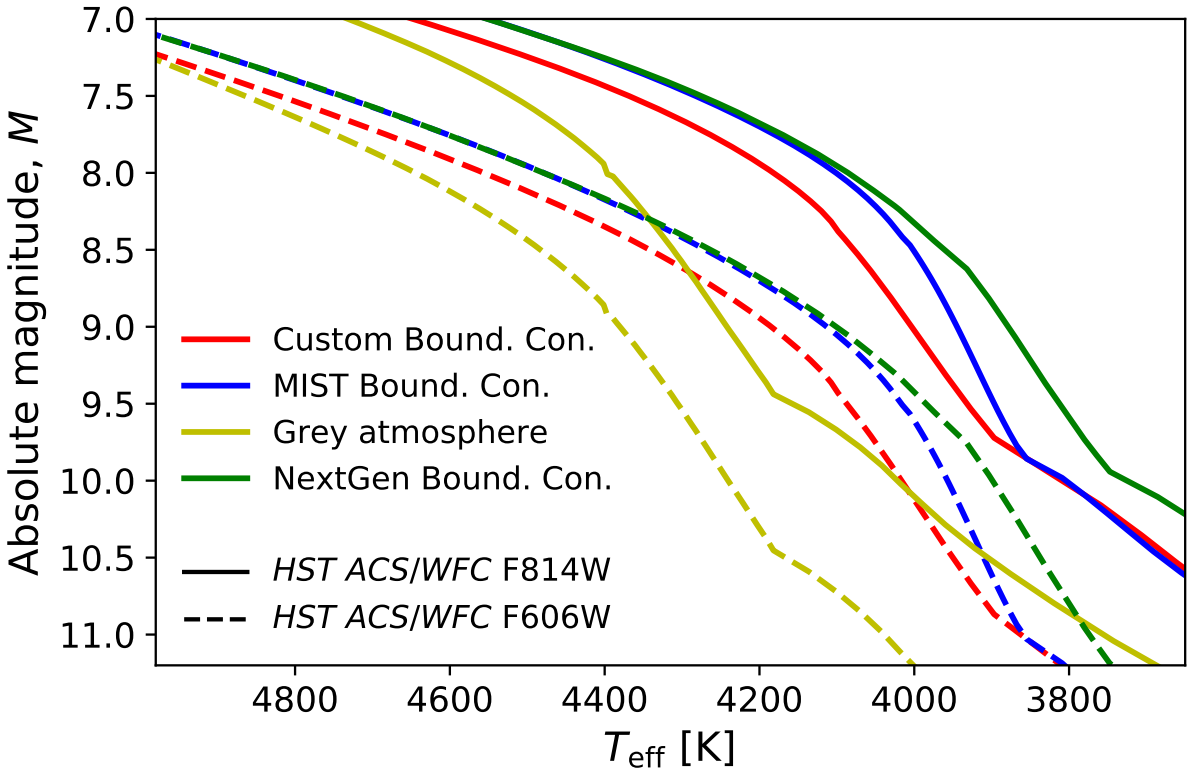

Figure 3.5. Effect of the choice of approach to atmosphere-interior coupling on synthetic photometry. The curves represent expected absolute magnitudes of the nominal population (see Table 3.1) as a function of effective temperature in two of the HST ACS/WFC bands: `F814W` (solid lines) and `F606W` (dashed lines), without interstellar extinction. The coupling schemes with pre-tabulated boundary conditions (Bound. Con.) are identical to those in Figure 3.4. The grey atmosphere coupling scheme at $\tau = 2/3$ is shown for comparison, which is the default scheme in `MESA`.

Choi et al. [2016] relies on boundary condition tables calculated at $\tau = 100$ for a wide range of effective temperatures, surface gravities and metallicities. However, the accuracy of the tables at $T_{\rm eff} \lessapprox 3500$ K is questionable, as they were derived from ATLAS atmospheres that fail to account for significant low-temperature effects such as condensation and molecular features.

In this study, we compared four different approaches to atmosphere-interior coupling:

- Run time calculation assuming grey atmosphere and drawing temperature and pressure at $\tau = 2/3$;
- $\tau = 100$ tables from Choi et al. [2016] at the ω Centauri metallicity, but not accounting for individual element enhancements or low-temperature atmospheric effects absent in ATLAS atmospheres;
- Custom $\tau = 100$ tables drawn from NextGen, a publicly available PHOENIX grid [Hauschildt et al., 1999; Allard et al., 2000] without condensates or gravitational settling. The grid covers the ω Centauri metallicity, but not the individual element enhancements; and
- Custom $\tau = 100$ tables drawn from our own atmosphere grids described above based on ATLAS at high temperatures and PHOENIX at low temperatures, including condensation and gravitational settling. The grids include all individual element enhancements for each of the considered populations.

The grids of model atmospheres calculated in this study span surface gravities from $\log_{10}(g) = 4$ to $\log_{10}(g) = 6$. At early ages ($\lesssim 2$ Myr), stars and brown dwarfs may briefly experience surface gravities under $\log_{10}(g) = 4$, falling outside of the calculated atmosphere grid. In such instances, the boundary conditions from Choi et al. [2016] were used instead. By applying random perturbations to those low-gravity boundary conditions, we established that their accuracy has a negligible effect on the final results.

The temperature and pressure at $\tau = 100$ for the tabular options are plotted as functions of effective temperature in Figure 3.4 at $\log_{10}(g) = 6.0$. The effect of the chosen boundary

conditions on synthetic photometry (described below) is shown in Figure 3.5. Both figures demonstrate good agreement between approaches at high effective temperatures, and increasing deviation at lower temperatures where atmosphere-interior coupling becomes important. The final set of interior models in our analysis use custom $\tau = 100$ tables based on our own model atmospheres, which we believe to offer the highest accuracy. The comparison of different sets of boundary conditions is presented here to emphasize the importance of atmosphere-interior coupling and to demonstrate how significant changes in metallicity and element enhancements could be "mimicked" by inaccurate boundary conditions.

3.3.4 Synthetic photometry

Synthetic photometry of each modelled population of ω Centauri was computed by first evaluating the bolometric corrections of each bandpass of interest for each of the calculated model atmospheres. The bolometric correction is defined as

$$\mathrm{BC}_x = M_b - M_x = M_b + 2.5 \log_{10} \left(\frac{F_x}{F_x'} \right) \tag{3.1}$$

where x is a given bandpass; BC_x is the bolometric correction for x between the absolute bolometric magnitude M_b and the absolute magnitude in band x, M_x; F_x is the total flux of the model through bandpass x; and F_x' is the total flux of the reference object through bandpass x. We used the `VEGAMAG` system for all comparisons to HST data and the `ABMAG` system for JWST predictions. For `VEGAMAG`, we used the apparent spectrum of Vega in Bohlin and Gilliland [2004] as our reference. For `ABMAG`, the reference spectrum is defined to be a constant flux density per unit frequency of ≈ 3631 Jy at all frequencies [Oke and Gunn, 1983]. Both F_x and F_x' are measured in *photons* per unit time per unit area [Bohlin et al., 2014] since all instruments of interest are photon-counting. F_x (but not F_x') is taken at the distance of 10 pc. By introducing the stellar radius R we can express F_x in terms of surface flux, Φ_x:

$$\mathrm{BC}_x = M_b + 2.5\log_{10}\left(\frac{\Phi_x}{F'_x}\right) + 5\log_{10}\left(\frac{R}{10\text{ pc}}\right) \tag{3.2}$$

Both R and M_b are dependent on the total luminosity of the model, L, which cannot be inferred from the model atmosphere on its own. For our purposes, BC_x must be re-expressed in terms of exclusively atmospheric parameters. The IAU definition of absolute bolometric magnitude [Mamajek et al., 2015] is

$$M_b = -2.5\log_{10}(L/[1\text{ W}]) + \Delta \tag{3.3}$$

with $\Delta = 71.197425$. Substituting in equation (3.2):

$$\mathrm{BC}_x = 2.5\log_{10}\left(\frac{\Phi_x}{F'_x}\right) - 10\log_{10}\left(\frac{T_{\text{eff}}}{1000\ K}\right) + C \tag{3.4}$$

where $C = -30.88138$ is a constant evaluated as

$$C = \Delta - 2.5\log_{10}\left[\frac{4\pi\sigma(10\text{ pc})^2(1000\text{ K})^4}{1\text{ W}}\right] \tag{3.5}$$

with σ representing the Stefan-Boltzmann constant.

Finally, we rewrite the flux ratio, Φ_x/F'_x, in terms of the synthetic *energy* spectrum ϕ_λ, reference *energy* spectrum f'_λ and the dimensionless transmission profile of x: x_λ:

$$\frac{\Phi_x}{F'_x} = \frac{\int_0^\infty \lambda\phi_\lambda x_\lambda 10^{-\frac{A_\lambda}{2.5}} d\lambda}{\int_0^\infty \lambda f'_\lambda x_\lambda d\lambda} \tag{3.6}$$

In the case of `ABMAG` magnitudes, f'_λ must be converted from constant flux density per unit frequency as

$$f'^{(\text{ABMAG})}_\lambda = (3631\text{ Jy})\frac{c}{\lambda^2} \tag{3.7}$$

where c is the speed of light. Note that both integrands in equation (3.6) are multiplied by λ to express the spectra in photon counts rather than units of energy. We have also introduced A_λ – the extinction law in units of magnitude as a function of wavelength λ. We used the extinction law from Fitzpatrick and Massa [2007] parameterized by the optical interstellar reddening, $E(B-V)$, and the total-to-selective extinction ratio, $R_V = A_V/E(B-V)$. We assumed $R_V = 3.1$ throughout and allowed $E(B-V)$ to be a free parameter, as described in Section 3.5.

For each of the modelled populations, a synthetic color-magnitude diagram was constructed by calculating a grid of interior models with initial masses spanning from the lowest mass covered by the calculated model atmospheres (0.03 $M_\odot$ for the best-fit isochrone) to the highest mass compatible with our atmosphere-interior coupling scheme (~ 0.5 $M_\odot$). At higher masses, $\tau = 100$ lies too deep in the atmosphere, requiring a change in the reference optical depth [Choi et al., 2016] and potentially causing a numerical discontinuity in the calculated results. Since the upper mass limit of 0.5 $M_\odot$ is sufficient to accommodate the vast majority of the available HST photometry (see Section 3.5), we chose to restrict our analysis to this upper mass limit, thereby avoiding the complexities of using multiple atmosphere-interior coupling schemes.

The bolometric corrections in the bands of interest were calculated as described above for each model atmosphere in the grid. Due to convergence issues associated with cloud formation at very low effective temperatures, a few models with maximum flux errors in radiative zones exceeding 10% were excluded from the atmosphere model grid. The remaining grid was then interpolated in effective temperature and surface gravity to the final surface parameters of each evolutionary interior model at the target age. Finally, the interpolated bolometric corrections were combined with the bolometric magnitudes of each interior model to obtain the desired synthetic photometry.

3.3.5 Results

Figure 3.6 shows the calculated isochrone of the nominal population of ω Centauri as defined in Table 3.1. The isochrone is plotted in the *absolute pre-extinction* color-magnitude spaces defined by the HST ACS/WFC `F606W` and `F814W` optical bands and the HST WFC3/IR `F110W` and `F160W` near infrared bands. The isochrone displays a characteristic inflection point around ~ 0.3 $M_\odot$ due to the change in the adiabatic gradient induced by the formation of molecules in the envelope [Copeland et al., 1970; Calamida et al., 2015; Pulone et al., 2003; Cassisi, 2011]. This feature is particularly valuable in our fitting process (Section 3.5) due to its sensitivity to chemical abundances and dense coverage by our observations. The near infrared isochrone shows a prominent main sequence knee at ~ 0.1 $M_\odot$ where the flux in `F160W` is suppressed by the onset of H_2 collision-induced absorption [Linsky, 1969; Saumon et al., 1994; Saracino et al., 2018], resulting in bluer colors at lower masses. This overall shift of peak emission towards shorter wavelengths has been spectroscopically observed in L and T subdwarfs [Burgasser et al., 2003; Schneider et al., 2020]. The hydrogen-burning limit (HBL) encompasses another reversal of the color-magnitude slope in both diagrams at a mass of ~ 0.07 $M_\odot$ (detailed calculation in Section 3.6 yields $M_{HBL} = 0.069$ $M_\odot$). As the stellar mass decreases past the limit, the population cools rapidly into the brown dwarf regime. At optical wavelengths, brown dwarfs of lower masses appear marginally bluer immediately after the HBL due to the pressure-broadened K I line absorption centered at 0.77 μm and extending across in the `F814W` band [Allard et al., 2007, 2016].

The behavior of secondary populations around the 0.3 $M_\odot$ inflection is shown in Figure 3.7 as differences to the nominal isochrone in absolute `F814W` magnitude. In general, all secondary populations are brighter than the nominal one at identical colors, redder at identical masses, and display a more prominent variation in slope. The effect becomes more apparent at higher metallicities and α-enhancements, but shows little dependence on the oxygen enhancement alone, suggesting that the lack of a well-defined oxygen peak in Figure 3.1 is not expected to pose

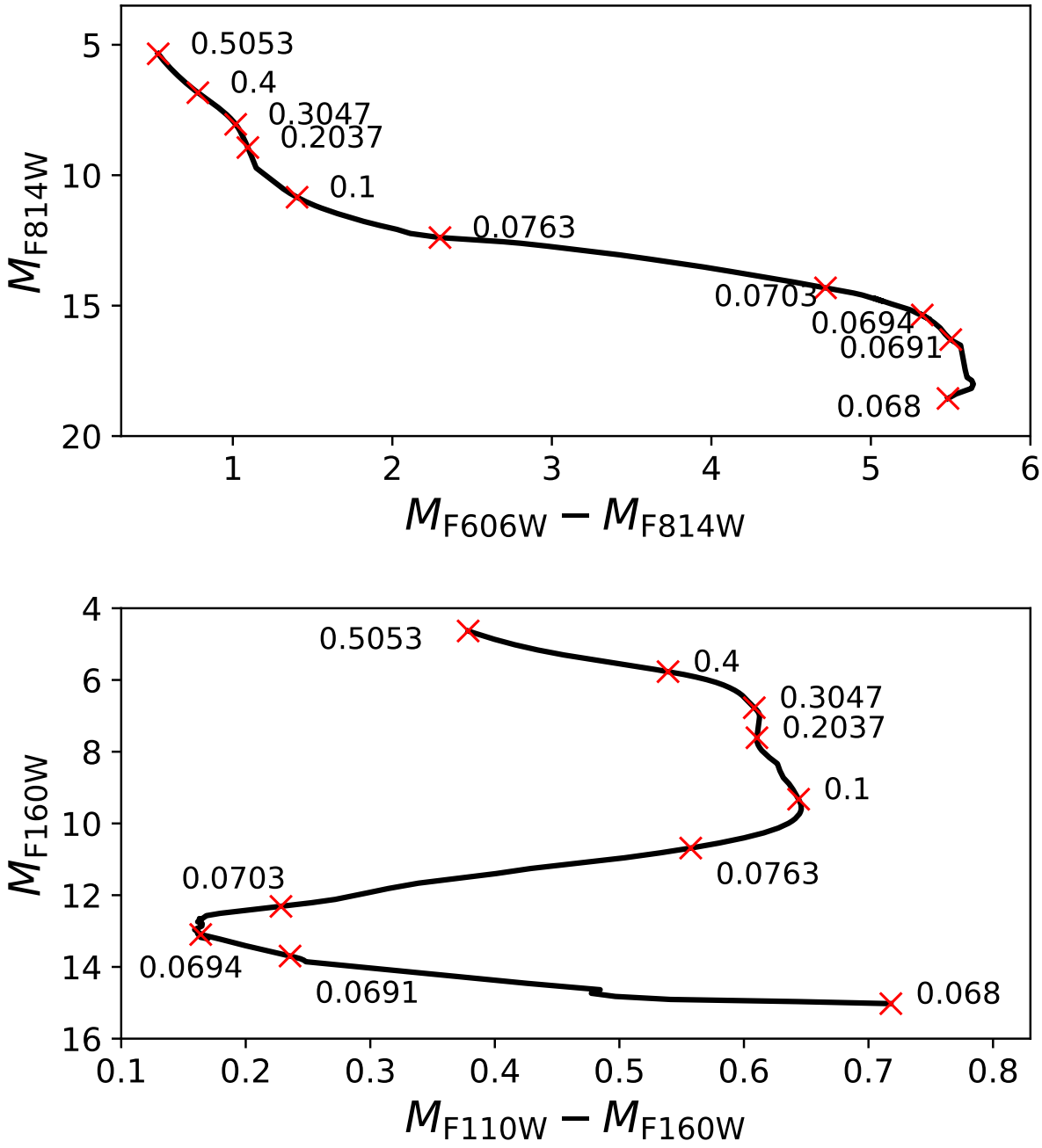

Figure 3.6. Isochrones derived for the nominal population of ω Centauri in optical (*top*) and near infrared (*bottom*) absolute color-magnitude spaces. The optical isochrone is evaluated for HST ACS/WFC filters, while the near infrared isochrone is evaluated for HST WFC3/IR filters. Red markers display the initial stellar masses of selected models along the isochrone in units of solar masses. Extinction effects are not included.

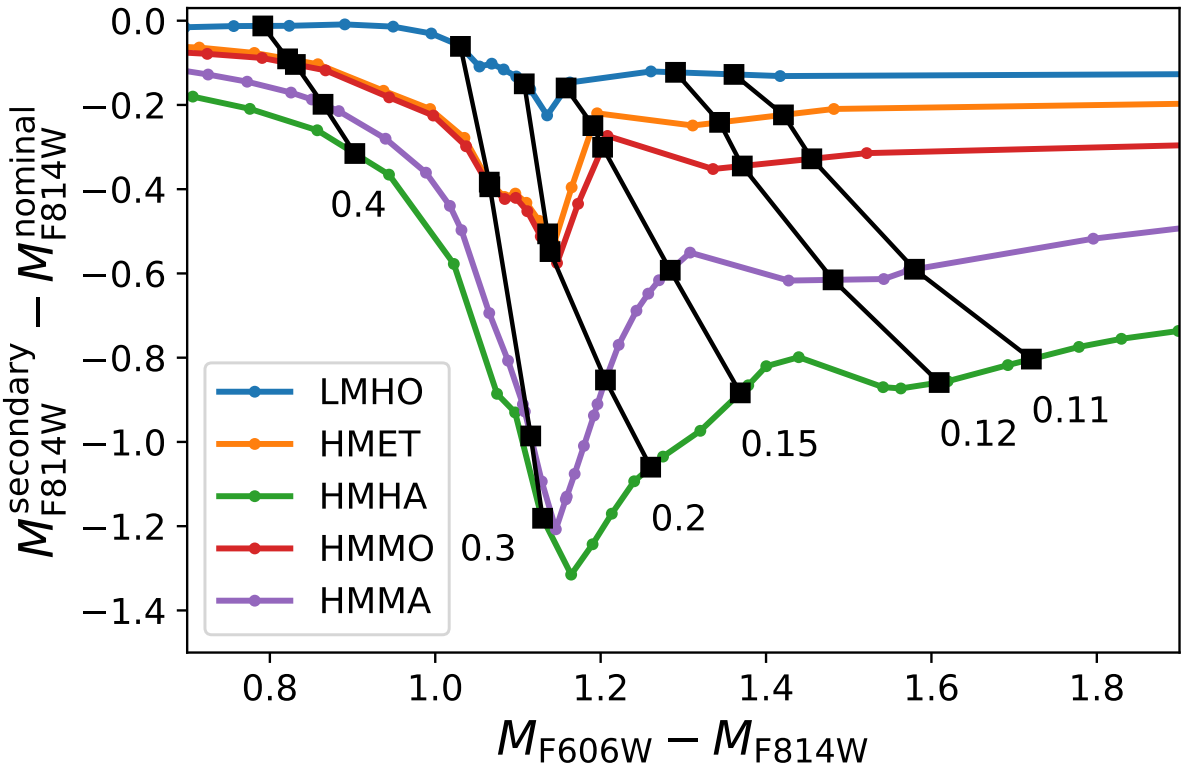

Figure 3.7. Isochrones for secondary populations listed in Table 3.2. Absolute magnitudes (vertical axis) are displayed as differences after subtracting the absolute magnitude of the nominal population in Fig 3.6 at the corresponding color. The range of colors displayed matches the range covered by the available HST data, even though some of the isochrones have been calculated at much redder colors. Black lines join the points of equal initial masses along the isochrones that are labeled in solar masses. Extinction effects not included. All magnitudes correspond to HST ACS/WFC filters.

difficulties to isochrone fitting.

3.4 Observations

To determine the best-fit isochrone for ω Centauri, we compared each population isochrone to photometric data acquired with HST ACS/WFC in the F606W and F814W bands (programs *GO-9444* and *GO-10101*; PI: King), and HST WFC3/IR in the F110W and F160W bands (programs *GO-14118* and *GO-14662* for *WFC3*; PI: Bedin). Observations were carried out in a $3' \times 3'$ field situated ~ 3 half-light radii ($\approx 7'$) southwest of the cluster centre (see field F1 in Figure 1a of [Bellini et al., 2018]). This is the deepest observed field for ω Centauri for which both optical and near infrared HST observations are available.

The primary data reduction followed the procedure described in Scalco et al. [2021] for two other HST ω Centauri fields, and is analogous to methods adopted in numerous previous works [Bellini et al., 2017a, 2018; Milone et al., 2017; Libralato et al., 2018; Bedin et al., 2019]. In brief, positions, fluxes and multiple diagnostic quality parameters were extracted using the point spread function (PSF) fitting software package KS2 [Anderson and King, 2006; Anderson et al., 2008]; see Scalco et al. [2021] and references therein. The photometric zero-point onto the VEGAMAG system was determined using the approach of Bedin et al. [2005]. The sample was filtered by quality parameters σ (photometric error), QFIT (correlation between pixel values and model PSF), and RADXS (flux outside the core in excess of PSF prediction; [Bellini et al., 2017a; Bedin et al., 2008]), as described in Scalco et al. [2021, Section 4].

We used the relative proper motions of sources in the observed region to separate field stars from cluster members. Proper motions were obtained by comparing the extracted positions of stars measured in the earliest and latest program (*GO-9444* and *GO-14662*, respectively), providing epoch baselines of up to 15 years. Photometry in each filter was corrected for systematic photometric offsets following Bedin et al. [2009]. A general correction for differential reddening

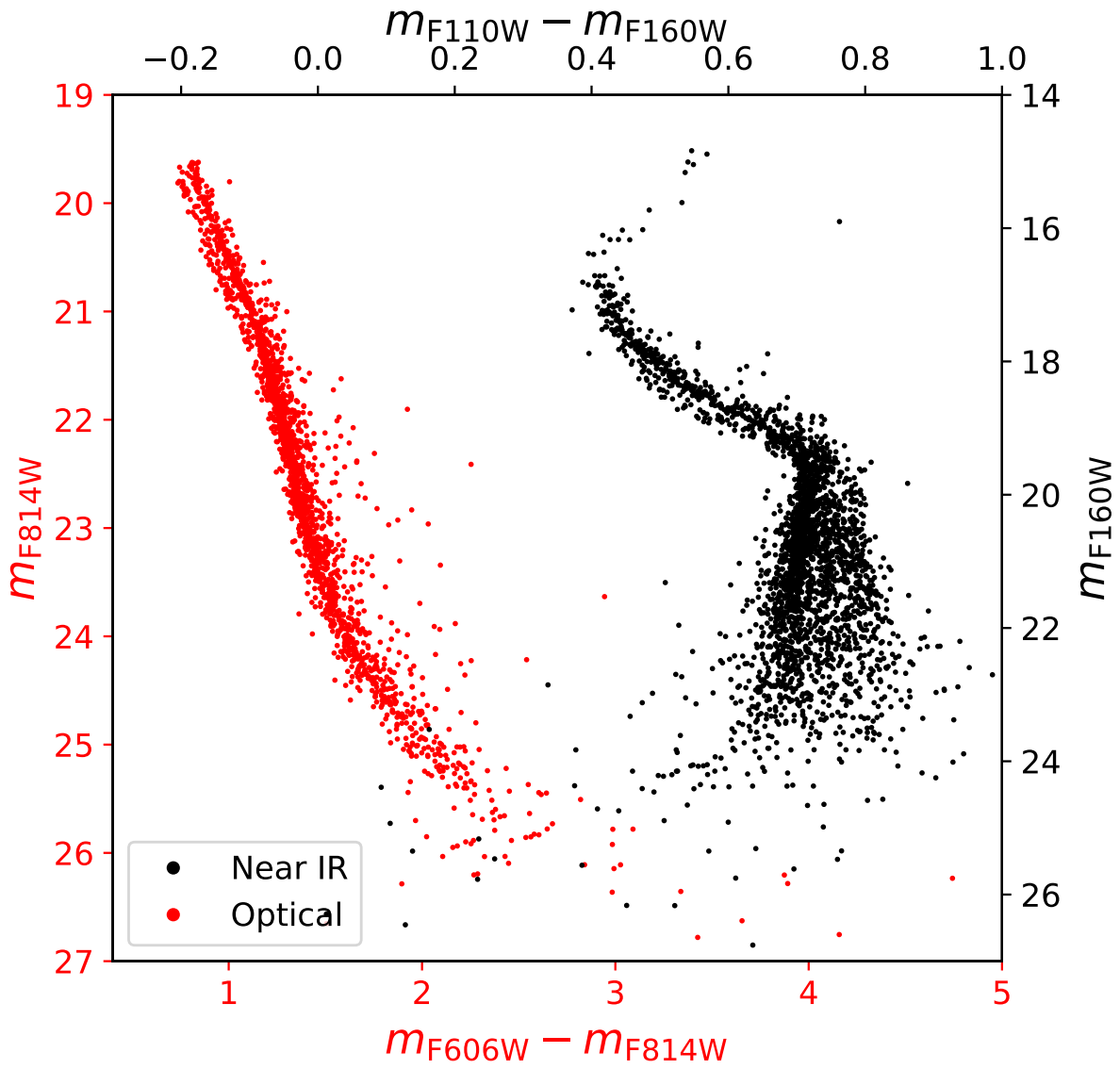

Figure 3.8. Proper motion-selected zero-pointed differential reddening-corrected photometry of the main sequence of ω Centauri. Optical photometry was acquired with HST ACS/WFC and near infrared photometry with HST WFC3/IR. Only unsaturated stars are shown for the optical photometry. The main sequence bifurcation can be seen in both datasets.

was also applied following the method described in Bellini et al. [2017b, Section 3].

Measurement of the LF (Section 3.5) requires quantification of source completeness as a function of color and magnitude, for which we followed the approach described in Bedin et al. [2009]. We generated a total of 2.5×10^5 artificial stars (AS) with random positions. For each AS, a `F606W` magnitude was drawn from a uniform distribution. The remaining three magnitudes (`F814W`, `F110W`, `F160W`) were then chosen to place the AS along the approximate ridgeline of the main sequence in various color-magnitude spaces. AS were introduced in each exposure and measured one at a time to avoid over-crowding, making the process independent of the LF. A star was considered recovered when the difference between the generated and measured star position was less than 0.1 pixels and the magnitude difference was less than 0.4 mag. Finally, the stars were divided into half-magnitude bins and the photometric errors and completeness for each bin were computed.

The near infrared and optical color-magnitude diagrams based on our observations are shown in Figure 3.8. The full catalogue of source astrometry, photometry, membership, and completeness is provided as an associated data product and described more fully in Appendix D.

3.5 Evaluation

With mass-luminosity and color-magnitude sequences computed for multiple populations, we were able to determine the optimal isochrone and IMF by comparing the predictions of those models to the HST-observed main sequence at optical and near infrared wavelengths.

3.5.1 Best-fit isochrone

We adopted a distance modulus of 13.60 ± 0.05 based on the distance to ω Centauri of 5.24 ± 0.11 kpc derived by Soltis et al. [2021] from the parallaxes of $\sim 7 \times 10^4$ members. The adopted value is marginally smaller than the distance modulus of 13.69 derived by Cassisi et al.

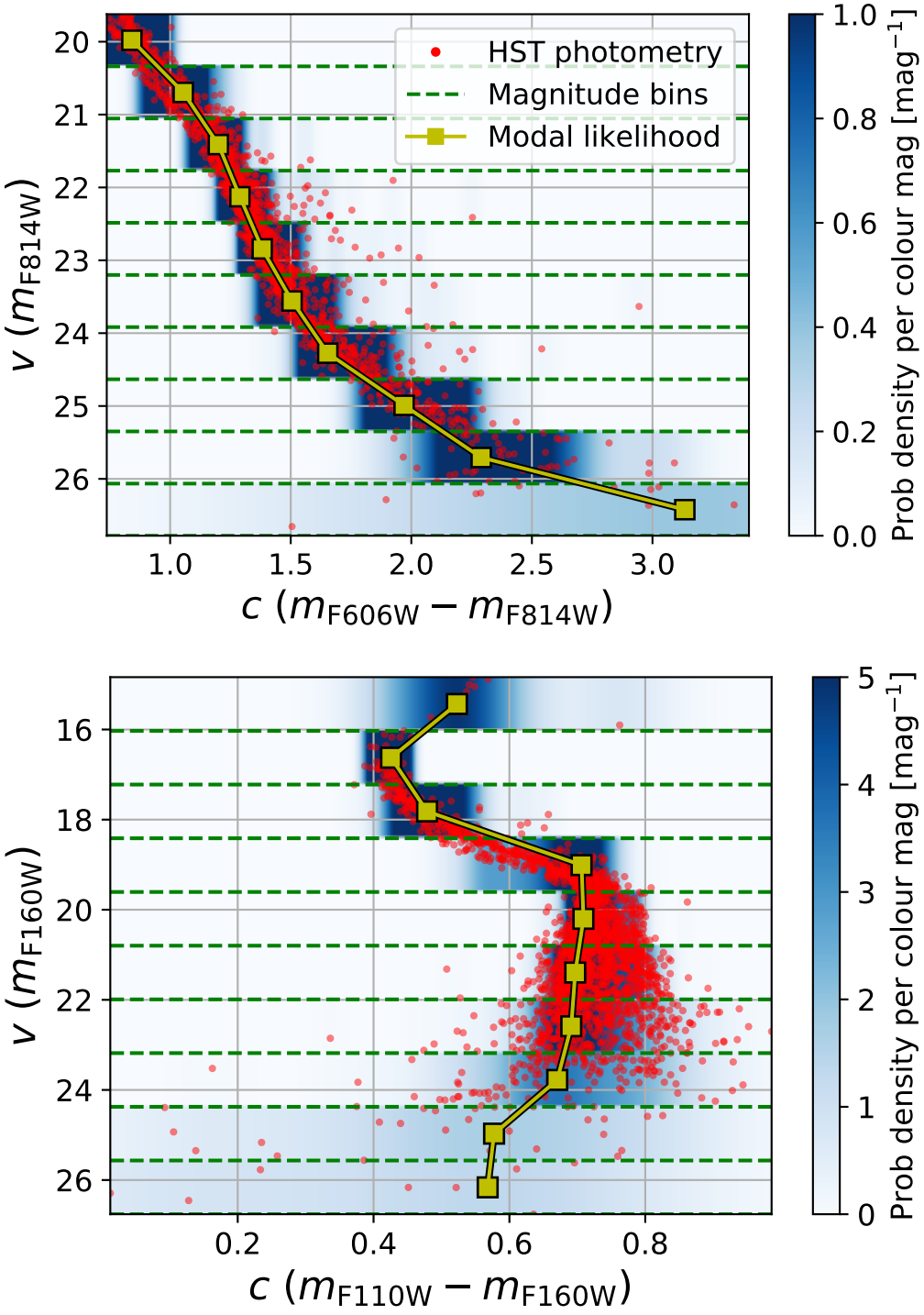

Figure 3.9. Colour probability distributions inferred from the observed scatter in HST photometry. Also shown are the boundaries of the magnitude bins used in our fitting analysis. Yellow markers indicate the mode of the distribution in each bin. *Top*: Optical data from HST ACS/WFC. *Bottom*: Near infrared data from HST WFC3/IR.

[2009] from isochrone fit to the CMD.

We sought an isochrone that is most statistically compatible with the observed photometry, accounting for the average spread in the data introduced by unmodelled astrophysical and instrumental phenomena, such as the variation in abundances across the cluster, multiple star systems, observational errors, etc. First, we developed a likelihood model that predicts the probability of finding a cluster member at a given point (c, v) in color-magnitude space assuming that the average population is well-described by one of our isochrones:

$$\mathcal{P}_E(c,v) \propto \int \xi(m) P\left(c, v \;\middle|\; c_0(m,E), v_0(m,E)\right) dm \tag{3.8}$$

In the equation, $P(...)$ is the probability of observing a member at (c, v) assuming that the "true" location of the star in the color-magnitude space (including reddening) is (c_0, v_0). Both c_0 and v_0 are functions of the initial stellar mass, m, and the optical interstellar reddening E. Finally, $\xi(m)$ is the IMF, such that $\xi(m)dm$ is the number of stars in the cluster with masses between m and $m + dm$. Note that a proportionality sign is used here as the likelihood function is not appropriately normalized in the given form.

The individual probability distribution, $P(...)$, encapsulates the scatter of photometry around the best-fit isochrone, and must account for all relevant effects including experimental uncertainties, unresolved multiple stars, and multiple distinct populations known to be present in ω Centauri. For our purposes, both $P(...)$ and $\xi(m)$ can be estimated empirically from the observed spread of HST data across the color-magnitude space without theoretical input. In this method, the scatter along the color axis is degenerate with that along the magnitude axis, as any observed distribution of data points may be reproduced by perturbing predicted photometry along only one axis and not the other. We therefore chose to sample the observed scatter in photometry along the color axis only and use the magnitude axis as an estimator of the initial stellar mass by

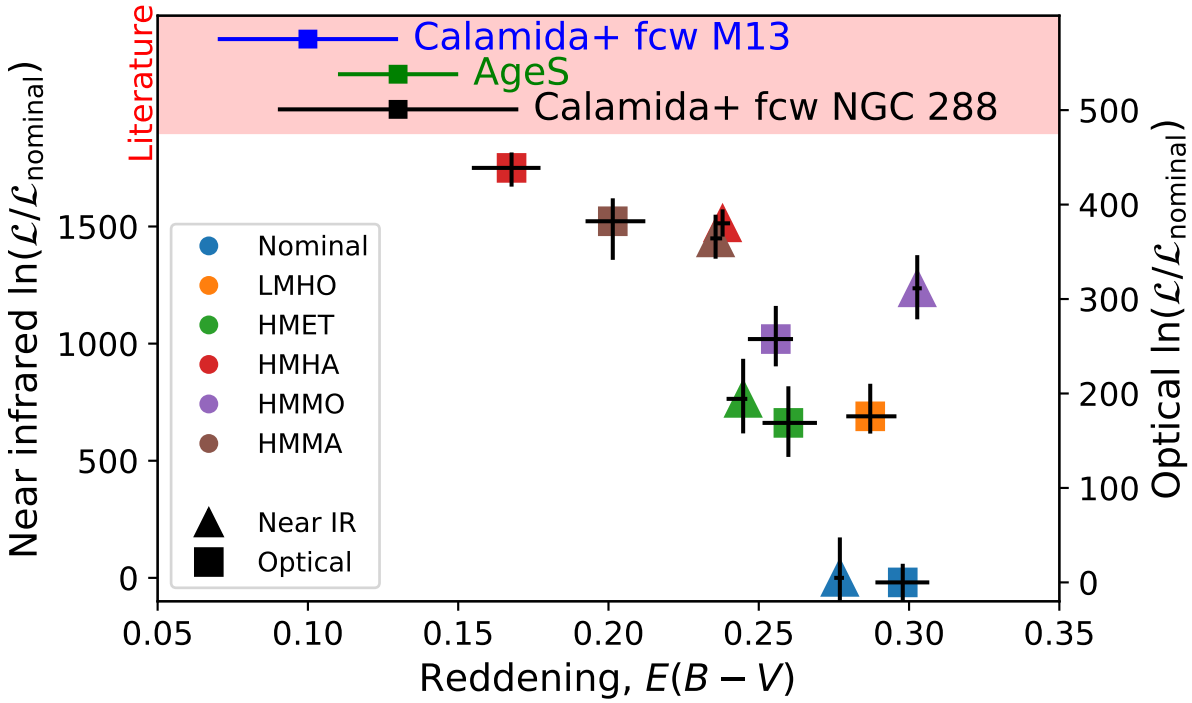

Figure 3.10. Likelihoods of compatibility and best-fit interstellar reddening for the population isochrones calculated in this study based on HST photometry. "Nominal" refers to the nominal population described in Section 3.3. Secondary populations are summarized in Table 3.2. The vertical axes are normalized to $\mathcal{L}_{\rm nominal}$. Error bars indicate random errors in the values as described in text. Selected reddening values from literature are also shown with their uncertainties. *AgeS* refers to the reddening estimate used in Thompson et al. [2001, green]. The other two values are taken from Calamida et al. [2005], calculated *from comparison with* (fcw) NGC 288 (black) and M13 (blue). Marker shapes differentiate between fits obtained using optical ACS/WFC (squares; right axis) and near infrared WFC3/IR photometry (triangles; left axis). The two sets of values have different vertical scaling and cannot be compared against each other.

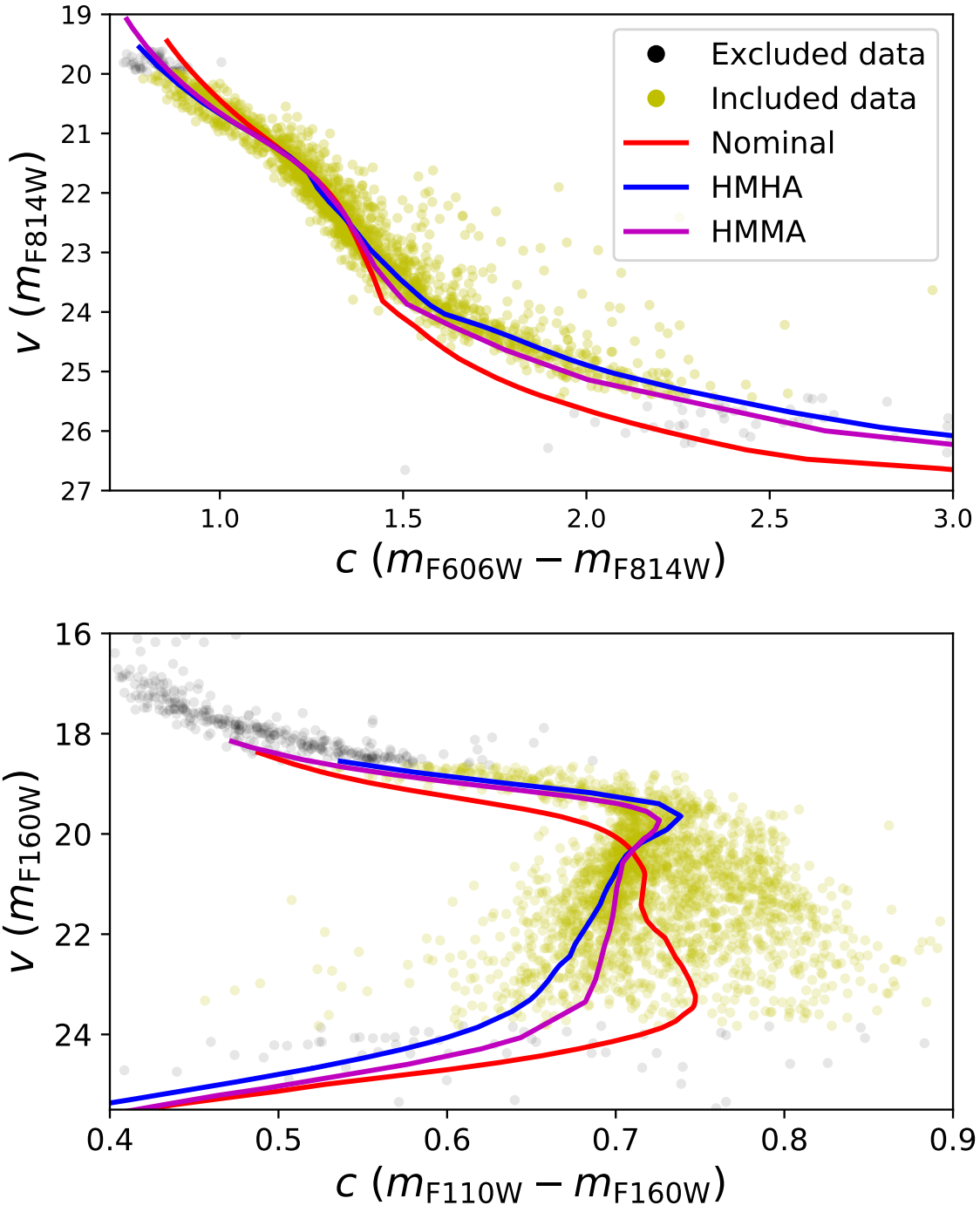

Figure 3.11. Nominal (Table 3.1) and two secondary (Table 3.2) population isochrones overplotted on HST photometry. The isochrones have been adjusted by the best-fit reddening values. The color of markers indicates whether any particular member was or was not included in the log-likelihood optimization described in text to evaluate the accuracy of the isochrone. *Top*: Optical data from HST ACS/WFC. *Bottom*: Near infrared data from HST WFC3/IR.

interpolating the theoretical mass-luminosity relation for the population under evaluation.

The empirical scatter was sampled from the observed data as follows. First, the range of apparent magnitudes in v (`F814` in the optical, `F160W` in the near infrared) was divided into 10 bins of equal widths as demonstrated in Figure 3.9. Within each bin, the variation of magnitude was ignored and the probability density function (PDF) of the color distribution was computed using Gaussian kernel density estimation with bandwidths calculated as in Scott [2015]. The distribution was then translated along the color axis to place the mode at the origin. The inferred PDF around the mode was then used as the scatter in color for all stars whose magnitudes fall within the magnitude bin.

The initial mass function in equation (3.8), $\xi(m)$, was evaluated by converting all measured magnitudes in the HST dataset to initial stellar masses using the linearly interpolated mass-magnitude relations derived from stellar models discussed in Section 3.3. The inferred distribution of masses was then converted into the mass PDF, $\xi(m)$, using the same kernel density estimation method as in the color spread [Scott, 2015], but trimmed on both sides at the lowest and highest modelled stellar masses respectively to avoid extrapolation.

The integral in equation (3.8) was computed numerically by drawing 10^4 masses from the inferred $\xi(m)$ PDF, evaluating the integrand for each and summing the results. Finally, the total likelihood of a given isochrone being compatible with the HST dataset ($\mathcal{L}(E)$) was calculated as in equation (3.9).

$$\mathcal{L}(E) \propto \prod_i \mathcal{P}_E(c_i, v_i) \tag{3.9}$$

In the equation, the product may, in principle, be taken over all individual measurements (c_i, v_i). In practice, we must only include those members in the HST dataset that fall within the magnitude range of *all* calculated isochrones, as stellar masses of members out of range cannot be reliably

estimated. Furthermore, since inferred stellar masses are dependent on interstellar reddening which is not *a priori* known, we must only select those cluster members for analysis that fall within the modelled range at all realistic reddenings, which we conservatively take to be $E(B-V) \in [0.0, 0.4]$. Our final choice of bounds was $v \in (18.65, 23.83)$ in the near infrared (WFC3/IR `F160W`) and $v \in (19.99, 25.44)$ in the optical (ACS/WFC `F814W`), accommodating approximately 85% and 94% of all available measurements, respectively. The subset of selected members is shown in Figure 3.11.

For the nominal and each of the secondary populations, we maximize $\mathcal{L}(E)$ with respect to the interstellar reddening, $E(B-V)$. We estimate the random error in the best-fit reddening value, E_0 by considering three contributions. The intrinsic fitting error may be adopted as the Cramér–Rao bound:

$$\mathrm{Var}\,(E_0) = -\left(\frac{\delta^2 \ln \mathcal{L}}{\delta E^2} \Big|_{E=E_0} \right)^{-1} \tag{3.10}$$

which in our case evaluated to $\sqrt{\mathrm{Var}\,(E_0)} \approx 0.001$ for all isochrones. The contributions of the random sampling of $\xi(m)$ during numerical integration and experimental uncertainties in the data were estimated by repeating the fitting process 10 times with different samples of $\xi(m)$ and random Gaussian perturbations in the data. Finally, the error induced by the uncertainty in the distance to the cluster was determined by repeating the fitting process for upper and lower 1σ bounds on the distance modulus value.

All of the aforementioned contributions were combined in quadrature. The resulting likelihoods and best-fit reddening values are shown in Figure 3.10 with uncertainties. Every secondary isochrone performs better than the nominal one, with `HMHA` offering the best fit in both optical and near infrared wavelengths. As such, we used `HMHA` for our predictions of brown dwarf photometry described in Section 3.6. The best-fit reddening values corresponding to this isochrone are $E(B-V) = 0.238 \pm 0.003$ from the near infrared data and $E(B-V) = 0.17 \pm 0.01$ from the optical data. The random errors in both $E(B-V)$ estimates quoted here and shown in Figure 3.10 are likely not representative of the true uncertainty in the value, which is primarily

driven by systematic effects due to the simplified population parameters, the reddening law, and errors intrinsic to the calculated stellar models. The scatter in $E(B-V)$ estimates between the optical and near infrared datasets suggests that the true value of the uncertainty in reddening is of the order of ~ 0.07.

Our reddening estimates exceed most literature values, of which three are shown in Figure 3.10. The *Cluster AgeS* experiment [Thompson et al., 2001] uses the value of $E(B-V) = 0.13 \pm 0.02$ based on the value of $E(B-V) = 0.132$ given by the map of dust emission from Schlegel et al. [1998] at a particular point within ω Centauri and assuming the uncertainty of 0.02 motivated by the variation of reddening across the cluster. In Calamida et al. [2005], two reddening values of $E(B-V) = 0.13 \pm 0.04$ and $E(B-V) = 0.10 \pm 0.03$ are derived from comparison with NGC 288 and M13, respectively. The apparent discrepancy in reddening values may be an artifact of our approach, since a single population is used to model both main sequences of the cluster.

Two best-fitting secondary isochrones – `HMHA` and `HMMA` – as well as the nominal isochrone are plotted against the HST data in Figure 3.11, visually illustrating the goodness-of-fit. Both isochrones in the figure have been corrected for the corresponding best-fit interstellar reddening parameters.

3.5.2 Best-fit luminosity and mass functions

Assuming the best-fit (`HMHA`) isochrone to be representative of the average distribution of ω Centauri members in color-magnitude space, we now seek a suitable IMF for the cluster to estimate the population density. As will be demonstrated shortly, the cluster is well described by a broken power law:

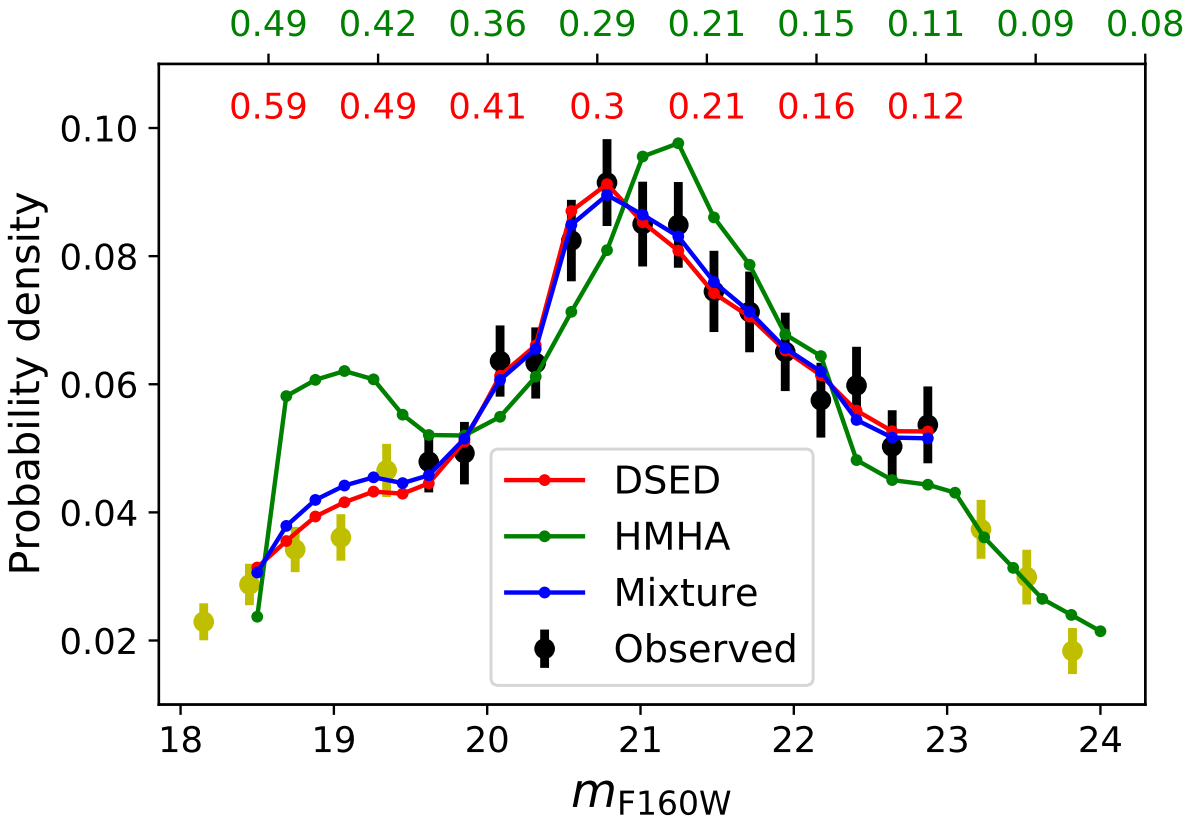

Figure 3.12. Observed luminosity function (LF) for ω Centauri (black) with three theoretical fits corresponding to the cases of $\mu = 0$ (red, solar helium population only), $\mu = 1$ (green, enhanced helium population only) and μ being a free parameter (both populations). The enhanced helium population is based on the mass-luminosity relation of the best-fit isochrone calculated in this study, `HMHA`. The solar helium population is based on the mass-luminosity relationship from Dotter et al. [2008, *DSED*]. In each case, a broken power law IMF is assumed (Equation 3.11) with the best-fit values $\gamma = 0.89 \pm 0.06$, $\gamma = 0.50 \pm 0.07$ and $\gamma = 0.83 \pm 0.08$ for the three cases respectively. The best-fit mixing fraction in the case of two populations was calculated as $\mu = 0.15 \pm 0.14$. The fitting is carried out between the apparent magnitudes of 19.5 and 23 only since *DSED* models are not available at the faint end and photometry becomes increasingly unreliable at the bright end due to saturation [Scalco et al., 2021]. Nonetheless, the observed LF outside this range is shown in yellow for completeness. The normalization on the vertical axis is such that the sum of all bins used in the fit is unity. The upper color-coded horizontal axis indicates the initial stellar masses corresponding to magnitudes for the solar helium population (red) and the enhanced helium population (green) in solar masses.

$$\xi(m) \propto \begin{cases} m^{-2.3}, & \text{if } m > 0.5\ \mathrm{M}_{\odot} \\ m^{-\gamma}, & \text{if } m \leq 0.5\ \mathrm{M}_{\odot} \end{cases} \tag{3.11}$$

The power index of the high-mass regime (-2.3) as well as the break point ($m = 0.5\ \mathrm{M}_{\odot}$) are fixed to the values employed in the "universal" IMF derived in Kroupa [2001]. It has been demonstrated by Sollima et al. [2007] that those values are well-suited to the high-mass regime of ω Centauri. The power index of the low-mass regime ($-\gamma$) is allowed to vary. For comparison, Sollima et al. [2007] use $\gamma = 0.8$, while the "universal" IMF introduces additional break points with different power indices.

The theoretical mass-luminosity relationship for `HMHA` was combined with the IMF to derive the theoretical luminosity function (LF) for ω Centauri as a function of γ. The best value of γ was determined by optimizing the χ^2 statistic for the goodness-of-fit between the theoretical and observed LFs. Our analysis of the LF was carried out in the `F160W` band of HST WFC3/IR between the apparent magnitudes of 19.5 and 23. Within this range, the data were divided into 15 uniform bins with the count uncertainty in each bin taken as the square root of the count. The counts have also been adjusted for estimated sample completeness in each bin as discussed in Section 3.4. The histogram was normalized and used as an estimate of the underlying PDF.

The theoretical LF was calculated from the IMF in equation (3.11) using the mass-luminosity relationship from `HMHA` and integrating the resulting PDF within each magnitude bin. Both observed and theoretical LFs within the fitting range are plotted in Figure 3.12 in green and black respectively for the best-fit value of $\gamma = 0.50 \pm 0.07$. The correspondence between the two LFs appears poor, indicating that the `HMHA` population alone cannot reproduce the observed LF. This result is not surprising as our best-fit isochrone was calculated for the helium mass fraction of the blue sequence in ω Centauri that is only representative of a minority of the members.

To improve the fit, we added a second population with a solar helium mass fraction and a mass-luminosity relationship adopted from the Dartmouth Stellar Evolution Database (*DSED*;

[Dotter et al., 2008]) for $[M/H] = -1.7$ and $Y = 0.2456$. The extinction of 0.085 mag was applied to synthetic F160W photometry from *DSED* based on the average magnitude difference between the best-fit reddening ($E(B-V) = 0.17$, lower bound most consistent with literature) and reddening-free ($E(B-V) = 0$) HMHA isochrones. The mixing fraction between the two populations, μ, was treated as a free parameter varying between 0 (*DSED* population only) and 1 (HMHA only). The best-fit LF based on both HMHA and *DSED* as well as the best-fit based on *DSED* alone ($\mu = 0$) are shown in Figure 3.12. The calculated best-fit value of $\mu = 0.15$, is comparable to its uncertainty of ± 0.14. Therefore, we present this result as the 2σ upper limit on the blue sequence population fraction, $\mu < 0.45$. The blue sequence thus contributes less than 45% of the cluster population in the observed region, in agreement with Bellini et al. [2009]. The best-fit value of γ when both HMHA and *DSED* LFs are included is 0.83 ± 0.08, which matches the adopted value of γ in Sollima et al. [2007].

3.6 Predictions

3.6.1 Substellar population of ω Centauri

In this section, we present our predictions of colors, magnitudes and CMD densities of brown dwarfs in ω Centauri using the best-fit isochrone (HMHA) and the best-fit IMF (Equation 3.11) calculated in Section 3.5. Figure 3.13 shows predicted CMDs for the cluster in three different sets of filters: F814W vs F606W-F814W for HST ACS/WFC, F160W vs F110W-F160W for HST WFC3/IR and F322W2 vs F150W2-F322W2 for JWST NIRCam.

For the first two diagrams, observed main sequence photometry is available and shown alongside predicted colors and magnitudes in blue. The density of points in the predicted set is proportional to the PDF luminosity function (Figure 3.12) extended into the brown dwarf regime. The normalization is such that approximately 1700 points fall between the initial masses of 0.1 $M_\odot$ and 0.3 $M_\odot$. This choice closely matches the number of members within the same

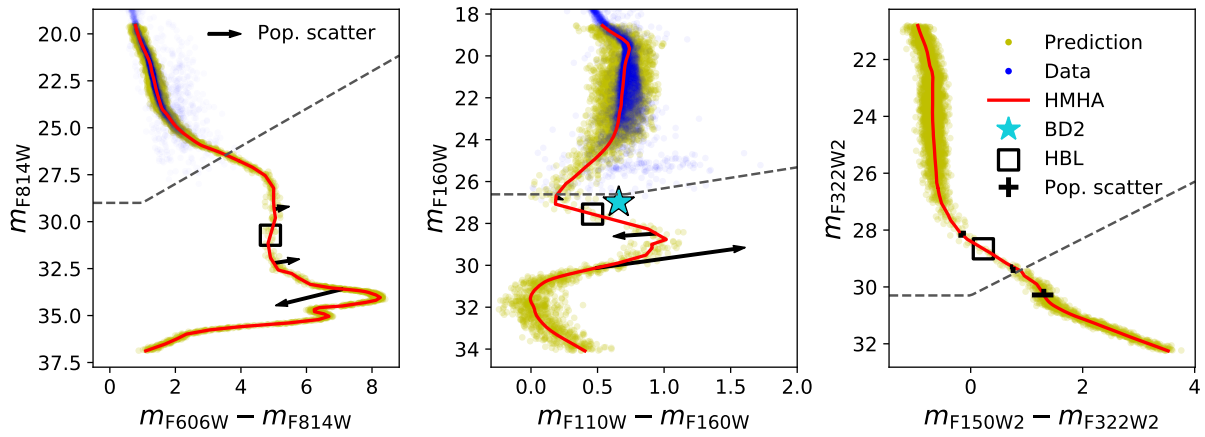

Figure 3.13. Predicted color-magnitude diagrams for ω Centauri from the main sequence through the stellar/substellar gap and down to the appearance of first brown dwarfs. Predicted points are based on the best-fit `HMHA` isochrone and the best-fit IMF. For clarity, a Gaussian scatter in color by 0.1 magnitudes was added to each point. Where available, predicted CMDs are shown alongside existing HST photometry reaching the cool end of the main sequence. All CMDs are normalized to 1700 objects between 0.1 $M_\odot$ and 0.3 $M_\odot$. The instruments used are HST ACS/WFC (*left*), HST WFC3/IR (*middle*) and JWST NIRCam (*right*). The cyan star shows the near infrared color and magnitude of BD2 – a candidate brown dwarf in the globular cluster M4 from Dieball et al. [2019]. The magnitude of BD2 shown here has been adjusted for the difference between the distance moduli of ω Centauri and M4 using the distance measurement from Neeley et al. [2015]. The grey dashed line indicates the approximate faint limit for both HST datasets and the expected faint limit of future JWST measurements, calculated using the JWST Exposure Time Calculator [Pontoppidan et al., 2016] for a 1 hr exposure and signal-to-noise ratio of 2. The color and magnitude corresponding to the hydrogen-burning limit (HBL) are highlighted in each case. The arrows in the HST plots (*left* and *middle*) indicate the approximate direction and relative magnitude of the effect of decreasing metallicity and α-enhancement as estimated from the difference between the best-fitting `HMHA` and `HMMA` secondary populations as well as the nominal population. In the case of JWST, the scatter among isochrones does not display a clear direction and is shown with error bars instead.

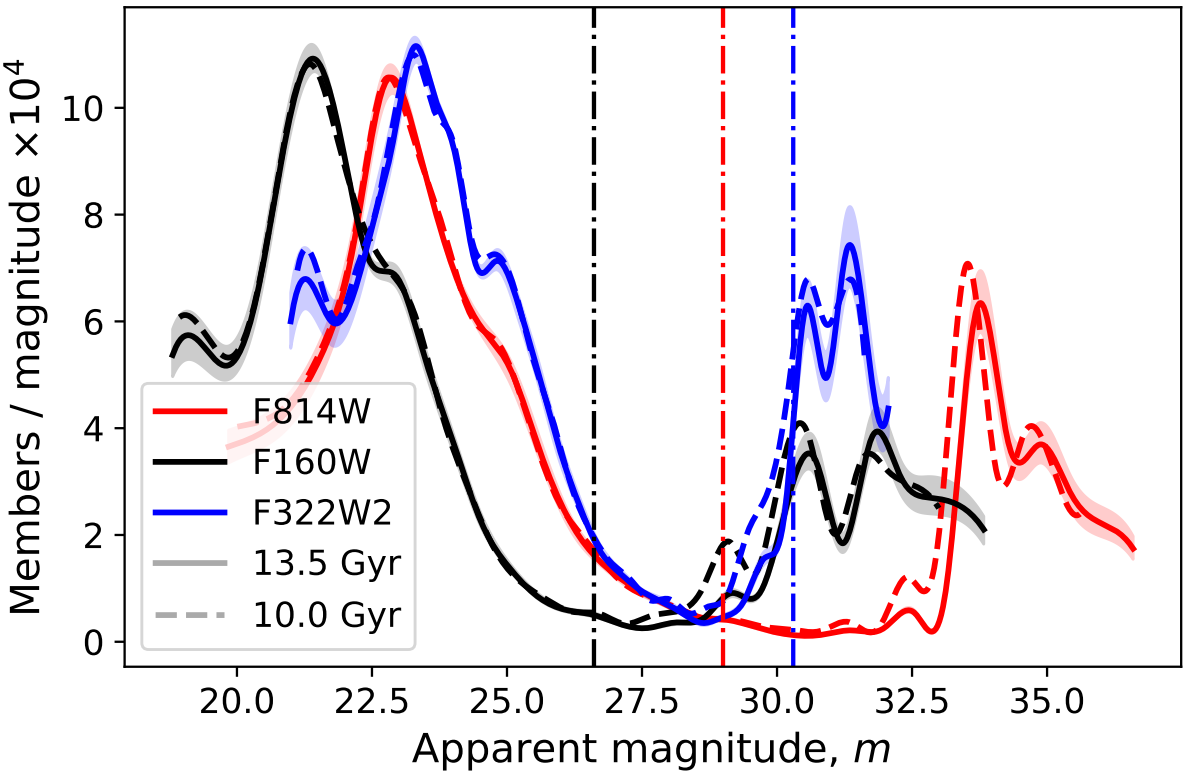

Figure 3.14. Predicted luminosity function for the HST ACS/WFC `F814W` band, the HST WFC3/IR `F160W` band, and the JWST NIRCam filter `F322W2`. Curves are shown for the population ages of 13.5 Gyr (solid) and 10 Gyr (dashed). The two peaks correspond to the main sequence and brown dwarfs in the cluster with a stellar/substellar gap in between. The vertical dash-dotted lines indicate the approximate faint limits for the instruments shown, calculated identically to Figure 3.13. The shaded areas around the curves indicate the range of our predictions based on the uncertainty in the determined IMF. While the shown ranges are for the age of 13.5 Gyr, similar uncertainties apply to the case of 10 Gyr. This figure demonstrates the superiority of infrared observations with JWST as the apparent magnitude of brown dwarfs enters the limit of the instrument.

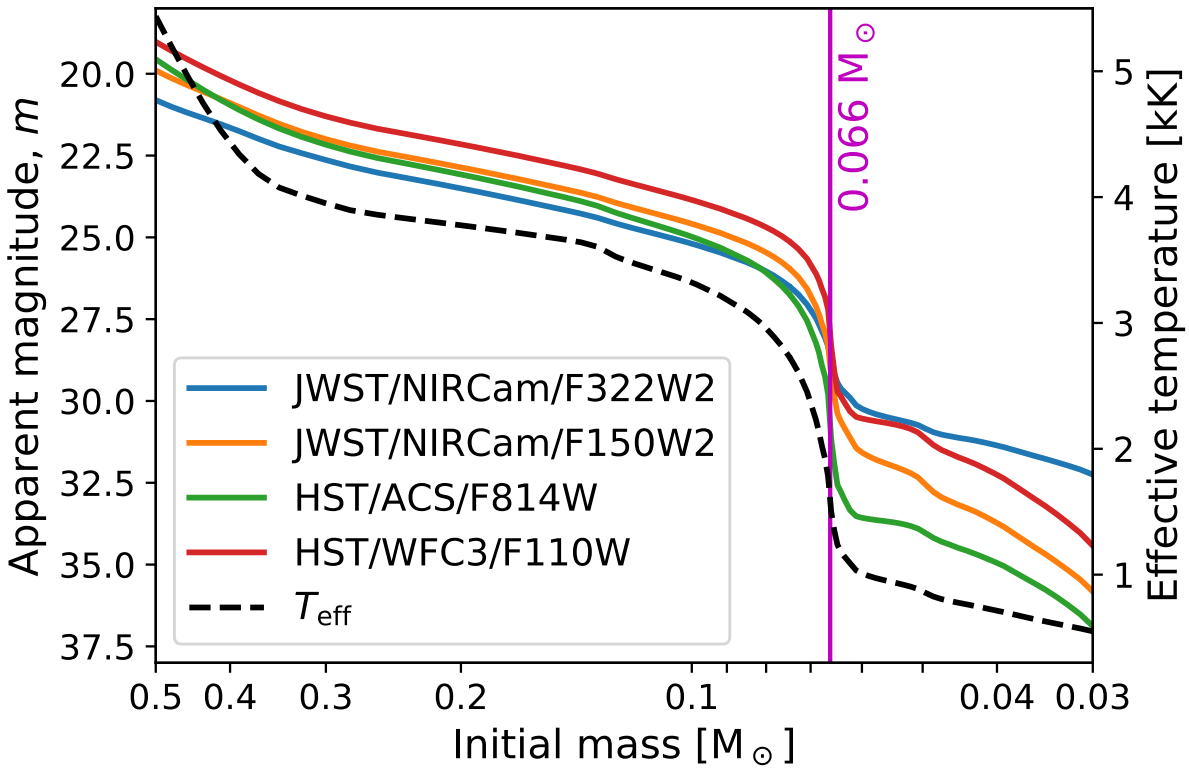

Figure 3.15. Predicted mass-luminosity relations for the same set of instruments as in Figure 3.14 as well as the predicted mass-effective temperature relationship (dashed). The approximate mass of the hydrogen-burning limit is highlighted with a vertical line and labelled.

range of masses in the optical HST dataset used in this analysis. For clarity, a Gaussian spread with a standard deviation of 0.1 magnitudes was applied to each point from the predicted set along the color axis. Each CMD contains a region of low source density below the cool end of the main sequence (the stellar/substellar gap) followed by an increase in density at fainter magnitudes, corresponding to the accumulation of cooling brown dwarfs.

The effects of metallicity and α-enhancement on the predicted brown dwarf colors and magnitudes are indicated by error bars and arrows in Figure 3.13 at three effective temperatures: 1900 K, 1300 K, and 1000 K. The first temperature is just above the HBL, while and the latter two are below the HBL. The effect size was inferred from the scatter among the two best-fit isochrones, `HMHA` and `HMMA`, and the nominal isochrone. Note that at $T_{\rm eff} = 1000$ K, only the best-fit isochrone (`HMHA`) has computed atmosphere models, so scatter at this temperature is based on extrapolated bolometric corrections for both `HMMA` and the nominal isochrones and may be unreliable. The scatter is substantial in the optical and near infrared HST bands, but appears far less significant in infrared JWST bands, as the `F150W2` band accommodates most of the prominent metallicity features in the spectrum (see Figure 3.3). A different choice of narrow-band filters would make color measurements more sensitive to chemical abundances at the expense of worse signal-to-noise ratio.

The extended luminosity functions that the CMD predictions are based on are shown in Figure 3.14. As before, both the main peak corresponding to the main sequence and the brown dwarf peak just emerging at the faint end can be seen with a gap in between. In the figure, each plot is given for two cluster ages of 10 Gyr and 13.5 Gyr corresponding to the expected ages of the youngest and oldest members in ω Centauri. While the main sequence peaks appear relatively unaffected by age, the brown dwarf peaks emerge at slightly brighter magnitudes at 10 Gyr. As expected for objects in energy equilibrium, the main sequence evolves slowly with time. By contrast, substellar objects have entered their cooling curves and are moving steadily across color-magnitude space. Hence, the luminosity function gap for ω Centauri and other globular

clusters provides a potential age diagnostic for the system, assuming the evolutionary timescales are correctly modeled [Caiazzo et al., 2017, 2019; Burgasser, 2004, 2009]. We also show in Figure 3.14 the variance in LF predictions taking into account uncertainty in the inferred IMF. In general, a higher value of the power index results in fewer low-mass members in the cluster and vice versa. Note that the width of the stellar/substellar gap is insensitive to the adopted IMF and is primarily determined by the mass-effective temperature relationship of the population. The normalization in Figure 3.14 is for the *total* number of helium-enriched members in the entire cluster based on the best-fit IMF (Equation 3.11), the best-fix mixing ratio ($\mu = 0.15$) and the assumed total cluster mass of 4×10^6 $M_\odot$ [D'Souza and Rix, 2013].

Finally, we provide a set of mass-luminosity relations for the aforementioned JWST and HST filters in Figure 3.15 alongside the mass-effective temperature relationship. All curves are based on the best-fit isochrone (`HMHA`). The predicted initial stellar mass at the hydrogen-burning limit (HBL) was taken as the mass for which the total proton-proton chain luminosity output corresponds to a half of the total luminosity output at 13.5 Gyr. This limit was found to be M_{HBL} = 0.066 $M_\odot$ for `HMHA` (Figure 3.15). For comparison, the HBL for the nominal population is at a marginally higher value of M_{HBL} = 0.069 $M_\odot$. A higher HBL mass is expected for stars with lower metallicity as the corresponding reduction in atmospheric opacity results in faster cooling and requires a higher rate of nuclear burning (higher core temperature) to sustain thermal equilibrium. We note that the hydrogen-burning limits calculated here are lower than most literature estimates (e.g. [Chabrier and Baraffe, 1997]) due to the increased helium mass fraction that stimulates faster hydrogen fusion in the core, allowing stars of lower masses to establish energy equilibrium.

3.6.2 Unresolved binary systems

A fraction of brown dwarfs in ω Centauri may be multiple systems which will appear brighter due to the superposition of fluxes from individual components. Existing constraints

from the luminosity function [Elson et al., 1995] and the radial velocity distribution [Mayor et al., 1996] suggest that ωCentauri has an unusually low binary fraction of at most a few percent among hydrogen-burning members which is likely to be lower yet for the substellar population of the cluster [Burgasser et al., 2007a; Fontanive et al., 2018]. We may therefore safely ignore the effect of triple and higher-order systems that are far less likely to form than binary systems [Raghavan et al., 2010].

The effect of unresolved binary systems is determined by the binary fraction of the cluster as well as the distribution of the component mass ratio, $q = M_s/M_p$ where M_s and M_p are the masses of the secondary and primary components respectively and $q \leq 1$. To quantify the effect, we carried out numerical simulations where a number of randomly chosen objects in the JWST predicted dataset received secondary components with masses drawn according to the commonly used [Kouwenhoven et al., 2009] power law distribution of mass ratios, $P(q) \propto q^{\beta}$. In each case, the probability distribution was trimmed at the minimum value of q that ensures the secondary mass remains within the mass range of the best-fit isochrone `HMHA`. We considered a range of β values from $\beta = -0.5$ calculated by Reggiani and Meyer [2011] for a variety of star forming regions, to $\beta = 4$ used by Burgasser et al. [2006] for field brown dwarfs. We found the companion mass distribution at the lowest value of q to closely resemble that obtained through random pairing of cluster members for our IMF. On the other hand, the highest considered value of β emphasizes preference for components with similar masses corresponding to the so-called "twin peaks" effect [Lucy and Ricco, 1979; Kouwenhoven et al., 2009].

We found that the width of the stellar/substellar gap shown in Fig. 3.14 is not noticeably affected by binary systems for binary fractions under 0.5 due to the smooth rise in brown dwarf number density with magnitude. The average brightness of modelled brown dwarfs increased by ~ 0.1 mag for the case of $\beta = 4$ and a binary fraction of 0.2. For the more realistic binary fraction of 0.05, the magnitude difference did not exceed 0.03 mag for all considered values of β, falling well within the expected uncertainty of future *JWST* measurements. We therefore conclude that

magnitude predictions for brown dwarfs in ω Centauri presented in this work are not noticeably affected by any realistic population of unresolved multiple star systems in the cluster.

3.7 Discussion

In this study, we calculated a new set of theoretical isochrones, mass-luminosity relations, and color-magnitude diagrams for the helium-rich members of the globular cluster ω Centauri. Our predictions provide a theoretical expectation for the first observations of brown dwarfs in globular clusters anticipated with JWST. At present, globular cluster photometry extends below the faint end of the main sequence, but not deep enough to robustly sample the brown dwarf population. The predictions presented in this chapter of the dissertation are adjusted for the metallicity and enhancements of individual elements in ω Centauri. The necessary parameters were determined by starting with a set of abundances derived from literature spectroscopy of bright members and iteratively perturbing them until the best correspondence of the synthetic color-magnitude diagram with the existing main sequence HST photometry was achieved. Our main findings are summarized below:

- In agreement with qualitative expectations, our predictions show that the main sequence is followed by a large stellar/substellar gap in the color-magnitude space populated by a small number of objects. The specific size of the gap depends on the age of the cluster and the evolutionary rate of brown dwarfs, the latter of which depends on the helium mass fraction and metal abundances.

- The modal trend in the color-magnitude diagram of ω Centauri cannot be reproduced with solar or scaled solar chemical abundances as evidenced by the dependence of compatibility likelihood on enhancements of individual elements shown in Figure 3.10. For this reason, our analysis required new evolutionary interior and atmosphere models.

- The best-fit abundances calculated in this study are summarized in Tables 3.1 and 3.2 corresponding to the HMHA population. We found that the helium-rich members are most consistent with the metal-rich end ($[\mathrm{M/H}] \approx -1.4$) of the metallicity distribution in ω Centauri in agreement with the hypothesis of Bedin et al. [2004].

- The best-fit isochrone, HMHA, is based on the distinct modal peaks of the $[\mathrm{C/M}]$ and $[\mathrm{N/M}]$ distributions inferred from spectroscopy of bright members in Marino et al. [2012]. The positions of the peaks within their distributions are consistent with the second generation of stars discussed in Marino et al. [2012] that is most resembling of the blue helium-rich sequence in the cluster.

- On the other hand, the broad $[\mathrm{O/M}]$ distribution in Marino et al. [2012] lacked a well-defined peak. Figure 3.7 demonstrates that the oxygen abundance cannot be reliably constrained by our method as the optical color-magnitude diagram of the cluster does not change significantly while $[\mathrm{O/M}]$ is varied within the limits of its distribution. However, we established that the CMD depends strongly on the abundance of α elements. The two best-fitting secondary populations, HMHA and HMMA, both require considerable α-enhancement with specific values of $[\alpha/\mathrm{M}] = 0.6$ and $[\alpha/\mathrm{M}] = 0.4$.

- The HST-observed luminosity distribution of the cluster can be reproduced within uncertainties by a broken power law IMF and two populations with solar and enhanced helium mass fractions, with the latter containing fewer than 45% of the members, in agreement with measurements in Bellini et al. [2009] away from the center of the cluster.

- We calculated the hydrogen-burning limit for the helium-rich members of ω Centauri as 0.066 $\mathrm{M}_{\odot}$. This value falls below the literature predictions for a solar helium mass fraction ($\sim$ 0.07 $\mathrm{M}_{\odot}$ at solar metallicity [Baraffe et al., 1998]) as larger helium mass fraction increases the core mean molecular weight, allowing faster nuclear burning and, hence, energy equilibrium in objects of lower mass.

- We predict that the brightest brown dwarfs in ω Centauri will have magnitude 28 in JWST NIRCam `F322W2` (Figure 3.14). Within our modelling range, the density of brown dwarfs appears to reach its maximum around magnitude 30, where the brown dwarf count per magnitude is comparable to the star count per magnitude around the peak of the main sequence within a factor of two. Based on our exposure calculations for JWST, we predict that the brown dwarf peak is just detectable with a 1 hr exposure, while signal-to-noise ratios between 5 and 10 can be attained for the brightest brown dwarfs for the same exposure time.

The analysis in this study is based on a new set of evolutionary models and model atmospheres, which was necessitated by the significant departures of ω Centauri abundances from the scaled solar standard that is assumed in most publicly available grids. Our grid reaches $T_{\rm eff} \sim$ 1 kK which is just sufficient to model the reappearance of brown dwarfs after the stellar/substellar gap in globular clusters. Extending the grid to even lower temperatures is currently not feasible with our present setup due to incomplete molecular opacities and associated convergence issues, requiring a future follow-up study with an improved modelling framework.

The analysis presented here relies on the assumption that a single best-fit isochrone is sufficient to describe the average trend of ω Centauri members in the color-magnitude space. A more complete study must model the population with multiple simultaneous isochrones capturing the chemical complexity of the cluster that may host as many as 15 distinct populations [Bellini et al., 2017c]. In fact, the bifurcation of the optical main sequence at the high temperature end into the helium-enriched and solar helium sequences is visually apparent in Figure 3.11, suggesting that the approximation is invalid in that temperature regime, which may explain the mismatch in the main sequence turn-off points between our best-fit prediction and the infrared dataset in the lower panel of Figure 3.11. At lower temperatures, the sequences appear more blended due to intrinsic scatter as well as increasing experimental uncertainties. However, the separation between the isochrones of different populations may be similar to or more prominent than differences

around the turn-off point [Milone et al., 2017]. Other globular clusters, such as NGC 6752, also show highly distinct populations in the near infrared CMDs [Milone et al., 2019].

In this study, mixing in additional isochrones from public grids allowed us to construct a model luminosity function that approximated its observed counterpart reasonably well; however, future studies will need to produce a more extensive grid of both evolutionary and atmosphere models to capture the multiple cluster populations present.

The current scarcity of known metal-poor brown dwarfs necessitates over-reliance on theoretical models of complex low-temperature physics that remain largely unconfirmed. The predictions drawn in this chapter of the dissertation will be directly comparable to new globular cluster photometry expected over the next few years from both JWST and other next generation facilities under construction. The observed size of the stellar/substellar gap as well as positions and densities of metal-poor brown dwarfs in the color-magnitude space will then provide direct input into state-of-the-art stellar models, offering a potential to improve our understanding of molecular opacities, clouds and other low-temperature phenomena in the atmospheres of the lowest-mass stars and brown dwarfs.

Chapter 3, in full, was submitted with minor alterations and accepted for publication in the Astrophysical Journal Series 2022. An edited version of this chapter is now available in print in Volume 930, Issue 1, authored by Roman Gerasimov, Adam J. Burgasser, Derek Homeier, Luigi R. Bedin, Jon M. Rees, Michele Scalco, Jay Anderson, and Maurizio Salaris. The dissertation author was the primary investigator of this study.

Chapter 4

Population II Stars in 47 Tucanae

4.1 Background

Globular clusters are large gravitationally bound conglomerations of stars, commonly observed in the stellar halos of galaxies including our own [Harris, 1991; Harris and Racine, 1979; Hubble, 1932]. Since the brightest examples (e.g. M5, ω Centauri, 47 Tucanae) are prominent naked-eye targets, the study of globular clusters dates back multiple centuries [de Lacaille, 1755; Messier, 1781]. A typical globular cluster hosts over 10^5 members [Hilker et al., 2020], far outnumbering the populations of typical open clusters (~ 20 – 10^4 members, [Qin et al., 2023; Sampedro et al., 2017]) that form in the present-day Milky Way. This points to the origin of globular clusters in the early phases of the hierarchical assembly of galaxies [Freeman and Bland-Hawthorn, 2002], making them some of the oldest objects in the universe, often exceeding 12 Gyr in age [Carretta et al., 2000; VandenBerg et al., 2013]. By consequence, the members of most globular clusters exhibit sub-solar metallicities ($[\mathrm{Fe/H}] \lesssim -1$ dex, [Bailin, 2019; Harris, 1996; Baum, 1952]) and have a distinct color distribution [ten Bruggencate, 1927; Hachenberg, 1939; Greenstein, 1939] that motivated the original definition of stellar populations [Baade, 1944; Oort, 1926].

Globular clusters are prime stellar astrophysics laboratories [Moehler, 2001] and probes of galactic formation and evolution [Lee, 2012; Recio-Blanco, 2018; Arkelyan and Pilipenko, 2022; Strader et al., 2004]. The old ages of globular clusters provide a direct constraint on the age of the universe [Krauss and Chaboyer, 2003; Valcin et al., 2020, 2021], while their kinematic properties trace the distribution of dark matter [Doppel et al., 2021; Vitral and Boldrini, 2022; Alabi et al., 2017]. Furthermore, tidally disrupted globular clusters are responsible for the production of stellar streams, alongside dwarf galaxies [Newberg, 2016]. Understanding the properties and evolution of these unique objects is therefore of uttermost importance to stellar astrophysics, galactic science and cosmology.

Naively, the coeval nature of star clusters leads to the expectation of uniformity in element abundances among their members. Nonetheless, the presence of star-to-star chemical variations within globular clusters was evident since the early spectroscopic observations that found differing cyanogen (CN) absorption strength [Lindblad, 1922; Popper, 1947] in stars of identical spectral types and luminosity classes[1] (the "*cyanogen discrepancy*", [Keenan and Keller, 1953]), followed by the first discoveries of carbon star members [Harding, 1962; Wing and Stock, 1973]. At first, these anomalies were largely attributed to evolutionary effects rather than a genuine primordial inhomogeneity (e.g., [Zinn, 1973; Norris and Bessell, 1975; Dickens and Bell, 1976; Sweigart and Mengel, 1979]), in part, because the comparable features of peculiar field stars were generally consistent with internal processing [Wallerstein and Greenstein, 1964; Wallerstein, 1969]. This consensus was eventually challenged by the observed spread in CNO abundances at early evolutionary stages [Da Costa and Demarque, 1982; Norris and Freeman, 1979; Hesser and Bell, 1980], evidence of variations in [Na/Fe] and [Al/Fe] [Cottrell and Da Costa, 1981; Norris et al., 1981] and the discovery of heavy element (atomic number greater than 13) variations in the globular cluster ω Centauri [Freeman and Rodgers, 1975].

Closely related to chemical heterogeneity is the so-called *second parameter problem*,

[1] Note that Lindblad [1922] did not claim the discovery, erroneously interpreting the result as a luminosity misclassification.

characterized by the diversity of horizontal branch morphologies among color-magnitude diagrams (CMDs) of globular clusters with comparable metallicities [Sandage and Wildey, 1967; van den Bergh, 1967]. In some cases, the horizontal branch is distinctly bimodal (e.g., NGC 2808, [Harris, 1974]), which led Rood and Crocker [1985] (also see [Crocker et al., 1988]) to suggest the presence of *multiple populations* (MP) of stars with distinct histories of chemical enrichment. In this scenario, a fraction of members (the *primordial population*, using the terminology of [Bastian and Lardo, 2018]) form similarly to regular halo stars, while the rest (the *enriched population*) are influenced by the unique environment of the cluster. The MP origin of the observed chemical anomalies was proposed by Smith and Norris [1983] on the basis of the observed bimodality in CN absorption among globular clusters with split horizontal branches. This hypothesis is now firmly established based on detailed spectroscopic abundance measurements of the horizontal branch members [Marino et al., 2011].

Over the last three decades, the existence of MP in globular clusters has been confirmed by detailed spectroscopic abundances of giant (e.g., [Sneden et al., 1992; Thygesen et al., 2014; Cordero et al., 2014; Marino et al., 2012; Yong et al., 2008]), subgiant and main sequence turn-off stars (e.g., [Marino et al., 2016; Gratton et al., 2001; Briley et al., 1996]), integrated spectroscopy [Rennó et al., 2020], and splitting of main sequence (e.g., [Anderson, 1997; Bedin et al., 2004; Piotto et al., 2007; Milone et al., 2013]) and post-main sequence (e.g., [Cassisi et al., 2008; Piotto et al., 2012]) CMDs. A more comprehensive summary of available evidence of MP may be found in numerous reviews of the subject ([Bastian and Lardo, 2018; Gratton et al., 2004, 2015; Smith, 1987; Gratton et al., 2019; Milone and Marino, 2022; Dotter, 2013] and references within).

The enriched population is characterized by distinct light element abundances: most prominently, the overabundance of nitrogen and sodium, and the depletion of carbon and oxygen, compared to the primordial population [Sneden et al., 1992; Dickens et al., 1991]. On the other hand, the abundances of heavy elements generally do not display star-to-star variations (globular clusters are said to be *mono-metallic*, in the sense that $[\mathrm{Fe/H}] \approx \text{const}$), with the exception of a

few *anomalous globular clusters* [Marino, 2013], of which ω Centauri is the most well-known [Gratton, 1982; Johnson and Pilachowski, 2010]. By contrast, these characteristic abundance patterns are not observed in open clusters [MacLean et al., 2015; Martell and Smith, 2009; de Silva et al., 2009] and are rare ($\sim 3\%$ of the $[\mathrm{Fe/H}] \leq -1$ local sample, [Martell et al., 2011]) among field stars [Kraft, 1994; Gratton et al., 2000; Martell and Grebel, 2010; Carretta et al., 2010], motivating the common assumption that the handful of known examples were ejected from globular clusters in the past [Ramírez et al., 2012; Lind et al., 2015].

The physical origin of MP remains largely unexplained [Bastian and Lardo, 2018]. The mono-metallic nature of non-anomalous globular clusters is usually attributed to the high velocity of supernova ejecta that expel a significant amount of pristine gas from the cluster, alongside most of the material enriched with heavy elements, shortly after the onset of star formation (~ 30 Myr, [D'Ercole et al., 2008, 2016]). Many of the proposed MP theories fall under one of two broad categories. In *multiple generation models* (e.g., [Cottrell and Da Costa, 1981; Decressin et al., 2007a; Breen, 2018]), star formation proceeds in two or more bursts with a sufficient time interval to allow the earlier generations of stars to build up a reservoir of enriched gas, from which later generations are assembled. Alternatively, *concurrent formation models* (e.g., [Gieles et al., 2018; Bastian et al., 2013; Winter and Clarke, 2023]) invoke a single generation of coeval stars, in which a fraction of the members are polluted by stellar ejecta to attain the chemical abundances of the enriched population. Both approaches suffer from major shortcomings. Since nuclear processing primarily occurs in massive stars, and since these stars make a subdominant contribution to the overall mass budget for commonly assumed initial mass functions (e.g., [Kroupa, 2001]), it is unclear how a sufficient amount of processed material can be produced in multiple generation models to assemble the enriched population of stars (enriched stars make up the majority of members in most globular clusters, [Bastian and Lardo, 2015]). This *mass budget problem* is easier to resolve in concurrent formation models, where the enriched population is envisioned to form from pristine gas prior to the onset of supernovae; however, considerable fine-tuning is

needed to match the required pollution timescales [Salaris and Cassisi, 2014] and to reproduce the discreetness of populations that arises naturally when multiple generations are involved.

A potential observational signature of concurrent formation models is the possible dependence of element abundances on the initial stellar mass [Ziliotto et al., 2023; Milone, 2023], related to the fact that the magnitude of chemical enrichment is determined not only by the composition of the polluted material produced by the primordial generation, but also by the ability of the enriched generation of stars to accrete it. If the polluted material is primarily accreted onto circumstellar disks, the accretion efficiency is expected to be proportional to the surface area of the disk and its longevity, which, in turn, depends on the mass and evolution of the parent star [Carpenter et al., 2006; Ohtani and Tsuribe, 2013]. If instead the material is accreted onto the surface of the star, the accretion rate is expected to be proportional to the squared stellar mass (e.g., in the Bondi accretion formalism, [Bondi, 1952]). The accreted material may then be diluted by convective mixing within the star, which also depends on the stellar mass [Chabrier and Baraffe, 1997]. Finally, the density of polluted material may not be uniform throughout the cluster. For example, in the concurrent formation model of Bastian et al. [2013], the polluted material is only available in the core of the cluster. In this case, the accretion efficiency will depend on the kinematic properties of the stars, which are also related to stellar mass [Anderson and van der Marel, 2010; Anderson, 2002].

Due to the large distances to globular clusters ($\gtrsim 5\,\mathrm{kpc}$, [Harris, 1996]), high signal-to-noise ratio spectra can only be obtained for the brightest members that fall within a narrow mass range. Studying the variation of chemical abundances over a wider mass range inevitably requires the inference of chemistry from multiband photometry. In general, the photometric colors of low-mass stars are highly sensitive to the variations in element abundances due to the dominant molecular chemistry and opacity in low-temperature atmospheres [Marley et al., 2002; Gerasimov et al., 2022]. Furthermore, low-mass stars are particularly valuable as chemical tracers, since molecular absorption is less affected by the non-equilibrium radiation field [Johnson, 1994],

while the interiors of low-mass stars are fully mixed and undergo minimal nuclear processing [Chabrier and Baraffe, 1997]. Sophisticated stellar models are required to take full advantage of this potential. Accurate simulation of the intricate physics and chemistry in low-temperature atmospheres remains extremely challenging.

Considerable progress in the photometric analysis of cool stars near the end of the main sequence ($\gtrsim 0.1\,M_\odot$) in globular clusters has been made since the advent of space-based observations with the Hubble Space Telescope (HST) and the James Webb Space Telescope (JWST). Recent results include measurement of the [O/Fe] spread in the globular clusters NGC 6752 [Dotter et al., 2015], M92 [Ziliotto et al., 2023] and 47 Tucanae [Milone, 2023] and photometric characterization of individual populations in NGC 6752 [Milone et al., 2019; Gerasimov et al., 2022]. Our measurement of α-enhancement in ω Centauri is described in Chapter 3 of this dissertation.

The CMDs of globular clusters are expected to extend far beyond the end of the main sequence into the brown dwarf regime. Unlike stars, brown dwarfs do not establish energy equilibrium and, instead, undergo long-term cooling, thereby creating a stellar/substellar gap in the CMD between the faintest main sequence star and the brightest brown dwarf [Burgasser, 2004; Caiazzo et al., 2017, 2019]. Photometric observations of the substellar sequence in globular clusters would then not only extend the mass baseline of MP studies, but also provide an independent constraint on the cluster age from the width of the gap. The faint magnitudes of globular cluster brown dwarfs pose a major challenge to their detection. The results of dedicated searches for brown dwarf candidates in the globular cluster M4 [Dieball et al., 2016, 2019] with HST remain inconclusive. In Chapter 3, we estimated the colors and magnitudes of the brown dwarfs in the globular cluster ω Centauri and concluded that the substellar sequences of nearby globular clusters fall within the sensitivity limit of JWST. Nardiello et al. [2023] recently reported the first tentative discovery of a brown dwarf in the globular cluster 47 Tucanae, designated *BD10*. While the substellar nature of this object remains to be confirmed, we anticipate that many similar

discoveries will follow in the near future from the ongoing Cycle 1 JWST campaigns [Bedin et al., 2021; Caiazzo et al., 2021] and subsequent cycles.

In this chapter, we describe a new method to determine the chemical abundances and other fundamental parameters of globular clusters based on their CMDs from the subgiant branch to the substellar regime. Our approach involves the computation of new evolutionary models and model atmospheres with fully self-consistent chemical abundances. Model isochrones are calculated and fitted to the observed distribution of photometric colors in an iterative manner. The computational efficiency of the process is attained by identifying the components of the stellar models that are most sensitive to particular elements, and recalculating them only when the abundances of those elements are updated. We apply our method to the brightest mono-metallic (non-anomalous) globular cluster 47 Tucanae.

This chapter of the dissertation is organized as follows. In Section 4.2 we describe our compilation of spectroscopic 47 Tucanae abundances in the literature. The archival HST photometry that was used in this study is briefly described in Section 4.3. Section 4.4 details the process of calculating a theoretical isochrone for a given set of chemical abundances, and includes a thorough analysis of associated systematic errors. Our method of isochrone fitting to the observed CMD is presented and applied to 47 Tucanae in Section 4.5. In Section 4.6, we derive the mass function of the cluster and predict the anticipated properties of its substellar members. Our results are discussed and the conclusions are drawn in Section 4.7.

4.2 Nominal chemistry

In this study, we adopt spectroscopically inferred chemical abundances of 47 Tucanae as a baseline for comparison against their photometric counterparts, as well as an initial guess in CMD fitting (Section 4.5). We refer to this set of abundances as the *nominal* composition of the cluster. The nominal abundances are compiled from three sources: Thygesen et al. [2014], Cordero et al.

[2014] and Marino et al. [2016]. The set is similar to that used in Zhou et al. [2022]. Here, we provide a more complete description of its derivation.

Thygesen et al. [2014] list metallicity ([Fe/H]) and the abundances of 26 other elements, measured for 13 stars at the tip of the red giant branch ($3900\,\mathrm{K} \lesssim T_{\mathrm{eff}} \lesssim 4300\,\mathrm{K}$, $0.3 \lesssim \log_{10}(g) \lesssim 1.5$) in 47 Tucanae. For [Fe/H], [Ti/Fe] and [Sc/Fe], separate measurements are made for the lines of neutral and ionized species. Both estimates of [Fe/H] are consistent and treated as independent in our analysis. Since titanium and scandium have much lower ionization potentials than iron [Lide, 2004], the neutral lines of these elements may be affected by unaccounted ultraviolet overionization, particularly prominent at low effective temperatures and metallicities [Bergemann, 2011; Zhang et al., 2008; Mashonkina, 2010]. As such, we discard the neutral line measurements of [Ti/Fe] and [Sc/Fe] in Thygesen et al. [2014]. We further discard all measurements without uncertainties.

Cordero et al. [2014] obtained 181 composition measurements for 164 unique red giant and asymptotic giant members of 47 Tucanae ($\log_{10}(g) \lesssim 3$). The dataset includes [Fe/H] and 9 other elements. Of 164 observed stars, 5 have also been analyzed in Thygesen et al. [2014]. Abundance measurements reported in both references are generally consistent within the published error bars, with the exception of [Al/Fe], for which the value in Cordero et al. [2014] exceeds that of Thygesen et al. [2014] by ~ 2 and ~ 2.5 sigma for the stars 2618 and 3622 respectively (catalog numbers from [Lee, 1977]). The difference may be partially caused by the more detailed modelling of Al lines in Thygesen et al. [2014], following Andrievsky et al. [2008].

The measurements in Marino et al. [2016] extend our sample to the fainter red giant and sub-giant members with $3 < \log_{10}(g) < 4$. The dataset lists metallicities and abundances of 7 individual elements for 74 stars. For sodium, we adopt the values with non-local thermodynamic equilibrium corrections based on the curves-of-growth from Lind et al. [2011]. Following the authors' recommendation, we use uncertainties of 0.1 dex, 0.1 dex and 0.15 dex in [Mg/Fe], [Al/Fe] and [Si/Fe] respectively, instead of the quoted measurement errors due to the effect of

CN molecular features on the analyzed lines of these elements around 0.8 µm.

The final sample includes measurements from multiple sources for [Fe/H], [Al/Fe], [Ca/Fe], [Eu/Fe], [La/Fe], [Mg/Fe], [Na/Fe], [Ni/Fe], [O/Fe], [Si/Fe] and [Ti/Fe]. We carried out a Kolmogorov–Smirnov statistical test for each of these elements to determine whether the measurements from different sources in literature are consistent with a shared parent population. The null-hypothesis (measurements are consistent) was rejected with 99% confidence for [Al/Fe], [Eu/Fe], [Mg/Fe], [Na/Fe], [Ni/Fe] and [Si/Fe]. Since the spectroscopic measurements used in this study span a vast range of post-main sequence evolutionary stages, the discrepancy may reflect a genuine alteration of surface abundances by the first dredge-up [Salaris et al., 2020], meridional circulation [Sweigart and Mengel, 1979], thermohaline mixing [Angelou et al., 2011] or other mechanisms. However, the effect is normally most pronounced in the products of the CNO cycle [Messenger and Lattanzio, 2002], all of which have passed the consistency test in our compilation. Therefore, the observed discrepancies between different literature sources are likely systematic in nature, exemplified by the aforementioned mismatch in aluminum measurements between Thygesen et al. [2014] and Cordero et al. [2014].

All spectroscopic composition measurements from the three literature sources were combined into a single set of chemical abundances, available in Table E.1 of Appendix E. We assumed that each abundance measurement ($x_i^{(X)}$ for the i-th measurement of element X out of $N^{(X)}$ measurements in total) is drawn from a normal distribution with the standard deviation composed of two components added in quadrature: the physical variation in chemistry among cluster members ($s^{(X)}$, identical for all measurements of X) and the measurement error ($\sigma_i^{(X)}$). The physical variation of each element may then be estimated as in Equation 4.1:

$$\left(s^{(X)}\right)^2 = \frac{N^{(X)}\mathrm{Var}\left(x_i^{(X)}\right)}{N^{(X)} - 1.5} - \left\langle \left(\sigma_i^{(X)}\right)^2 \right\rangle \tag{4.1}$$

Since we are ultimately interested in the standard deviation of the physical spread, we

evaluated the unbiased sample variances assuming $N^{(X)} - 1.5$ degrees of freedom [Brugger, 1969]. In cases where the average measurement error exceeds the observed scatter in the data, $s^{(X)}$ cannot be estimated, and the data may be considered consistent with lack of star-to-star variations in X. The mean abundance of each element and its uncertainty were calculated using the square reciprocal measurement errors as statistical weights with $s^{(X)}$ added to the measurement error in quadrature if available. Finally, we note that the estimates of $s^{(X)}$ for the six elements that did not pass the Kolmogorov–Smirnov test are likely biased by systematic errors that may have been unaccounted for in the quoted measurement uncertainties.

Since the helium abundance cannot be measured spectroscopically at low effective temperatures, the nominal helium mass fraction of 47 Tucanae was adopted as $Y = 0.25$, following the isochrone fit of eclipsing binary members in Thompson et al. [2020].

4.3 Archival photometry

Throughout this chapter, all mentions of the optical bands `F606W` and `F814W` will implicitly refer to the wide field channel of the Advanced Camera for Surveys (ACS) on HST. Likewise, all mentions of the near infrared bands `F110W` and `F160W` will refer to the near infrared channel of the Wide Field Camera 3 (WFC3) on HST. Finally, the infrared bands `F150W2` and `F322W2` will refer to the Near Infrared Camera (NIRCam) on JWST.

Our analysis is based on archival HST photometry (*GO-11677*, PI: H. Richer) of 47 Tucanae presented in Kalirai et al. [2012]. The primary field was imaged in the `F606W` and `F814W` bands. The field spans ~ 5 arcmin and is located at 6.7 arcmin (2.1 half-light radii, [Harris, 1996]) from the center of the cluster. Parallel fields were imaged in the `F110W` and `F160W` bands, as well as additional bands of the ultraviolet and visible light channel that are not used in this study. The parallel fields span a 250 degree arc, centered at the primary field with the radius of ~ 6 arcmin and facing away from the center of the cluster (see Figure 2 of [Kalirai et al., 2012]). This work

is based on the observations of the primary field and one of the parallel fields with the largest cumulative exposure time (field 13, referred to as the "stare").

All magnitudes quoted in this chapter are VEGAMAG.

4.4 Model isochrones

We derive the properties of 47 Tucanae by comparing theoretical model isochrones to the observed CMD of the cluster. Due to the presence of MP, an accurate model of the CMD requires multiple theoretical isochrones that capture the observed spread in photometric colors. We therefore aim to find three isochrones with distinct chemical compositions that approximately trace out the *blue tail*, the *red tail* and the *ridgeline* of the CMD. We adopt the convention of identifying the blue and red tails of the distribution based on the F110W − F160W near infrared color of the lower main sequence.

We search for the desired isochrones through iterative perturbations of the nominal chemical composition. In this section, we describe the general process of calculating a theoretical isochrone for a given chemical composition. Our approach to isochrone fitting and the treatment of multiple populations in the cluster are presented in Section 4.5.

4.4.1 Evolutionary models

Stellar evolution is simulated using the MESA (Modules for Experiments in Stellar Astrophysics) code [Paxton et al., 2011, 2013, 2015, 2018, 2019], version 15140. The evolution begins at the pre-main sequence (PMS) phase and is allowed to proceed either until the age of 13.5 Gyr or until the tip of the subgiant branch, whichever occurs sooner. For our purposes, we define the tip of the subgiant branch as the point, at which the innermost shell that satisfies $\varepsilon_{\rm nuc} > 10^3\,{\rm erg\,g^{-1}\,s^{-1}}$ begins to fall outside the central 10% of the stellar mass ($\varepsilon_{\rm nuc}$ is the specific nuclear energy release rate). This criterion was empirically determined to be a reliable indicator of the hydrogen shell

ignition that characterizes the onset of the red giant branch [Gamow and Keller, 1945]. Evolving the model further into the red giant branch incurs a larger computational cost due to the rapid variation of surface parameters with age, and is beyond the scope of this study; however, see Salaris et al. [2020].

The initial stellar masses are sampled on an adaptive grid that guarantees the difference in luminosities and effective temperatures between adjacent grid masses of $|\Delta \log_{10} L| < 0.12\,\mathrm{dex}$ and $|\Delta T_{\mathrm{eff}}| < 120\,\mathrm{K}$, respectively, at the *checkpoint* ages between 10 Gyr and 13.5 Gyr in steps of 0.5 Gyr (the typical average differences at 13.5 Gyr are $\langle|\Delta \log_{10} L|\rangle \approx 0.07\,\mathrm{dex}$ and $\langle|\Delta T_{\mathrm{eff}}|\rangle \approx 70\,\mathrm{K}$). The lowest mass in the grid ($\sim 0.04\,\mathrm{M}_{\odot} - 0.05\,\mathrm{M}_{\odot}$) is chosen to attain an evolved T_{eff} of $\lesssim 700\,\mathrm{K}$ at 13.5 Gyr, while the highest mass ($\sim 0.9\,\mathrm{M}_{\odot}$) is set by requiring that the star takes at least 10 Gyr to reach the tip of the subgiant branch.

PMS stars at zero age are initialized with uniform chemical abundances and central temperature of $T_c = 5 \times 10^5\,\mathrm{K}$. This choice follows Choi et al. [2016], and ensures that the stars of all considered initial masses are found within the boundary condition tables (Section 4.4.2) at the completion of the main PMS relaxation routine in `MESA`. The additional PMS relaxation for $> 0.3\,\mathrm{M}_{\odot}$ stars until the formation of the radiative core, introduced in version `15140` (`pre_ms_relax_to_start_radiative_core`), was disabled in all of our evolutionary models to provide a consistent definition of zero age for all calculated evolutionary tracks.

The interior convective mixing length (in the formalism of *mixing length theory*, MLT; [Böhm-Vitense, 1958]) in all models was set to the solar-calibrated value of $\alpha_{\mathrm{MLT}} = 1.82$ scale heights [Salaris and Cassisi, 2015; Choi et al., 2016]. The effect of other choices for this parameter is discussed in Section 4.5.

4.4.2 Boundary conditions

At each evolutionary step, energy conservation requires the pressure-temperature profile to be consistent with the luminosity output of the star. Evaluating this condition near the

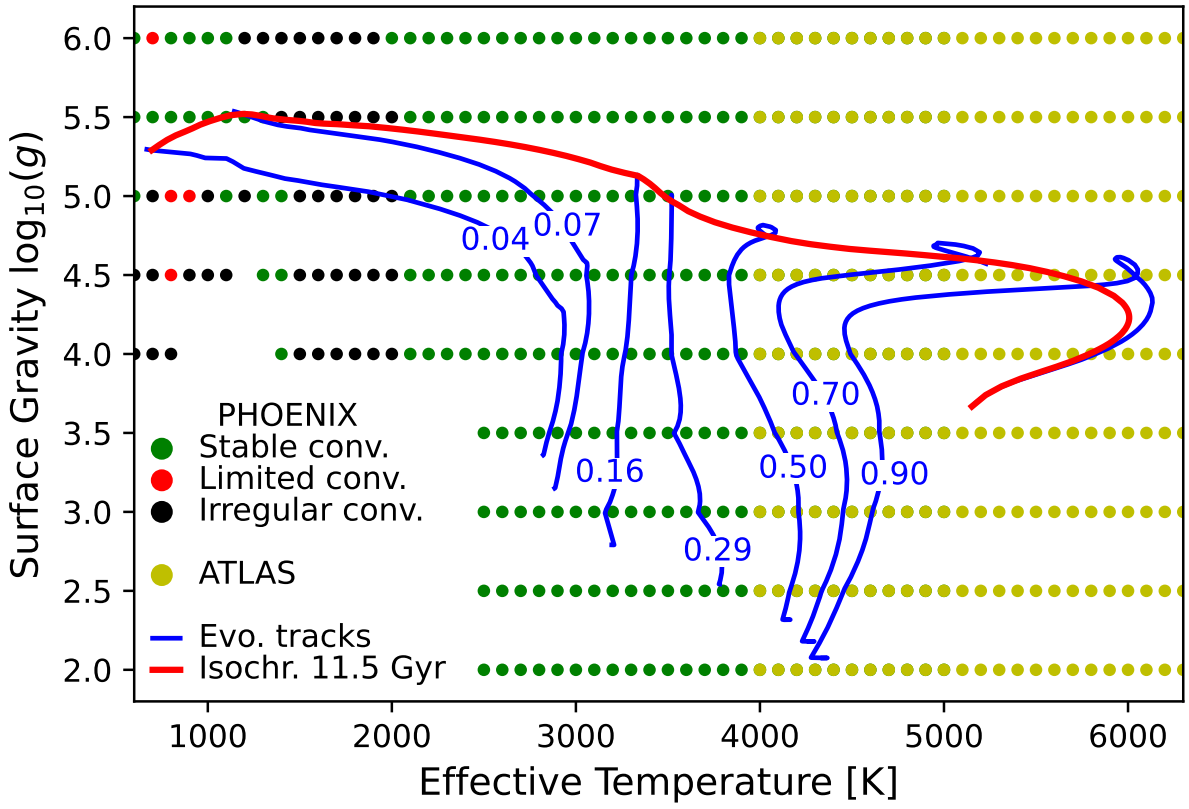

Figure 4.1. Effective temperatures and surface gravities of the model atmospheres, calculated in this study for the final *ridgeline* isochrone of 47 Tucanae. The PHOENIX models are color-coded by their convergence parameters, as detailed in Section 4.4.4. The evolutionary tracks of selected MESA models in the $T_{\rm eff} - \log_{10}(g)$ space are shown for comparison, as well as the final isochrone at 11.5 Gyr. The tracks are labeled by their initial stellar masses in $M_{\odot}$.

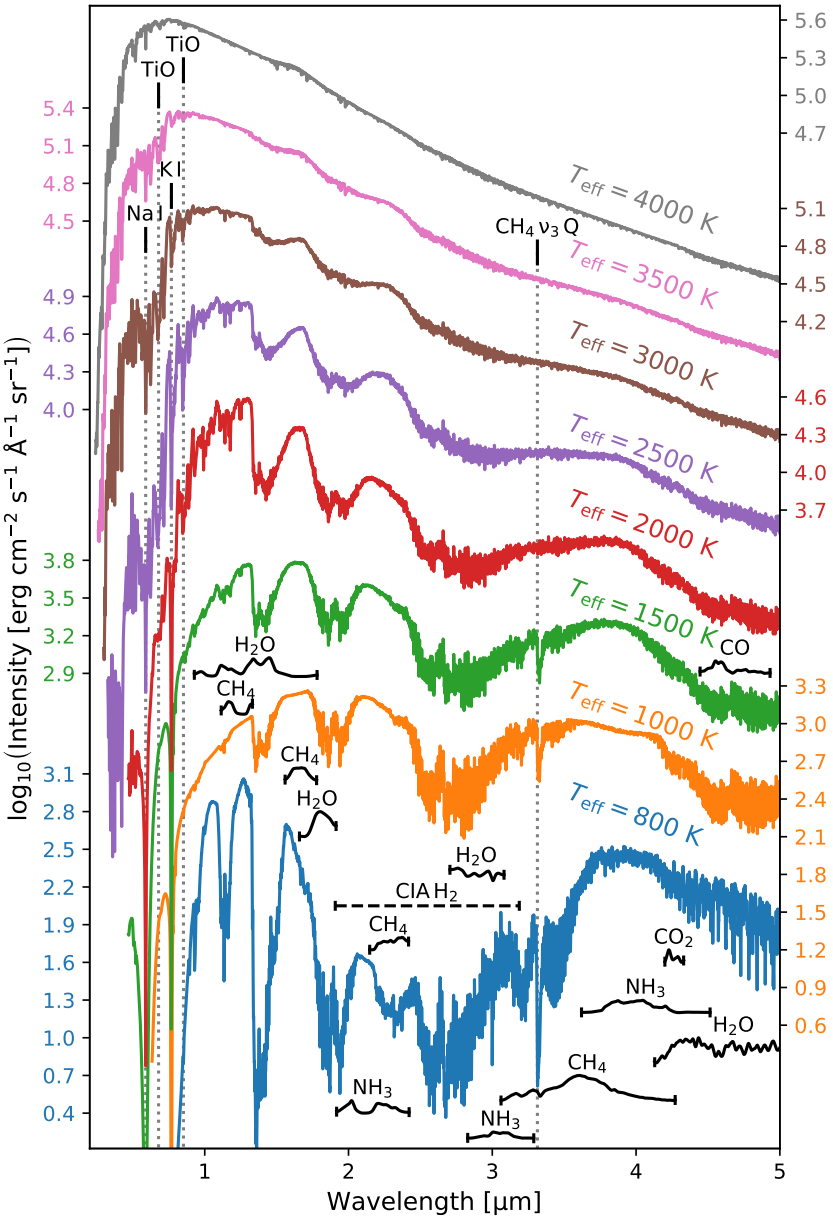

Figure 4.2. Synthetic spectra of selected model atmospheres at $\log_{10}(g) = 5$, calculated in this study for the *ridgeline* isochrone of 47 Tucanae. The important absorption bands of CH_4, CO, CO_2, H_2O and NH_3 are labeled with ragged black lines that represent the variation of absorption strength within the band for the $T_{\rm eff} = 800\,$K model. The central wavelengths of prominent TiO bands, Na and K atomic lines and the peak of the CH_4 ν_3 (asymmetric stretching vibration band) Q-branch are shown with vertical dotted lines. The approximate wavelength range of strong collision-induced H_2 absorption (CIA) is shown with the horizontal dashed line. The spectra have been convolved with a 10 Å Gaussian kernel for clarity.

surface of low-mass stars is challenging due to the complex relationship between the pressure-temperature profile and the outgoing energy flux, caused by low-temperature phenomena such as non-grey molecular opacity, cloud formation and convective instabilities. This issue is particularly prominent at $T_{\rm eff} \lesssim 4500\,{\rm K}$, as the structure of the stellar atmosphere begins to significantly deviate from the Eddington approximation [Mihalas, 1978; Burrows et al., 1989; Dorman et al., 1989; Zhou et al., 2022]. More accurate atmospheric pressure-temperature profiles may be extracted from model atmospheres, precomputed for the entire range of surface parameters that may be encountered by the star during its evolution.

Following Chabrier and Baraffe [1997]; Choi et al. [2016]; Phillips et al. [2020], we calculated a grid of model atmospheres (Section 4.4.3) for each theoretical isochrone, spanning $2 \leq \log_{10}(g) \leq 6$ for $2500\,{\rm K} \leq T_{\rm eff} \leq 7500\,{\rm K}$, and $4 \leq \log_{10}(g) \leq 6$ for $500\,{\rm K} \leq T_{\rm eff} \leq 2400\,{\rm K}$, with steps of 100 K in $T_{\rm eff}$ and 0.5 in $\log_{10}(g)$. Models with $\log_{10}(g) < 4$ & $T_{\rm eff} < 2500\,{\rm K}$ were not required, since such low gravities are only encountered during the early evolution ($< 5\,{\rm Myr}$) and the subgiant phase, both of which are characterized by higher effective temperatures ($T_{\rm eff} > 2500\,{\rm K}$). For some of the calculated isochrones, a small number of model atmospheres could not be computed due to convergence issues (Section 4.4.4). The corresponding empty grid points were then filled in using linear Delaunay triangulation [Barber et al., 2013]. The temperatures and gravities of the atmosphere models calculated for the final *ridgeline* isochrone are plotted in Figure 4.1 alongside the $T_{\rm eff} - \log_{10}(g)$ tracks of selected evolutionary models.

The model atmospheres were converted to tables of gas pressure and temperature at a prescribed depth and provided to `MESA` as the outer boundary conditions at each evolutionary step and for each iteration in the solution of the stellar structure equations. In general, specifying the boundary conditions at larger Rosseland optical depths (τ) is preferred, as it minimizes the discontinuity in opacity between the atmosphere and interior, and ensures adiabatic behavior at the boundary [Chabrier and Baraffe, 1997, 2000; Spada et al., 2017]. However, the reduced atmospheric opacity in more massive stars shifts the boundary to larger physical depths, where

the non-ideal gas behavior may be significant [Burke et al., 2004], and is not accounted for in our high-$T_{\rm eff}$ model atmospheres. We therefore employed two distinct atmosphere-interior coupling regimes with boundary conditions at $\tau = 100$ for $M < 0.5\,\mathrm{M}_\odot$, and at $T(\tau) = T_{\rm eff}$ (photosphere) for $M > 0.6\,\mathrm{M}_\odot$, where $T(\tau)$ is the temperature profile of the star and M is the initial stellar mass. At intermediate stellar masses, $0.5\,\mathrm{M}_\odot \leq M \leq 0.6\,\mathrm{M}_\odot$, a linear ramp between the two regimes was applied. The range of transition was chosen to approximately coincide with the maximum value of $dT(\tau = 100)/dM$ for main sequence stars. The implications of this choice on the synthetic photometry are discussed in Section 4.4.6.

By default, `MESA` falls back on the Eddington approximation when the range of pre-tabulated boundary conditions is exceeded. Near the edges of the table, a smooth blending between the on-table and off-table boundary conditions is carried out, which may result in numerical instabilities at low $T_{\rm eff}$ due to the extreme inaccuracy of the Eddington formula. Since our models do not leave the table range during regular evolution, we modified the source code of `MESA` to disable the off-table blending once the PMS phase has been completed. We also updated the code to interpolate the tables linearly rather than bicubically to address unphysical temperatures and pressures resulting from spline overshoots [Fried and Zietz, 1973] in the vicinity of poorly converged model atmospheres (Section 4.4.4).

4.4.3 Model atmospheres

Model atmospheres were calculated using the `PHOENIX` code [Hauschildt et al., 1997], version `15.05.05D` [Allard et al., 2011, 2012; Gerasimov et al., 2020] at $T_{\rm eff} \leq 5000\,\mathrm{K}$; and the `ATLAS` code [Kurucz, 1970], version `9` [Kurucz, 2005, 2014] at $T_{\rm eff} > 5000\,\mathrm{K}$. The use of `ATLAS` for "warm" atmospheres is advantageous due to its superior computational efficiency (see Section 4.4.5), attained by virtue of opacity sampling from pre-tabulated opacity distribution functions (ODFs; [Kurucz et al., 1974; Carbon, 1984]), simplified chemical equilibrium (only gaseous species are considered, molecule-molecule interactions are ignored) and the ideal equation

of state. The ODFs for the chemical composition of each isochrone were computed for $9\,\mathrm{nm} \lesssim \lambda \lesssim 160\,\mu\mathrm{m}$ at 57 temperatures between $\approx 2 \times 10^3\,\mathrm{K}$ and $\approx 2 \times 10^5\,\mathrm{K}$ using the satellite package `DFSYNHTE` [Castelli, 2005b; Castelli and Kurucz, 2003]. `ATLAS` atmospheres are stratified into 72 plane-parallel layers, spanning $10^{-7} < \tau < 100$ with logarithmic spacing. The synthetic spectra for each model atmosphere were calculated using the `SYNTHE` code [Kurucz and Avrett, 1981] within $0.1\,\mu\mathrm{m} < \lambda < 5\,\mu\mathrm{m}$, at the constant resolution[2] of $\lambda/\Delta\lambda \sim 6 \times 10^5$. All three codes are packaged in the open source *Python* dispatcher `BasicATLAS`[3], alongside a suite of internal consistency checks and a synthetic photometry calculator.

`PHOENIX` allows for a more accurate treatment of low-T_{eff} atmospheres through direct sampling of opacity at the wavelengths of interest, a more complete chemical reaction network (including condensation, see [Allard et al., 2001] for a review), a comprehensive molecular line database (most importantly, H_2O lines from [Barber et al., 2006] and CH_4 lines from [Brown, 2005] and [Wenger and Champion, 1998; Homeier et al., 2003]; other included lines are listed in Table 3.3), and a non-ideal equation of state [Saumon et al., 1995], among other features. The inclusion of condensate species (*clouds*) in the chemical equilibrium and the opacity model is necessary to reproduce the observed reddening of photometric colors at $T_{\mathrm{eff}} \lesssim 3000\,\mathrm{K}$ compared to gas-only models [Allard et al., 2001; Lunine et al., 1986]. Our setup of `PHOENIX` also includes the *Allard & Homeier* treatment of gravitational settling for condensate species [Allard et al., 2012; Helling et al., 2008] that gradually removes clouds from the spectrum-forming region of the atmosphere at $T_{\mathrm{eff}} \ll 2000\,\mathrm{K}$ [Tsuji and Nakajima, 2003]. For computational efficiency, we only consider gravitational settling at $T_{\mathrm{eff}} < 2500\,\mathrm{K}$ and, otherwise, assume that the condensate species remain at chemical equilibrium.

Our `PHOENIX` models are stratified into 250 layers when gravitational settling is used and 128 layers otherwise. Unlike `ATLAS`, the atmospheric layers in `PHOENIX` are spherical and defined

[2] `SYNTHE` treats all line profiles as symmetric with respect to the nearest point on the wavelength grid. For this reason, high resolutions of order $\lambda/\Delta\lambda \sim 10^5 - 10^6$ are typically recommended even when not required for intended science [Kurucz, 2014; Sbordone and Bonifacio, 2005].

[3] https://github.com/Roman-UCSD/BasicATLAS

by the optical depth at a fixed wavelength (τ_λ, where $\lambda = 1.275\,\mu$m) instead of the Rosseland mean. The bottom of the atmosphere is set to $\tau_\lambda = 10^3$ for the models without gravitational settling, but reduced to $\tau_\lambda = 316$ when settling is enabled to avoid the numerical issues associated with settling calculations at large depths. The top of the atmosphere is defined by the gas pressure, rather than optical depth, set to $10^{-3}\,\mathrm{dyn/cm^2}$. The optical depth grid is approximately logarithmic. For all models considered in this study, the atmospheres at the final evolutionary state are negligibly thin compared to the stellar radius (the $\tau = 100$ layer is always found within the outer 0.1% of the photospheric radius, calculated at $T(\tau) = T_{\rm eff}$). Therefore, the effect of spherical geometry is expected to be subdominant, allowing the use of approximate atmospheric radii from literature [Baraffe et al., 2015] instead of introducing additional dimensions to our model atmosphere grids. The wavelength sampling and spectral synthesis for all PHOENIX models are carried out within $1\,\text{Å} < \lambda < 1\,$mm with a median resolution of $\lambda/\Delta\lambda \sim 18\,250$ between $0.5\,\mu$m and $3\,\mu$m. A few examples of the synthetic spectra for the chemical abundances of the *ridgeline* isochrone and $\log_{10}(g) = 5.0$ are provided in Figure 4.2.

We assume that the chemical composition of the atmosphere is unaffected by stellar evolution and is identical to the initial composition of the PMS star, with the exception of [Li/Fe] that is reduced by 3 dex in all PHOENIX models compared to the PMS abundance. This assumption is justified by the fact that low-mass stars ($\lesssim 0.6\,\mathrm{M_\odot}$) undergo minimal nuclear processing (with the exception of lithium burning), while their higher-mass counterparts establish radiative zones at young ages, thereby preventing the nuclear burning products from reaching the atmosphere. The behavior of [Li/Fe] in the interior and the atmosphere of the star as a function of mass was explored in detail in Chapter 3.

4.4.4 Model convergence

In both model atmospheres and the time steps of evolutionary models, the equations of input physics are solved using iterative methods. At the high effective temperatures of ATLAS

atmospheres, the parameter space maintains approximate local linearity [Gustafsson et al., 2008], allowing for fast and reliable convergence onto a self-consistent solution. We carry out ATLAS iterations in batches of 15 until the maximum flux error and the maximum flux derivative error across all layers drop below 1% and 10%, respectively (following [Sbordone and Bonifacio, 2005; Mészáros et al., 2012]; see Appendix A), or until no further progress can be made. These convergence standards have been met by nearly all ATLAS atmospheres computed in this study, with the exception of a few $T_{\rm eff} > 6500\,{\rm K}$ models that generally fall outside the region of parameter space, explored by the calculated evolutionary tracks (Figure 4.1).

The evolution of convergence parameters across iterations in low-$T_{\rm eff}$ PHOENIX atmospheres is more involved. In models with subdominant cloud settling ($T_{\rm eff} \gtrsim 2000\,{\rm K}$), the flux errors generally decrease with every iteration until the model arrives at a stable solution with the typical maximum and average flux errors across all radiative layers of $\sim 3\%$ and 0.5%, correspondingly. In this work, we refer to this convergence pattern as *stable*, and the models that exhibit this pattern are shown in *green* in Figure 4.1 for the *ridgeline* isochrone. A small number of models with stable convergence may occasionally encounter iterations with ill-conditioned temperature corrections that break the trend in convergence and increase the flux errors by over an order of magnitude, effectively restarting the computation. In those cases, the iteration with the minimum average error, from which we derive the final synthetic spectrum, is still expected to produce a reliable result; however, the gain in accuracy from an increased number of iterations may be limited.

At lower $T_{\rm eff}$, the effects of condensate settling become more prominent, resulting in a far more complex relationship between the model parameters that restricts the effectiveness of the temperature correction scheme. In this regime, the flux errors typically oscillate between high and low values across iterations. While the flux errors of the best iteration are usually comparable to those of the atmospheres with stable convergence, the final solutions to the structure equations may lack uniqueness (i.e. for some $T_{\rm eff}$ and $\log_{10}(g)$ there may be multiple atmosphere structures with

similar flux errors but vastly different emergent spectra). Furthermore, the pronounced sensitivity of the model to temperature corrections casts doubt on the usefulness of the radiative flux errors as a diagnostic of self-consistency. We refer to the convergence pattern in this temperature regime as *irregular*. Selected PHOENIX atmospheres with irregular convergence had to be excluded from the grid due to the rapid growth of the oscillation amplitude in the temperature structure between iterations. However, solutions with satisfactory flux errors have been found for the vast majority of models with this convergence pattern, and are shown in Figure 4.1 with *black* markers for the *ridgeline* isochrone.

A small number of models displayed a convergence pattern, intermediate between that of stable convergence and irregular convergence, which we refer to as *limited* convergence. In those cases, the model may exhibit stable convergence for the first few iterations, but then transition into the irregular convergence pattern before a solution with satisfactory flux errors can be reached. In some cases, the transition between the two convergence patterns may occur multiple times over the course of ~ 100 iterations. The models with limited convergence are shown in Figure 4.1 with *red* markers for the *ridgeline* isochrone. At very low temperatures ($T_{\rm eff} \lesssim 1200\,{\rm K}$) and high gravities ($\log_{10}(g) \gtrsim 5.5$), the condensate species are almost completely removed from the spectrum-forming region of the atmosphere, restoring the stable convergence pattern (see Figure 4.1).

For most PHOENIX models computed in this study, we used the nearest atmosphere structure from the NEXTGEN model grid [Hauschildt et al., 1999; Allard et al., 2014] as the initial guess in the solver, with the exception of models with particularly poor convergence that were recalculated, using the nearest well-converged atmospheres from our grid as the initial models instead. In principle, the accuracy of our low-temperature atmospheres may be improved by calculating the models in small batches with progressively decreasing $T_{\rm eff}$ and $\log_{10}(g)$, and using the atmospheres from the preceding batch as initial guesses. In fact, we adopted this approach for the ATLAS models. However, the high computational demand of PHOENIX (Section 4.4.5) makes

the un-parallelized computation extremely time-consuming. Furthermore, it is unclear how the potential gain in numerical precision would compare to the systematic errors in the input physics and grid interpolation errors. We therefore chose to focus on identifying the outlier models based on their synthetic photometry and excluding them from the isochrone calculation instead, as described in Section 4.4.7.

Nearly all evolutionary MESA models in our grids have converged at every time step within the "*gold tolerances*" [Paxton et al., 2019], with the exception of a few lowest-mass models ($\lesssim 0.05\,M_\odot$), where the tolerances were relaxed to their standard values to allow evolution over the discontinuities in $dT(\tau = 100)/d\log_{10}(g)$, caused by the sparse gravity sampling in the boundary condition tables.

4.4.5 Computational demand of model atmospheres

All model atmospheres used in this chapter were calculated on the *Bridges-2* supercomputer [Brown et al., 2021], operated by the Pittsburgh Supercomputing Center. Our PHOENIX models were calculated to ~ 100 iterations, requiring between ~ 0.15 processor hours per iteration at the highest temperatures to ~ 1.5 processor hours at the lowest. The high memory demand of PHOENIX ($\gtrsim 4$ GB per model) necessitated requesting at least 2 (and occasionally 3) service units for each processor hour.

The computational demand of ATLAS models is dominated by the spectral synthesis, carried out by the SYNTHE package. The calculation of the emergent spectra for most ATLAS models required between 1.5 and 3.5 processor hours per spectrum (and the same number of service units). For comparison, the structure calculations only took ≈ 0.005 processor hours per model for all iterations.

The computational demand of a complete atmosphere grid for each chemical composition is approximately 5×10^4 service units, with nearly 98% taken by PHOENIX calculations. This estimate does not include recalculation of failed models, ODF calculations, calculations of partial

pressure tables for each chemical composition used in PHOENIX, and evolutionary calculations with MESA. This estimate only applies to the final isochrones (*ridgeline*, *blue tail* and *red tail*) presented in Section 4.5: to calculate the intermediate isochrones used during the fitting process, we took advantage of various optimizations described in Section 4.5.

4.4.6 Isochrone stitching

The process of calculating theoretical isochrones described earlier in this section required a choice of three "stitching points", where distinct modelling setups were blended together: the effective temperature where ATLAS models are replaced with PHOENIX models (5000 K), the effective temperature where the gravitational settling in PHOENIX models was disabled (2500 K) and the initial stellar mass, where the $\tau = 100$ boundary condition tables were replaced with $T(\tau) = T_{\rm eff}$ (smooth ramp between $0.5\,M_\odot$ and $0.6\,M_\odot$). Here, we briefly review the implications of those choices for synthetic photometry.

Our choice of the ATLAS/PHOENIX transition temperature (5000 K) is higher than that used in Chapter 3 (4000 K). For comparison, the published grid of ATLAS models with the updated molecular opacities [Castelli and Kurucz, 2003] reaches 3500 K, although the low-temperature extension has known issues [Plez, 2011]. We calculated an additional test set of ATLAS models for the parameters of the *ridgeline* isochrone at $4000\,{\rm K} \leq T_{\rm eff} \leq 5000\,{\rm K}$, as well as an additional grid of evolutionary models with the updated boundary conditions. We found the synthetic photometry at 11.5 Gyr of the regular *ridgeline* isochrone and its altered version to be indistinguishable at $T_{\rm eff} = 5000\,{\rm K}$, but rapidly increasing at lower temperatures to attain the difference of ≈ 0.025 mag in F606W − F814W and F150W2 − F322W2 at $T_{\rm eff} = 4000\,{\rm K}$. The difference originates almost entirely from the synthetic spectra with only a minor contribution from the boundary conditions.

Our choice of the minimum $T_{\rm eff}$ without gravitational settling (2500 K) is, on the other hand, lower than that employed in Chapter 3 (3000 K), which allowed us to significantly reduce the computational demand. We calculated a test grid of PHOENIX atmospheres for the *ridgeline*

isochrone with $2500\,\mathrm{K} \leq T_{\mathrm{eff}} \leq 3000\,\mathrm{K}$ and enabled settling of condensates, as well as a test set of corresponding evolutionary models. We found that at $T_{\mathrm{eff}} = 2500\,\mathrm{K}$ and at the age of 11.5 Gyr, the effect of gravitational settling on the same colors as before is ≈ 0.01 mag. In the optical regime, both the boundary conditions and the synthetic spectra make comparable contributions to the observed difference, while the latter dominate in the infrared. At $T_{\mathrm{eff}} > 2500\,\mathrm{K}$, the effect of gravitational settling decreases rapidly in the infrared, but remains approximately constant in the optical up to the warm end of the test grid at 3000 K, primarily due to the effect of the updated boundary conditions on stellar evolution.

Lastly, we examine the effect of the transition between the atmosphere-interior coupling schemes by disabling the linear ramp at $0.5\,\mathrm{M}_{\odot} \leq M \leq 0.6\,\mathrm{M}_{\odot}$. The effect on synthetic photometry at 11.5 Gyr is most prominent in `F606W` $-$ `F814W` when the range of $T(\tau) = T_{\mathrm{eff}}$ boundary condition tables is extended down to $0.5\,\mathrm{M}_{\odot}$, resulting in the discontinuity of $\lesssim 0.01$ mag between the two regimes. The discontinuity is less prominent when the $\tau = 100$ tables are extended to $0.6\,\mathrm{M}_{\odot}$ or when other photometric colors are considered.

In summary, our choice of "stitching points" in the isochrone is not expected to introduce errors larger than 0.01 mag in any of the photometric colors considered in this study; however, it appears that the optimal choice of the transition between the two atmosphere-interior coupling schemes falls at somewhat larger masses, and a small gain in accuracy may be attained by allowing gravitational settling of condensates at $T_{\mathrm{eff}} > 2500\,\mathrm{K}$.

4.4.7 Synthetic photometry and hammering

The preliminary synthetic photometry for the calculated isochrones is obtained by applying the reddening law to the synthetic spectra, evaluating the bolometric corrections for each model atmosphere in the bandpasses of interest, and interpolating the result to T_{eff} and $\log_{10}(g)$, predicted by the evolutionary model at the required initial mass and age. The resulting magnitudes were corrected by the distance modulus of (13.2418 ± 0.0625) mag [Chen et al., 2018]. To calculate

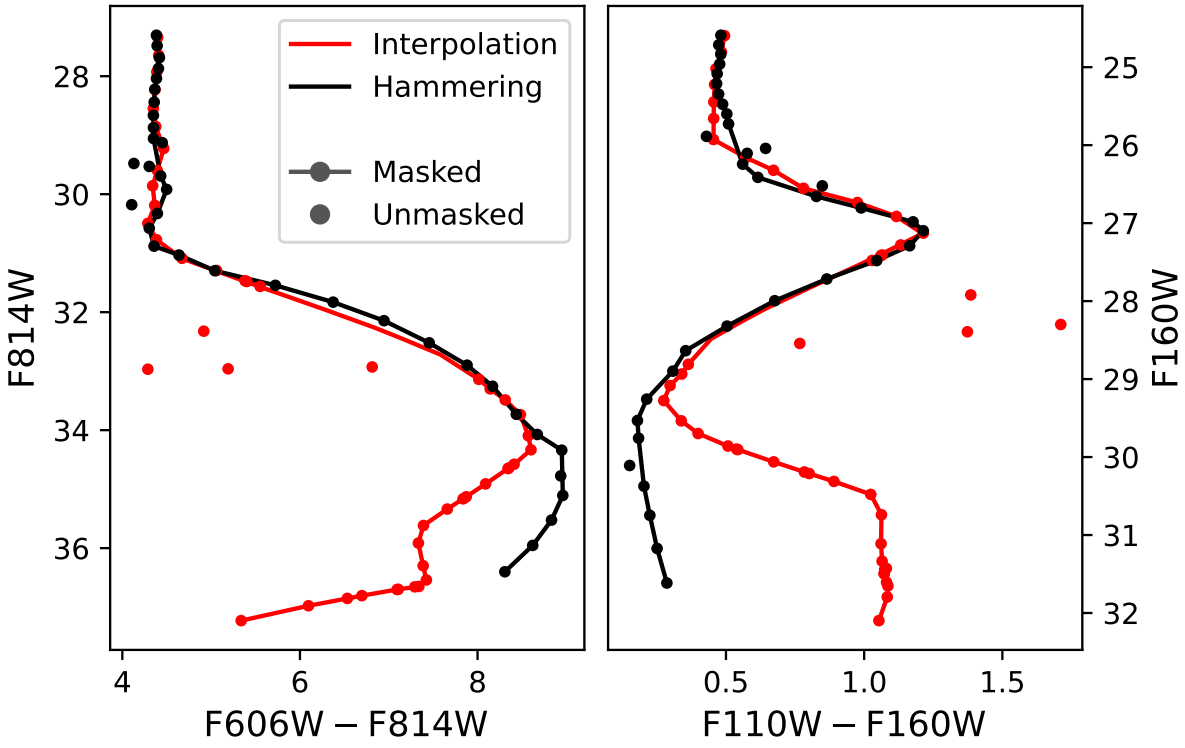

Figure 4.3. Comparison of synthetic photometry at 11.5 Gyr and $T_{\rm eff} \leq 2350$ K for the *blue tail* isochrone, calculated using the two methods described in Section 4.4.7: atmosphere hammering (*black*) and linear interpolation of the bolometric corrections (*red*). The outlier models were identified manually in each isochrone and excluded from the "masked" result.

the bolometric corrections, we used the `synphot()` routine of the `BasicATLAS` package. The process uses the reddening law from Fitzpatrick and Massa [2007], parameterized only by the optical reddening, $E(B-V)$, and assuming the total-to-selective extinction ratio of $R_V = 3.1$.

The strong dependency of low-$T_{\rm eff}$ spectra on surface parameters and the highly non-linear behavior of cool atmospheres pose a challenge to the interpolation of bolometric corrections. Linear interpolation of a sparsely sampled grid leads to large unphysical discontinuities in the derivatives, and is known to introduce noticeable errors even at relatively high temperatures [Mészáros and Allende Prieto, 2013; Gustafsson et al., 2008]. On the other hand, higher-order interpolation methods are less robust against outliers [Fried and Zietz, 1973], such as those introduced by the models with poor convergence. Specialized interpolation methods for atmosphere grids with non-convergent models (e.g. [Nendwich et al., 2004]) generally require a means to reliably identify the outliers, which is not straightforward in the case of irregular convergence, as discussed in Section 4.4.4.

To address these issues, we decided to avoid interpolating the grid at low temperatures altogether and, instead, to calculate additional `PHOENIX` atmospheres at $600\,{\rm K} \leq T_{\rm eff} < 2400\,{\rm K}$ in 50 K steps, with $\log_{10}(g)$ set to the values predicted by the isochrone for each effective temperature at the target age. We refer to this process as atmosphere *hammering*. In addition to removing the need to interpolate bolometric corrections at low temperatures, hammering serves two other purposes. First, it reduces the effective number of dimensions in the atmosphere grid from 2 to 1 (since the hammering models obey a known $T_{\rm eff}$ – $\log_{10}(g)$ relationship), allowing the outlier models to be easily identified, e.g., by their placement in the color-magnitude space. Second, it allows us to derive the synthetic photometry at $T_{\rm eff} < 2500\,{\rm K}$ from higher-gravity model atmospheres that have better convergence (e.g., from Figure 4.1, to calculate the bolometric corrections at the $T_{\rm eff} = 2000\,{\rm K}$ point on the 11.5 Gyr isochrone, one would require both $\log_{10}(g) = 5.0$ and $\log_{10}(g) = 5.5$ model atmospheres for the interpolation method, but only one $\log_{10}(g) \approx 5.5$ model for the hammering method). The major drawbacks of the hammering

method are the added computational cost and the resulting commitment to a particular target age, since the hammering models fix the $T_{\rm eff} - \log_{10}(g)$ relationship.

The linear interpolation and hammering methods of calculating synthetic photometry at $T_{\rm eff} \leq 2350\,{\rm K}$ are compared in Figure 4.3. The figure demonstrates that at $T_{\rm eff} \lesssim 1000\,{\rm K}$ (the brown dwarf regime), linear interpolation may be off by as much as 2 mag in the optical regime and $\gtrsim 0.5$ mag in the near infrared. It is also apparent that the two methods converge at $T_{\rm eff} \gtrsim 2000\,{\rm K}$, suggesting that linear interpolation of bolometric corrections is valid across the main sequence. In this study, we use linear interpolation for all models with $T_{\rm eff} > 2350\,{\rm K}$.

4.5 Isochrone fitting

4.5.1 Main sequence turn-off and subgiant branch

The high effective temperatures of the main sequence turn-off and the subgiant branch in 47 Tucanae ($T_{\rm eff} \gtrsim 5000\,{\rm K}$) suppress molecular formation in the atmosphere and minimize the impact of chemical abundances on the observed photometry. The notable exceptions are the overall metallicity, [Fe/H], and the helium mass fraction, Y, as they have a significant effect on the mean molecular weight and opacity of the interior that, in turn, guide the evolutionary track of the star [Salaris and Cassisi, 2005, Ch. 5.5]. These high-mass stars are also sensitive to the adopted energy transport parameters (in particular, the mixing length, $\alpha_{\rm MLT}$) due to the emergence of an outer convective zone [Joyce and Chaboyer, 2018]. To reduce the degree of degeneracy in the determination of chemical abundances, it is advantageous to constrain as many parameters as possible from the main sequence turn-off and the subgiant branch before analyzing the lower main sequence. We used this part of the CMD to assess our choice of $\alpha_{\rm MLT} = 1.82$, fix the cluster age and the optical reddening, $E(B-V)$, as well as to evaluate the accuracy of the helium mass fraction and metallicity in the nominal chemical composition (Section 4.2, $Y = 0.25$, $[{\rm Fe/H}] = -0.75$).

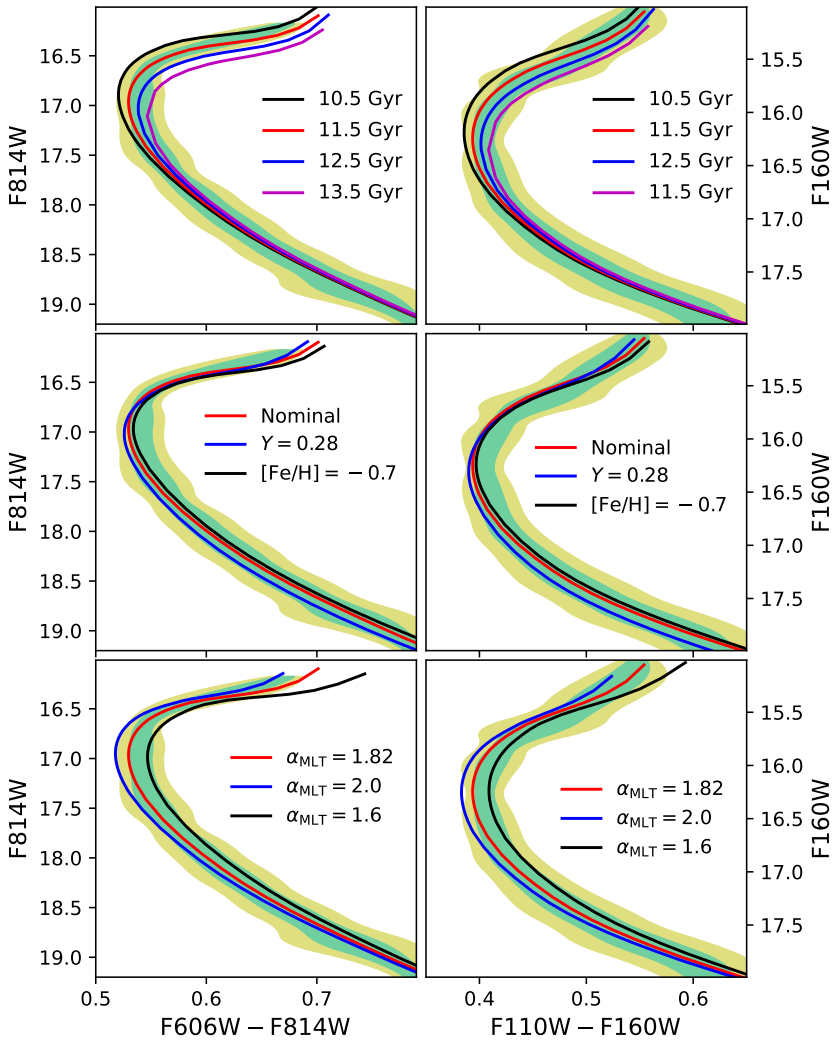

Figure 4.4. *Top: ridgeline* isochrones of 47 Tucanae at different ages, overplotted on the distribution of observed colors in optical (*left*) and near infrared (*right*). *Middle*: comparison of the *ridgeline* isochrone at 11.5 Gyr with the nominal [Fe/H] and Y (*red*) to the helium-rich (*blue*) and metal-rich (*black*) isochrones at the same age. *Bottom:* effect of the mixing length parameter on the *ridgeline* isochrone at the age of 11.5 Gyr. The cyan and yellow regions of the color-magnitude diagram subtend the 1σ and 2σ contours in the data distribution, respectively. $E(B-V) = 0.04$ mag for all shown isochrones.

The upper panels of Figure 4.4 show the turn-off point and the subgiant branch of the *ridgeline* isochrone, evaluated at 4 distinct ages and overplotted on the color-magnitude distribution of the archival photometry (Section 4.3) in the optical (*left*) and near infrared (*right*). The isochrones were calculated using the nominal metallicity and helium mass fraction, as well as $E(B-V) = 0.04\,\mathrm{mag}$, in agreement with Percival et al. [2002]. In the figure, the 11.5 Gyr isochrone is the only one that matches both the color of the turn-off point and the luminosity of the subgiant branch within one standard deviation. Furthermore, the presented fit firmly fixes the reddening at 0.04 mag, as lower values would result in the isochrone being "too blue" at the turn-off point, while higher values would make the isochrone "too faint" at the tip of the subgiant branch. This age estimate broadly agrees with the literature (e.g. [VandenBerg, 2000]; also see [Rennó et al., 2020] for a compilation of recent age measurements).

To explore the effect of the helium mass fraction and the overall metallicity, we calculated two additional isochrones with $Y = 0.28$ and $[\mathrm{Fe/H}] = -0.7$, with all other parameters matching those of the *ridgeline* isochrone. The results are plotted in the middle panels of Figure 4.4. While the enhanced metallicity offers a marginal improvement of the fit at the turn-off point, the corresponding decrease in luminosity of the subgiant branch reduces the overall goodness of fit. On the other hand, the higher helium mass fraction improves the fit at the subgiant branch, at the expense of mismatching the color of the turn-off point by nearly two standard deviations in near infrared. Based on these results, we chose to use the nominal metallicity and helium mass fraction for all isochrone calculations henceforth.

The lower panels of the figure demonstrate how our choice of the mixing length compares to two alternative values: $\alpha_{\mathrm{MLT}} = 1.6$ and $\alpha_{\mathrm{MLT}} = 2.0$, of which the latter is the default value in `MESA`. The isochrones are shown at 11.5 Gyr. Around the turn-off point, the effect is practically indistinguishable from that of the cluster age, emphasizing the limitations of using the color of the turn-off point as an age diagnostic for globular clusters. Our earlier claim that the 11.5 Gyr isochrone is the only one that fits the observed scatter within one standard deviation is invalid if

the mixing length is allowed to vary as a free parameter. We found that a comparable goodness-of-fit is obtained at 12.5 Gyr for $\alpha_{\rm MLT} = 2.0$, or 10.5 Gyr for $\alpha_{\rm MLT} = 1.6$. Figure 4.4 appears to indicate that the effect of the mixing length is most significant at the tip of the subgiant branch. If the trend continues into the red giant branch, it is possible that a better estimate of the cluster age may be obtained from higher-mass stars. Since the degeneracy cannot be broken within the mass range considered in this study, we chose to adopt the solar-calibrated $\alpha_{\rm MLT} = 1.82$ for all isochrones and the corresponding best-fit age of 11.5 Gyr.

4.5.2 Lower main sequence

Below the main sequence inflection point ($\sim 0.5\,M_\odot$, [Calamida et al., 2015]), the abundances of individual chemical elements have a significant influence on the shape of the CMD. In this study, we consider the variations in 11 element abundances: [C/Fe], [N/Fe], [O/Fe], [Na/Fe], [Mg/Fe], [Al/Fe], [Si/Fe], [S/Fe], [Ca/Fe], [Ti/Fe], and [V/Fe].

The effect of atomic abundances is twofold. First, variations in abundances displace the chemical equilibrium of the atmosphere and change the corresponding opacity distribution, resulting in altered photometric colors. Second, the new atmospheric structure affects the boundary conditions of the atmosphere-interior coupling (Section 4.4.2), thereby offsetting the end-point of the evolutionary track to different $T_{\rm eff}$ and $\log_{10}(g)$. The importance of the latter effect approximately correlates with $\delta\kappa = |d\kappa/d[{\rm X/Fe}]|$ at $T(\tau) = T_{\rm eff}$, where [X/Fe] is the abundance of the element of interest and κ is the Rosseland mean opacity. For the range $0.1\,M_\odot < M < 0.5\,M_\odot$, this diagnostic is by far the largest for [O/Fe] and [Ti/Fe] ($\sim 10^{-7}\,{\rm cm^{-1}dex^{-1}}$ at $0.2\,M_\odot$) due to the prominent TiO and H_2O absorption bands (see Figure 4.2). For comparison, the next two most important elements, [C/Fe] and [Al/Fe], have $\delta\kappa \sim 2\times10^{-8}\,{\rm cm^{-1}dex^{-1}}$ and $\sim 10^{-8}\,{\rm cm^{-1}dex^{-1}}$, respectively, at the same initial stellar mass.

The relative importance of the two effects depends on the chosen photometric bands. For instance, the optical main sequence spectra for fixed $T_{\rm eff}$ and $\log_{10}(g)$ are only weakly sensitive

to the oxygen abundance, since H_2O bands are mostly confined to infrared wavelengths, while the rate of TiO production in the atmosphere is primarily determined by [Ti/Fe]. As such, the atmosphere-interior coupling alone is responsible for over 50% of the correlation between the optical colors ($\texttt{F606W} - \texttt{F814W}$) and [O/Fe] for main sequence stars. This example emphasizes that accounting for the enhancements of individual elements in the atmosphere-interior coupling scheme is essential for the accurate photometric determination of the chemical composition. Since 47 Tucanae is known to have a significant spread in [O/Fe] based on spectroscopic measurements, the corresponding distribution of photometric colors cannot be captured with atmosphere-interior boundary conditions based on solar or even solar-scaled abundances. Furthermore, since both [Ti/Fe] and [O/Fe] have comparable $\delta\kappa$, and since both are considered to be α-elements, even solar-scaled boundary conditions with adjustable α-enhancement would not be adequate.

4.5.3 Abundance variation grids

We determine the final *red tail*, *blue tail* and *ridgeline* isochrones for 47 Tucanae by iteratively correcting the nominal element abundances, derived in Section 4.2. Each iteration begins by calculating the theoretical isochrone with fully self-consistent chemistry as detailed in Section 4.4. However, since the available datasets only extend to the end of the main sequence (Section 4.3), we terminate all intermediate isochrones at $T_{\rm eff} = 3000\,{\rm K}$ to avoid unnecessary calculations of model atmospheres.

To determine the corrections in the element abundances for the next iteration, we first compute an *abundance variation grid* of model atmospheres for the current isochrone. The grid spans 5 initial stellar masses between $0.13\,{\rm M}_\odot$ and $0.7\,{\rm M}_\odot$ that sample the main sequence of the cluster with approximately even intervals in the CMD. At this stage, we assume that the effect of chemistry on the atmosphere-interior coupling is negligible and compute new model atmospheres (Section 4.4.3) for the $T_{\rm eff}$ and $\log_{10}(g)$ of the chosen masses, based on the parameter relationships of the current isochrone. For each stellar mass, we calculate 22 new model atmospheres with each

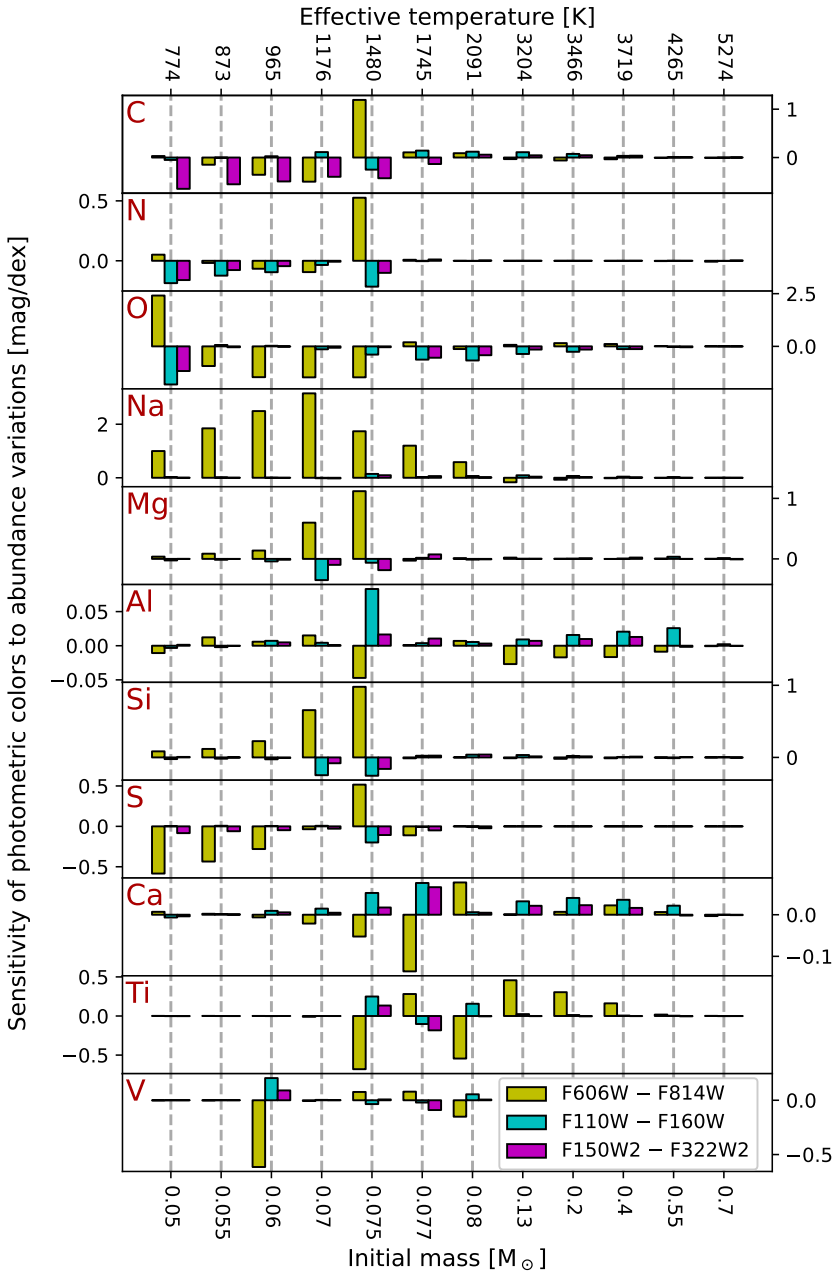

Figure 4.5. Photometric sensitivity plot for the initial iteration with nominal chemistry at $M > 0.1\,\mathrm{M}_\odot$ and for the final *ridgeline* isochrone at $M < 0.1\,\mathrm{M}_\odot$. The plot shows the effect of changes in the abundances of individual elements on the photometric colors as a function of stellar mass (or, equivalently, T_{eff}) assuming that the atmosphere-interior coupling remains constant, i.e. for fixed T_{eff} and $\log_{10}(g)$. Note that the horizontal axis is categorical, i.e. the labels are evenly spaced regardless of their values.

of the 11 elements considered in this study perturbed by 0.5 dex and -0.5 dex, one element at a time. A *photometric sensitivity plot* (Figure 4.5) is then produced that shows the effect of each element on the relevant photometric colors. Since the abundance variation grids are based on the assumption of constant atmosphere-interior coupling, we also calculate $\delta\kappa$ for each element to estimate our confidence in the derived correlation between colors and abundances.

The abundance corrections are then determined manually based on the current discrepancies between the isochrones and the data, the photometric sensitivity plot and estimated adjustments to the photometric sensitivity based on the $\delta\kappa$ values and our experience with earlier iterations. At each iteration, we follow the reductionist approach of adopting the smallest possible number of corrections in the chemical composition to reproduce the data. In principle, the derivation of abundance corrections may be automated by introducing a quantitative goodness-of-fit criterion, similar to the one derived in Chapter 3 for fitting a single isochrone to the CMD. However, since there is no straightforward way to extend that criterion to simultaneous fitting of multiple isochrones, and since the automated routine must be "trained" to take advantage of the abundance variation grids based on experience, we chose to use human input at every iteration instead.

A satisfactory fit was obtained after 10 iterations. The final isochrones were extended to $T_{\rm eff} \gtrsim 700$ K to reach the substellar regime, as required for our further analysis. For the final *ridgeline* isochrone, an additional abundance variation grid was computed for 7 initial masses below the end of the main sequence at $0.05\,{\rm M}_\odot \leq M \leq 0.08\,{\rm M}_\odot$. The derived photometric sensitivity is shown in Figure 4.5. We determined that corrections in [Ti/Fe] and [O/Fe] are sufficient to reproduce the photometric spread in both optical and infrared colors, while variations in other abundances compared to their spectroscopic means do not offer a noticeable improvement to the fit. While the value of [Ti/Fe] needed to be offset from its nominal value to fit the data, we found that the observations are most consistent with a constant value of [Ti/Fe] across all three final isochrones.

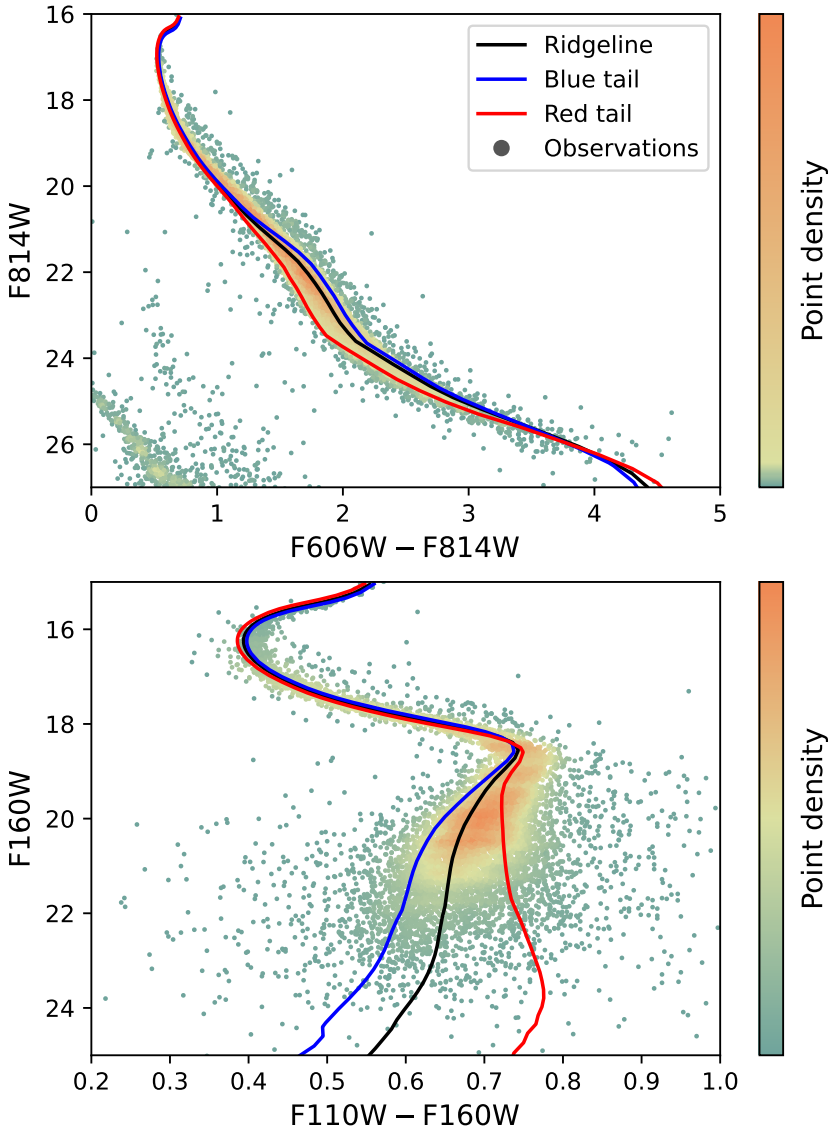

Figure 4.6. The final *best fit*, *blue tail* and *red tail* isochrones, overplotted on the observed photometric spread in the optical (*top*) and the near infrared (*bottom*) bands. The parameters of the isochrones are given in Table 4.1.

Table 4.1. Best-fit parameters of the final isochrones for 47 Tucanae

Parameter	Blue tail	Ridgeline	Red tail
$E(B-V)$ [mag]	0.04	0.04	0.04
$\alpha_{\rm MLT}$	1.82	1.82	1.82
Age [Gyr]	11.5	11.5	11.5
[Fe/H] [dex]	-0.75	-0.75	-0.75
Y	0.25	0.25	0.25
[Ti/Fe] [dex]	0.64	0.64	0.64
[O/Fe] [dex]	0.48	0.33	0.03

Note. — The abundances of individual elements unlisted in the table are set to their nominal values, derived in Section 4.2 and summarized in Appendix E.

The final isochrones are plotted in Figure 4.6, while their best-fit properties are summarized in Table 4.1. In near infrared bands, the photometric spread noticeably overflows the *red tail* isochrone around the main sequence inflection point (F160W ~ 19 mag). A similar red excess in the optical CMD is also seen at the corresponding evolutionary phase (F160W ~ 20.5 mag), despite the inverted [O/Fe]-color relationship. This prominent discrepancy between the data and the model isochrones cannot be accounted for by varying any of the considered elements.

4.6 Analysis

4.6.1 Oxygen abundance

Figure 4.6 demonstrates that the near infrared photometry of the lower main sequence is particularly sensitive to the oxygen abundance of 47 Tucanae. Here, we calculate the lower main sequence distribution of [O/Fe] in the cluster. Each of the three isochrones shown in the figure defines the relationship between the initial mass of the star and its position in the CMD space for

a given oxygen abundance ($[\mathrm{O/Fe}] = 0.48\,\mathrm{dex}$ for the *blue tail* isochrone, $[\mathrm{O/Fe}] = 0.33\,\mathrm{dex}$ for *ridgeline* and $[\mathrm{O/Fe}] = 0.03\,\mathrm{dex}$ for *red tail*; see Table 4.1). Equivalent relationships for other values of [O/Fe] may be approximated by interpolating or extrapolating the calculated isochrones. It is therefore possible to define a curvilinear transformation from the CMD space in Figure 4.6 to the $M - [\mathrm{O/Fe}]$ space.

To obtain the desired transformation, we first generated a 1000×300 regular grid of synthetic stars at 1000 evenly spaced initial masses from the minimum ($\approx 0.045\,\mathrm{M}_\odot$) to the maximum ($\approx 0.875\,\mathrm{M}_\odot$) value within the range of all three isochrones, and 300 evenly spaced values of [O/Fe] from $-0.57\,\mathrm{dex}$ to $0.78\,\mathrm{dex}$. The chosen range of oxygen abundances corresponds to tripled distances from the *ridgeline* oxygen abundance to the other two isochrones. Each synthetic star was projected onto the near infrared color-magnitude plane by, first, linearly interpolating the CMD of each of the three isochrones to the mass of the synthetic star and, second, linearly interpolating and extrapolating the resulting three points to the oxygen abundance of the synthetic star. The curvilinear transformation of the observed CMD of the cluster was carried out by identifying the closest synthetic star to each real observation in the color-magnitude space, and assigning the mass and [O/Fe] values of the closest synthetic star to the real star. This method is unreliable above the main sequence inflection point, where all three isochrones merge and the curvilinear transformation becomes non-unique. We carry out this analysis below the inflection point ($0.1\,\mathrm{M}_\odot \leq M \leq 0.5\,\mathrm{M}_\odot$), where the isochrones are well-separated, and the transformation is accurate to $10^{-3}\,\mathrm{M}_\odot$ in mass and $10^{-2}\,\mathrm{dex}$ in the oxygen abundance, as estimated by applying the transformation to 10^4 synthetic stars with randomly chosen masses and oxygen abundances. We further restrict our analysis to stars that satisfy $-0.27\,\mathrm{dex} < [\mathrm{O/Fe}] < 0.63\,\mathrm{dex}$ (doubled distances between the calculated isochrones) to avoid excessive extrapolation and to discard the occasional outlying measurements that fell outside the range of synthetic stars.

The result of the transformation is shown in the *right* panel of Figure 4.7. The distribution of [O/Fe] in selected mass bins is shown in the left panel of the figure. We note that the highest

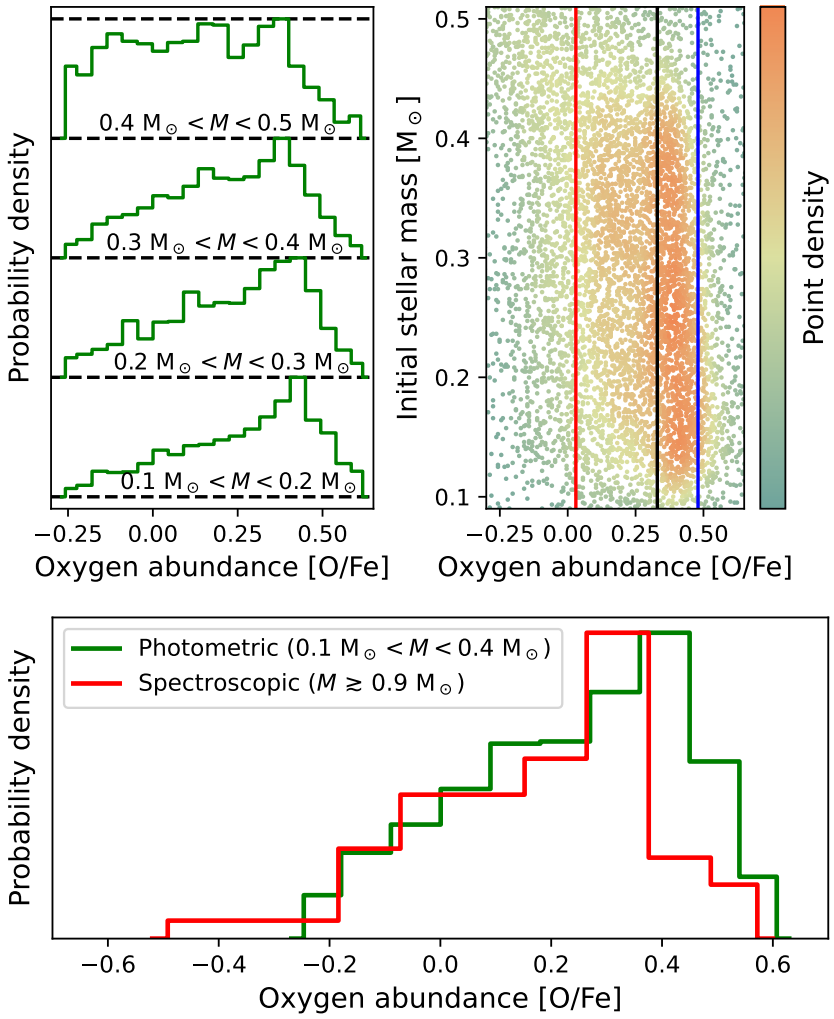

Figure 4.7. *Left:* distribution histograms of [O/Fe] in 47 Tucanae in different initial mass bins. The flattening of the highest-mass distribution is likely an artifact of the poor isochrone fit in the vicinity of the main sequence inflection point (see Section 4.5.3). *Right:* the near infrared CMD of 47 Tucanae, transformed into the initial mass – oxygen abundance space using the calculated isochrones. The transformed *red tail*, *ridgeline* and *blue tail* isochrones are indicated with the *red*, *black* and *blue* vertical lines, respectively. *Bottom:* combined [O/Fe] distribution at $0.1\,\mathrm{M}_\odot < M < 0.4\,\mathrm{M}_\odot$, overplotted on the distribution of spectroscopic measurements in the literature (Section 4.2).

Table 4.2. Comparison of synthetic and real distributions of spectroscopically inferred oxygen abundance in 47 Tucanae

Statistic	Synthetic		Real
Mean	0.239	$\pm$0.023	0.174
Standard deviation	0.252	$\pm$0.015	0.214
5$^{\text{th}}$ percentile	$-$0.190	$\pm$0.047	$-$0.170
25$^{\text{th}}$ percentile	0.067	$\pm$0.036	0.030
75$^{\text{th}}$ percentile	0.421	$\pm$0.029	0.320
95$^{\text{th}}$ percentile	0.621	$\pm$0.038	0.476

Note. — All values are quoted in dex. The indicated uncertainty of the synthetic values was calculated as the standard deviation across 10^5 Monte-Carlo trials.

mass bin ($0.4\,\mathrm{M}_\odot < M < 0.5\,\mathrm{M}_\odot$) is likely unreliable due to the proximity of the main sequence inflection point, where the isochrone fit is noticeably poorer. The remaining mass bins are combined into a single oxygen abundance distribution in the lower panel of Figure 4.7. A histogram of the spectroscopic measurements of higher-mass stars ($M \gtrsim 0.9\,\mathrm{M}_\odot$) is plotted in the same panel for reference.

To compare the spectroscopic and photometric abundances quantitatively, we began with a null-hypothesis that (1) the photometric distribution is free of systematic errors and represents the true chemistry in the lower main sequence, and (2) photometric and spectroscopic abundances are identical, i.e. there is no dependence of [O/Fe] on stellar mass. The spectroscopic distribution of oxygen, as described in Section 4.2, consists of 117 individual measurements with published uncertainties. We generated 10^5 synthetic equivalents of the spectroscopic dataset by drawing 117 random measurements from the photometric distribution for each trial and applying simulated Gaussian noise according to the published spectroscopic uncertainties. For each synthetic set, we estimated the mean, standard deviation, 5$^{\text{th}}$, 25$^{\text{th}}$, 75$^{\text{th}}$ and 95$^{\text{th}}$ percentiles. The averages

and spreads in those statistics across all 10^5 Monte-Carlo trials are summarized in Table 4.2, alongside the equivalent values calculated for the real spectroscopic dataset.

The null-hypothesis was rejected, since the statistical parameters of the real spectroscopic distribution fall outside the synthetic range by up to ~ 4 standard deviations. If the systematic errors in the photometrically inferred abundances are the dominant contributor to the estimated discrepancy, their expected magnitude varies from ≈ 0.02 dex at the oxygen-poor tail of the distribution (inferred from the 5^{th} percentile) to ≈ 0.15 dex at the oxygen-rich tail (inferred from the 95^{th} percentile). We note that the latter value is comparable to the average spectroscopic uncertainty of 0.147 dex across the 117 measurements.

Alternatively, a genuine variation in chemistry with stellar mass may be responsible for the discrepancy between spectroscopic and photometric values. Under the standard assumption that the enriched population of 47 Tucanae is oxygen-deficient [Dickens et al., 1991], the values of the higher percentiles are expected to be primarily determined by the oxygen content of the primordial population, while the values of the lower percentiles would be mostly set by [O/Fe] of the enriched population. As discussed in Section 4.1, the chemistry of the enriched population may depend on stellar mass in concurrent formation models. We, however, disfavor this explanation, since the spectroscopic/photometric discrepancy in Table 4.2 appears largest at the oxygen-rich (primordial) tail of the [O/Fe] distribution, rather than the anticipated oxygen-poor (enriched) tail.

Both photometric and spectroscopic distributions in the lower panel of Figure 4.7 exhibit a clear negative skewness (i.e. the oxygen-poor tail is longer than the oxygen-rich one). To assess the statistical significance of this feature, we calculated the Fisher-Pearson coefficient of skewness for both distributions, obtaining -0.22 ± 0.03 and -0.43 ± 0.19 for the photometric and spectroscopic cases respectively. Hence, spectroscopic and photometric measurements are consistent with each other, and indicate that the distribution of [O/Fe] in 47 Tucanae is indeed negatively skewed. While both skewness estimates have high confidence, the photometric value is vastly more statistically significant than its spectroscopic counterpart (7.3 vs ~ 2.3 standard

deviations, respectively), due to the number of photometric measurements (5046) exceeding the number of spectroscopic measurements (117) by over an order of magnitude.

4.6.2 Mass function

The mass functions of globular clusters retain a footprint of their dynamical evolution [Sollima and Baumgardt, 2017; Baumgardt and Sollima, 2017] and may vary between populations if they have distinct kinematic properties. Furthermore, an estimate of the mass function is required to predict the luminosity function and the CMD of the substellar sequence. In this subsection, we seek a mass function that can reproduce the observed `F160W` magnitude distribution of 47 Tucanae, assuming that the isochrones calculated earlier and the oxygen abundance distribution derived above accurately capture the properties of the cluster. The choice of the photometric band is motivated by the fact that the oxygen abundances were inferred from the near infrared CMD and the fact that lower main sequence members are brighter in `F160W` than in `F110W` (Figure 4.6). We also assumed that the mass function (ξ) is of the form of a broken power law [Kroupa, 2001]:

$$\xi(M) \propto \begin{cases} M^{-\beta}, & \text{if } M > M_{\rm bp} \\ M^{-\gamma}, & \text{if } M \leq M_{\rm bp} \end{cases} \tag{4.2}$$

Here, β and γ are the power law indices in the high- and low-mass regimes respectively, separated by the break-point stellar mass $M_{\rm bp}$. We keep all three parameters as free variables. The magnitude function, $\phi(m)$, where m is the apparent magnitude of the star (in our case, `F160W`), is related to the mass function as in Equation 4.3:

$$\phi(m) = -\xi\left(M(m)\right) \frac{dM(m)}{dm} \tag{4.3}$$

In Equation 4.3, we treat the stellar mass, M, as a function of magnitude, m, as given by the mass-magnitude relationship provided by the isochrone. In practice, the mass-magnitude

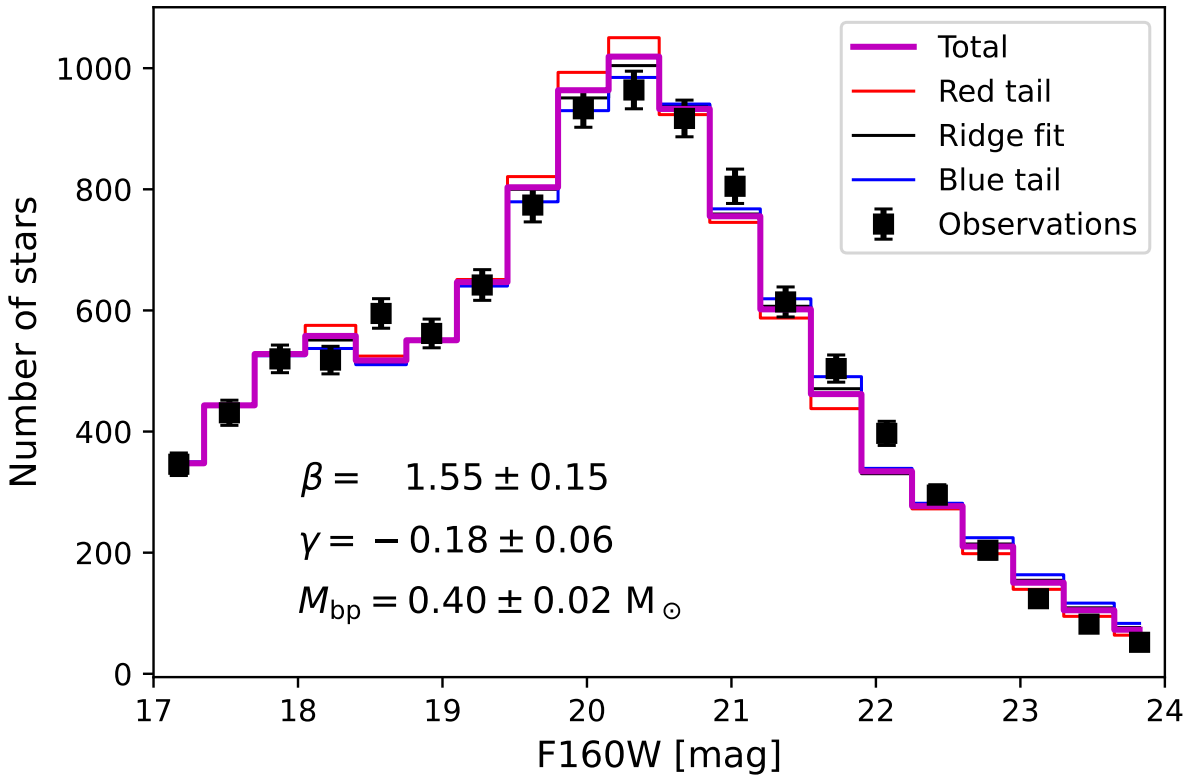

Figure 4.8. The observed magnitude function of 47 Tucanae in `F160W` with the best-fit theoretical magnitude function in *magenta*. Additional magnitude functions that use only one of the theoretical isochrones instead of the abundance-weighted average are shown for comparison. The displayed error bars are Poisson counting errors.

relationship is sampled at a set of masses, M_i, and magnitudes, m_i, corresponding to the initial masses of the calculated evolutionary models. We therefore rewrite Equation 4.3 in the form of finite differences:

$$\phi\left(\frac{m_i + m_{i+1}}{2}\right) = -\xi\left(\frac{M_i + M_{i+1}}{2}\right)\frac{M_{i+1} - M_i}{m_{i+1} - m_i} \tag{4.4}$$

Here, the magnitude function is evaluated at the mid-points between the adjacent evolutionary models on the mass grid. We calculated three distinct magnitude functions for each of the three final isochrones (*red tail*, *blue tail* and *ridgeline*). The magnitude function for an arbitrary [O/Fe] can be obtained by linearly interpolating/extrapolating between the three calculated magni-

tude functions to the desired oxygen abundance. The combined magnitude function for the entire cluster was computed as the average of individual magnitude functions, evaluated for the oxygen abundance of every star that satisfies $0.1\,\mathrm{M}_\odot < M < 0.4\,\mathrm{M}_\odot$ and $-0.27\,\mathrm{dex} < [\mathrm{O/Fe}] < 0.63\,\mathrm{dex}$ (the same restrictions as in the lower panel of Figure 4.7). Finally, the magnitude function was binned into 20 uniform bins in the range $17 < m < 24$ using trapezoid integration.

To determine the parameters of the mass function, β, γ and M_{bp}, we applied the same binning to the observed magnitude function in `F160W` and fitted the theoretical magnitude function to the result, using least squares regression, weighted by the Poisson errors in each bin. The observed magnitude function and the theoretical best fit are shown in Figure 4.8. The best-fit parameters of the mass function are $\beta = 1.55 \pm 0.15$, $\gamma = -0.18 \pm 0.06$ and $M_{\mathrm{bp}} = (0.40 \pm 0.02)\,\mathrm{M}_\odot$. In addition to the combined magnitude function, three more theoretical magnitude functions were calculated for the same parameters as the best fit, but using only one of the three isochrones instead of a weighted average of all three. As seen in Figure 4.8, the scatter among the theoretical magnitude functions is consistent with the Poisson counting errors in the corresponding magnitude bins, suggesting that for main sequence members the distribution of oxygen abundance has a subdominant effect on the luminosity function of the cluster.

4.6.3 Substellar population of 47 Tucanae

In this sub-section, we predict the colors, magnitudes and number densities of the brown dwarfs in 47 Tucanae, as they may be observed with JWST *NIRCam*. The color-magnitude space considered in this study is `F322W2` vs `F150W2` − `F322W2`, since brown dwarfs are most likely to be detected in wide bands at long wavelengths due to their faint magnitudes and red colors. Our predictions are based on the assumption that the mass function (Equation 4.2 with the best-fit parameters in Figure 4.8), the calculated isochrones (Figure 4.6) and the inferred distribution of chemical abundances (Figure 4.7) remain unchanged in the substellar regime.

We re-calculated the synthetic magnitude function of 47 Tucanae in 30 evenly spaced

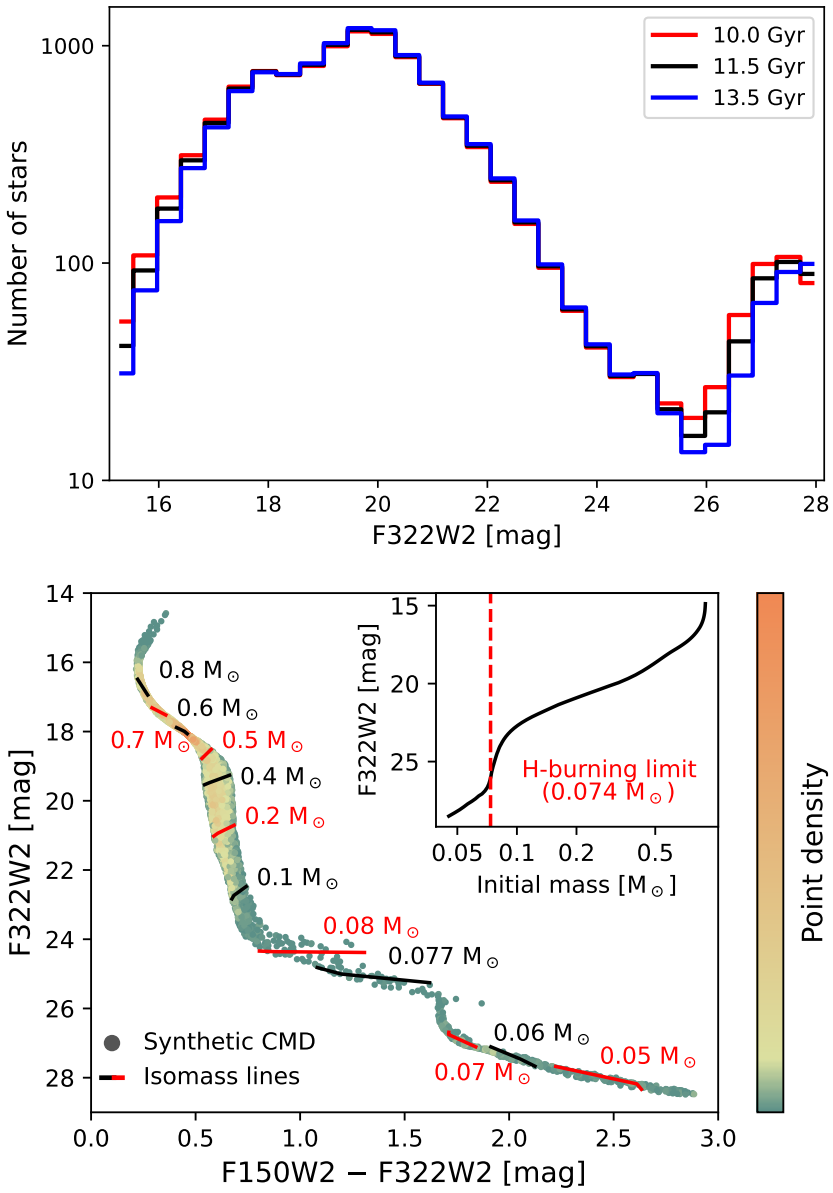

Figure 4.9. *Top:* predicted magnitude distribution of stars and brown dwarfs in 47 Tucanae at different ages. The bright and faint peaks represent the main sequence and the brown dwarfs of the cluster, respectively, with a clear stellar/substellar gap in between. The distribution is normalized to the number of stars in the dataset (Section 4.3). *Bottom:* predicted CMD of 47 Tucanae from the subgiant branch to the substellar sequence. Isomass lines are shown for selected masses. The color scatter in the figure is derived from the inferred distribution of [O/Fe] near the end of the main sequence. The inset sub-figure in the upper right corner shows the mass-magnitude relationship for the *ridgeline* isochrone with the hydrogen-burning limit highlighted.

magnitude bins between $m = 15.1$ and $m = 28.25$ in F322W2, using the best-fit mass function parameters. The calculations were carried out for three different ages: 10 Gyr, 11.5 Gyr (best-fit age) and 13.5 Gyr. The resulting magnitude functions are shown in the upper panel of Figure 4.9. At all ages, the magnitude function exhibits a clear stellar/substellar gap at $m \sim 26$, where the brown dwarf density per magnitude is reduced by nearly an order of magnitude (compared to the maximum density within the modelled range that is predicted to occur around $m = 27.5$). While the lower main sequence is virtually unaffected by the cluster age, both the turn-off point and the substellar sequence undergo noticeable evolution.

A synthetic CMD based on the inferred oxygen abundance in Figure 4.7, the isochrones in Figure 4.6 and the predicted mass function at 11.5 Gyr is shown in the lower panel of Figure 4.9. Lines of constant mass (isomass lines) for selected masses and $-0.27\,\mathrm{dex} < [\mathrm{O/Fe}] < 0.63\,\mathrm{dex}$ are also shown for reference. Since the isochrones of the substellar sequence in 47 Tucanae appear almost exactly parallel to the isomass lines, the effect of evolution on the brown dwarf colors is highly degenerate with [O/Fe]. This presents a potential challenge to the use of brown dwarfs as chemical tracers, since the masses of individual brown dwarfs (and, hence, their evolutionary phases) are not *a priori* known. The degeneracy also reduces the observed photometric scatter, making the substellar sequence far narrower than the main sequence in the CMD space.

The predicted mass-magnitude relationship for the *ridgeline* isochrone is shown in an inset sub-figure of the lower panel of Figure 4.9 with the hydrogen-burning limit (HBL) highlighted. We define the HBL as the mass, at which the energy output from nuclear reactions contributes 50% of the stellar luminosity at 11.5 Gyr. In this case, the HBL was computed as $0.074\,\mathrm{M}_\odot$.

4.7 Discussion

We developed a general method for determining the chemical compositions, ages and mass functions of globular clusters from the observed CMDs in optical and near infrared bands.

Our method relies on state-of-the-art model atmospheres and evolutionary models that are fully self-consistent and incorporate the full set of non-solar abundances in every component, including the interior structure and evolution, nuclear processing, atmosphere-interior coupling, atmospheric structures and spectral synthesis. Our modelling framework was applied to the brightest mono-metallic globular cluster 47 Tucanae. We reproduce for the first time the observed scatter in the photometric colors of main sequence stars without any *a priori* assumptions of its magnitude. We also provide the first measurements of chemical compositions for individual stars of the lower main sequence in a globular cluster (Figure 4.7). An extension of our models to the substellar regime predicts the expected colors and magnitudes of brown dwarfs in the cluster, reproducing the anticipated stellar/substellar gap. The predicted brown dwarf CMD for the first time incorporates the inferred distribution of chemical abundances. The best-fit parameters of 47 Tucanae determined in this study are listed in Table 4.1. The key findings are as follows:

- The photometric scatter of 47 Tucanae in both optical and near infrared bands can be reproduced with unaltered average spectroscopic abundances for all elements (Appendix E) with the exception of [O/Fe] and [Ti/Fe]. Constraining the abundances of elements other than oxygen and titanium from the CMDs considered in this study is challenging due to the subdominant effect of those elements on stellar atmospheres, as illustrated in Figure 4.5.

- The observed photometric scatter is predominantly driven by [O/Fe]. Our best-fit model CMD is consistent with the absence of star-to-star variations in [Ti/Fe], in agreement with the spectroscopic measurements and the mono-metallic nature of 47 Tucanae.

- The photometric distribution of the oxygen abundance estimated in this study (Figure 4.7) at $M < 0.4\,\mathrm{M}_{\odot}$ is statistically consistent with the spectroscopic distribution, inferred from evolved stars, under the assumption of systematic errors in the photometric estimates of order $0.15\,\mathrm{dex}$. These errors are comparable to the experimental uncertainties in available spectroscopic measurements, demonstrating that lower main sequence CMDs of globular

clusters may be used in chemical analyses.

- The discrepancy between the spectroscopic and photometric [O/Fe] values appears largest at the oxygen-rich tail of the distribution. If a genuine mass dependence of chemistry makes a significant contribution to the observed discrepancy in addition to the suspected systematic offset, the variation of [O/Fe] with stellar mass would be most prominent in the primordial population of the cluster instead of the enriched population. Since this conclusion contradicts the theoretical expectation, we disfavor this explanation and suggest that the mass dependence of chemistry makes a subdominant contribution compared to the systematic offset, if any. We therefore expect the difference in [O/Fe] between the lower main sequence and evolved stars to be less than the estimated systematic offset of $0.15\,\mathrm{dex}$.

- Corroborating our previous study of $\omega\,$Centauri, we confirm that the JWST CMD of 47 Tucanae is expected to have a stellar/substellar gap below the end of the main sequence, followed by a large number of brown dwarfs (Figure 4.9, *top*). The gap occurs around $\texttt{F322W2} \sim 26\,\mathrm{mag}$ and the maximum density of brown dwarfs within the modelling range is attained at $\texttt{F322W2} \sim 27\,\mathrm{mag}$.

- While our models indicate that the colors of brown dwarfs are highly sensitive to chemical abundances (Figure 4.5), the apparent degeneracy between their isomass lines and isochrones (Figure 4.9, *bottom*) will make the inference of photometric abundances challenging in the considered color-magnitude space ($\texttt{F322W2}$ vs $\texttt{F150W2} - \texttt{F322W2}$).

The constraints on the mass dependence of the oxygen abundance inferred in this study restrict the allowed parameter space of concurrent formation MP models, in agreement with previous studies of the photometric spread near the end of the main sequence [Ziliotto et al., 2023; Milone, 2023]. However, a detailed model of pollution as a function of stellar mass is required to carry out a thorough evaluation of proposed concurrent formation models, which may be challenging to derive due to the uncertain properties and evolution of circumstellar disks.

Future observations of the substellar sequences in nearby globular clusters, including 47 Tucanae, might extend the mass baseline of photometric analysis by nearly an order of magnitude and explore the abundances of other elements such as carbon and nitrogen that are far more important in the atmospheres of brown dwarfs than main sequence stars (Figure 4.5). The aforementioned isomass-isochrone degeneracy suggests that the luminosity function of brown dwarfs in globular clusters needs to be considered in conjunction with the CMD when deriving photometric chemical abundances. We further emphasize that JWST and HST bands other than the ones considered here may be more sensitive to chemical variations in substellar atmospheres, necessitating a follow-up study that explores all possible color combinations rather than a small subset of filters used in this chapter of the dissertation.

We note that the predicted substellar CMD of 47 Tucanae in Figure 4.9 was calculated under the assumption that the variation in [O/Fe] alone is sufficient to reproduce the photometric scatter. While this assumption was shown to be accurate for the main sequence stars, it likely has limited validity in the substellar regime and a more accurate theoretical CMD may be obtained by calculating additional isochrones that incorporate the spectroscopically inferred scatter in other elements.

If the spectroscopic/photometric discrepancy discussed here and in Section 4.6.1 is primarily caused by systematic offsets, their nature must be investigated in a future study, e.g., by comparing the synthetic spectra to observations of nearby metal-poor low-mass stars and brown dwarfs.

Chapter 4, in full, is being prepared for submission to the Astrophysical Journal Series 2023, authored by Roman Gerasimov, Adam J. Burgasser, Ilaria Caiazzo, Derek Homeier, Harvey Richer, Matteo Correnti and Jeremy Heyl. The dissertation author is the primary investigator of this study.

Chapter 5

Conclusion

5.1 Summary of findings

This dissertation explored the chemical evolution of the universe from the early metal-free Population III stars emerging some 100 Myr after the beginning of time, to the Milky Way globular clusters ω Centauri and 47 Tucanae that contain some of the oldest stars in our galaxy and retain the archaeological record of its assembly.

The study of each of the three environments was based on newly calculated evolutionary models and model atmospheres that were specifically tailored to the expected properties of these stellar populations. Most notably, the models of Population III stars capture the extreme non-equilibrium radiation fields in the metal-free atmospheres that cause significant ultraviolet excess in the spectral energy distribution, while the models of UCDs in globular clusters account for the peculiar chemistry of these objects, including its effect on the chemical equilibrium, opacity, cloud formation and transport, and atmosphere-interior coupling. In each case it was unambiguously demonstrated that the commonly adopted generic modelling techniques, such as the use of grey atmospheres for Population III stars or solar metallicity models for globular clusters, are not adequate to address the problems at hand.

The overarching theme of this dissertation is the importance of ongoing and future JWST observations, as well as other next-generation facilities, in the upcoming studies of chemical evolution. In Chapter 2, it was demonstrated that Population III stars can be observed directly at redshifts $\lesssim 12$ under favourable gravitational lensing ($\mu \sim 10^4$), if their masses exceed 100 $M_\odot$. We note that lensing events of this magnitude have already been observed [Chen et al., 2022], the range of redshifts is believed to be dominated by Population III stars [Bromm et al., 2009], and the required mass range matches the classical formation scenario, where the fragmentation scale is determined by the lowest roto-vibration level of molecular hydrogen in the absence of metal coolants [Abel et al., 2000]. In both ω Centauri and 47 Tucanae, as well as other nearby globular clusters, JWST can discern the onset and, possibly, the peak of the substellar sequence under the assumption that the initial mass function does not change significantly between the stellar and substellar regimes. This assumption is almost certainly justified at least for the highest-mass brown dwarfs, since the lowest-temperature stellar members with only marginally larger masses have already been detected in abundance with both HST and JWST, and the star formation process that sets the initial mass function operates before hydrogen ignition.

The key advantage of studying the ancient stellar populations with stellar modelling is the "behind-the-scenes" insight into the inner workings of stars and brown dwarfs that cannot be obtained from more data-driven techniques such as atmospheric retrieval [Madhusudhan, 2018]. Particularly noteworthy findings of this dissertation that may be attributed to this category include the following:

1. Despite their metal-free nature, Population III stars are able to fuse hydrogen through the CNO cycle at masses above 16 $M_\odot$, since the conditions in their hot cores are sufficient to create the necessary amount of metals using the triple-α process.

2. Around the mass of 6 $M_\odot$, Population III stars enter an intricate balance between the intensity of short-wavelength out-of-equilibrium radiation from the deep layers of the

atmosphere and the absorption of same wavelengths by the second excited state of helium that results in a brief inversion of the color-magnitude trend, such that the star gets redder at higher temperatures. This feature of the CMD (the helium loop) may serve as a diagnostic of the helium mass fraction.

3. The hydrogen-burning limit in the enriched population of globular clusters like ω Centauri may be $10\% - 15\%$ lower than its Population I value ($\gtrsim 0.075$ $M_\odot$, [Baraffe et al., 1998]) due to the large helium mass fraction ($Y \approx 0.4$) despite the much lower metallicity of the cluster. This reduction may potentially allow objects as cold as $T_{\rm eff} \sim 1800$ K to remain stellar.

4. The photometric difference between primordial and enriched brown dwarfs in globular clusters is nearly degenerate with the effect of stellar mass, giving the substellar sequence a narrower appearance on the CMD despite the fact that JWST colors may vary by over 0.5 mag between populations for a fixed mass.

The studies of ω Centauri in Chapter 3 and 47 Tucanae in Chapter 4 provide a framework for inferring the chemical abundances of globular clusters by fitting theoretical isochrones to the observed multiband photometry of the lower main sequence. In each case, I was able to obtain detailed abundances of key elements, including oxygen and titanium, by exploiting the different effects these elements have on the spectral energy distribution of stars with different masses. Most importantly, for 47 Tucanae I was able to recover the distribution of $[{\rm O}/{\rm Fe}]$ near the end of the main sequence without any posterior assumptions of the existence of multiple populations or the expected chemical spread. This technique has an affordable computational cost ($\sim 10^5$ CPU hours per population) and can be adapted to any globular cluster or coeval stellar population in the future.

5.2 Implications for the origin of multiple populations

The main findings related to the issue of multiple populations in globular clusters are as follows:

1. The spread of oxygen abundance near the end of the main sequence of 47 Tucanae is closely comparable to that inferred from the spectroscopic observations of post-main sequence members.

2. The titanium abundance does not vary noticeably among main sequence stars.

3. The inferred oxygen distribution displays a high degree of asymmetry.

4. The luminosity functions of both 47 Tucanae and ω Centauri are consistent with identical initial mass functions in both primordial and enriched populations.

The consistency of the chemical spread between main and post-main sequence members indicates that the operating chemical enrichment mechanism is insensitive to the initial stellar mass between $\lesssim 0.1$ $M_\odot$ and $\lesssim 0.9$ $M_\odot$. Since accretion on both circumstellar disks and stellar atmospheres is expected to depend strongly on the stellar mass [Bondi, 1952; Carpenter et al., 2006; Ohtani and Tsuribe, 2013], I conclude that multiple generation models are most consistent with the observations. Therefore, the chemical peculiarity of the enriched population was most likely already present in the interstellar gas at the onset of formation of the second generation of stars. Furthermore, turbulent separation [Hopkins, 2014] is unlikely to have played a key role in the observed chemical scatter, since the asymmetry of the inferred oxygen distribution implies that the total number of oxygen atoms in the cluster was not conserved by the enrichment mechanism.

5.3 Future work

While the stellar models presented in Chapter 2 already capture many of the key physical processes that operate in metal-free stars, the following improvements are required to realistically simulate the high-redshift environment where these stars originate:

1. Population III stars likely existed in galaxies, which are easier to detect with JWST than individual stars due to the combined luminosity of the large number of members. Since the properties and evolution of stars are set by their initial masses, the expected spectral energy distribution of the early galaxies and its redshift dependence will be strongly regulated by the initial mass function. Extracting the Population III mass function from high-redshift galactic surveys requires distinguishing the Population III contribution from that of other luminous sources such as the first Population II stars. The short lifetimes of Population III stars and high metallicity yields of their supernova explosions [Schneider et al., 2006b] ensure that even at very high redshifts, the contribution of Population II stars to the combined luminosity remains significant [Sarmento et al., 2018; Xu et al., 2013]. A comprehensive mass function-dependent model of the spectral energy distribution in Population III-dominated galaxies can be developed by combining the existing simulations of star formation and feedback (e.g., Sarmento and Scannapieco [2022]; Riaz et al. [2022]) with detailed stellar models such as the ones presented in Chapter 2. The predictions calculated in this framework would be directly comparable to the future surveys of $z \gtrsim 10$ galaxies with JWST, and will provide constraints on both the early evolution of the initial mass function and the chemical enrichment mechanisms that contributed the first metals in the universe.

2. While individual Population III stars may form up to $z = 6$ or later in surviving metal-free pockets of the universe [Trenti et al., 2009], the competing formation rate of Population II stars favours the search for these objects at pre-ionization redshifts ($z \gtrsim 9$, Sarmento et al.

[2018]) to avoid cross-contamination. The neutral interstellar gas around Population III stars of that epoch absorbs the emergent flux blueward of the Lyman α wavelength [Meiksin, 2006] and reprocesses it into longer wavelengths in the form of nebular emission that can be included in the spectral model. The observed spectral energy distribution will have both stellar and nebular components. The specific weight of each component depends on the ability of Population III stars to expel the surrounding gas beyond the virial radius of the underlying dark matter halo through radiative feedback [Johnson et al., 2009b], which, in turn, depends on the initial mass function. The uncertain nature of the Population III mass function requires consideration of all possible regimes.

The first tentative detection of a brown dwarf in 47 Tucanae was recently announced [Nardiello et al., 2023]. The ongoing [Bedin et al., 2021; Caiazzo et al., 2021] and future observations of globular clusters with JWST will likely reveal many more substellar members in these unique environments. In Chapters 3 and 4, I demonstrated that the luminosity function of the substellar sequence is sensitive to the cluster age. Therefore, an independent age diagnostic of globular clusters may be obtained from these future observations. While the effect of chemical peculiarities on the colors of brown dwarfs appears degenerate with stellar mass (Chapter 4), the extreme sensitivity of cool atmospheres to atomic abundances is expected to translate into the substellar luminosity function instead. As such, future observations may be sensitive to more subtle variations in the initial mass function between individual sub-populations.

Finally, it is important to note that our understanding of the complex processes responsible for the observed UCD spectra remains incomplete. While the chemical abundances of the enriched population are almost exclusive to globular clusters, direct comparisons of synthetic spectra to chemically peculiar ultracool subdwarfs in the galactic halo [Burgasser, 2014] may still be highly valuable. The spectroscopic observations from large-scale surveys of Population II stars (e.g., the galactic archaeology component of the Subaru Prime Focus Spectrograph survey, [Takada et al., 2014]) may be particularly suitable to establish the sought comparison baseline.

5.4 Afterword

The oldest globular clusters in the Milky Way may have formed over 13.5 Gyr ago. Over the last century of astronomical research, their members were promoted to the status of the first stars in the universe, only to be demoted shortly after to give way to Population III competitors. But even if globular clusters do not represent the primordial stellar population themselves, they have definitely "experienced" that population firsthand through its radiative feedback. I find it even more remarkable that globular clusters are almost certainly the oldest objects that can be observed with an unaided eye. In the same year when Walter Baade first defined stellar populations, Tennessee Williams famously wrote that "*time is the longest distance between places*". It is perhaps safe to assume that neither of them realized just how close they could see to the beginning of time by simply looking up.

The prospect of observing the first stars at high redshift and the recent progress in the field of galactic archaeology are a clear reminder that our stellar past is not lost but merely scrambled and in need of more sophisticated analysis. The framework for inferring the properties of stellar populations from multiband photometry presented in this dissertation contributes yet another instrument to that analysis. It is my hope that in no-so-distant future, the early days of our galaxy will be no more obscured than ancient globular clusters on a dark starry night.

Appendix A

Model parameters of Population III stars

Table A.1 lists the defining parameters and convergence criteria of all ATLAS-9 model atmospheres calculated in Chapter 3. Initial masses are sampled logarithmically between 1 $M_{\odot}$ and the estimated Eddington limit (820 $M_{\odot}$). The corresponding stellar radii, luminosities, effective temperatures and surface gravities are calculated using Eqs. 2.1, 2.2, 2.4 and 2.5 as well as the best-fit parameters in Table 2.1. Only the effective temperature and surface gravity are used as inputs to model atmospheres. The final convergence is parameterized in terms of the maximum absolute flux error and the maximum absolute flux derivative error with respect to the depth-integrated mass density (see [Kurucz, 1970]). Flux errors and flux derivative errors are used to calculate the temperature corrections between iterations using the Avrett and Krook [1963] scheme at large optical depths and the Λ-iteration scheme ([Böhm-Vitense, 1964], [Mihalas, 1978, Ch. 3-3]) at shallow optical depths, respectively. All models calculated in this study meet the standard convergence target of flux error below 1% and flux derivative error below 10% [Sbordone and Bonifacio, 2005; Mészáros et al., 2012].

Table A.1. Parameters of Population III models calculated in this study

Init. Mass M $[M_\odot]$	Eff. Temp. $T_{\rm eff}$ [K]	Gravity $\log_{10}(g)$	Radius R $[R_\odot]$	Lum. $\log_{10}(L/L_\odot)$	Max Flux Err. [%]	Max Flux Der. Err. [%]
1.000	7180	4.550	0.879	0.267	0.24	6.58
1.124	8047	4.581	0.900	0.485	0.62	1.54
1.264	9000	4.612	0.921	0.700	0.61	3.11
1.421	10045	4.642	0.942	0.911	0.71	7.49
1.597	11189	4.673	0.964	1.118	0.76	8.30
1.796	12437	4.704	0.987	1.322	0.78	7.88
2.019	13796	4.734	1.010	1.523	0.85	6.84
2.270	15273	4.765	1.034	1.719	0.79	5.00
2.551	16873	4.796	1.058	1.912	0.84	3.89
2.868	18602	4.827	1.083	2.102	0.74	4.94
3.225	20466	4.857	1.108	2.288	0.58	5.76
3.625	22472	4.888	1.134	2.471	0.53	5.73
4.075	24623	4.919	1.161	2.650	0.45	5.17
4.582	26924	4.949	1.188	2.825	0.35	4.50
5.151	29381	4.980	1.216	2.997	0.34	3.23
5.790	31996	5.011	1.245	3.165	0.31	1.63
6.510	34772	5.042	1.274	3.330	0.23	1.31
7.318	37712	5.072	1.304	3.491	0.24	0.93
8.227	40817	5.103	1.334	3.648	0.28	0.60
9.249	44087	5.134	1.365	3.802	0.31	0.65
10.398	47521	5.164	1.397	3.953	0.32	0.47
11.690	51118	5.195	1.430	4.100	0.32	0.36
13.141	54874	5.226	1.464	4.243	0.27	0.27
14.774	58785	5.256	1.498	4.383	0.24	0.23
16.609	62432	5.276	1.554	4.519	0.20	0.26
18.672	65238	5.270	1.658	4.652	0.18	0.31
20.991	68031	5.265	1.769	4.781	0.17	0.46
23.598	70799	5.260	1.887	4.906	0.15	0.49
26.529	73528	5.254	2.013	5.028	0.12	0.56
29.825	76205	5.249	2.148	5.147	0.14	0.59
33.529	78819	5.243	2.291	5.261	0.15	0.70

Continued on next page

Table A.1 (*continued*)

Init. Mass M $[M_\odot]$	Eff. Temp. $T_{\rm eff}$ [K]	Gravity $\log_{10}(g)$	Radius R $[R_\odot]$	Lum. $\log_{10}(L/L_\odot)$	Max Flux Err. [%]	Max Flux Der. Err. [%]
37.694	81355	5.238	2.445	5.373	0.21	0.74
42.376	83800	5.233	2.608	5.480	0.26	0.75
47.639	86143	5.227	2.783	5.584	0.20	0.84
53.557	88369	5.222	2.969	5.685	0.22	1.09
60.209	90467	5.216	3.167	5.782	0.17	1.15
67.688	92425	5.211	3.379	5.875	0.21	1.08
76.095	94232	5.206	3.605	5.965	0.22	0.93
85.547	95878	5.200	3.846	6.052	0.23	0.69
96.172	97352	5.195	4.103	6.134	0.23	0.64
108.118	98647	5.189	4.378	6.214	0.23	0.65
121.547	99754	5.184	4.671	6.289	0.26	0.53
136.645	100666	5.179	4.983	6.361	0.31	0.45
153.617	101379	5.173	5.317	6.430	0.37	0.51
172.698	102000	5.168	5.672	6.497	0.44	0.59
194.149	102624	5.162	6.052	6.563	0.47	0.60
218.264	103253	5.157	6.456	6.630	0.40	0.49
245.375	103885	5.152	6.888	6.697	0.46	0.54
275.853	104521	5.146	7.349	6.764	0.32	0.38
310.117	105160	5.141	7.840	6.831	0.19	0.26
348.637	105804	5.136	8.365	6.898	0.13	0.26
391.941	106452	5.130	8.924	6.964	0.15	0.39
440.624	107103	5.125	9.521	7.031	0.18	0.43
495.354	107759	5.119	10.158	7.098	0.19	0.41
556.881	108419	5.114	10.838	7.165	0.22	0.44
626.052	109082	5.109	11.562	7.232	0.25	0.48
703.814	109750	5.103	12.336	7.299	0.30	6.53
791.234	110422	5.098	13.161	7.365	0.37	7.67
820.200	110629	5.096	13.425	7.386	0.60	4.59

Appendix B

Evolutionary configuration for ω Centauri

Table B.1 lists all MESA v15140 settings employed in Chapter 3 that differ from their default values. The initial settings were adopted from Choi et al. [2016]. The boundary condition tables for atmosphere-interior coupling were then replaced with the tables calculated in this study as detailed in Section 3.3. Since the setup in Choi et al. [2016] is based on the older version of MESA (v7503), some of the settings were replaced with their modern equivalents. Finally, all parameters that have insignificantly small effect on the range of stellar masses considered in this study (e.g. nuclear reaction networks) were restored to MESA defaults.

Table B.1. Configuration options chosen in evolutionary models calculated in this study

Parameter	Value	Explanation
Zbase	Same as initial_z	Nominal metallicity for opacity calculations
kap_file_prefix	a09	Opacity tables pre-computed for the solar abundances in Asplund et al. [2009] which match the abundances adopted in this study the closest. Also following Choi et al. [2016]
kappa_lowT_prefix	lowT_fa05_a09p	
kappa_CO_prefix	a09_co	
create_pre_main_sequence_model	True	Begin evolution at the PMS, following [Choi et al., 2016]

Continued on next page

Table B.1 (*continued*)

Parameter	Value	Explanation
`pre_ms_T_C`	5×10^5 K	Initial central temperature for the PMS, following [Choi et al., 2016]
`atm_option`	`T_tau` for the first 100 steps and `table` after that	Boundary conditions for the atmosphere-interior coupling. Use grey atmosphere temperature relation initially, following [Choi et al., 2016], then switch to custom atmosphere tables
`atm_table`	`tau_100`	Use pre-tabulated atmosphere-interior coupling boundary conditions at the optical depth of $\tau = 100$
`initial_zfracs`	`0`	Use custom initial abundances of elements
`initial_z`	Metal mass fraction corresponding to the population of interest	$[M/H]$ is converted to metal mass fraction using the abundances in Tables 3.1 and 3.2 as well as solar baseline abundances in Table C.1
`initial_y`	0.4	Enhanced helium mass fraction, $Y = 0.4$, considered in this study
`z_fraction_*`	Abundances of all elements corresponding to the population of interest	Enhancements in Tables 3.1 and 3.2 as well as solar baseline abundances in Table C.1
`initial_mass`	Range from ~ 0.03 $M_\odot$ to ~ 0.5 $M_\odot$	Evolutionary models are calculated from the lowest mass covered by the atmosphere grid to the upper limit of ~ 0.5 $M_\odot$ where the atmosphere-interior coupling scheme can no longer be used
`max_age`	13.5 Gyr	Terminate evolution at 13.5 Gyr for all stars as the maximum expected age of cluster members
`mixing_length_alpha`	1.82 scale heights	Convective mixing length determined by solar calibration in Choi et al. [2016]

Continued on next page

Table B.1 (*continued*)

Parameter	Value	Explanation
`do_element_diffusion`	True	Carry out element diffusion
`diffusion_dt_limit`	3.15×10^7 s but disabled in fully convective stars	Minimum time step required by `MESA` to calculate element diffusion. The default value, 3.15×10^7 s, is changed to a much larger number, 3.15×10^{16} s, once the mass of the convective core is within 0.01 $M_\odot$ of the mass of the star to suppress diffusion in fully convective objects due to poor convergence

Appendix C

Solar abundances

In this appendix, we list the solar element abundances adopted in this study for both atmosphere and evolutionary models (Table C.1). Solar abundances are presented as logarithmic (dex) number densities compared to hydrogen whose abundance is set to 12.00 dex exactly. All elements omitted in the table were not included in the modeling. The abundances listed here correspond to hydrogen, helium, and metal mass fractions of $X = 0.714$, $Y = 0.271$ and $Z = 0.015$ respectively.

Table C.1. Solar abundances adopted in this study

Symbol	Element	Abundance	Error	Reference
H	Hydrogen	12.00	–	(1)
He	Helium	10.98	0.01	(2)
Li	Lithium	3.26	0.05	(4)
Be	Beryllium	1.38	0.09	(3)
B	Boron	2.79	0.04	(4)
C	Carbon	8.50	0.06	(6)
N	Nitrogen	7.86	0.12	(6)
O	Oxygen	8.76	0.07	(6)
F	Fluorine	4.56	0.30	(3)
Ne	Neon	8.02	0.09	(8)

Continued on next page

Table C.1 (*continued*)

Symbol	Element	Abundance	Error	Reference
Na	Sodium	6.24	0.04	(3)
Mg	Magnesium	7.60	0.04	(3)
Al	Aluminium	6.45	0.03	(3)
Si	Silicon	7.51	0.03	(3)
P	Phosphorus	5.46	0.04	(6)
S	Sulfur	7.16	0.05	(6)
Cl	Chlorine	5.50	0.30	(3)
Ar	Argon	6.40	0.13	(5)
K	Potassium	5.11	0.09	(6)
Ca	Calcium	6.34	0.04	(3)
Sc	Scandium	3.15	0.04	(3)
Ti	Titanium	4.95	0.05	(3)
V	Vanadium	3.93	0.08	(3)
Cr	Chromium	5.64	0.04	(3)
Mn	Manganese	5.43	0.04[1]	(3)
Fe	Iron	7.52	0.06	(6)
Co	Cobalt	4.99	0.07	(3)
Ni	Nickel	6.22	0.04	(3)
Cu	Copper	4.19	0.04	(3)
Zn	Zinc	4.56	0.05	(3)
Ga	Gallium	3.04	0.09	(3)
Ge	Germanium	3.65	0.10	(3)
As	Arsenic	2.30	0.04	(4)
Se	Selenium	3.34	0.03	(4)
Br	Bromine	2.54	0.06	(4)
Kr	Krypton	3.25	0.06	(5)
Rb	Rubidium	2.36	0.03	(4)
Sr	Strontium	2.87	0.07	(3)
Y	Yttrium	2.21	0.05	(3)
Zr	Zirconium	2.62	0.06	(7)
Nb	Niobium	1.46	0.04	(3)

Continued on next page

[1]The uncertainty in Mn abundance differs between the preprint (arXiv:0909.0948) and published versions of Asplund et al. [2009] by 0.01 dex. The latter is presented here.

Table C.1 (*continued*)

Symbol	Element	Abundance	Error	Reference
Mo	Molybdenum	1.88	0.08	(3)
Ru	Ruthenium	1.75	0.08	(3)
Rh	Rhodium	1.06	0.04	(4)
Pd	Palladium	1.65	0.02	(4)
Ag	Silver	1.20	0.02	(4)
Cd	Cadmium	1.71	0.03	(4)
In	Indium	0.76	0.03	(4)
Sn	Tin	2.04	0.10	(3)
Sb	Antimony	1.01	0.06	(4)
Te	Tellurium	2.18	0.03	(4)
I	Iodine	1.55	0.08	(4)
Xe	Xenon	2.24	0.06	(5)
Cs	Caesium	1.08	0.02	(4)
Ba	Barium	2.18	0.09	(3)
La	Lanthanum	1.10	0.04	(3)
Ce	Cerium	1.58	0.04	(3)
Pr	Praseodymium	0.72	0.04	(3)
Nd	Neodymium	1.42	0.04	(3)
Sm	Samarium	0.96	0.04	(3)
Eu	Europium	0.52	0.04	(3)
Gd	Gadolinium	1.07	0.04	(3)
Tb	Terbium	0.30	0.10	(3)
Dy	Dysprosium	1.10	0.04	(3)
Ho	Holmium	0.48	0.11	(3)
Er	Erbium	0.92	0.05	(3)
Tm	Thulium	0.10	0.04	(3)
Yb	Ytterbium	0.92	0.02	(4)
Lu	Lutetium	0.10	0.09	(3)
Hf	Hafnium	0.87	0.04	(6)
Ta	Tantalum	−0.12	0.04	(4)
W	Tungsten	0.65	0.04	(4)
Re	Rhenium	0.26	0.04	(4)
Os	Osmium	1.36	0.19	(6)

Continued on next page

Table C.1 (*continued*)

Symbol	Element	Abundance	Error	Reference
Ir	Iridium	1.38	0.07	(3)
Pt	Platinum	1.62	0.03	(4)
Au	Gold	0.80	0.04	(4)
Hg	Mercury	1.17	0.08	(4)
Tl	Thallium	0.77	0.03	(4)
Pb	Lead	2.04	0.03	(4)
Bi	Bismuth	0.65	0.04	(4)
Th	Thorium	0.08	0.03	(6)
U	Uranium	−0.54	0.03	(4)

Note. — (1) – Hydrogen abundance is 12.00 by definition. (2) – Helium PMS abundance calibrated to the initial helium mass fraction of $Y = 0.27 \pm 0.01$ as estimated from an ensemble of solar models in literature calibrated to observed photospheric metallicity, luminosity and helioseismic frequencies [Christensen-Dalsgaard, 1998; Boothroyd and Sackmann, 2003]. (3) – Present day spectroscopic photospheric abundances from Asplund et al. [2009], Table 1. (4) – Meteoritic abundances from Asplund et al. [2009], Table 1. (5) – Present day indirect photospheric abundances from Asplund et al. [2009], Table 1. (6) – Present day spectroscopic photospheric abundances from Caffau et al. [2011b], Table 5. (7) – Present day spectroscopic photospheric abundance of zirconium from Caffau et al. [2011a], (8) – Present day spectroscopic photospheric abundance of neon inferred from a representative sample of B-type stars [Takeda et al., 2010].

Appendix D

Photometric catalog for ω Centauri

We include with this dissertation an astro-photometric catalogue of measured sources in the HST imaged fields, and multi-band atlases for each filter. The main catalogue (filename: `Catalog`) includes right ascensions and declinations in units of decimal degrees; as well as `VEGAMAG` magnitudes in `F606W`, `F814W`, `F110W` and `F160W` before zero-pointing and differential reddening corrections. The last three columns contains flags to differentiate unsaturated and saturated stars for `F606W` and `F814W` filters and a proper motion-based flag to distinguish between field stars and cluster members.

Four additional catalogues `R-I_vs_I.dat`, `J-H_vs_H.dat`, `C_RIH_vs_H.dat` and `I-H_-vs_J.dat` contain differential reddening-corrected, zero-pointed colours and magnitudes diagrams in the $m_{\rm F606W} - m_{\rm F814W}$ vs $m_{\rm F814W}$, $m_{\rm F110W} - m_{\rm F160W}$ vs $m_{\rm F160W}$, $(m_{\rm F606W} - m_{\rm F814W}) - (m_{\rm F814W} - m_{\rm F160W})$ vs $m_{\rm F160W}$, and $m_{\rm F814W} - m_{\rm F160W}$ vs $m_{\rm F110W}$ observational planes. All four files have the same number of entries and ordering as the main catalogue with one-to-one correspondence.

Finally, for each filter we provide two additional files containing the estimated photometric errors (`F606W_err.dat`, `F814W_err.dat`, `F110W_err.dat` and `F160W_err.dat`) and completeness (`F606W_comp.dat`, `F814W_comp.dat`, `F110W_comp.dat` and `F160W_comp.dat`) computed

in each half-magnitude bin.

We also release the atlases of the imaged field in each of the four filters. These atlases consist of stacked images produced with two sampling versions: one atlas sampled at the nominal pixel resolution and one atlas sampled at 2×-supersampled pixel resolution. The stacked images adhere to standard *FITS* format and contain headers with astrometric *WCS* (*World Coordinate System*) solutions tied to Gaia Early Data Release 3 astrometry [Gaia Collaboration et al., 2021]. We provide a single stacked view for each of `F606W` and `F814W` fields, and two stacked views for each of `F110W` and `F160W` fields separated into short and long exposure images.

The catalogues and atlases are available online[1].

[1] https://web.oapd.inaf.it/bedin/files/PAPERs_eMATERIALs/wCen_HST_LargeProgram/P05/

Appendix E

Nominal composition of 47 Tucanae

Table E.1 lists the nominal composition of 47 Tucanae adopted in this work, based on spectroscopic observations of giant and sub-giant members of the cluster in the literature. The derivation of the abundances listed in the table is described in Section 4.2. The physical member-to-member spread provided in the table ($s^{(X)}$) was calculated using Equation 4.1.

Table E.1. Average chemical composition of 47 Tucanae inferred from spectroscopic measurements in literature

	Best estimate	Unc.	Physical spread	# of measurements	Reference(s)
[Fe/H]	−0.75	0.01	–	281	(1)(2)(3)
[Al/Fe]	0.35	0.01	0.06	195	(1)(2)(3)
[Ba/Fe]	0.25	0.07	–	13	(1)
[C/Fe]	−0.25	0.01	0.10	70	(3)
[Ca/Fe]	0.26	0.01	–	162	(1)(2)
[Ce/Fe]	−0.04	0.10	–	11	(1)
[Co/Fe]	−0.00	0.02	–	13	(1)
[Cr/Fe]	−0.04	0.03	–	13	(1)
[Cu/Fe]	−0.14	0.10	–	13	(1)
[Dy/Fe]	0.70	0.07	–	13	(1)
[Eu/Fe]	0.44	0.01	–	150	(1)(2)
[La/Fe]	0.20	0.01	–	144	(1)(2)
[Mg/Fe]	0.35	0.01	–	87	(1)(3)
[Mn/Fe]	−0.19	0.04	–	13	(1)
[Mo/Fe]	0.55	0.04	–	13	(1)
[N/Fe]	0.85	0.05	0.33	54	(3)
[Na/Fe]	0.27	0.01	0.15	236	(1)(2)(3)
[Nd/Fe]	0.04	0.07	–	13	(1)
[Ni/Fe]	−0.06	0.01	–	174	(1)(2)(3)
[O/Fe]	0.18	0.02	0.16	117	(1)(2)
[Pr/Fe]	−0.03	0.06	–	13	(1)
[Ru/Fe]	0.50	0.04	–	13	(1)
[Sc/Fe]	0.21	0.05	–	13	(1)
[Si/Fe]	0.32	0.01	–	222	(1)(2)(3)
[Ti/Fe]	0.34	0.01	–	163	(1)(2)
[V/Fe]	0.17	0.04	–	13	(1)
[Y/Fe]	0.07	0.05	–	13	(1)
[Zn/Fe]	0.26	0.04	–	13	(1)
[Zr/Fe]	0.41	0.06	0.10	13	(1)

Note. — All values are quoted in dex with respect to solar abundances. (1) – Thygesen et al. [2014]. (2) – Cordero et al. [2014]. (3) – Marino et al. [2016].

Bibliography

M. Abe, H. Yajima, S. Khochfar, C. Dalla Vecchia, and K. Omukai. Formation of the first galaxies in the aftermath of the first supernovae. MNRAS, 508(3):3226–3238, December 2021. doi:10.1093/mnras/stab2637.

T. Abel, G. L. Bryan, and M. L. Norman. The Formation and Fragmentation of Primordial Molecular Clouds. ApJ, 540(1):39–44, September 2000. doi:10.1086/309295.

A. Abohalima and A. Frebel. JINAbase—A Database for Chemical Abundances of Metal-poor Stars. ApJS, 238(2):36, October 2018. doi:10.3847/1538-4365/aadfe9.

W. S. Adams and A. H. Joy. A Spectroscopic Method of Determining the Absolute Magnitudes of A-Type Stars and the Parallaxes of 544 Stars. ApJ, 56:242, November 1922. doi:10.1086/142704.

W. S. Adams, A. H. Joy, M. L. Humason, and A. M. Brayton. The Spectroscopic Absolute Magnitudes and Parallaxes of 4179 Stars. ApJ, 81:187, April 1935. doi:10.1086/143628.

A. B. Alabi, D. A. Forbes, A. J. Romanowsky, J. P. Brodie, J. Strader, J. Janz, C. Usher, L. R. Spitler, S. Bellstedt, and A. Ferré-Mateu. The SLUGGS survey: dark matter fractions at large radii and assembly epochs of early-type galaxies from globular cluster kinematics. MNRAS, 468(4):3949–3964, July 2017. doi:10.1093/mnras/stx678.

F. Allard, D. Homeier, and B. Freytag. Model Atmospheres From Very Low Mass Stars to Brown Dwarfs. In *Cool Stars 16*, volume 448, page 91, December 2011. doi:10.48550/arXiv.1011.5405.

F. Allard, D. Homeier, and B. Freytag. Models of very-low-mass stars, brown dwarfs and exoplanets. *Philosophical Transactions of the Royal Society of London Series A*, 370(1968): 2765–2777, June 2012. doi:10.1098/rsta.2011.0269.

F. Allard, P. H. Hauschildt, and A. Schweitzer. Spherically Symmetric Model Atmospheres for Low-Mass Pre-Main-Sequence Stars with Effective Temperatures between 2000 and 6800 K. *The Astrophysical Journal*, 539(1):366–371, August 2000. doi:10.1086/309218.

F. Allard, P. H. Hauschildt, D. R. Alexander, A. Tamanai, and A. Schweitzer. The Limiting Effects of Dust in Brown Dwarf Model Atmospheres. ApJ, 556(1):357–372, July 2001. doi:10.1086/321547.

F. Allard, D. Homeier, and C. Sharp. Star, brown dwarf and planet simulator, 2014. URL https://phoenix.ens-lyon.fr/simulator/index.faces.

N. F. Allard, F. Spiegelman, and J. F. Kielkopf. Study of the K-H{_2} quasi-molecular line satellite in the potassium resonance line. A&A, 465(3):1085–1091, April 2007. doi:10.1051/0004-6361:20066616.

N. F. Allard, F. Spiegelman, and J. F. Kielkopf. K-H_2 line shapes for the spectra of cool brown dwarfs. A&A, 589:A21, May 2016. doi:10.1051/0004-6361/201628270.

L. H. Aller and J. L. Greenstein. The Abundances of the Elements in G-Type Subdwarfs. ApJS, 5:139, November 1960. doi:10.1086/190054.

R. A. Alpher, H. Bethe, and G. Gamow. The Origin of Chemical Elements. *Physical Review*, 73 (7):803–804, April 1948. doi:10.1103/PhysRev.73.803.

A. J. Anderson. *Mass Segregation in Globular Clusters M92, 47 Tucanae, and Omega Centauri*. PhD thesis, UNIVERSITY OF CALIFORNIA, BERKELEY, January 1997.

J. Anderson. Main-Sequence Observations with HST. In F. van Leeuwen, J. D. Hughes, and G. Piotto, editors, *Omega Centauri, A Unique Window into Astrophysics*, volume 265 of *Astronomical Society of the Pacific Conference Series*, page 87, January 2002.

J. Anderson and I. R. King. PSFs, Photometry, and Astronomy for the ACS/WFC. Instrument Science Report ACS 2006-01, February 2006.

J. Anderson and R. P. van der Marel. New Limits on an Intermediate-Mass Black Hole in Omega Centauri. I. Hubble Space Telescope Photometry and Proper Motions. ApJ, 710(2):1032–1062, February 2010. doi:10.1088/0004-637X/710/2/1032.

J. Anderson, A. Sarajedini, L. R. Bedin, I. R. King, G. Piotto, I. N. Reid, M. Siegel, S. R. Majewski, N. E. Q. Paust, A. Aparicio, A. P. Milone, B. Chaboyer, and A. Rosenberg. The Acs Survey of Globular Clusters. V. Generating a Comprehensive Star Catalog for each Cluster. AJ, 135(6):2055–2073, June 2008. doi:10.1088/0004-6256/135/6/2055.

S. M. Andrievsky, M. Spite, S. A. Korotin, F. Spite, P. Bonifacio, R. Cayrel, V. Hill, and P. François. NLTE determination of the aluminium abundance in a homogeneous sample of extremely metal-poor stars. A&A, 481(2):481–487, April 2008. doi:10.1051/0004-6361:20078837.

G. C. Angelou, R. P. Church, R. J. Stancliffe, J. C. Lattanzio, and G. H. Smith. Thermohaline Mixing and its Role in the Evolution of Carbon and Nitrogen Abundances in Globular Cluster Red Giants: The Test Case of Messier 3. ApJ, 728(2):79, February 2011. doi:10.1088/0004-637X/728/2/79.

V. A. Antonov and A. D. Chernin. "Hidden masses" and dynamical evolution of stellar systems. *Astrofizika*, 13:271–274, May 1977.

N. R. Arkelyan and S. V. Pilipenko. Globular Cluster as Indicators of Galactic Evolution. *Astronomy Reports*, 66(3):191–199, March 2022. doi:10.1134/S1063772922030015.

M. Asplund, N. Grevesse, A. J. Sauval, and P. Scott. The Chemical Composition of the Sun. ARA&A, 47(1):481–522, September 2009. doi:10.1146/annurev.astro.46.060407.145222.

Astropy Collaboration, T. P. Robitaille, E. J. Tollerud, P. Greenfield, M. Droettboom, E. Bray, T. Aldcroft, M. Davis, A. Ginsburg, A. M. Price-Whelan, W. E. Kerzendorf, A. Conley, N. Crighton, K. Barbary, D. Muna, H. Ferguson, F. Grollier, M. M. Parikh, P. H. Nair, H. M. Unther, C. Deil, J. Woillez, S. Conseil, R. Kramer, J. E. H. Turner, L. Singer, R. Fox, B. A. Weaver, V. Zabalza, Z. I. Edwards, K. Azalee Bostroem, D. J. Burke, A. R. Casey, S. M. Crawford, N. Dencheva, J. Ely, T. Jenness, K. Labrie, P. L. Lim, F. Pierfederici, A. Pontzen, A. Ptak, B. Refsdal, M. Servillat, and O. Streicher. Astropy: A community Python package for astronomy. A&A, 558:A33, October 2013. doi:10.1051/0004-6361/201322068.

Astropy Collaboration, A. M. Price-Whelan, B. M. Sipőcz, H. M. Günther, P. L. Lim, S. M. Crawford, S. Conseil, D. L. Shupe, M. W. Craig, N. Dencheva, A. Ginsburg, J. T. VanderPlas, L. D. Bradley, D. Pérez-Suárez, M. de Val-Borro, T. L. Aldcroft, K. L. Cruz, T. P. Robitaille, E. J. Tollerud, C. Ardelean, T. Babej, Y. P. Bach, M. Bachetti, A. V. Bakanov, S. P. Bamford, G. Barentsen, P. Barmby, A. Baumbach, K. L. Berry, F. Biscani, M. Boquien, K. A. Bostroem, L. G. Bouma, G. B. Brammer, E. M. Bray, H. Breytenbach, H. Buddelmeijer, D. J. Burke, G. Calderone, J. L. Cano Rodríguez, M. Cara, J. V. M. Cardoso, S. Cheedella, Y. Copin, L. Corrales, D. Crichton, D. D'Avella, C. Deil, É. Depagne, J. P. Dietrich, A. Donath, M. Droettboom, N. Earl, T. Erben, S. Fabbro, L. A. Ferreira, T. Finethy, R. T. Fox, L. H. Garrison, S. L. J. Gibbons, D. A. Goldstein, R. Gommers, J. P. Greco, P. Greenfield, A. M. Groener, F. Grollier, A. Hagen, P. Hirst, D. Homeier, A. J. Horton, G. Hosseinzadeh, L. Hu, J. S. Hunkeler, Ž. Ivezić, A. Jain, T. Jenness, G. Kanarek, S. Kendrew, N. S. Kern, W. E. Kerzendorf, A. Khvalko, J. King, D. Kirkby, A. M. Kulkarni, A. Kumar, A. Lee, D. Lenz, S. P. Littlefair, Z. Ma, D. M. Macleod, M. Mastropietro, C. McCully, S. Montagnac, B. M. Morris, M. Mueller, S. J. Mumford, D. Muna, N. A. Murphy, S. Nelson, G. H. Nguyen, J. P. Ninan, M. Nöthe, S. Ogaz, S. Oh, J. K. Parejko, N. Parley, S. Pascual, R. Patil, A. A. Patil, A. L. Plunkett, J. X. Prochaska, T. Rastogi, V. Reddy Janga, J. Sabater, P. Sakurikar, M. Seifert, L. E. Sherbert, H. Sherwood-Taylor, A. Y. Shih, J. Sick, M. T. Silbiger, S. Singanamalla, L. P. Singer, P. H. Sladen, K. A. Sooley, S. Sornarajah, O. Streicher, P. Teuben, S. W. Thomas, G. R. Tremblay, J. E. H. Turner, V. Terrón, M. H. van Kerkwijk, A. de la Vega, L. L. Watkins, B. A. Weaver, J. B. Whitmore, J. Woillez, V. Zabalza, and Astropy Contributors. The Astropy Project: Building an Open-science Project and Status of the v2.0 Core Package. AJ, 156(3): 123, September 2018. doi:10.3847/1538-3881/aabc4f.

L. H. Auer and D. Mihalas. Non-Lte Model Atmospheres. VII. The Hydrogen and Helium Spectra of the O Stars. ApJS, 24:193, February 1972. doi:10.1086/190253.

E. H. Avrett and M. Krook. The Temperature Distribution in a Stellar Atmosphere. ApJ, 137:874, April 1963. doi:10.1086/147564.

W. Baade. The Resolution of Messier 32, NGC 205, and the Central Region of the Andromeda Nebula. ApJ, 100:137, September 1944. doi:10.1086/144650.

J. Bailin. Globular Cluster Intrinsic Iron Abundance Spreads. I. Catalog. ApJS, 245(1):5, November 2019. doi:10.3847/1538-4365/ab4812.

I. Baraffe, G. Chabrier, F. Allard, and P. H. Hauschildt. Evolutionary models for metal-poor low-mass stars. Lower main sequence of globular clusters and halo field stars. A&A, 327: 1054–1069, November 1997.

I. Baraffe, G. Chabrier, F. Allard, and P. H. Hauschildt. Evolutionary models for solar metallicity low-mass stars: mass-magnitude relationships and color-magnitude diagrams. A&A, 337: 403–412, September 1998.

I. Baraffe, G. Chabrier, T. S. Barman, F. Allard, and P. H. Hauschildt. Evolutionary models for cool brown dwarfs and extrasolar giant planets. The case of HD 209458. A&A, 402:701–712, May 2003. doi:10.1051/0004-6361:20030252.

I. Baraffe, D. Homeier, F. Allard, and G. Chabrier. New evolutionary models for pre-main sequence and main sequence low-mass stars down to the hydrogen-burning limit. *Astronomy & Astrophysics*, 577:A42, May 2015. doi:10.1051/0004-6361/201425481.

C. B. Barber, D. P. Dobkin, and H. Huhdanpaa. Qhull: Quickhull algorithm for computing the convex hull. Astrophysics Source Code Library, record ascl:1304.016, April 2013.

R. J. Barber, J. Tennyson, G. J. Harris, and R. N. Tolchenov. A high-accuracy computed water line list. MNRAS, 368(3):1087–1094, May 2006. doi:10.1111/j.1365-2966.2006.10184.x.

G. Basri, G. W. Marcy, and J. R. Graham. Lithium in Brown Dwarf Candidates: The Mass and Age of the Faintest Pleiades Stars. ApJ, 458:600, February 1996. doi:10.1086/176842.

N. Bastian, H. J. G. L. M. Lamers, S. E. de Mink, S. N. Longmore, S. P. Goodwin, and M. Gieles. Early disc accretion as the origin of abundance anomalies in globular clusters. MNRAS, 436 (3):2398–2411, December 2013. doi:10.1093/mnras/stt1745.

N. Bastian and C. Lardo. Globular cluster mass-loss in the context of multiple populations. MNRAS, 453(1):357–364, October 2015. doi:10.1093/mnras/stv1661.

N. Bastian and C. Lardo. Multiple Stellar Populations in Globular Clusters. ARA&A, 56:83–136, September 2018. doi:10.1146/annurev-astro-081817-051839.

W. A. Baum. Globular clusters. 1. Photoelectric spectroscopic observations in M3 and M92. AJ, 57:222, November 1952. doi:10.1086/106758.

H. Baumgardt and S. Sollima. The global mass functions of 35 Galactic globular clusters - II. Clues on the initial mass function and black hole retention fraction. MNRAS, 472(1):744–750, November 2017. doi:10.1093/mnras/stx2036.

M. A. Beasley. *Globular Cluster Systems and Galaxy Formation*, pages 245–277. Springer International Publishing, 2020. doi:10.1007/978-3-030-38509-5_9.

S. Becerril, M. A. Sánchez, M. C. Cárdenas, O. Rabaza, A. Ramón, M. Abril, L. P. Costillo, R. Morales, A. Rodríguez, P. J. Amado, International CARMENES Team, and C. del Burgo. Comprehensive transient-state study for CARMENES NIR high-thermal stability. *SPIE*, 7735: 77352S, July 2010. doi:10.1117/12.856455.

L. R. Bedin, M. Salaris, J. Anderson, M. Libralato, D. Apai, D. Nardiello, R. M. Rich, A. Bellini, A. Dieball, P. Bergeron, A. J. Burgasser, A. P. Milone, and A. F. Marino. The HST large programme on NGC 6752 - III. Detection of the peak of the white dwarf luminosity function. MNRAS, 488(3):3857–3865, September 2019. doi:10.1093/mnras/stz1968.

L. R. Bedin, J. Anderson, I. R. King, and G. Piotto. Color-Magnitude Diagram and Luminosity Function of M4 near the Hydrogen-burning Limit. ApJ, 560(1):L75–L78, October 2001. doi:10.1086/324174.

L. R. Bedin, G. Piotto, J. Anderson, S. Cassisi, I. R. King, Y. Momany, and G. Carraro. ω Centauri: The Population Puzzle Goes Deeper. ApJ, 605(2):L125–L128, April 2004. doi:10.1086/420847.

L. R. Bedin, S. Cassisi, F. Castelli, G. Piotto, J. Anderson, M. Salaris, Y. Momany, and A. Pietrinferni. Transforming observational data and theoretical isochrones into the ACS/WFC Vega-mag system. MNRAS, 357(3):1038–1048, March 2005. doi:10.1111/j.1365-2966.2005.08735.x.

L. R. Bedin, I. R. King, J. Anderson, G. Piotto, M. Salaris, S. Cassisi, and A. Serenelli. Reaching the End of the White Dwarf Cooling Sequence in NGC 6791. ApJ, 678(2):1279–1291, May 2008. doi:10.1086/529370.

L. R. Bedin, M. Salaris, G. Piotto, J. Anderson, I. R. King, and S. Cassisi. The End of the White Dwarf Cooling Sequence in M4: An Efficient Approach. ApJ, 697(2):965–979, June 2009. doi:10.1088/0004-637X/697/2/965.

L. R. Bedin, J. Anderson, D. Apai, A. Bellini, P. Bergeron, A. J. Burgasser, A. Dieball, R. Gerasimov, M. Libralato, D. Nardiello, and M. Salaris. The faintest and coolest stars in the two closest globulars. JWST Proposal. Cycle 1, March 2021.

K. Bekki, T. Jeřábková, and P. Kroupa. The origin of discrete multiple stellar populations in globular clusters. MNRAS, 471(2):2242–2253, October 2017. doi:10.1093/mnras/stx1609.

K. Bekki. Globular cluster formation with multiple stellar populations: a single-binary composite scenario. MNRAS, 518(3):3274–3285, January 2023. doi:10.1093/mnras/stac3163.

K. Bekki and J. E. Norris. The Origin of the Double Main Sequence in ω Centauri: Helium Enrichment due to Gas Fueling from Its Ancient Host Galaxy? ApJ, 637(2):L109–L112, February 2006. doi:10.1086/500413.

A. Bellini, G. Piotto, L. R. Bedin, I. R. King, J. Anderson, A. P. Milone, and Y. Momany. Radial distribution of the multiple stellar populations in ω Centauri. A&A, 507(3):1393–1408, December 2009. doi:10.1051/0004-6361/200912757.

A. Bellini, J. Anderson, L. R. Bedin, I. R. King, R. P. van der Marel, G. Piotto, and A. Cool. The State-of-the-art HST Astro-photometric Analysis of the Core of ω Centauri. I. The Catalog. ApJ, 842(1):6, June 2017a. doi:10.3847/1538-4357/aa7059.

A. Bellini, J. Anderson, R. P. van der Marel, I. R. King, G. Piotto, and L. R. Bedin. The State-of-the-art HST Astro-photometric Analysis of the Core of ω Centauri. II. Differential-reddening Map. ApJ, 842(1):7, June 2017b. doi:10.3847/1538-4357/aa705f.

A. Bellini, A. P. Milone, J. Anderson, A. F. Marino, G. Piotto, R. P. van der Marel, L. R. Bedin, and I. R. King. The State-of-the-art HST Astro-photometric Analysis of the Core of ω Centauri. III. The Main Sequence's Multiple Populations Galore. ApJ, 844(2):164, August 2017c. doi:10.3847/1538-4357/aa7b7e.

A. Bellini, M. Libralato, L. R. Bedin, A. P. Milone, R. P. van der Marel, J. Anderson, D. Apai, A. J. Burgasser, A. F. Marino, and J. M. Rees. The HST Large Programme on ω Centauri. II. Internal Kinematics. ApJ, 853(1):86, January 2018. doi:10.3847/1538-4357/aaa3ec.

C. L. Bennett, D. Larson, J. L. Weiland, N. Jarosik, G. Hinshaw, N. Odegard, K. M. Smith, R. S. Hill, B. Gold, M. Halpern, E. Komatsu, M. R. Nolta, L. Page, D. N. Spergel, E. Wollack, J. Dunkley, A. Kogut, M. Limon, S. S. Meyer, G. S. Tucker, and E. L. Wright. Nine-year Wilkinson Microwave Anisotropy Probe (WMAP) Observations: Final Maps and Results. ApJS, 208(2):20, October 2013. doi:10.1088/0067-0049/208/2/20.

T. Bensby, S. Feltzing, and I. Lundström. Elemental abundance trends in the Galactic thin and thick disks as traced by nearby F and G dwarf stars. A&A, 410:527–551, November 2003. doi:10.1051/0004-6361:20031213.

M. Bergemann. Ionization balance of Ti in the photospheres of the Sun and four late-type stars. MNRAS, 413(3):2184–2198, May 2011. doi:10.1111/j.1365-2966.2011.18295.x.

P. F. Bernath. MoLLIST: Molecular Line Lists, Intensities and Spectra. J. Quant. Spec. Radiat. Transf., 240:106687, January 2020. doi:10.1016/j.jqsrt.2019.106687.

W. M. J. Best, T. J. Dupuy, M. C. Liu, R. J. Siverd, and Z. Zhang. The UltracoolSheet, November 2020.

H. A. Bethe. Energy Production in Stars. *Physical Review*, 55(5):434–456, March 1939. doi:10.1103/PhysRev.55.434.

M. V. Beznogov, D. Page, and E. Ramirez-Ruiz. Thermal Evolution of Neo-neutron Stars. I. Envelopes, Eddington Luminosity Phase, and Implications for GW170817. ApJ, 888(2):97, January 2020. doi:10.3847/1538-4357/ab5fd6.

P. Bianchini, R. Ibata, and B. Famaey. Exploring the Outskirts of Globular Clusters: The Peculiar Kinematics of NGC 3201. ApJ, 887(1):L12, December 2019. doi:10.3847/2041-8213/ab58d1.

J. Birky, D. W. Hogg, A. W. Mann, and A. Burgasser. Temperatures and Metallicities of M Dwarfs in the APOGEE Survey. ApJ, 892(1):31, March 2020. doi:10.3847/1538-4357/ab7004.

M. R. Blanton and S. Roweis. K-Corrections and Filter Transformations in the Ultraviolet, Optical, and Near-Infrared. AJ, 133(2):734–754, February 2007. doi:10.1086/510127.

R. C. Bohlin and R. L. Gilliland. Hubble Space Telescope Absolute Spectrophotometry of Vega from the Far-Ultraviolet to the Infrared. AJ, 127(6):3508–3515, June 2004. doi:10.1086/420715.

R. C. Bohlin, K. D. Gordon, and P. E. Tremblay. Techniques and Review of Absolute Flux Calibration from the Ultraviolet to the Mid-Infrared. PASP, 126(942):711, August 2014. doi:10.1086/677655.

E. Böhm-Vitense. Über die Wasserstoffkonvektionszone in Sternen verschiedener Effektivtemperaturen und Leuchtkräfte. Mit 5 Textabbildungen. *Zeitschrift für Astrophysik*, 46:108, Jan 1958.

E. Böhm-Vitense. An Integral Equation for the Temperature Correction in a Nongray Atmosphere. *SAO Special Report*, 167:99, December 1964.

E. Bolmont, F. Selsis, J. E. Owen, I. Ribas, S. N. Raymond, J. Leconte, and M. Gillon. Water loss from terrestrial planets orbiting ultracool dwarfs: implications for the planets of TRAPPIST-1. MNRAS, 464(3):3728–3741, January 2017. doi:10.1093/mnras/stw2578.

H. E. Bond. A Search for Metal-Deficient Stars. ApJS, 22:117, September 1970. doi:10.1086/190220.

H. Bondi. On spherically symmetrical accretion. MNRAS, 112:195, January 1952. doi:10.1093/mnras/112.2.195.

A. I. Boothroyd and I. J. Sackmann. Our Sun. IV. The Standard Model and Helioseismology: Consequences of Uncertainties in Input Physics and in Observed Solar Parameters. ApJ, 583 (2):1004–1023, February 2003. doi:10.1086/345407.

P. G. Breen. Light element variations in globular clusters via nucleosynthesis in black hole accretion discs. MNRAS, 481(1):L110–L114, November 2018. doi:10.1093/mnrasl/sly169.

M. M. Briley, V. V. Smith, N. B. Suntzeff, D. L. Lambert, R. A. Bell, and J. E. Hesser. Sodium abundance variations in main-sequence stars of the globular cluster 47 Tucanae. Nature, 383 (6601):604–606, October 1996. doi:10.1038/383604a0.

V. Bromm, A. Ferrara, P. S. Coppi, and R. B. Larson. The fragmentation of pre-enriched primordial objects. MNRAS, 328(3):969–976, December 2001a. doi:10.1046/j.1365-8711.2001.04915.x.

V. Bromm and C. J. Clarke. The Formation of the First Globular Clusters in Dwarf Galaxies before the Epoch of Reionization. ApJ, 566(1):L1–L4, February 2002. doi:10.1086/339440.

V. Bromm, R. P. Kudritzki, and A. Loeb. Generic Spectrum and Ionization Efficiency of a Heavy Initial Mass Function for the First Stars. ApJ, 552(2):464–472, May 2001b. doi:10.1086/320549.

V. Bromm, P. S. Coppi, and R. B. Larson. The Formation of the First Stars. I. The Primordial Star-forming Cloud. ApJ, 564(1):23–51, January 2002. doi:10.1086/323947.

V. Bromm, N. Yoshida, L. Hernquist, and C. F. McKee. The formation of the first stars and galaxies. Nature, 459(7243):49–54, May 2009. doi:10.1038/nature07990.

L. R. Brown. Empirical line parameters of methane from 1.1 to 2.1 μm. J. Quant. Spec. Radiat. Transf., 96(2):251–270, December 2005. doi:10.1016/j.jqsrt.2004.12.037.

S. T. Brown, P. Buitrago, E. Hanna, S. Sanielevici, R. Scibek, and N. A. Nystrom. Bridges-2: A platform for rapidly-evolving and data intensive research. In *Practice and Experience in Advanced Research Computing*. ACM, July 2021. doi:10.1145/3437359.3465593. URL https://doi.org/10.1145/3437359.3465593.

R. M. Brugger. A note on unbiased estimation of the standard deviation. *The American Statistician*, 23(4):32–32, 1969. doi:10.1080/00031305.1969.10481865. URL https://www.tandfonline.com/doi/epdf/10.1080/00031305.1969.10481865.

J. S. Bullock and K. V. Johnston. Tracing Galaxy Formation with Stellar Halos. I. Methods. ApJ, 635(2):931–949, December 2005. doi:10.1086/497422.

E. M. Burbidge, G. R. Burbidge, W. A. Fowler, and F. Hoyle. Synthesis of the Elements in Stars. *Reviews of Modern Physics*, 29(4):547–650, January 1957. doi:10.1103/RevModPhys.29.547.

A. J. Burgasser, I. N. Reid, N. Siegler, L. Close, P. Allen, P. Lowrance, and J. Gizis. Not Alone: Tracing the Origins of Very-Low-Mass Stars and Brown Dwarfs Through Multiplicity Studies. In B. Reipurth, D. Jewitt, and K. Keil, editors, *Protostars and Planets V*, page 427, January 2007a.

A. J. Burgasser. T Dwarfs and the Substellar Mass Function. I. Monte Carlo Simulations. ApJS, 155(1):191–207, November 2004. doi:10.1086/424386.

A. J. Burgasser. Brown dwarfs as Galactic chronometers. In E. E. Mamajek, D. R. Soderblom, and R. F. G. Wyse, editors, *The Ages of Stars*, volume 258, pages 317–326, June 2009. doi:10.1017/S1743921309031974.

A. J. Burgasser. The SpeX Prism Library: 1000+ low-resolution, near-infrared spectra of ultracool M, L, T and Y dwarfs. In *ASI Conf*, volume 11, pages 7–16, January 2014. doi:10.48550/arXiv.1406.4887.

A. J. Burgasser, M. S. Marley, A. S. Ackerman, D. Saumon, K. Lodders, C. C. Dahn, H. C. Harris, and J. D. Kirkpatrick. Evidence of Cloud Disruption in the L/T Dwarf Transition. ApJ, 571(2): L151–L154, June 2002. doi:10.1086/341343.

A. J. Burgasser, J. D. Kirkpatrick, A. Burrows, J. Liebert, I. N. Reid, J. E. Gizis, M. R. McGovern, L. Prato, and I. S. McLean. The First Substellar Subdwarf? Discovery of a Metal-poor L Dwarf with Halo Kinematics. ApJ, 592(2):1186–1192, August 2003. doi:10.1086/375813.

A. J. Burgasser, J. D. Kirkpatrick, K. L. Cruz, I. N. Reid, S. K. Leggett, J. Liebert, A. Burrows, and M. E. Brown. Hubble Space Telescope NICMOS Observations of T Dwarfs: Brown Dwarf Multiplicity and New Probes of the L/T Transition. ApJS, 166(2):585–612, October 2006. doi:10.1086/506327.

A. J. Burgasser, K. L. Cruz, and J. D. Kirkpatrick. Optical Spectroscopy of 2MASS Color-selected Ultracool Subdwarfs. ApJ, 657(1):494–510, March 2007b. doi:10.1086/510148.

A. J. Burgasser, D. L. Looper, J. D. Kirkpatrick, K. L. Cruz, and B. J. Swift. Clouds, Gravity, and Metallicity in Blue L Dwarfs: The Case of 2MASS J11263991-5003550. ApJ, 674(1): 451–465, February 2008. doi:10.1086/524726.

C. J. Burke, M. H. Pinsonneault, and A. Sills. Theoretical Examination of the Lithium Depletion Boundary. ApJ, 604(1):272–283, March 2004. doi:10.1086/381242.

A. Burrows and J. Liebert. The science of brown dwarfs. *Reviews of Modern Physics*, 65(2): 301–336, April 1993. doi:10.1103/RevModPhys.65.301.

A. Burrows, W. B. Hubbard, and J. I. Lunine. Theoretical Models of Very Low Mass Stars and Brown Dwarfs. ApJ, 345:939, October 1989. doi:10.1086/167964.

A. Burrows, K. Heng, and T. Nampaisarn. The Dependence of Brown Dwarf Radii on Atmospheric Metallicity and Clouds: Theory and Comparison with Observations. ApJ, 736(1):47, July 2011. doi:10.1088/0004-637X/736/1/47.

E. Caffau, R. Faraggiana, H. G. Ludwig, P. Bonifacio, and M. Steffen. The solar photospheric abundance of zirconium. *Astronomische Nachrichten*, 332(2):128, February 2011a. doi:10.1002/asna.201011485.

E. Caffau, H. G. Ludwig, M. Steffen, B. Freytag, and P. Bonifacio. Solar Chemical Abundances Determined with a CO5BOLD 3D Model Atmosphere. Sol. Phys., 268(2):255–269, February 2011b. doi:10.1007/s11207-010-9541-4.

I. Caiazzo, J. S. Heyl, H. Richer, and J. Kalirai. Globular cluster absolute ages from cooling brown dwarfs. *arXiv e-prints*, art. arXiv:1702.00091, January 2017.

I. Caiazzo, A. Burgasser, J. M. Rees, F. Allard, A. Dieball, J. Heyl, H. Richer, I. Baraffe, and C. Knigge. Hunting for ancient brown dwarfs: the developing field of brown dwarfs in globular clusters. BAAS, 51(3):521, May 2019.

I. Caiazzo, H. B. Richer, A. C. Boley, A. J. Burgasser, M. Correnti, A. Dieball, R. Gerasimov, J. Heyl, J. Parada, and P.-E. Tremblay. Brown Dwarfs, White Dwarfs and Planetary Disks in an Ancient Stellar System. JWST Proposal. Cycle 1, March 2021.

A. Calamida, P. B. Stetson, G. Bono, L. M. Freyhammer, F. Grundahl, M. Hilker, M. I. Andersen, R. Buonanno, S. Cassisi, C. E. Corsi, M. Dall'Ora, M. Del Principe, I. Ferraro, M. Monelli, A. Munteanu, M. Nonino, A. M. Piersimoni, A. Pietrinferni, L. Pulone, and T. Richtler. Reddening Distribution across the Center of the Globular Cluster ω Centauri. ApJ, 634(1): L69–L72, November 2005. doi:10.1086/498691.

A. Calamida, K. C. Sahu, S. Casertano, J. Anderson, S. Cassisi, M. Gennaro, M. Cignoni, T. M. Brown, N. Kains, H. Ferguson, M. Livio, H. E. Bond, R. Buonanno, W. Clarkson, I. Ferraro, A. Pietrinferni, M. Salaris, and J. Valenti. New Insights on the Galactic Bulge Initial Mass Function. ApJ, 810(1):8, September 2015. doi:10.1088/0004-637X/810/1/8.

D. F. Carbon. *Line blanketing.*, pages 395–426. Cambridge University Press, 1984.

J. M. Carpenter, E. E. Mamajek, L. A. Hillenbrand, and M. R. Meyer. Evidence for Mass-dependent Circumstellar Disk Evolution in the 5 Myr Old Upper Scorpius OB Association. ApJ, 651(1):L49–L52, November 2006. doi:10.1086/509121.

E. Carretta, A. Bragaglia, R. G. Gratton, A. Recio-Blanco, S. Lucatello, V. D'Orazi, and S. Cassisi. Properties of stellar generations in globular clusters and relations with global parameters. A&A, 516:A55, June 2010. doi:10.1051/0004-6361/200913451.

E. Carretta, R. G. Gratton, G. Clementini, and F. Fusi Pecci. Distances, Ages, and Epoch of Formation of Globular Clusters. ApJ, 533(1):215–235, April 2000. doi:10.1086/308629.

L. Casagrande, I. Ramírez, J. Meléndez, M. Bessell, and M. Asplund. An absolutely calibrated T_{eff} scale from the infrared flux method. Dwarfs and subgiants. A&A, 512:A54, March 2010. doi:10.1051/0004-6361/200913204.

S. Cassisi, M. Salaris, A. Pietrinferni, G. Piotto, A. P. Milone, L. R. Bedin, and J. Anderson. The Double Subgiant Branch of NGC 1851: The Role of the CNO Abundance. ApJ, 672(2):L115, January 2008. doi:10.1086/527035.

S. Cassisi. Very Low-Mass Stars: structural and evolutionary properties. *arXiv e-prints*, art. arXiv:1111.6464, November 2011.

S. Cassisi, M. Salaris, J. Anderson, G. Piotto, A. Pietrinferni, A. Milone, A. Bellini, and L. R. Bedin. Hot Horizontal Branch Stars in ω Centauri: Clues about their Origin from the Cluster Color Magnitude Diagram. ApJ, 702(2):1530–1535, September 2009. doi:10.1088/0004-637X/702/2/1530.

F. Castelli. ATLAS12: how to use it. *Memorie della Societa Astronomica Italiana Supplementi*, 8:25, Jan 2005a.

F. Castelli. DFSYNTHE: how to use it. *Memorie della Societa Astronomica Italiana Supplementi*, 8:34, January 2005b.

F. Castelli and R. L. Kurucz. New Grids of ATLAS9 Model Atmospheres. In N. Piskunov, W. W. Weiss, and D. F. Gray, editors, *Modelling of Stellar Atmospheres*, volume 210, page A20, January 2003.

R. Cen. Synchronized Formation of Subgalactic Systems at Cosmological Reionization: Origin of Halo Globular Clusters. ApJ, 560(2):592–598, October 2001. doi:10.1086/323071.

R. Cen. The Implications of Wilkinson Microwave Anisotropy Probe Observations for Population III Star Formation Processes. ApJ, 591(1):L5–L8, July 2003a. doi:10.1086/377068.

R. Cen. The Universe Was Reionized Twice. ApJ, 591(1):12–37, July 2003b. doi:10.1086/375217.

G. Chabrier and M. Küker. Large-scale $\alpha\hat{2}$-dynamo in low-mass stars and brown dwarfs. A&A, 446(3):1027–1037, February 2006. doi:10.1051/0004-6361:20042475.

G. Chabrier and I. Baraffe. Structure and evolution of low-mass stars. A&A, 327:1039–1053, November 1997. doi:10.48550/arXiv.astro-ph/9704118.

G. Chabrier and I. Baraffe. Theory of Low-Mass Stars and Substellar Objects. ARA&A, 38: 337–377, January 2000. doi:10.1146/annurev.astro.38.1.337.

J. W. Chamberlain and L. H. Aller. The Atmospheres of A-Type Subdwarfs and 95 Leonis. ApJ, 114:52, July 1951. doi:10.1086/145451.

K. C. Chambers, E. A. Magnier, N. Metcalfe, H. A. Flewelling, M. E. Huber, C. Z. Waters, L. Denneau, P. W. Draper, D. Farrow, D. P. Finkbeiner, C. Holmberg, J. Koppenhoefer, P. A. Price, A. Rest, R. P. Saglia, E. F. Schlafly, S. J. Smartt, W. Sweeney, R. J. Wainscoat, W. S. Burgett, S. Chastel, T. Grav, J. N. Heasley, K. W. Hodapp, R. Jedicke, N. Kaiser, R. P. Kudritzki, G. A. Luppino, R. H. Lupton, D. G. Monet, J. S. Morgan, P. M. Onaka, B. Shiao, C. W. Stubbs, J. L. Tonry, R. White, E. Bañados, E. F. Bell, R. Bender, E. J. Bernard, M. Boegner, F. Boffi, M. T. Botticella, A. Calamida, S. Casertano, W. P. Chen, X. Chen, S. Cole, N. Deacon, C. Frenk, A. Fitzsimmons, S. Gezari, V. Gibbs, C. Goessl, T. Goggia, R. Gourgue, B. Goldman, P. Grant, E. K. Grebel, N. C. Hambly, G. Hasinger, A. F. Heavens, T. M. Heckman, R. Henderson, T. Henning, M. Holman, U. Hopp, W. H. Ip, S. Isani, M. Jackson, C. D. Keyes, A. M. Koekemoer, R. Kotak, D. Le, D. Liska, K. S. Long, J. R. Lucey, M. Liu, N. F. Martin, G. Masci, B. McLean, E. Mindel, P. Misra, E. Morganson, D. N. A. Murphy, A. Obaika, G. Narayan, M. A. Nieto-Santisteban, P. Norberg, J. A. Peacock, E. A. Pier, M. Postman, N. Primak, C. Rae, A. Rai, A. Riess, A. Riffeser, H. W. Rix, S. Röser, R. Russel, L. Rutz, E. Schilbach, A. S. B. Schultz, D. Scolnic, L. Strolger, A. Szalay, S. Seitz, E. Small, K. W. Smith, D. R. Soderblom, P. Taylor, R. Thomson, A. N. Taylor, A. R. Thakar, J. Thiel, D. Thilker, D. Unger, Y. Urata, J. Valenti, J. Wagner, T. Walder, F. Walter, S. P. Watters, S. Werner, W. M. Wood-Vasey, and R. Wyse. The Pan-STARRS1 Surveys. *arXiv*, art. arXiv:1612.05560, December 2016. doi:10.48550/arXiv.1612.05560.

S. Chen, H. Richer, I. Caiazzo, and J. Heyl. Distances to the Globular Clusters 47 Tucanae and NGC 362 Using Gaia DR2 Parallaxes. ApJ, 867(2):132, November 2018. doi:10.3847/1538-4357/aae089.

W. Chen, P. L. Kelly, T. Treu, X. Wang, G. Roberts-Borsani, A. Keen, R. A. Windhorst, R. Zhou, M. Bradac, G. Brammer, V. Strait, T. J. Broadhurst, J. M. Diego, B. L. Frye, A. K. Meena, A. Zitrin, M. Pascale, M. Castellano, D. Marchesini, T. Morishita, and L. Yang. Early results from GLASS-JWST VIII: An Extremely Magnified Blue Supergiant Star at Redshift 2.65 in the Abell 2744 Cluster Field. *arXiv e-prints*, art. arXiv:2207.11658, July 2022.

J. Choi, A. Dotter, C. Conroy, M. Cantiello, B. Paxton, and B. D. Johnson. Mesa Isochrones and Stellar Tracks (MIST). I. Solar-scaled Models. *The Astrophysical Journal*, 823(2):102, Jun 2016. doi:10.3847/0004-637X/823/2/102.

J. Christensen-Dalsgaard. The 'Standard' Sun Modelling and Helioseismology. Space Sci. Rev., 85:19–36, May 1998. doi:10.1023/A:1005116132024.

P. C. Clark, S. C. O. Glover, and R. S. Klessen. The First Stellar Cluster. ApJ, 672(2):757–764, January 2008. doi:10.1086/524187.

P. C. Clark, S. C. O. Glover, R. S. Klessen, and V. Bromm. Gravitational Fragmentation in Turbulent Primordial Gas and the Initial Mass Function of Population III Stars. ApJ, 727(2): 110, February 2011. doi:10.1088/0004-637X/727/2/110.

B. Coşkunoğlu, S. Ak, S. Bilir, S. Karaali, E. Yaz, G. Gilmore, G. M. Seabroke, O. Bienaymé, J. Bland-Hawthorn, R. Campbell, K. C. Freeman, B. Gibson, E. K. Grebel, U. Munari, J. F. Navarro, Q. A. Parker, A. Siebert, A. Siviero, M. Steinmetz, F. G. Watson, R. F. G. Wyse, and T. Zwitter. Local stellar kinematics from RAVE data - I. Local standard of rest. MNRAS, 412 (2):1237–1245, April 2011. doi:10.1111/j.1365-2966.2010.17983.x.

A. D. Code. The Energy Distribution of Subdwarfs. ApJ, 130:473, September 1959. doi:10.1086/146738.

P. Cojazzi, A. Bressan, F. Lucchin, O. Pantano, and M. Chavez. Zero-metallicity stellar sources and the reionization epoch. MNRAS, 315(4):L51–L55, July 2000. doi:10.1046/j.1365-8711.2000.03670.x.

C. Conroy and P. G. van Dokkum. The Stellar Initial Mass Function in Early-type Galaxies From Absorption Line Spectroscopy. II. Results. ApJ, 760(1):71, November 2012. doi:10.1088/0004-637X/760/1/71.

H. Copeland, J. O. Jensen, and H. E. Jorgensen. Homogeneous Models for Population I and Population II Compositions. A&A, 5:12, March 1970.

M. J. Cordero, C. A. Pilachowski, C. I. Johnson, I. McDonald, A. A. Zijlstra, and J. Simmerer. Detailed Abundances for a Large Sample of Giant Stars in the Globular Cluster 47 Tucanae (NGC 104). ApJ, 780(1):94, January 2014. doi:10.1088/0004-637X/780/1/94.

P. L. Cottrell and G. S. Da Costa. Correlated cyanogen and sodium anomalies in the globular clusters 47 TUC and NGC 6752. ApJ, 245:L79–L82, April 1981. doi:10.1086/183527.

N. H. M. Crighton, J. M. O'Meara, and M. T. Murphy. Possible Population III remnants at redshift 3.5. MNRAS, 457(1):L44–L48, March 2016. doi:10.1093/mnrasl/slv191.

D. A. Crocker, R. T. Rood, and R. W. O'Connell. Multiple Populations on the Horizontal Branch. I. Observations in the (log g, log T eff)–Diagram. ApJ, 332:236, September 1988. doi:10.1086/166648.

R. H. Cyburt, B. D. Fields, and K. A. Olive. An update on the big bang nucleosynthesis prediction for ^{7}Li: the problem worsens. J. Cosm. Astropart. Phys., 2008(11):012, November 2008. doi:10.1088/1475-7516/2008/11/012.

G. S. Da Costa and P. Demarque. Nitrogen variations on the main sequence of 47 Tucanae - Implications from stellar structure theory. ApJ, 259:193–197, August 1982. doi:10.1086/160159.

N. de Lacaille. Sur les étoiles nébuleuses du ciel austral. *Mémoires de l'Académie Royale des Sciences*, pages 194–199, 1755. URL `http://www.messier.seds.org/xtra/history/lac1755.html`.

J. R. de Medeiros, J. R. P. Silva, J. Do Nascimento, J. D., B. L. Canto Martins, L. da Silva, C. Melo, and M. Burnet. A catalog of rotational and radial velocities for evolved stars. IV. Metal-poor stars. A&A, 458(3):895–898, November 2006. doi:10.1051/0004-6361:20065642.

S. E. de Mink, O. R. Pols, N. Langer, and R. G. Izzard. Massive binaries as the source of abundance anomalies in globular clusters. A&A, 507(1):L1–L4, November 2009. doi:10.1051/0004-6361/200913205.

G. M. de Silva, B. K. Gibson, J. Lattanzio, and M. Asplund. On and Na abundance patterns in open clusters of the Galactic disk. A&A, 500(2):L25–L28, June 2009. doi:10.1051/0004-6361/200912279.

T. Decressin, C. Charbonnel, and G. Meynet. Origin of the abundance patterns in Galactic globular clusters: constraints on dynamical and chemical properties of globular clusters. A&A, 475(3):859–873, December 2007a. doi:10.1051/0004-6361:20078425.

T. Decressin, G. Meynet, C. Charbonnel, N. Prantzos, and S. Ekström. Fast rotating massive stars and the origin of the abundance patterns in galactic globular clusters. A&A, 464(3):1029–1044, March 2007b. doi:10.1051/0004-6361:20066013.

O. Demircan and G. Kahraman. Stellar Mass / Luminosity and Mass / Radius Relations. Ap&SS, 181(2):313–322, July 1991. doi:10.1007/BF00639097.

P. A. Denissenkov and F. D. A. Hartwick. Supermassive stars as a source of abundance anomalies of proton-capture elements in globular clusters. MNRAS, 437(1):L21–L25, January 2014. doi:10.1093/mnrasl/slt133.

A. D'Ercole, F. D'Antona, and E. Vesperini. Accretion of pristine gas and dilution during the formation of multiple-population globular clusters. MNRAS, 461(4):4088–4098, October 2016. doi:10.1093/mnras/stw1583.

A. D'Ercole, E. Vesperini, F. D'Antona, S. L. W. McMillan, and S. Recchi. Formation and dynamical evolution of multiple stellar generations in globular clusters. MNRAS, 391(2): 825–843, December 2008. doi:10.1111/j.1365-2966.2008.13915.x.

A. D'Ercole, F. D'Antona, and E. Vesperini. Formation of multiple populations in globular clusters: constraints on the dilution by pristine gas. MNRAS, 415(2):1304–1309, August 2011. doi:10.1111/j.1365-2966.2011.18776.x.

A. L. DeSouza and S. Basu. The luminosity of Population III star clusters. MNRAS, 450(1): 295–304, June 2015. doi:10.1093/mnras/stv523.

R. J. Dickens and R. A. Bell. Enhanced abundances of nitrogen and s-process elements in red giant stars in Omega Centauri. ApJ, 207:506–517, July 1976. doi:10.1086/154518.

R. J. Dickens, B. F. W. Croke, R. D. Cannon, and R. A. Bell. Evidence from stellar abundances for a large age difference between two globular clusters. Nature, 351(6323):212–214, May 1991. doi:10.1038/351212a0.

A. Dieball, L. R. Bedin, C. Knigge, M. Geffert, R. M. Rich, A. Dotter, H. Richer, and D. Zurek. Hunting for brown dwarfs in the globular cluster M4: second epoch HST NIR observations. MNRAS, 486(2):2254–2264, June 2019. doi:10.1093/mnras/stz996.

A. Dieball, F. Allard, L. R. Bedin, A. L. Dotter, C. Knigge, R. M. Rich, H. B. Richer, and D. R. Zurek. Hunting for Brown Dwarfs in Globular Clusters: Second Epoch Deep IR observations of the Globular Clusters M4. HST Proposal, June 2016.

J. M. Diego. The Universe at extreme magnification. A&A, 625:A84, May 2019. doi:10.1051/0004-6361/201833670.

J. M. Diego, N. Kaiser, T. Broadhurst, P. L. Kelly, S. Rodney, T. Morishita, M. Oguri, T. W. Ross, A. Zitrin, M. Jauzac, J. Richard, L. Williams, J. Vega-Ferrero, B. Frye, and A. V. Filippenko. Dark Matter under the Microscope: Constraining Compact Dark Matter with Caustic Crossing Events. ApJ, 857(1):25, April 2018. doi:10.3847/1538-4357/aab617.

M. Dijkstra, Z. Haiman, M. J. Rees, and D. H. Weinberg. Photoionization Feedback in Low-Mass Galaxies at High Redshift. ApJ, 601(2):666–675, February 2004. doi:10.1086/380603.

S. Dodelson. *Modern Cosmology*. Academic Press, 2003.

J. E. Doppel, L. V. Sales, J. F. Navarro, M. G. Abadi, E. W. Peng, E. Toloba, and F. Ramos-Almendares. Globular clusters as tracers of the dark matter content of dwarfs in galaxy clusters. MNRAS, 502(2):1661–1677, April 2021. doi:10.1093/mnras/staa3915.

B. Dorman, L. A. Nelson, and W. Y. Chau. Theoretical Models of Low-Mass Stars and Brown Dwarfs. I. The Lower Main Sequence. ApJ, 342:1003, July 1989. doi:10.1086/167658.

A. Dotter. The Second Parameter Problem(s). Mem. Soc. Astron. Italiana, 84:97, January 2013. doi:10.48550/arXiv.1307.5589.

A. Dotter, B. Chaboyer, D. Jevremović, V. Kostov, E. Baron, and J. W. Ferguson. The Dartmouth Stellar Evolution Database. ApJS, 178(1):89–101, September 2008. doi:10.1086/589654.

A. Dotter, J. W. Ferguson, C. Conroy, A. P. Milone, A. F. Marino, and D. Yong. Stellar models of multiple populations in globular clusters - I. The main sequence of NGC 6752. MNRAS, 446 (2):1641–1656, January 2015. doi:10.1093/mnras/stu2170.

L. Dressel. Wide Field Camera 3 Instrument Handbook for Cycle 21 v. 5.0. In *Wide Field Camera 3*, page 5. Space Telescope Science Institute, 2012.

R. D'Souza and H.-W. Rix. Mass estimates from stellar proper motions: the mass of ω Centauri. MNRAS, 429(3):1887–1901, March 2013. doi:10.1093/mnras/sts426.

J. Dunlop. A Catalogue of Nebulae and Clusters of Stars in the Southern Hemisphere, Observed at Paramatta in New South Wales. *Philosophical Transactions of the Royal Society of London Series I*, 118:113–151, January 1828.

A. S. Eddington. On the Conditions in the Interior of a Star. ApJ, 48:205, November 1918. doi:10.1086/142427.

R. A. W. Elson, G. F. Gilmore, B. X. Santiago, and S. Casertano. HST Observations of the Stellar Population of the Globular Cluster W CEN. AJ, 110:682, August 1995. doi:10.1086/117553.

ESA. The HIPPARCOS and TYCHO catalogues. Astrometric and photometric star catalogues derived from the ESA HIPPARCOS Space Astrometry Mission. In *ESA Special Publication*, volume 1200 of *ESA Special Publication*, January 1997.

J. K. Faherty, A. R. Riedel, K. L. Cruz, J. Gagne, J. C. Filippazzo, E. Lambrides, H. Fica, A. Weinberger, J. R. Thorstensen, C. G. Tinney, V. Baldassare, E. Lemonier, and E. L. Rice. Population Properties of Brown Dwarf Analogs to Exoplanets. ApJS, 225(1):10, July 2016. doi:10.3847/0067-0049/225/1/10.

S. M. Fall and M. J. Rees. Survival and disruption of galactic substructure. MNRAS, 181: 37P–42P, November 1977. doi:10.1093/mnras/181.1.37P.

S. M. Fall and Q. Zhang. Dynamical Evolution of the Mass Function of Globular Star Clusters. ApJ, 561(2):751–765, November 2001. doi:10.1086/323358.

J. W. Ferguson, D. R. Alexander, F. Allard, T. Barman, J. G. Bodnarik, P. H. Hauschildt, A. Heffner-Wong, and A. Tamanai. Low-Temperature Opacities. ApJ, 623(1):585–596, April 2005. doi:10.1086/428642.

E. L. Fitzpatrick and D. Massa. An Analysis of the Shapes of Interstellar Extinction Curves. V. The IR-through-UV Curve Morphology. ApJ, 663(1):320–341, July 2007. doi:10.1086/518158.

D. J. Fixsen. The Temperature of the Cosmic Microwave Background. ApJ, 707(2):916–920, December 2009. doi:10.1088/0004-637X/707/2/916.

C. Fontanive, B. Biller, M. Bonavita, and K. Allers. Constraining the multiplicity statistics of the coolest brown dwarfs: binary fraction continues to decrease with spectral type. MNRAS, 479 (2):2702–2727, September 2018. doi:10.1093/mnras/sty1682.

D. A. Forbes, N. Bastian, M. Gieles, R. A. Crain, J. M. D. Kruijssen, S. S. Larsen, S. Ploeckinger, O. Agertz, M. Trenti, A. M. N. Ferguson, J. Pfeffer, and O. Y. Gnedin. Globular cluster formation and evolution in the context of cosmological galaxy assembly: open questions. *Proceedings of the Royal Society of London Series A*, 474(2210):20170616, February 2018. doi:10.1098/rspa.2017.0616.

N. M. Förster Schreiber and S. Wuyts. Star-Forming Galaxies at Cosmic Noon. ARA&A, 58: 661–725, August 2020. doi:10.1146/annurev-astro-032620-021910.

R. A. E. Fosbury, M. Villar-Martín, A. Humphrey, M. Lombardi, P. Rosati, D. Stern, R. N. Hook, B. P. Holden, S. A. Stanford, G. K. Squires, M. Rauch, and W. L. W. Sargent. Massive Star Formation in a Gravitationally Lensed H II Galaxy at z = 3.357. ApJ, 596(2):797–809, October 2003. doi:10.1086/378228.

A. Frebel, E. N. Kirby, and J. D. Simon. Linking dwarf galaxies to halo building blocks with the most metal-poor star in Sculptor. Nature, 464(7285):72–75, March 2010. doi:10.1038/nature08772.

K. C. Freeman and A. W. Rodgers. The Chemical Inhomogeneity of Omega Centauri. ApJ, 201: L71, October 1975. doi:10.1086/181945.

K. Freeman and J. Bland-Hawthorn. The New Galaxy: Signatures of Its Formation. ARA&A, 40: 487–537, January 2002. doi:10.1146/annurev.astro.40.060401.093840.

J. Fried and S. Zietz. Curve fitting by spline and akima methods: possibility of interpolation error and its suppression. *Physics in Medicine and Biology*, 18(4):550–558, July 1973. doi:10.1088/0031-9155/18/4/306.

X. Fu, A. Bressan, P. Molaro, and P. Marigo. Lithium evolution in metal-poor stars: from pre-main sequence to the Spite plateau. MNRAS, 452(3):3256–3265, September 2015. doi:10.1093/mnras/stv1384.

G. M. Fuller, S. E. Woosley, and T. A. Weaver. The Evolution of Radiation-dominated Stars. I. Nonrotating Supermassive Stars. ApJ, 307:675, August 1986. doi:10.1086/164452.

Gaia Collaboration, A. G. A. Brown, A. Vallenari, T. Prusti, J. H. J. de Bruijne, C. Babusiaux, M. Biermann, O. L. Creevey, D. W. Evans, L. Eyer, A. Hutton, F. Jansen, C. Jordi, S. A. Klioner, U. Lammers, L. Lindegren, X. Luri, F. Mignard, C. Panem, D. Pourbaix, S. Randich, P. Sartoretti, C. Soubiran, N. A. Walton, F. Arenou, C. A. L. Bailer-Jones, U. Bastian, M. Cropper, R. Drimmel, D. Katz, M. G. Lattanzi, F. van Leeuwen, J. Bakker, C. Cacciari, J. Castañeda, F. De Angeli, C. Ducourant, C. Fabricius, M. Fouesneau, Y. Frémat, R. Guerra, A. Guerrier, J. Guiraud, A. Jean-Antoine Piccolo, E. Masana, R. Messineo, N. Mowlavi, C. Nicolas, K. Nienartowicz, F. Pailler, P. Panuzzo, F. Riclet, W. Roux, G. M. Seabroke, R. Sordo, P. Tanga, F. Thévenin, G. Gracia-Abril, J. Portell, D. Teyssier, M. Altmann, R. Andrae, I. Bellas-Velidis, K. Benson, J. Berthier, R. Blomme, E. Brugaletta, P. W. Burgess, G. Busso, B. Carry, A. Cellino, N. Cheek, G. Clementini, Y. Damerdji, M. Davidson, L. Delchambre, A. Dell'Oro, J. Fernández-Hernández, L. Galluccio, P. García-Lario, M. Garcia-Reinaldos, J. González-Núñez, E. Gosset, R. Haigron, J. L. Halbwachs, N. C. Hambly, D. L. Harrison, D. Hatzidimitriou, U. Heiter, J. Hernández, D. Hestroffer, S. T. Hodgkin, B. Holl, K. Janßen, G. Jevardat de Fombelle, S. Jordan, A. Krone-Martins, A. C. Lanzafame, W. Löffler, A. Lorca, M. Manteiga, O. Marchal, P. M. Marrese, A. Moitinho, A. Mora, K. Muinonen, P. Osborne, E. Pancino, T. Pauwels, J. M. Petit, A. Recio-Blanco, P. J. Richards, M. Riello, L. Rimoldini, A. C. Robin, T. Roegiers, J. Rybizki, L. M. Sarro, C. Siopis, M. Smith, A. Sozzetti, A. Ulla, E. Utrilla, M. van Leeuwen, W. van Reeven, U. Abbas, A. Abreu Aramburu, S. Accart, C. Aerts, J. J. Aguado, M. Ajaj, G. Altavilla, M. A. Álvarez, J. Álvarez Cid-Fuentes, J. Alves, R. I. Anderson, E. Anglada Varela, T. Antoja, M. Audard, D. Baines, S. G. Baker, L. Balaguer-Núñez, E. Balbinot, Z. Balog, C. Barache, D. Barbato, M. Barros, M. A. Barstow, S. Bartolomé, J. L. Bassilana, N. Bauchet, A. Baudesson-Stella, U. Becciani, M. Bellazzini, M. Bernet, S. Bertone, L. Bianchi, S. Blanco-Cuaresma, T. Boch, A. Bombrun, D. Bossini, S. Bouquillon, A. Bragaglia, L. Bramante, E. Breedt, A. Bressan, N. Brouillet, B. Bucciarelli, A. Burlacu, D. Busonero, A. G. Butkevich, R. Buzzi, E. Caffau, R. Cancelliere, H. Cánovas, T. Cantat-Gaudin, R. Carballo, T. Carlucci, M. I. Carnerero, J. M. Carrasco, L. Casamiquela, M. Castellani, A. Castro-Ginard, P. Castro Sampol, L. Chaoul, P. Charlot, L. Chemin, A. Chiavassa, M. R. L. Cioni, G. Comoretto, W. J. Cooper, T. Cornez, S. Cowell, F. Crifo, M. Crosta, C. Crowley, C. Dafonte, A. Dapergolas, M. David, P. David, P. de Laverny, F. De Luise, R. De March, J. De Ridder, R. de Souza, P. de Teodoro, A. de Torres, E. F. del Peloso, E. del Pozo, M. Delbo, A. Delgado, H. E. Delgado, J. B. Delisle, P. Di Matteo, S. Diakite, C. Diener, E. Distefano, C. Dolding, D. Eappachen, B. Edvardsson, H. Enke, P. Esquej, C. Fabre, M. Fabrizio, S. Faigler, G. Fedorets, P. Fernique, A. Fienga, F. Figueras, C. Fouron, F. Fragkoudi, E. Fraile, F. Franke, M. Gai, D. Garabato, A. Garcia-Gutierrez, M. García-Torres, A. Garofalo, P. Gavras, E. Gerlach, R. Geyer, P. Giacobbe, G. Gilmore, S. Girona, G. Giuffrida, R. Gomel, A. Gomez, I. Gonzalez-Santamaria, J. J. González-Vidal, M. Granvik, R. Gutiérrez-Sánchez, L. P. Guy, M. Hauser, M. Haywood, A. Helmi, S. L. Hidalgo, T. Hilger, N. Hładczuk, D. Hobbs, G. Holland, H. E. Huckle, G. Jasniewicz, P. G. Jonker, J. Juaristi Campillo, F. Julbe, L. Karbevska, P. Kervella, S. Khanna, A. Kochoska, M. Kontizas, G. Kordopatis, A. J. Korn, Z. Kostrzewa-Rutkowska, K. Kruszyńska, S. Lambert, A. F. Lanza, Y. Lasne, J. F. Le Campion, Y. Le Fustec, Y. Lebreton, T. Lebzelter, S. Leccia, N. Leclerc, I. Lecoeur-Taibi, S. Liao, E. Licata, E. P. Lindstrøm, T. A. Lister, E. Livanou, A. Lobel, P. Madrero Pardo, S. Managau, R. G. Mann, J. M. Marchant,

M. Marconi, M. M. S. Marcos Santos, S. Marinoni, F. Marocco, D. J. Marshall, L. Martin Polo, J. M. Martín-Fleitas, A. Masip, D. Massari, A. Mastrobuono-Battisti, T. Mazeh, P. J. McMillan, S. Messina, D. Michalik, N. R. Millar, A. Mints, D. Molina, R. Molinaro, L. Molnár, P. Montegriffo, R. Mor, R. Morbidelli, T. Morel, D. Morris, A. F. Mulone, D. Munoz, T. Muraveva, C. P. Murphy, I. Musella, L. Noval, C. Ordénovic, G. Orrù, J. Osinde, C. Pagani, I. Pagano, L. Palaversa, P. A. Palicio, A. Panahi, M. Pawlak, X. Peñalosa Esteller, A. Penttilä, A. M. Piersimoni, F. X. Pineau, E. Plachy, G. Plum, E. Poggio, E. Poretti, E. Poujoulet, A. Prša, L. Pulone, E. Racero, S. Ragaini, M. Rainer, C. M. Raiteri, N. Rambaux, P. Ramos, M. Ramos-Lerate, P. Re Fiorentin, S. Regibo, C. Reylé, V. Ripepi, A. Riva, G. Rixon, N. Robichon, C. Robin, M. Roelens, L. Rohrbasser, M. Romero-Gómez, N. Rowell, F. Royer, K. A. Rybicki, G. Sadowski, A. Sagristà Sellés, J. Sahlmann, J. Salgado, E. Salguero, N. Samaras, V. Sanchez Gimenez, N. Sanna, R. Santoveña, M. Sarasso, M. Schultheis, E. Sciacca, M. Segol, J. C. Segovia, D. Ségransan, D. Semeux, S. Shahaf, H. I. Siddiqui, A. Siebert, L. Siltala, E. Slezak, R. L. Smart, E. Solano, F. Solitro, D. Souami, J. Souchay, A. Spagna, F. Spoto, I. A. Steele, H. Steidelmüller, C. A. Stephenson, M. Süveges, L. Szabados, E. Szegedi-Elek, F. Taris, G. Tauran, M. B. Taylor, R. Teixeira, W. Thuillot, N. Tonello, F. Torra, J. Torra, C. Turon, N. Unger, M. Vaillant, E. van Dillen, O. Vanel, A. Vecchiato, Y. Viala, D. Vicente, S. Voutsinas, M. Weiler, T. Wevers, Ł. Wyrzykowski, A. Yoldas, P. Yvard, H. Zhao, J. Zorec, S. Zucker, C. Zurbach, and T. Zwitter. Gaia Early Data Release 3. Summary of the contents and survey properties. A&A, 649:A1, May 2021. doi:10.1051/0004-6361/202039657.

G. Gamow. Mixed Types of Stellar Populations. Nature, 162(4125):816, November 1948. doi:10.1038/162816a0.

G. Gamow. Hydrogen Exhaustion and Explosions of Stars. Nature, 168(4263):72–73, July 1951. doi:10.1038/168072a0.

G. Gamow and G. Keller. A Shell Source Model for Red Giant Stars. *Reviews of Modern Physics*, 17(2-3):125–137, April 1945. doi:10.1103/RevModPhys.17.125.

R. Gerasimov, D. Homeier, A. Burgasser, and L. R. Bedin. A New Grid of Model Atmospheres for Metal-poor Ultracool Brown Dwarfs. *Research Notes of the American Astronomical Society*, 4(12):214, December 2020. doi:10.3847/2515-5172/abcf2c.

R. Gerasimov, A. J. Burgasser, D. Homeier, L. R. Bedin, M. Scalco, J. M. Rees, M. Salaris, and J. Anderson. Mass function and chemical abundances of the three distinct populations in the globular cluster NGC 6752. In *Cool Stars 21*, October 2022. doi:10.5281/zenodo.7217153.

H. Gerola, P. E. Seiden, and L. S. Schulman. Theory of dwarf galaxies. ApJ, 242:517–527, December 1980. doi:10.1086/158485.

M. Gieles, C. Charbonnel, M. G. H. Krause, V. Hénault-Brunet, O. Agertz, H. J. G. L. M. Lamers, N. Bastian, A. Gualandris, A. Zocchi, and J. A. Petts. Concurrent formation of supermassive stars and globular clusters: implications for early self-enrichment. MNRAS, 478(2):2461–2479, August 2018. doi:10.1093/mnras/sty1059.

M. Giersz and D. C. Heggie. A simple dynamical evolutionary model for ω Cen. MNRAS, 339 (2):486–490, February 2003. doi:10.1046/j.1365-8711.2003.06191.x.

A. Gimenez and J. Zamorano. The mass-radius relation in binary systems. Ap&SS, 114(2): 259–269, September 1985. doi:10.1007/BF00653969.

J. E. Gizis. M-Subdwarfs: Spectroscopic Classification and the Metallicity Scale. AJ, 113: 806–822, February 1997. doi:10.1086/118302.

O. Y. Gnedin and J. P. Ostriker. Destruction of the Galactic Globular Cluster System. ApJ, 474 (1):223–255, January 1997. doi:10.1086/303441.

D. Goorvitch. Infrared CO Line List for the X 1 Sigma + State. ApJS, 95:535, December 1994. doi:10.1086/192110.

R. Gratton, S. Lucatello, E. Carretta, and A. Bragaglia. Spectroscopic evidence of multiple populations in globular clusters. *Highlights of Astronomy*, 16:230–231, March 2015. doi:10.1017/S1743921314005547.

R. G. Gratton. Abundances in metal-poor stars. II. The anomalous globular cluster omega Centauri. A&A, 115:336–346, November 1982.

R. G. Gratton, C. Sneden, E. Carretta, and A. Bragaglia. Mixing along the red giant branch in metal-poor field stars. A&A, 354:169–187, February 2000.

R. G. Gratton, P. Bonifacio, A. Bragaglia, E. Carretta, V. Castellani, M. Centurion, A. Chieffi, R. Claudi, G. Clementini, F. D'Antona, S. Desidera, P. François, F. Grundahl, S. Lucatello, P. Molaro, L. Pasquini, C. Sneden, F. Spite, and O. Straniero. The O-Na and Mg-Al anticorrelations in turn-off and early subgiants in globular clusters. A&A, 369:87–98, April 2001. doi:10.1051/0004-6361:20010144.

R. Gratton, C. Sneden, and E. Carretta. Abundance Variations Within Globular Clusters. ARA&A, 42(1):385–440, September 2004. doi:10.1146/annurev.astro.42.053102.133945.

R. Gratton, A. Bragaglia, E. Carretta, V. D'Orazi, S. Lucatello, and A. Sollima. What is a globular cluster? An observational perspective. A&A Rev., 27(1):8, November 2019. doi:10.1007/s00159-019-0119-3.

L. C. Green. Observational Aspects of Cosmology. S&T, 31:199, April 1966.

J. L. Greenstein. Magnitudes and Colors in the Globular Cluster Messier 4. ApJ, 90:387, October 1939. doi:10.1086/144115.

T. H. Greif, J. L. Johnson, V. Bromm, and R. S. Klessen. The First Supernova Explosions: Energetics, Feedback, and Chemical Enrichment. ApJ, 670(1):1–14, November 2007. doi:10.1086/522028.

T. H. Greif, J. L. Johnson, R. S. Klessen, and V. Bromm. The first galaxies: assembly, cooling and the onset of turbulence. MNRAS, 387(3):1021–1036, July 2008. doi:10.1111/j.1365-2966.2008.13326.x.

T. H. Greif, J. L. Johnson, R. S. Klessen, and V. Bromm. The observational signature of the first HII regions. MNRAS, 399(2):639–649, October 2009. doi:10.1111/j.1365-2966.2009.15336.x.

T. H. Greif, S. C. O. Glover, V. Bromm, and R. S. Klessen. The First Galaxies: Chemical Enrichment, Mixing, and Star Formation. ApJ, 716(1):510–520, June 2010. doi:10.1088/0004-637X/716/1/510.

T. H. Greif, V. Springel, S. D. M. White, S. C. O. Glover, P. C. Clark, R. J. Smith, R. S. Klessen, and V. Bromm. Simulations on a Moving Mesh: The Clustered Formation of Population III Protostars. ApJ, 737(2):75, August 2011. doi:10.1088/0004-637X/737/2/75.

B. Gustafsson, B. Edvardsson, K. Eriksson, U. G. Jørgensen, Å. Nordlund, and B. Plez. A grid of MARCS model atmospheres for late-type stars. I. Methods and general properties. A&A, 486 (3):951–970, August 2008. doi:10.1051/0004-6361:200809724.

O. Hachenberg. Der Aufbau des kugelförmigen Sternhaufens Messier 92. Mit 9 Abbildungen. ZAp, 18:49, January 1939.

Z. Haiman and A. Loeb. Signatures of Stellar Reionization of the Universe. ApJ, 483(1):21–37, July 1997. doi:10.1086/304238.

E. Halley. An Account of several Nebulae or lucid Spots like Clouds, lately discovered among the Fixt Stars by help of the Telescope. *Philosophical Transactions of the Royal Society of London Series I*, 29(347):390–392, January 1715.

G. A. Harding. A CH star in omega Centauri. *The Observatory*, 82:205–207, October 1962.

W. E. Harris and R. Racine. Globular clusters in galaxies. ARA&A, 17:241–274, January 1979. doi:10.1146/annurev.aa.17.090179.001325.

W. E. Harris. The Unusual Horizontal Branch of NGC 2808. ApJ, 192:L161, September 1974. doi:10.1086/181616.

W. E. Harris. Globular cluster systems in galaxies beyond the Local Group. ARA&A, 29:543–579, January 1991. doi:10.1146/annurev.aa.29.090191.002551.

W. E. Harris. A Catalog of Parameters for Globular Clusters in the Milky Way. AJ, 112:1487, October 1996. doi:10.1086/118116.

A. P. Hatzes and H. Rauer. A Definition for Giant Planets Based on the Mass-Density Relationship. ApJ, 810(2):L25, September 2015. doi:10.1088/2041-8205/810/2/L25.

P. H. Hauschildt, E. Baron, and F. Allard. Parallel Implementation of the PHOENIX Generalized Stellar Atmosphere Program. ApJ, 483(1):390–398, July 1997. doi:10.1086/304233.

P. H. Hauschildt, F. Allard, and E. Baron. The NextGen Model Atmosphere Grid for 3000<=T_{eff}<=10,000 K. ApJ, 512(1):377–385, February 1999. doi:10.1086/306745.

C. Hayashi and T. Nakano. Evolution of Stars of Small Masses in the Pre-Main-Sequence Stages. *Progress of Theoretical Physics*, 30(4):460–474, October 1963. doi:10.1143/PTP.30.460.

A. C. Hayes, M. E. Gooden, E. Henry, G. Jungman, J. B. Wilhelmy, R. S. Rundberg, C. Yeamans, G. Kyrala, C. Cerjan, D. L. Danielson, J. Daligault, C. Wilburn, P. Volegov, C. Wilde, S. Batha, T. Bredeweg, J. L. Kline, G. P. Grim, E. P. Hartouni, D. Shaughnessy, C. Velsko, W. S. Cassata, K. Moody, L. F. Berzak Hopkins, D. Hinkel, T. Döppner, S. Le Pape, F. Graziani, D. A. Callahan, O. A. Hurricane, and D. Schneider. Plasma stopping-power measurements reveal transition from non-degenerate to degenerate plasmas. *Nature Physics*, 16(4):432–437, March 2020. doi:10.1038/s41567-020-0790-3.

A. Heger and S. E. Woosley. The Nucleosynthetic Signature of Population III. ApJ, 567(1): 532–543, March 2002. doi:10.1086/338487.

C. Helling, A. Ackerman, F. Allard, M. Dehn, P. Hauschildt, D. Homeier, K. Lodders, M. Marley, F. Rietmeijer, T. Tsuji, and P. Woitke. A comparison of chemistry and dust cloud formation in ultracool dwarf model atmospheres. MNRAS, 391(4):1854–1873, December 2008. doi:10.1111/j.1365-2966.2008.13991.x.

V. Hénault-Brunet, M. Gieles, J. Strader, M. Peuten, E. Balbinot, and K. E. K. Douglas. On the black hole content and initial mass function of 47 Tuc. MNRAS, 491(1):113–128, January 2020. doi:10.1093/mnras/stz2995.

N. P. Herrington, D. J. Whalen, and T. E. Woods. Modeling Supermassive Primordial Stars with MESA. *arXiv e-prints*, art. arXiv:2208.00008, July 2022.

J. E. Hesser and R. A. Bell. CN variations among main-sequence 47 Tucanae stars. ApJ, 238: L149–L153, June 1980. doi:10.1086/183276.

M. Hilker, H. Baumgardt, A. Sollima, and A. Bellini. Galactic Globular Clusters: A new catalog of masses, structural parameters, velocity dispersion profiles, proper motions and space orbits. In A. Bragaglia, M. Davies, A. Sills, and E. Vesperini, editors, *Star Clusters: From the Milky Way to the Early Universe*, volume 351, pages 451–454, January 2020. doi:10.1017/S1743921319006823.

S. Hirano, T. Hosokawa, N. Yoshida, K. Omukai, and H. W. Yorke. Primordial star formation under the influence of far ultraviolet radiation: 1540 cosmological haloes and the stellar mass distribution. MNRAS, 448(1):568–587, March 2015. doi:10.1093/mnras/stv044.

S. Hirano, T. Hosokawa, N. Yoshida, H. Umeda, K. Omukai, G. Chiaki, and H. W. Yorke. One Hundred First Stars: Protostellar Evolution and the Final Masses. ApJ, 781(2):60, February 2014. doi:10.1088/0004-637X/781/2/60.

D. Hollenbach, D. Johnstone, S. Lizano, and F. Shu. Photoevaporation of Disks around Massive Stars and Application to Ultracompact H II Regions. ApJ, 428:654, June 1994. doi:10.1086/174276.

D. Homeier, P. H. Hauschildt, and F. Allard. Methane and the Spectra of T Dwarfs. In E. Martín, editor, *Brown Dwarfs*, volume 211, page 419, June 2003.

S. Honda, W. Aoki, T. Kajino, H. Ando, T. C. Beers, H. Izumiura, K. Sadakane, and M. Takada-Hidai. Spectroscopic Studies of Extremely Metal-Poor Stars with the Subaru High Dispersion Spectrograph. II. The r-Process Elements, Including Thorium. ApJ, 607(1):474–498, May 2004. doi:10.1086/383406.

P. F. Hopkins. Some Stars are Totally Metal: A New Mechanism Driving Dust across Star-forming Clouds, and Consequences for Planets, Stars, and Galaxies. ApJ, 797(1):59, December 2014. doi:10.1088/0004-637X/797/1/59.

T. Hosokawa, K. Omukai, N. Yoshida, and H. W. Yorke. Protostellar Feedback Halts the Growth of the First Stars in the Universe. *Science*, 334(6060):1250, December 2011. doi:10.1126/science.1207433.

F. Hoyle. On Nuclear Reactions Occuring in Very Hot STARS.I. the Synthesis of Elements from Carbon to Nickel. ApJS, 1:121, September 1954. doi:10.1086/190005.

W. B. Hubbard, T. Guillot, J. I. Lunine, A. Burrows, D. Saumon, M. S. Marley, and R. S. Freedman. Liquid metallic hydrogen and the structure of brown dwarfs and giant planets. *Physics of Plasmas*, 4(5):2011–2015, May 1997. doi:10.1063/1.872570.

E. Hubble. Nebulous Objects in Messier 31 Provisionally Identified as Globular Clusters. ApJ, 76:44, July 1932. doi:10.1086/143397.

I. Hubeny and T. Lanz. Non-LTE Line-blanketed Model Atmospheres of Hot Stars. I. Hybrid Complete Linearization/Accelerated Lambda Iteration Method. ApJ, 439:875, February 1995. doi:10.1086/175226.

J. Hughes and G. Wallerstein. Age and Metallicity Effects in ω Centauri: StrÖmgren Photometry at the Main-Sequence Turnoff. AJ, 119(3):1225–1238, March 2000. doi:10.1086/301241.

J. A. Hynek. Giant Binary Stars and the Mass-Luminosity Law. Nature, 162(4125):815–816, November 1948a. doi:10.1038/162815a0.

J. A. Hynek. The Russell-Moore discordant parallax stars. AJ, 54:40, October 1948b. doi:10.1086/106184.

F. Iocco, G. Mangano, G. Miele, O. Pisanti, and P. D. Serpico. Path to metallicity: Synthesis of CNO elements in standard BBN. Phys. Rev. D, 75(8):087304, April 2007. doi:10.1103/PhysRevD.75.087304.

J. Jaacks, S. L. Finkelstein, and V. Bromm. Legacy of star formation in the pre-reionization universe. MNRAS, 488(2):2202–2221, September 2019. doi:10.1093/mnras/stz1529.

R. Jimenez. Globular Cluster Ages. *Proceedings of the National Academy of Science*, 95(1): 13–17, January 1998. doi:10.1073/pnas.95.1.13.

C. I. Johnson and C. A. Pilachowski. Chemical Abundances for 855 Giants in the Globular Cluster Omega Centauri (NGC 5139). ApJ, 722(2):1373–1410, October 2010. doi:10.1088/0004-637X/722/2/1373.

C. I. Johnson, C. A. Pilachowski, R. Michael Rich, and J. P. Fulbright. A Large Sample Study of Red Giants in the Globular Cluster Omega Centauri (NGC 5139). ApJ, 698(2):2048–2065, June 2009a. doi:10.1088/0004-637X/698/2/2048.

C. I. Johnson, A. K. Dupree, M. Mateo, I. Bailey, John I., E. W. Olszewski, and M. G. Walker. The Most Metal-poor Stars in Omega Centauri (NGC 5139). AJ, 159(6):254, June 2020. doi:10.3847/1538-3881/ab8819.

H. B. Johnson. Effects of Non-Local Thermodynamic Equilibrium (NLTE) on Molecular Opacities. In *IAU Colloq. 146*, volume 428. Springer-Verlag, 1994. doi:10.1007/3-540-57747-5_47.

J. L. Johnson. Population III star clusters in the reionized Universe. MNRAS, 404(3):1425–1436, May 2010. doi:10.1111/j.1365-2966.2010.16351.x.

J. L. Johnson. The chemical signature of surviving Population III stars in the Milky Way. MNRAS, 453(3):2771–2778, November 2015. doi:10.1093/mnras/stv1815.

J. L. Johnson, T. H. Greif, and V. Bromm. Occurrence of metal-free galaxies in the early Universe. MNRAS, 388(1):26–38, July 2008. doi:10.1111/j.1365-2966.2008.13381.x.

J. L. Johnson, T. H. Greif, V. Bromm, R. S. Klessen, and J. Ippolito. The first galaxies: signatures of the initial starburst. MNRAS, 399(1):37–47, October 2009b. doi:10.1111/j.1365-2966.2009.15158.x.

J. E. Jones. Primordial stars - The precursors to galaxy formation. In *The Origin and Evolution of Galaxies*, pages 179–187, January 1983.

U. G. Jorgensen and M. Larsson. Molecular opacities of astrophysical interest - The A2Pi-X2Sigma(+) system of CN. A&A, 238:424–434, November 1990.

M. Joyce and B. Chaboyer. Not All Stars Are the Sun: Empirical Calibration of the Mixing Length for Metal-poor Stars Using One-dimensional Stellar Evolution Models. ApJ, 856(1): 10, March 2018. doi:10.3847/1538-4357/aab200.

M. Jurić, Ž. Ivezić, A. Brooks, R. H. Lupton, D. Schlegel, D. Finkbeiner, N. Padmanabhan, N. Bond, B. Sesar, C. M. Rockosi, G. R. Knapp, J. E. Gunn, T. Sumi, D. P. Schneider, J. C. Barentine, H. J. Brewington, J. Brinkmann, M. Fukugita, M. Harvanek, S. J. Kleinman, J. Krzesinski, D. Long, J. Neilsen, Eric H., A. Nitta, S. A. Snedden, and D. G. York. The Milky Way Tomography with SDSS. I. Stellar Number Density Distribution. ApJ, 673(2):864–914, February 2008. doi:10.1086/523619.

J. S. Kalirai, H. B. Richer, J. Anderson, A. Dotter, G. G. Fahlman, B. M. S. Hansen, J. Hurley, I. R. King, D. Reitzel, R. M. Rich, M. M. Shara, P. B. Stetson, and K. A. Woodley. A Deep, Wide-field, and Panchromatic View of 47 Tuc and the SMC with HST: Observations and Data Analysis Methods. AJ, 143(1):11, January 2012. doi:10.1088/0004-6256/143/1/11.

A. I. Karakas, Y. Fenner, A. Sills, S. W. Campbell, and J. C. Lattanzio. The Chemical Evolution of Helium in Globular Clusters: Implications for the Self-Pollution Scenario. ApJ, 652(2): 1240–1245, December 2006. doi:10.1086/508504.

A. Kashlinsky. Cosmic Infrared Background from Population III Stars and Its Effect on Spectra of High-z Gamma-Ray Bursts. ApJ, 633(1):L5–L8, November 2005. doi:10.1086/498243.

A. Kashlinsky, R. G. Arendt, J. Mather, and S. H. Moseley. Detecting Population III stars in cosmic infrared background anisotropies from deep Spitzer data. In *American Astronomical Society Meeting Abstracts*, volume 207 of *American Astronomical Society Meeting Abstracts*, page 100.02, December 2005.

Katrin Collaboration, M. Aker, A. Beglarian, J. Behrens, A. Berlev, U. Besserer, B. Bieringer, F. Block, S. Bobien, M. Böttcher, B. Bornschein, L. Bornschein, T. Brunst, T. S. Caldwell, R. M. D. Carney, L. La Cascio, S. Chilingaryan, W. Choi, K. Debowski, M. Deffert, M. Descher, D. Díaz Barrero, P. J. Doe, O. Dragoun, G. Drexlin, K. Eitel, E. Ellinger, R. Engel, S. Enomoto, A. Felden, J. A. Formaggio, F. M. Fränkle, G. B. Franklin, F. Friedel, A. Fulst, K. Gauda, W. Gil, F. Glück, R. Grössle, R. Gumbsheimer, V. Gupta, T. Höhn, V. Hannen, N. Haußmann, K. Helbing, S. Hickford, R. Hiller, D. Hillesheimer, D. Hinz, T. Houdy, A. Huber, A. Jansen, C. Karl, F. Kellerer, J. Kellerer, M. Kleifges, M. Klein, C. Köhler, L. Köllenberger, A. Kopmann, M. Korzeczek, A. Kovalík, B. Krasch, H. Krause, N. Kunka, T. Lasserre, T. L. Le, O. Lebeda, B. Lehnert, A. Lokhov, M. Machatschek, E. Malcherek, M. Mark, A. Marsteller, E. L. Martin, C. Melzer, A. Menshikov, S. Mertens, J. Mostafa, K. Müller, H. Neumann, S. Niemes, P. Oelpmann, D. S. Parno, A. W. P. Poon, J. M. L. Poyato, F. Priester, S. Ramachandran, R. G. H. Robertson, W. Rodejohann, M. Röllig, C. Röttele, C. Rodenbeck, M. Ryšavý, R. Sack, A. Saenz, P. Schäfer, A. Schaller Née Pollithy, L. Schimpf, K. Schlösser, M. Schlösser, L. Schlüter, S. Schneidewind, M. Schrank, B. Schulz, A. Schwemmer, M. Šefčík, V. Sibille, D. Siegmann, M. Slezák, F. Spanier, M. Steidl, M. Sturm, M. Sun, D. Tcherniakhovski, H. H. Telle, L. A. Thorne, T. Thümmler, N. Titov, I. Tkachev, K. Urban, K. Valerius, D. Vénos, A. P. Vizcaya Hernández, C. Weinheimer, S. Welte, J. Wendel, J. F. Wilkerson, J. Wolf, S. Wüstling, J. Wydra, W. Xu, Y. R. Yen, S. Zadoroghny, and G. Zeller. Direct neutrino-mass measurement with sub-electronvolt sensitivity. *Nature Physics*, 18(2):160–166, February 2022. doi:10.1038/s41567-021-01463-1.

P. C. Keenan and G. Keller. Spectral Classification of the High-Velocity Stars. ApJ, 117:241, March 1953. doi:10.1086/145687.

S. C. Keller, M. S. Bessell, A. Frebel, A. R. Casey, M. Asplund, H. R. Jacobson, K. Lind, J. E. Norris, D. Yong, A. Heger, Z. Magic, G. S. da Costa, B. P. Schmidt, and P. Tisserand. A single low-energy, iron-poor supernova as the source of metals in the star SMSS J031300.36-670839.3. Nature, 506(7489):463–466, February 2014. doi:10.1038/nature12990.

P. L. Kelly, J. M. Diego, S. Rodney, N. Kaiser, T. Broadhurst, A. Zitrin, T. Treu, P. G. Pérez-González, T. Morishita, M. Jauzac, J. Selsing, M. Oguri, L. Pueyo, T. W. Ross, A. V. Filippenko, N. Smith, J. Hjorth, S. B. Cenko, X. Wang, D. A. Howell, J. Richard, B. L. Frye, S. W. Jha, R. J. Foley, C. Norman, M. Bradac, W. Zheng, G. Brammer, A. M. Benito, A. Cava, L. Christensen, S. E. de Mink, O. Graur, C. Grillo, R. Kawamata, J.-P. Kneib, T. Matheson, C. McCully, M. Nonino, I. Pérez-Fournon, A. G. Riess, P. Rosati, K. B. Schmidt, K. Sharon, and B. J. Weiner. Extreme magnification of an individual star at redshift 1.5 by a galaxy-cluster lens. *Nature Astronomy*, 2:334–342, April 2018. doi:10.1038/s41550-018-0430-3.

J.-h. Kim, X. Ma, M. Y. Grudić, P. F. Hopkins, C. C. Hayward, A. Wetzel, C.-A. Faucher-Giguère, D. Kereš, S. Garrison-Kimmel, and N. Murray. Formation of globular cluster candidates in merging proto-galaxies at high redshift: a view from the FIRE cosmological simulations. MNRAS, 474(3):4232–4244, March 2018. doi:10.1093/mnras/stx2994.

I. R. King, L. R. Bedin, S. Cassisi, A. P. Milone, A. Bellini, G. Piotto, J. Anderson, A. Pietrinferni, and D. Cordier. Hubble Space Telescope Observations of an Outer Field in Omega Centauri: A Definitive Helium Abundance. AJ, 144(1):5, July 2012. doi:10.1088/0004-6256/144/1/5.

T. Kinugawa, K. Inayoshi, K. Hotokezaka, D. Nakauchi, and T. Nakamura. Possible indirect confirmation of the existence of Pop III massive stars by gravitational wave. MNRAS, 442(4): 2963–2992, August 2014. doi:10.1093/mnras/stu1022.

R. Kippenhahn and A. Weigert. *Stellar Structure and Evolution*. Springer Berlin / Heidelberg, 1994.

E. N. Kirby, J. D. Simon, M. Geha, P. Guhathakurta, and A. Frebel. Uncovering Extremely Metal-Poor Stars in the Milky Way's Ultrafaint Dwarf Spheroidal Satellite Galaxies. ApJ, 685 (1):L43, September 2008. doi:10.1086/592432.

J. D. Kirkpatrick, C. R. Gelino, M. C. Cushing, G. N. Mace, R. L. Griffith, M. F. Skrutskie, K. A. Marsh, E. L. Wright, P. R. Eisenhardt, I. S. McLean, A. K. Mainzer, A. J. Burgasser, C. G. Tinney, S. Parker, and G. Salter. Further Defining Spectral Type "Y" and Exploring the Low-mass End of the Field Brown Dwarf Mass Function. ApJ, 753(2):156, July 2012. doi:10.1088/0004-637X/753/2/156.

J. D. Kirkpatrick, C. R. Gelino, J. K. Faherty, A. M. Meisner, D. Caselden, A. C. Schneider, F. Marocco, A. J. Cayago, R. L. Smart, P. R. Eisenhardt, M. J. Kuchner, E. L. Wright, M. C. Cushing, K. N. Allers, D. C. Bardalez Gagliuffi, A. J. Burgasser, J. Gagné, S. E. Logsdon, E. C.

Martin, J. G. Ingalls, P. J. Lowrance, E. S. Abrahams, C. Aganze, R. Gerasimov, E. C. Gonzales, C.-C. Hsu, N. Kamraj, R. Kiman, J. Rees, C. Theissen, K. Ammar, N. S. Andersen, P. Beaulieu, G. Colin, C. A. Elachi, S. J. Goodman, L. Gramaize, L. K. Hamlet, J. Hong, A. Jonkeren, M. Khalil, D. W. Martin, W. Pendrill, B. Pumphrey, A. Rothermich, A. Sainio, A. Stenner, C. Tanner, M. Thévenot, N. V. Voloshin, J. Walla, Z. Wędracki, and Backyard Worlds: Planet 9 Collaboration. The Field Substellar Mass Function Based on the Full-sky 20 pc Census of 525 L, T, and Y Dwarfs. ApJS, 253(1):7, March 2021. doi:10.3847/1538-4365/abd107.

T. Kitayama, N. Yoshida, H. Susa, and M. Umemura. The Structure and Evolution of Early Cosmological H II Regions. ApJ, 613(2):631–645, October 2004. doi:10.1086/423313.

A. Kogut. WMAP polarization results. New A Rev., 47(11-12):977–986, December 2003. doi:10.1016/j.newar.2003.09.029.

K. Köhler, N. Langer, A. de Koter, S. E. de Mink, P. A. Crowther, C. J. Evans, G. Gräfener, H. Sana, D. Sanyal, F. R. N. Schneider, and J. S. Vink. The evolution of rotating very massive stars with LMC composition. A&A, 573:A71, January 2015. doi:10.1051/0004-6361/201424356.

E. Komatsu, K. M. Smith, J. Dunkley, C. L. Bennett, B. Gold, G. Hinshaw, N. Jarosik, D. Larson, M. R. Nolta, L. Page, D. N. Spergel, M. Halpern, R. S. Hill, A. Kogut, M. Limon, S. S. Meyer, N. Odegard, G. S. Tucker, J. L. Weiland, E. Wollack, and E. L. Wright. Seven-year Wilkinson Microwave Anisotropy Probe (WMAP) Observations: Cosmological Interpretation. ApJS, 192 (2):18, February 2011. doi:10.1088/0067-0049/192/2/18.

M. B. N. Kouwenhoven, A. G. A. Brown, S. P. Goodwin, S. F. Portegies Zwart, and L. Kaper. Exploring the consequences of pairing algorithms for binary stars. A&A, 493(3):979–1016, January 2009. doi:10.1051/0004-6361:200810234.

I. Kowalska, T. Bulik, and K. Belczynski. Gravitational wave background from Population III binaries. A&A, 541:A120, May 2012. doi:10.1051/0004-6361/201118604.

R. P. Kraft. Abundance Differences among Globular Cluster Giants: Primordial vs. Evolutionary Scenarios. PASP, 106:553, June 1994. doi:10.1086/133416.

L. M. Krauss and B. Chaboyer. Age Estimates of Globular Clusters in the Milky Way: Constraints on Cosmology. *Science*, 299(5603):65–70, January 2003. doi:10.1126/science.1075631.

L. Kreidberg, J. L. Bean, J.-M. Désert, B. Benneke, D. Deming, K. B. Stevenson, S. Seager, Z. Berta-Thompson, A. Seifahrt, and D. Homeier. Clouds in the atmosphere of the super-Earth exoplanet GJ1214b. Nature, 505(7481):69–72, January 2014. doi:10.1038/nature12888.

P. Kroupa. On the variation of the initial mass function. MNRAS, 322(2):231–246, April 2001. doi:10.1046/j.1365-8711.2001.04022.x.

J. M. D. Kruijssen, J. L. Pfeffer, M. Reina-Campos, R. A. Crain, and N. Bastian. The formation and assembly history of the Milky Way revealed by its globular cluster population. MNRAS, 486(3):3180–3202, July 2019. doi:10.1093/mnras/sty1609.

S. S. Kumar. Study of Degeneracy in Very Light Stars. AJ, 67:579, January 1962. doi:10.1086/108658.

S. S. Kumar. The Structure of Stars of Very Low Mass. ApJ, 137:1121, May 1963. doi:10.1086/147589.

R. L. Kurucz. Atlas: a Computer Program for Calculating Model Stellar Atmospheres. *SAO Special Report*, 309, Feb 1970.

R. L. Kurucz. The Kurucz Smithsonian Atomic and Molecular Database. In S. J. Adelman and W. L. Wiese, editors, *Astrophysical Applications of Powerful New Databases*, volume 78 of *Astronomical Society of the Pacific Conference Series*, page 205, January 1995.

R. L. Kurucz. ATLAS12, SYNTHE, ATLAS9, WIDTH9, et cetera. *Memorie della Societa Astronomica Italiana Supplementi*, 8:14, Jan 2005.

R. L. Kurucz. *Model Atmosphere Codes: ATLAS12 and ATLAS9*, pages 39–51. Springer International Publishing, 2014. doi:10.1007/978-3-319-06956-2_4.

R. L. Kurucz and E. H. Avrett. Solar Spectrum Synthesis. I. A Sample Atlas from 224 to 300 nm. *SAO Special Report*, 391, May 1981.

R. L. Kurucz, E. Peytremann, and E. H. Avrett. *Blanketed model atmospheres for early-type stars*. Smithsonian Astrophysical Observatory, 1974.

C. H. Lacy. Distances to eclipsing binaries. III. Masses, radii and absolute magnitudes of 96 stars. ApJ, 228:817–827, March 1979. doi:10.1086/156908.

S. S. Larsen, J. Strader, and J. P. Brodie. Constraints on mass loss and self-enrichment scenarios for the globular clusters of the Fornax dSph. A&A, 544:L14, August 2012. doi:10.1051/0004-6361/201219897.

S. S. Larsen, J. P. Brodie, D. A. Forbes, and J. Strader. Chemical composition and constraints on mass loss for globular clusters in dwarf galaxies: WLM and IKN. A&A, 565:A98, May 2014. doi:10.1051/0004-6361/201322672.

R. B. Larson. Early star formation and the evolution of the stellar initial mass function in galaxies. MNRAS, 301(2):569–581, December 1998. doi:10.1046/j.1365-8711.1998.02045.x.

M. Latour, A. Calamida, T. O. Husser, S. Kamann, S. Dreizler, and J. Brinchmann. A stellar census in globular clusters with MUSE. A new perspective on the multiple main sequences of ω Centauri. A&A, 653:L8, September 2021. doi:10.1051/0004-6361/202141791.

G. Laughlin, P. Bodenheimer, and F. C. Adams. The End of the Main Sequence. ApJ, 482(1): 420–432, June 1997. doi:10.1086/304125.

M. G. Lee. Galactic Archaeology Using Star Clusters in Nearby Galaxies. In W. Aoki, M. Ishigaki, T. Suda, T. Tsujimoto, and N. Arimoto, editors, *Galactic Archaeology: Near-Field Cosmology and the Formation of the Milky Way*, volume 458 of *Astronomical Society of the Pacific Conference Series*, page 291, August 2012.

S. W. Lee. UBV photometry of bright stars in 47 Tuc. A&AS, 27:381–401, March 1977.

M. Libralato, A. Bellini, L. R. Bedin, E. Moreno D., J. G. Fernández-Trincado, B. Pichardo, R. P. van der Marel, J. Anderson, D. Apai, A. J. Burgasser, A. Fabiola Marino, A. P. Milone, J. M. Rees, and L. L. Watkins. The HST Large Programme on ω Centauri. III. Absolute Proper Motion. ApJ, 854(1):45, February 2018. doi:10.3847/1538-4357/aaa59e.

D. Lide. *CRC Handbook of Chemistry and Physics, 85th Edition*. Number v. 85 in CRC Handbook of Chemistry and Physics, 85th Ed. Taylor & Francis, 2004. ISBN 9780849304859. URL https://books.google.com/books?id=WDll8hA006AC.

K. Lind, M. Asplund, P. S. Barklem, and A. K. Belyaev. Non-LTE calculations for neutral Na in late-type stars using improved atomic data. A&A, 528:A103, April 2011. doi:10.1051/0004-6361/201016095.

K. Lind, S. E. Koposov, C. Battistini, A. F. Marino, G. Ruchti, A. Serenelli, C. C. Worley, A. Alves-Brito, M. Asplund, P. S. Barklem, T. Bensby, M. Bergemann, S. Blanco-Cuaresma, A. Bragaglia, B. Edvardsson, S. Feltzing, P. Gruyters, U. Heiter, P. Jofre, A. J. Korn, T. Nordlander, N. Ryde, C. Soubiran, G. Gilmore, S. Randich, A. M. N. Ferguson, R. D. Jeffries, A. Vallenari, C. Allende Prieto, E. Pancino, A. Recio-Blanco, D. Romano, R. Smiljanic, M. Bellazzini, F. Damiani, V. Hill, P. de Laverny, R. J. Jackson, C. Lardo, and S. Zaggia. The Gaia-ESO Survey: A globular cluster escapee in the Galactic halo. A&A, 575:L12, March 2015. doi:10.1051/0004-6361/201425554.

B. Lindblad. Spectrophotometric methods for determining stellar luminosity. ApJ, 55:85–118, March 1922. doi:10.1086/142660.

J. L. Linsky. On the Pressure-Induced Opacity of Molecular Hydrogen in Late-Type Stars. ApJ, 156:989, June 1969. doi:10.1086/150030.

B. Liu and V. Bromm. When did Population III star formation end? MNRAS, 497(3):2839–2854, September 2020. doi:10.1093/mnras/staa2143.

B. Liu, Y. Sibony, G. Meynet, and V. Bromm. Stellar winds and metal enrichment from fast-rotating Population III stars. MNRAS, 506(4):5247–5267, October 2021. doi:10.1093/mnras/stab2057.

N. Lodieu, M. Espinoza Contreras, M. R. Zapatero Osorio, E. Solano, M. Aberasturi, and E. L. Martín. New ultracool subdwarfs identified in large-scale surveys using Virtual Observatory tools. I. UKIDSS LAS DR5 vs. SDSS DR7. A&A, 542:A105, June 2012. doi:10.1051/0004-6361/201118717.

N. Lodieu, M. Espinoza Contreras, M. R. Zapatero Osorio, E. Solano, M. Aberasturi, E. L. Martín, and C. Rodrigo. New ultracool subdwarfs identified in large-scale surveys using Virtual Observatory tools. A&A, 598:A92, February 2017. doi:10.1051/0004-6361/201629410.

L. B. Lucy and E. Ricco. The significance of binaries with nearly identical components. AJ, 84: 401–412, March 1979. doi:10.1086/112434.

J. I. Lunine, W. B. Hubbard, and M. S. Marley. Evolution and Infrared Spectra of Brown Dwarfs. ApJ, 310:238, November 1986. doi:10.1086/164678.

J. Mackey, V. Bromm, and L. Hernquist. Three Epochs of Star Formation in the High-Redshift Universe. ApJ, 586(1):1–11, March 2003. doi:10.1086/367613.

B. T. MacLean, G. M. De Silva, and J. Lattanzio. O, Na, Ba and Eu abundance patterns in open clusters. MNRAS, 446(4):3556–3561, February 2015. doi:10.1093/mnras/stu2348.

P. Madau and M. Dickinson. Cosmic Star-Formation History. ARA&A, 52:415–486, August 2014. doi:10.1146/annurev-astro-081811-125615.

P. Madau and M. J. Rees. Massive Black Holes as Population III Remnants. ApJ, 551(1):L27–L30, April 2001. doi:10.1086/319848.

P. Madau and J. Silk. Population III and the near-infrared background excess. MNRAS, 359(1): L37–L41, May 2005. doi:10.1111/j.1745-3933.2005.00031.x.

N. Madhusudhan. Atmospheric Retrieval of Exoplanets. In H. J. Deeg and J. A. Belmonte, editors, *Handbook of Exoplanets*, page 104. Springer International, 2018. doi:10.1007/978-3-319-55333-7_104.

U. Maio, B. Ciardi, K. Dolag, L. Tornatore, and S. Khochfar. The transition from population III to population II-I star formation. MNRAS, 407(2):1003–1015, September 2010. doi:10.1111/j.1365-2966.2010.17003.x.

U. Maio, M. Petkova, G. De Lucia, and S. Borgani. Radiative feedback and cosmic molecular gas: the role of different radiative sources. MNRAS, 460(4):3733–3752, August 2016. doi:10.1093/mnras/stw1196.

E. E. Mamajek, G. Torres, A. Prsa, P. Harmanec, M. Asplund, P. D. Bennett, N. Capitaine, J. Christensen-Dalsgaard, E. Depagne, W. M. Folkner, M. Haberreiter, S. Hekker, J. L. Hilton, V. Kostov, D. W. Kurtz, J. Laskar, B. D. Mason, E. F. Milone, M. M. Montgomery, M. T. Richards, J. Schou, and S. G. Stewart. IAU 2015 Resolution B2 on Recommended Zero Points for the Absolute and Apparent Bolometric Magnitude Scales. *arXiv e-prints*, art. arXiv:1510.06262, October 2015.

G. Mangano, G. Miele, S. Pastor, and M. Peloso. A precision calculation of the effective number of cosmological neutrinos. *Physics Letters B*, 534(1-4):8–16, May 2002. doi:10.1016/S0370-2693(02)01622-2.

A. Marín-Franch, A. Aparicio, G. Piotto, A. Rosenberg, B. Chaboyer, A. Sarajedini, M. Siegel, J. Anderson, L. R. Bedin, A. Dotter, M. Hempel, I. King, S. Majewski, A. P. Milone, N. Paust, and I. N. Reid. The ACS Survey of Galactic Globular Clusters. VII. Relative Ages. ApJ, 694 (2):1498–1516, April 2009. doi:10.1088/0004-637X/694/2/1498.

A. F. Marino. Anomalous globular clusters: insights from neutron capture elements abundances. Mem. Soc. Astron. Italiana, 84:29, January 2013. doi:10.48550/arXiv.1302.2306.

A. F. Marino, S. Villanova, A. P. Milone, G. Piotto, K. Lind, D. Geisler, and P. B. Stetson. Sodium-Oxygen Anticorrelation Among Horizontal Branch Stars in the Globular Cluster M4. ApJ, 730(2):L16, April 2011. doi:10.1088/2041-8205/730/2/L16.

A. F. Marino, A. P. Milone, G. Piotto, S. Cassisi, F. D'Antona, J. Anderson, A. Aparicio, L. R. Bedin, A. Renzini, and S. Villanova. The C+N+O Abundance of ω Centauri Giant Stars: Implications for the Chemical-enrichment Scenario and the Relative Ages of Different Stellar Populations. *The Astrophysical Journal*, 746(1):14, Feb 2012. doi:10.1088/0004-637X/746/1/14.

A. F. Marino, A. P. Milone, L. Casagrande, R. Collet, A. Dotter, C. I. Johnson, K. Lind, L. R. Bedin, H. Jerjen, A. Aparicio, and L. Sbordone. Chemical abundances in the multiple sub-giant branch of 47 Tucanae: insights on its faint sub-giant branch component. MNRAS, 459(1): 610–623, June 2016. doi:10.1093/mnras/stw611.

M. S. Marley, S. Seager, D. Saumon, K. Lodders, A. S. Ackerman, R. S. Freedman, and X. Fan. Clouds and Chemistry: Ultracool Dwarf Atmospheric Properties from Optical and Infrared Colors. ApJ, 568(1):335–342, March 2002. doi:10.1086/338800.

S. L. Martell and E. K. Grebel. Light-element abundance variations in the Milky Way halo. A&A, 519:A14, September 2010. doi:10.1051/0004-6361/201014135.

S. L. Martell, J. P. Smolinski, T. C. Beers, and E. K. Grebel. Building the Galactic halo from globular clusters: evidence from chemically unusual red giants. A&A, 534:A136, October 2011. doi:10.1051/0004-6361/201117644.

S. L. Martell and G. H. Smith. CN Variations in High-Metallicity Globular and Open Clusters. PASP, 121(880):577, June 2009. doi:10.1086/599979.

E. L. Martín, N. Lodieu, Y. Pavlenko, and V. J. S. Béjar. The Lithium Depletion Boundary and the Age of the Hyades Cluster. ApJ, 856(1):40, March 2018. doi:10.3847/1538-4357/aaaeb8.

S. Martocchia, F. Niederhofer, E. Dalessandro, N. Bastian, N. Kacharov, C. Usher, I. Cabrera-Ziri, C. Lardo, S. Cassisi, D. Geisler, M. Hilker, K. Hollyhead, V. Kozhurina-Platais, S. Larsen, D. Mackey, A. Mucciarelli, I. Platais, and M. Salaris. The search for multiple populations in

Magellanic Cloud clusters - IV. Coeval multiple stellar populations in the young star cluster NGC 1978. MNRAS, 477(4):4696–4705, July 2018. doi:10.1093/mnras/sty916.

L. Mashonkina. Mechanisms of departure from lte. In R. Monier, B. Smalley, G. Wahlgren, and P. Stee, editors, *EAS Publications Series*, volume 43 of *EAS Publications Series*, pages 189–197, November 2010. doi:10.1051/eas/1043014.

M. Mayor, A. Duquennoy, S. Udry, J. Andersen, and B. Nordstrom. Primordial Binaries in the Globular Cluster ω Centauri. In E. F. Milone and J. C. Mermilliod, editors, *The Origins, Evolution, and Destinies of Binary Stars in Clusters*, volume 90 of *Astronomical Society of the Pacific Conference Series*, page 190, January 1996.

C. F. McKee and J. C. Tan. The Formation of the First Stars. II. Radiative Feedback Processes and Implications for the Initial Mass Function. ApJ, 681(2):771–797, July 2008. doi:10.1086/587434.

A. Meiksin. Colour corrections for high-redshift objects due to intergalactic attenuation. MNRAS, 365(3):807–812, January 2006. doi:10.1111/j.1365-2966.2005.09756.x.

B. B. Messenger and J. C. Lattanzio. An attempt to model globular cluster red giant abundance anomalies with a simulated hydrogen shell instability. MNRAS, 331(3):684–692, April 2002. doi:10.1046/j.1365-8711.2002.05234.x.

C. Messier. Catalogue des Nébuleuses et des Amas d'Étoiles (Catalog of Nebulae and Star Clusters). Connoissance des Temps ou des Mouvements Célestes, for 1784, p. 227-267, January 1781.

S. Mészáros and C. Allende Prieto. On the interpolation of model atmospheres and high-resolution synthetic stellar spectra. MNRAS, 430(4):3285–3291, April 2013. doi:10.1093/mnras/stt130.

S. Mészáros, C. Allende Prieto, B. Edvardsson, F. Castelli, A. E. García Pérez, B. Gustafsson, S. R. Majewski, B. Plez, R. Schiavon, M. Shetrone, and A. de Vicente. New ATLAS9 and MARCS Model Atmosphere Grids for the Apache Point Observatory Galactic Evolution Experiment (APOGEE). AJ, 144(4):120, October 2012. doi:10.1088/0004-6256/144/4/120.

G. Meylan and D. C. Heggie. Internal dynamics of globular clusters. A&A Rev., 8:1–143, January 1997. doi:10.1007/s001590050008.

D. Mihalas. *Stellar atmospheres*. W. H. Freeman, 1978.

A. P. Milone. Multiple Stellar Populations in Globular Clusters with JWST. *arXiv e-prints*, art. arXiv:2304.07770, April 2023. doi:10.48550/arXiv.2304.07770.

A. P. Milone, A. F. Marino, G. Piotto, L. R. Bedin, J. Anderson, A. Aparicio, A. Bellini, S. Cassisi, F. D'Antona, F. Grundahl, M. Monelli, and D. Yong. A WFC3/HST View of the Three Stellar Populations in the Globular Cluster NGC 6752. ApJ, 767(2):120, April 2013. doi:10.1088/0004-637X/767/2/120.

A. P. Milone, A. F. Marino, L. R. Bedin, J. Anderson, D. Apai, A. Bellini, P. Bergeron, A. J. Burgasser, A. Dotter, and J. M. Rees. The HST large programme on ω Centauri - I. Multiple stellar populations at the bottom of the main sequence probed in NIR-Optical. MNRAS, 469 (1):800–812, July 2017. doi:10.1093/mnras/stx836.

A. P. Milone, A. F. Marino, L. R. Bedin, J. Anderson, D. Apai, A. Bellini, A. Dieball, M. Salaris, M. Libralato, D. Nardiello, P. Bergeron, A. J. Burgasser, J. M. Rees, R. M. Rich, and H. B. Richer. The HST Large Programme on NGC 6752 - II. Multiple populations at the bottom of the main sequence probed in NIR. MNRAS, 484(3):4046–4053, April 2019. doi:10.1093/mnras/stz277.

A. P. Milone and A. F. Marino. Multiple Populations in Star Clusters. *Universe*, 8(7):359, June 2022. doi:10.3390/universe8070359.

J. Miralda-Escude. The Magnification of Stars Crossing a Caustic. I. Lenses with Smooth Potentials. ApJ, 379:94, September 1991. doi:10.1086/170486.

S. Moehler. Hot Stars in Globular Clusters: A Spectroscopist's View. PASP, 113(788):1162–1177, October 2001. doi:10.1086/323297.

B. Moore, J. Diemand, P. Madau, M. Zemp, and J. Stadel. Globular clusters, satellite galaxies and stellar haloes from early dark matter peaks. MNRAS, 368(2):563–570, May 2006. doi:10.1111/j.1365-2966.2006.10116.x.

W. W. Morgan, P. C. Keenan, and E. Kellman. *An atlas of stellar spectra, with an outline of spectral classification*. The University of Chicago press, 1943.

C. V. Morley, J. J. Fortney, M. S. Marley, C. Visscher, D. Saumon, and S. K. Leggett. Neglected Clouds in T and Y Dwarf Atmospheres. ApJ, 756(2):172, September 2012. doi:10.1088/0004-637X/756/2/172.

V. Muñoz, V. Takhistov, S. J. Witte, and G. M. Fuller. Exploring the origin of supermassive black holes with coherent neutrino scattering. J. Cosm. Astropart. Phys., 2021(11):020, November 2021. doi:10.1088/1475-7516/2021/11/020.

A. L. Muratov, O. Y. Gnedin, N. Y. Gnedin, and M. Zemp. Revisiting the First Galaxies: The Epoch of Population III Stars. ApJ, 773(1):19, August 2013. doi:10.1088/0004-637X/773/1/19.

K. Mužić, R. Schödel, A. Scholz, V. C. Geers, R. Jayawardhana, J. Ascenso, and L. A. Cieza. The low-mass content of the massive young star cluster RCW 38. MNRAS, 471(3):3699–3712, November 2017. doi:10.1093/mnras/stx1906.

T. Nakajima, B. R. Oppenheimer, S. R. Kulkarni, D. A. Golimowski, K. Matthews, and S. T. Durrance. Discovery of a cool brown dwarf. Nature, 378(6556):463–465, November 1995. doi:10.1038/378463a0.

R. Narayan and S. Wallington. Introduction to Basic Concepts of Gravitational Lensing. In R. Kayser, T. Schramm, and L. Nieser, editors, *Gravitational Lenses*, volume 406, page 12. Springer, Berlin, Heidelberg, 1992. doi:10.1007/3-540-55797-0_76.

D. Nardiello, M. Griggio, and L. R. Bedin. JWST unveils the brown dwarf sequence of 47 Tucanæ. MNRAS, 521(1):L39–L43, May 2023. doi:10.1093/mnrasl/slad021.

L. Neale and J. Tennyson. A High-Temperature Partition Function for H 3 +. ApJ, 454:L169, December 1995. doi:10.1086/309789.

J. R. Neeley, M. Marengo, G. Bono, V. F. Braga, M. Dall'Ora, P. B. Stetson, R. Buonanno, I. Ferraro, W. L. Freedman, G. Iannicola, B. F. Madore, N. Matsunaga, A. Monson, S. E. Persson, V. Scowcroft, and M. Seibert. On the Distance of the Globular Cluster M4 (NGC 6121) Using RR Lyrae Stars. II. Mid-infrared Period-luminosity Relations. ApJ, 808(1):11, July 2015. doi:10.1088/0004-637X/808/1/11.

J. Nendwich, U. Heiter, F. Kupka, N. Nesvacil, and W. W. Weiss. Interpolation of Stellar Model Grids and Application to the NEMO Grid. *Communications in Asteroseismology*, 144:43–78, June 2004. doi:10.48550/arXiv.astro-ph/0406381.

H. J. Newberg. Introduction to Tidal Streams. In H. J. Newberg and J. L. Carlin, editors, *Tidal Streams in the Local Group and Beyond*, volume 420 of *Astrophysics and Space Science Library*, page 1, January 2016. doi:10.1007/978-3-319-19336-6_1.

K. Nomoto, N. Tominaga, H. Umeda, and C. Kobayashi. Yields of Population III Supernovae and the Abundance Patterns of Extremely Metal-Poor Stars. In V. Hill, P. Francois, and F. Primas, editors, *From Lithium to Uranium: Elemental Tracers of Early Cosmic Evolution*, volume 228, pages 287–296, January 2005. doi:10.1017/S1743921305005843.

T. Nordlander, M. S. Bessell, G. S. Da Costa, A. D. Mackey, M. Asplund, A. R. Casey, A. Chiti, R. Ezzeddine, A. Frebel, K. Lind, A. F. Marino, S. J. Murphy, J. E. Norris, B. P. Schmidt, and D. Yong. The lowest detected stellar Fe abundance: the halo star SMSS J160540.18-144323.1. MNRAS, 488(1):L109–L113, September 2019. doi:10.1093/mnrasl/slz109.

J. Norris and M. S. Bessell. Abundance variations on the lower giant branch of Omega Centauri. ApJ, 201:L75–L79, October 1975. doi:10.1086/181946.

J. Norris and K. C. Freeman. The cyanogen distribution of the giants in 47 Tucanae. ApJ, 230: L179–L182, June 1979. doi:10.1086/182988.

J. Norris, P. L. Cottrell, K. C. Freeman, and G. S. Da Costa. The abundance spread in the giants of NGC 6752. ApJ, 244:205–220, February 1981. doi:10.1086/158698.

J. Norris. The Ellipticities of Globular Clusters and the Cyanogen Problem. ApJ, 313:L65, February 1987. doi:10.1086/184832.

J. E. Norris. The Helium Abundances of ω Centauri. ApJ, 612(1):L25–L28, September 2004. doi:10.1086/423986.

J. E. Norris and G. S. Da Costa. The Giant Branch of omega Centauri. IV. Abundance Patterns Based on Echelle Spectra of 40 Red Giants. ApJ, 447:680, July 1995. doi:10.1086/175909.

M. A. Norris, S. J. Kannappan, D. A. Forbes, A. J. Romanowsky, J. P. Brodie, F. R. Faifer, A. Huxor, C. Maraston, A. J. Moffett, S. J. Penny, V. Pota, A. Smith-Castelli, J. Strader, D. Bradley, K. D. Eckert, D. Fohring, J. McBride, D. V. Stark, and O. Vaduvescu. The AIMSS Project - I. Bridging the star cluster-galaxy divide. MNRAS, 443(2):1151–1172, September 2014. doi:10.1093/mnras/stu1186.

S. P. Oh and Z. Haiman. Second-Generation Objects in the Universe: Radiative Cooling and Collapse of Halos with Virial Temperatures above 10^4 K. ApJ, 569(2):558–572, April 2002. doi:10.1086/339393.

T. Ohtani and T. Tsuribe. Growth of a Protostar and a Young Circumstellar Disk with a High Mass-Accretion Rate onto the Disk. PASJ, 65:93, August 2013. doi:10.1093/pasj/65.4.93.

J. B. Oke and J. E. Gunn. Secondary standard stars for absolute spectrophotometry. ApJ, 266: 713–717, March 1983. doi:10.1086/160817.

K. Omukai, T. Tsuribe, R. Schneider, and A. Ferrara. Thermal and Fragmentation Properties of Star-forming Clouds in Low-Metallicity Environments. ApJ, 626(2):627–643, June 2005. doi:10.1086/429955.

J. H. Oort. *The Stars of High Velocity*. PhD thesis, -, January 1926.

T. Page. Observational Aspects of Cosmology. *Science*, 151(3716):1411–1414, March 1966. doi:10.1126/science.151.3716.1411.

H. Partridge and D. W. Schwenke. The determination of an accurate isotope dependent potential energy surface for water from extensive ab initio calculations and experimental data. J. Chem. Phys., 106(11):4618–4639, March 1997. doi:10.1063/1.473987.

B. Paxton, L. Bildsten, A. Dotter, F. Herwig, P. Lesaffre, and F. Timmes. Modules for Experiments in Stellar Astrophysics (MESA). ApJS, 192(1):3, January 2011. doi:10.1088/0067-0049/192/1/3.

B. Paxton, M. Cantiello, P. Arras, L. Bildsten, E. F. Brown, A. Dotter, C. Mankovich, M. H. Montgomery, D. Stello, F. X. Timmes, and R. Townsend. Modules for Experiments in Stellar Astrophysics (MESA): Planets, Oscillations, Rotation, and Massive Stars. ApJS, 208(1):4, September 2013. doi:10.1088/0067-0049/208/1/4.

B. Paxton, P. Marchant, J. Schwab, E. B. Bauer, L. Bildsten, M. Cantiello, L. Dessart, R. Farmer, H. Hu, N. Langer, R. H. D. Townsend, D. M. Townsley, and F. X. Timmes. Modules for Experiments in Stellar Astrophysics (MESA): Binaries, Pulsations, and Explosions. ApJS, 220 (1):15, September 2015. doi:10.1088/0067-0049/220/1/15.

B. Paxton, J. Schwab, E. B. Bauer, L. Bildsten, S. Blinnikov, P. Duffell, R. Farmer, J. A. Goldberg, P. Marchant, E. Sorokina, A. Thoul, R. H. D. Townsend, and F. X. Timmes. Modules for Experiments in Stellar Astrophysics (MESA): Convective Boundaries, Element Diffusion, and Massive Star Explosions. ApJS, 234(2):34, February 2018. doi:10.3847/1538-4365/aaa5a8.

B. Paxton, R. Smolec, J. Schwab, A. Gautschy, L. Bildsten, M. Cantiello, A. Dotter, R. Farmer, J. A. Goldberg, A. S. Jermyn, S. M. Kanbur, P. Marchant, A. Thoul, R. H. D. Townsend, W. M. Wolf, M. Zhang, and F. X. Timmes. Modules for Experiments in Stellar Astrophysics (MESA): Pulsating Variable Stars, Rotation, Convective Boundaries, and Energy Conservation. ApJS, 243(1):10, July 2019. doi:10.3847/1538-4365/ab2241.

S. M. Percival, M. Salaris, F. van Wyk, and D. Kilkenny. Resolving the 47 Tucanae Distance Problem. ApJ, 573(1):174–183, July 2002. doi:10.1086/340593.

M. W. Phillips, P. Tremblin, I. Baraffe, G. Chabrier, N. F. Allard, F. Spiegelman, J. M. Goyal, B. Drummond, and E. Hébrard. A new set of atmosphere and evolution models for cool T-Y brown dwarfs and giant exoplanets. A&A, 637:A38, May 2020. doi:10.1051/0004-6361/201937381.

G. Piotto, L. R. Bedin, J. Anderson, I. R. King, S. Cassisi, A. P. Milone, S. Villanova, A. Pietrinferni, and A. Renzini. A Triple Main Sequence in the Globular Cluster NGC 2808. ApJ, 661 (1):L53–L56, May 2007. doi:10.1086/518503.

G. Piotto, A. P. Milone, J. Anderson, L. R. Bedin, A. Bellini, S. Cassisi, A. F. Marino, A. Aparicio, and V. Nascimbeni. Hubble Space Telescope Reveals Multiple Sub-giant Branch in Eight Globular Clusters. ApJ, 760(1):39, November 2012. doi:10.1088/0004-637X/760/1/39.

G. Piotto, S. Villanova, L. R. Bedin, R. Gratton, S. Cassisi, Y. Momany, A. Recio-Blanco, S. Lucatello, J. Anderson, I. R. King, A. Pietrinferni, and G. Carraro. Metallicities on the Double Main Sequence of ω Centauri Imply Large Helium Enhancement. ApJ, 621(2):777–784, March 2005. doi:10.1086/427796.

Planck Collaboration, P. A. R. Ade, N. Aghanim, M. Arnaud, M. Ashdown, J. Aumont, C. Baccigalupi, A. J. Banday, R. B. Barreiro, J. G. Bartlett, N. Bartolo, E. Battaner, R. Battye, K. Benabed, A. Benoît, A. Benoit-Lévy, J. P. Bernard, M. Bersanelli, P. Bielewicz, J. J. Bock, A. Bonaldi, L. Bonavera, J. R. Bond, J. Borrill, F. R. Bouchet, F. Boulanger, M. Bucher, C. Burigana, R. C. Butler, E. Calabrese, J. F. Cardoso, A. Catalano, A. Challinor, A. Chamballu, R. R. Chary, H. C. Chiang, J. Chluba, P. R. Christensen, S. Church, D. L. Clements, S. Colombi, L. P. L. Colombo, C. Combet, A. Coulais, B. P. Crill, A. Curto, F. Cuttaia, L. Danese, R. D. Davies, R. J. Davis, P. de Bernardis, A. de Rosa, G. de Zotti, J. Delabrouille, F. X. Désert, E. Di Valentino, C. Dickinson, J. M. Diego, K. Dolag, H. Dole, S. Donzelli, O. Doré, M. Douspis, A. Ducout, J. Dunkley, X. Dupac, G. Efstathiou, F. Elsner, T. A. Enßlin, H. K. Eriksen, M. Farhang, J. Fergusson, F. Finelli, O. Forni, M. Frailis, A. A. Fraisse, E. Franceschi, A. Frejsel, S. Galeotta, S. Galli, K. Ganga, C. Gauthier, M. Gerbino, T. Ghosh, M. Giard, Y. Giraud-Héraud, E. Giusarma, E. Gjerløw, J. González-Nuevo, K. M. Górski,

S. Gratton, A. Gregorio, A. Gruppuso, J. E. Gudmundsson, J. Hamann, F. K. Hansen, D. Hanson, D. L. Harrison, G. Helou, S. Henrot-Versillé, C. Hernández-Monteagudo, D. Herranz, S. R. Hildebrandt, E. Hivon, M. Hobson, W. A. Holmes, A. Hornstrup, W. Hovest, Z. Huang, K. M. Huffenberger, G. Hurier, A. H. Jaffe, T. R. Jaffe, W. C. Jones, M. Juvela, E. Keihänen, R. Keskitalo, T. S. Kisner, R. Kneissl, J. Knoche, L. Knox, M. Kunz, H. Kurki-Suonio, G. Lagache, A. Lähteenmäki, J. M. Lamarre, A. Lasenby, M. Lattanzi, C. R. Lawrence, J. P. Leahy, R. Leonardi, J. Lesgourgues, F. Levrier, A. Lewis, M. Liguori, P. B. Lilje, M. Linden-Vørnle, M. López-Caniego, P. M. Lubin, J. F. Macías-Pérez, G. Maggio, D. Maino, N. Mandolesi, A. Mangilli, A. Marchini, M. Maris, P. G. Martin, M. Martinelli, E. Martínez-González, S. Masi, S. Matarrese, P. McGehee, P. R. Meinhold, A. Melchiorri, J. B. Melin, L. Mendes, A. Mennella, M. Migliaccio, M. Millea, S. Mitra, M. A. Miville-Deschênes, A. Moneti, L. Montier, G. Morgante, D. Mortlock, A. Moss, D. Munshi, J. A. Murphy, P. Naselsky, F. Nati, P. Natoli, C. B. Netterfield, H. U. Nørgaard-Nielsen, F. Noviello, D. Novikov, I. Novikov, C. A. Oxborrow, F. Paci, L. Pagano, F. Pajot, R. Paladini, D. Paoletti, B. Partridge, F. Pasian, G. Patanchon, T. J. Pearson, O. Perdereau, L. Perotto, F. Perrotta, V. Pettorino, F. Piacentini, M. Piat, E. Pierpaoli, D. Pietrobon, S. Plaszczynski, E. Pointecouteau, G. Polenta, L. Popa, G. W. Pratt, G. Prézeau, S. Prunet, J. L. Puget, J. P. Rachen, W. T. Reach, R. Rebolo, M. Reinecke, M. Remazeilles, C. Renault, A. Renzi, I. Ristorcelli, G. Rocha, C. Rosset, M. Rossetti, G. Roudier, B. Rouillé d'Orfeuil, M. Rowan-Robinson, J. A. Rubiño-Martín, B. Rusholme, N. Said, V. Salvatelli, L. Salvati, M. Sandri, D. Santos, M. Savelainen, G. Savini, D. Scott, M. D. Seiffert, P. Serra, E. P. S. Shellard, L. D. Spencer, M. Spinelli, V. Stolyarov, R. Stompor, R. Sudiwala, R. Sunyaev, D. Sutton, A. S. Suur-Uski, J. F. Sygnet, J. A. Tauber, L. Terenzi, L. Toffolatti, M. Tomasi, M. Tristram, T. Trombetti, M. Tucci, J. Tuovinen, M. Türler, G. Umana, L. Valenziano, J. Valiviita, F. Van Tent, P. Vielva, F. Villa, L. A. Wade, B. D. Wandelt, I. K. Wehus, M. White, S. D. M. White, A. Wilkinson, D. Yvon, A. Zacchei, and A. Zonca. Planck 2015 results. XIII. Cosmological parameters. A&A, 594:A13, September 2016. doi:10.1051/0004-6361/201525830.

Planck Collaboration, N. Aghanim, Y. Akrami, M. Ashdown, J. Aumont, C. Baccigalupi, M. Ballardini, A. J. Banday, R. B. Barreiro, N. Bartolo, S. Basak, R. Battye, K. Benabed, J. P. Bernard, M. Bersanelli, P. Bielewicz, J. J. Bock, J. R. Bond, J. Borrill, F. R. Bouchet, F. Boulanger, M. Bucher, C. Burigana, R. C. Butler, E. Calabrese, J. F. Cardoso, J. Carron, A. Challinor, H. C. Chiang, J. Chluba, L. P. L. Colombo, C. Combet, D. Contreras, B. P. Crill, F. Cuttaia, P. de Bernardis, G. de Zotti, J. Delabrouille, J. M. Delouis, E. Di Valentino, J. M. Diego, O. Doré, M. Douspis, A. Ducout, X. Dupac, S. Dusini, G. Efstathiou, F. Elsner, T. A. Enßlin, H. K. Eriksen, Y. Fantaye, M. Farhang, J. Fergusson, R. Fernandez-Cobos, F. Finelli, F. Forastieri, M. Frailis, A. A. Fraisse, E. Franceschi, A. Frolov, S. Galeotta, S. Galli, K. Ganga, R. T. Génova-Santos, M. Gerbino, T. Ghosh, J. González-Nuevo, K. M. Górski, S. Gratton, A. Gruppuso, J. E. Gudmundsson, J. Hamann, W. Handley, F. K. Hansen, D. Herranz, S. R. Hildebrandt, E. Hivon, Z. Huang, A. H. Jaffe, W. C. Jones, A. Karakci, E. Keihänen, R. Keskitalo, K. Kiiveri, J. Kim, T. S. Kisner, L. Knox, N. Krachmalnicoff, M. Kunz, H. Kurki-Suonio, G. Lagache, J. M. Lamarre, A. Lasenby, M. Lattanzi, C. R. Lawrence, M. Le Jeune, P. Lemos, J. Lesgourgues, F. Levrier, A. Lewis, M. Liguori, P. B. Lilje, M. Lilley, V. Lindholm, M. López-Caniego, P. M. Lubin, Y. Z. Ma, J. F. Macías-Pérez, G. Maggio, D. Maino, N. Mandolesi, A. Mangilli,

A. Marcos-Caballero, M. Maris, P. G. Martin, M. Martinelli, E. Martínez-González, S. Matarrese, N. Mauri, J. D. McEwen, P. R. Meinhold, A. Melchiorri, A. Mennella, M. Migliaccio, M. Millea, S. Mitra, M. A. Miville-Deschênes, D. Molinari, L. Montier, G. Morgante, A. Moss, P. Natoli, H. U. Nørgaard-Nielsen, L. Pagano, D. Paoletti, B. Partridge, G. Patanchon, H. V. Peiris, F. Perrotta, V. Pettorino, F. Piacentini, L. Polastri, G. Polenta, J. L. Puget, J. P. Rachen, M. Reinecke, M. Remazeilles, A. Renzi, G. Rocha, C. Rosset, G. Roudier, J. A. Rubiño-Martín, B. Ruiz-Granados, L. Salvati, M. Sandri, M. Savelainen, D. Scott, E. P. S. Shellard, C. Sirignano, G. Sirri, L. D. Spencer, R. Sunyaev, A. S. Suur-Uski, J. A. Tauber, D. Tavagnacco, M. Tenti, L. Toffolatti, M. Tomasi, T. Trombetti, L. Valenziano, J. Valiviita, B. Van Tent, L. Vibert, P. Vielva, F. Villa, N. Vittorio, B. D. Wandelt, I. K. Wehus, M. White, S. D. M. White, A. Zacchei, and A. Zonca. Planck 2018 results. VI. Cosmological parameters. A&A, 641:A6, September 2020. doi:10.1051/0004-6361/201833910.

B. Plez. MARCS model atmospheres. *Physica Scripta Volume T*, 133:014003, December 2008. doi:10.1088/0031-8949/2008/T133/014003.

B. Plez. Cool star model atmospheres for Gaia : ATLAS, MARCS, and PHOENIX. In *Journal of Physics Conference Series*, volume 328 of *Journal of Physics Conference Series*, page 012005, December 2011. doi:10.1088/1742-6596/328/1/012005.

K. M. Pontoppidan, T. E. Pickering, V. G. Laidler, K. Gilbert, C. D. Sontag, C. Slocum, M. J. Sienkiewicz, C. Hanley, N. M. Earl, L. Pueyo, S. Ravindranath, D. M. Karakla, M. Robberto, A. Noriega-Crespo, and E. A. Barker. Pandeia: a multi-mission exposure time calculator for JWST and WFIRST. In A. B. Peck, R. L. Seaman, and C. R. Benn, editors, *Observatory Operations: Strategies, Processes, and Systems VI*, volume 9910 of *Society of Photo-Optical Instrumentation Engineers (SPIE) Conference Series*, page 991016, July 2016. doi:10.1117/12.2231768.

D. M. Popper. Stellar masses. ARA&A, 18:115–164, January 1980. doi:10.1146/annurev.aa.18.090180.000555.

D. M. Popper. Spectral Types of Stars in the Globular Clusters Messier 3 and Messier 13. ApJ, 105:204, January 1947. doi:10.1086/144893.

N. Prantzos and C. Charbonnel. On the self-enrichment scenario of galactic globular clusters: constraints on the IMF. A&A, 458(1):135–149, October 2006. doi:10.1051/0004-6361:20065374.

L. Pulone, G. De Marchi, S. Covino, and F. Paresce. HST observations of the metal rich globular clusters NGC 6496 and NGC 6352. A&A, 399:121–131, February 2003. doi:10.1051/0004-6361:20021788.

S. Qin, J. Zhong, T. Tang, and L. Chen. Hunting for Neighboring Open Clusters with Gaia DR3: 101 New Open Clusters within 500 pc. ApJS, 265(1):12, March 2023. doi:10.3847/1538-4365/acadd6.

D. Raghavan, H. A. McAlister, T. J. Henry, D. W. Latham, G. W. Marcy, B. D. Mason, D. R. Gies, R. J. White, and T. A. ten Brummelaar. A Survey of Stellar Families: Multiplicity of Solar-type Stars. ApJS, 190(1):1–42, September 2010. doi:10.1088/0067-0049/190/1/1.

I. Ramírez, J. Meléndez, and J. Chanamé. Oxygen Abundances in Low- and High-α Field Halo Stars and the Discovery of Two Field Stars Born in Globular Clusters. ApJ, 757(2):164, October 2012. doi:10.1088/0004-637X/757/2/164.

T. Rauch, M. Demleitner, D. Hoyer, and K. Werner. Stellar parameters for the central star of the planetary nebula PRTM 1 using the German Astrophysical Virtual Observatory service TheoSSA. MNRAS, 475(3):3896–3908, April 2018. doi:10.1093/mnras/sty056.

R. Rebolo, M. R. Zapatero Osorio, and E. L. Martín. Discovery of a brown dwarf in the Pleiades star cluster. Nature, 377(6545):129–131, September 1995. doi:10.1038/377129a0.

R. Rebolo, E. L. Martin, and A. Magazzu. Spectroscopy of a Brown Dwarf Candidate in the alpha Persei Open Cluster. ApJ, 389:L83, April 1992. doi:10.1086/186354.

A. Recio-Blanco. From globular clusters to the disc: the dual life of our Galaxy. A&A, 620: A194, December 2018. doi:10.1051/0004-6361/201833179.

V. C. Reddish. The masses of the stars of Population II. MNRAS, 115:32, January 1955. doi:10.1093/mnras/115.1.32.

B. C. Reed. The Composite Observational-Theoretical HR Diagram. JRASC, 92:36, February 1998.

M. M. Reggiani and M. R. Meyer. Binary Formation Mechanisms: Constraints from the Companion Mass Ratio Distribution. ApJ, 738(1):60, September 2011. doi:10.1088/0004-637X/738/1/60.

C. Rennó, B. Barbuy, T. C. Moura, and M. Trevisan. Abundances from integrated spectra of 47 Tucanae (NGC 104). MNRAS, 498(4):5834–5854, November 2020. doi:10.1093/mnras/staa2697.

A. Renzini. Origin of multiple stellar populations in globular clusters and their helium enrichment. MNRAS, 391(1):354–362, November 2008. doi:10.1111/j.1365-2966.2008.13892.x.

S. Riaz, T. Hartwig, and M. A. Latif. Unveiling the Contribution of Population III Stars in Primeval Galaxies at Redshift $\geq$6. ApJ, 937(1):L6, September 2022. doi:10.3847/2041-8213/ac8ea6.

H. B. Richer, G. G. Fahlman, R. Buonanno, F. Fusi Pecci, L. Searle, and I. B. Thompson. Globular Cluster Mass Functions. ApJ, 381:147, November 1991. doi:10.1086/170637.

H. B. Richer, J. Anderson, J. Brewer, S. Davis, G. G. Fahlman, B. M. S. Hansen, J. Hurley, J. S. Kalirai, I. R. King, D. Reitzel, R. M. Rich, M. M. Shara, and P. B. Stetson. Probing the Faintest Stars in a Globular Star Cluster. *Science*, 313(5789):936–940, August 2006. doi:10.1126/science.1130691.

M. Ricotti and J. P. Ostriker. Reionization, chemical enrichment and seed black holes from the first stars: is Population III important? MNRAS, 350(2):539–551, May 2004. doi:10.1111/j.1365-2966.2004.07662.x.

A. G. Riess, L. M. Macri, S. L. Hoffmann, D. Scolnic, S. Casertano, A. V. Filippenko, B. E. Tucker, M. J. Reid, D. O. Jones, J. M. Silverman, R. Chornock, P. Challis, W. Yuan, P. J. Brown, and R. J. Foley. A 2.4% Determination of the Local Value of the Hubble Constant. ApJ, 826 (1):56, July 2016. doi:10.3847/0004-637X/826/1/56.

A. W. Rodgers and P. Harding. The finite width of the omega Centauri main sequence. PASP, 95: 979–985, December 1983. doi:10.1086/131276.

R. T. Rood and D. A. Crocker. Multiple Populations on the Horizontal Branch. In A. G. D. Philip, editor, *Horizontal-Branch and UV-Bright Stars*, pages 99–105, January 1985.

L. S. Rothman, D. Jacquemart, A. Barbe, D. Chris Benner, M. Birk, L. R. Brown, M. R. Carleer, C. Chackerian, K. Chance, L. H. Coudert, V. Dana, V. M. Devi, J. M. Flaud, R. R. Gamache, A. Goldman, J. M. Hartmann, K. W. Jucks, A. G. Maki, J. Y. Mandin, S. T. Massie, J. Orphal, A. Perrin, C. P. Rinsland, M. A. H. Smith, J. Tennyson, R. N. Tolchenov, R. A. Toth, J. Vander Auwera, P. Varanasi, and G. Wagner. The HITRAN 2004 molecular spectroscopic database. J. Quant. Spec. Radiat. Transf., 96(2):139–204, December 2005. doi:10.1016/j.jqsrt.2004.10.008.

L. S. Rothman, I. E. Gordon, A. Barbe, D. C. Benner, P. F. Bernath, M. Birk, V. Boudon, L. R. Brown, A. Campargue, J. P. Champion, K. Chance, L. H. Coudert, V. Dana, V. M. Devi, S. Fally, J. M. Flaud, R. R. Gamache, A. Goldman, D. Jacquemart, I. Kleiner, N. Lacome, W. J. Lafferty, J. Y. Mandin, S. T. Massie, S. N. Mikhailenko, C. E. Miller, N. Moazzen-Ahmadi, O. V. Naumenko, A. V. Nikitin, J. Orphal, V. I. Perevalov, A. Perrin, A. Predoi-Cross, C. P. Rinsland, M. Rotger, M. Šimečková, M. A. H. Smith, K. Sung, S. A. Tashkun, J. Tennyson, R. A. Toth, A. C. Vandaele, and J. Vander Auwera. The HITRAN 2008 molecular spectroscopic database. J. Quant. Spec. Radiat. Transf., 110(9-10):533–572, June 2009. doi:10.1016/j.jqsrt.2009.02.013.

M. Rowan-Robinson. Distortion of the microwave background by dust from population III. In G. O. Abell and G. Chincarini, editors, *Early Evolution of the Universe and its Present Structure*, volume 104, pages 109–112, January 1983.

H. N. Russell. On the Distribution of Absolute Magnitude in Populations I and II. PASP, 60(354): 202–204, June 1948. doi:10.1086/126036.

H. N. Russell and C. E. Moore. *The Masses of the Stars*. The University of Chicago press, 1940.

R. E. Ryan, P. Thorman, C. Aganze, A. J. Burgasser, S. H. Cohen, N. P. Hathi, B. Holwerda, N. Pirzkal, and R. A. Windhorst. A Self-consistent Model for Brown Dwarf Populations. ApJ, 932(2):96, June 2022. doi:10.3847/1538-4357/ac6de5.

G. B. Rybicki and A. P. Lightman. *Radiative Processes in Astrophysics*. Wiley-VCH, 1986.

C.-E. Rydberg, E. Zackrisson, P. Lundqvist, and P. Scott. Detection of isolated Population III stars with the James Webb Space Telescope. MNRAS, 429(4):3658–3664, March 2013. doi:10.1093/mnras/sts653.

J. E. Ryon. *Advanced Camera for Surveys Instrument Handbook for Cycle 27 v. 18.0*. Space Telescope Science Institute, 2019.

M. Salaris and S. Cassisi. *Evolution of Stars and Stellar Populations*. John Wiley and Sons, 2005.

M. Salaris and S. Cassisi. Lithium and oxygen in globular cluster dwarfs and the early disc accretion scenario. A&A, 566:A109, June 2014. doi:10.1051/0004-6361/201423722.

M. Salaris and S. Cassisi. Stellar models with mixing length and T(τ) relations calibrated on 3D convection simulations. A&A, 577:A60, May 2015. doi:10.1051/0004-6361/201525812.

M. Salaris, C. Usher, S. Martocchia, E. Dalessandro, N. Bastian, S. Saracino, S. Cassisi, I. Cabrera-Ziri, and C. Lardo. Photometric characterization of multiple populations in star clusters: the impact of the first dredge-up. MNRAS, 492(3):3459–3464, March 2020. doi:10.1093/mnras/staa089.

L. Sampedro, W. S. Dias, E. J. Alfaro, H. Monteiro, and A. Molino. A multimembership catalogue for 1876 open clusters using UCAC4 data. MNRAS, 470(4):3937–3945, October 2017. doi:10.1093/mnras/stx1485.

San Diego Supercomputer Center. Triton shared computing cluster, 2022. URL `https://tritoncluster.sdsc.edu`.

A. R. Sandage. The color-magnitude diagram for the globular cluster M 3. AJ, 58:61–75, January 1953. doi:10.1086/106822.

A. Sandage and R. Wildey. The Anomalous Color-Magnitude Diagram of the Remote Globular Cluster NGC 7006. ApJ, 150:469, November 1967. doi:10.1086/149350.

M. R. Santos, V. Bromm, and M. Kamionkowski. The contribution of the first stars to the cosmic infrared background. MNRAS, 336(4):1082–1092, November 2002. doi:10.1046/j.1365-8711.2002.05895.x.

S. Saracino, E. Dalessandro, F. R. Ferraro, B. Lanzoni, L. Origlia, M. Salaris, A. Pietrinferni, D. Geisler, J. S. Kalirai, M. Correnti, R. E. Cohen, F. Mauro, S. Villanova, and C. Moni Bidin. On the Use of the Main-sequence Knee (Saddle) to Measure Globular Cluster Ages. ApJ, 860 (2):95, June 2018. doi:10.3847/1538-4357/aac2c2.

R. Sarmento and E. Scannapieco. The Effects of Radiative Feedback and Supernova-induced Turbulence on Early Galaxies. ApJ, 935(2):174, August 2022. doi:10.3847/1538-4357/ac815c.

R. Sarmento, E. Scannapieco, and S. Cohen. Following the Cosmic Evolution of Pristine Gas. II. The Search for Pop III-bright Galaxies. ApJ, 854(1):75, February 2018. doi:10.3847/1538-4357/aa989a.

D. Saumon, P. Bergeron, J. I. Lunine, W. B. Hubbard, and A. Burrows. Cool Zero-Metallicity Stellar Atmospheres. ApJ, 424:333, March 1994. doi:10.1086/173892.

D. Saumon, G. Chabrier, and H. M. van Horn. An Equation of State for Low-Mass Stars and Giant Planets. ApJS, 99:713, August 1995. doi:10.1086/192204.

L. Sbordone, P. Bonifacio, F. Castelli, and R. L. Kurucz. ATLAS and SYNTHE under Linux. *Memorie della Societa Astronomica Italiana Supplementi*, 5:93, January 2004.

L. Sbordone and P. Bonifacio. Atlas cookbook, Jul 2005. URL `http://atmos.obspm.fr/index.php/documentation/7`.

M. Scalco, A. Bellini, L. R. Bedin, J. Anderson, P. Rosati, M. Libralato, M. Salaris, E. Vesperini, D. Nardiello, D. Apai, A. J. Burgasser, and R. Gerasimov. The HST large programme on ω Centauri - IV. Catalogue of two external fields. MNRAS, 505(3):3549–3561, August 2021. doi:10.1093/mnras/stab1476.

D. Schaerer. On the properties of massive Population III stars and metal-free stellar populations. A&A, 382:28–42, January 2002. doi:10.1051/0004-6361:20011619.

A. T. P. Schauer, V. Bromm, N. Drory, and M. Boylan-Kolchin. On the probability of the extremely lensed z=6.2 Earendel source being a Population III star. *arXiv e-prints*, art. arXiv:2207.02863, July 2022.

D. J. Schlegel, D. P. Finkbeiner, and M. Davis. Maps of Dust Infrared Emission for Use in Estimation of Reddening and Cosmic Microwave Background Radiation Foregrounds. ApJ, 500(2):525–553, June 1998. doi:10.1086/305772.

S. J. Schmidt, S. L. Hawley, A. A. West, J. J. Bochanski, J. R. A. Davenport, J. Ge, and D. P. Schneider. BOSS Ultracool Dwarfs. I. Colors and Magnetic Activity of M and L Dwarfs. AJ, 149(5):158, May 2015. doi:10.1088/0004-6256/149/5/158.

A. C. Schneider, A. J. Burgasser, R. Gerasimov, F. Marocco, J. Gagné, S. Goodman, P. Beaulieu, W. Pendrill, A. Rothermich, A. Sainio, M. J. Kuchner, D. Caselden, A. M. Meisner, J. K. Faherty, E. E. Mamajek, C.-C. Hsu, J. J. Greco, M. C. Cushing, J. D. Kirkpatrick, D. Bardalez-Gagliuffi, S. E. Logsdon, K. Allers, J. H. Debes, and Backyard Worlds: Planet 9 Collaboration. WISEA J041451.67-585456.7 and WISEA J181006.18-101000.5: The First Extreme T-type Subdwarfs? ApJ, 898(1):77, July 2020. doi:10.3847/1538-4357/ab9a40.

R. Schneider, A. Ferrara, P. Natarajan, and K. Omukai. First Stars, Very Massive Black Holes, and Metals. ApJ, 571(1):30–39, May 2002. doi:10.1086/339917.

R. Schneider, K. Omukai, A. K. Inoue, and A. Ferrara. Fragmentation of star-forming clouds enriched with the first dust. MNRAS, 369(3):1437–1444, July 2006a. doi:10.1111/j.1365-2966.2006.10391.x.

R. Schneider, R. Salvaterra, A. Ferrara, and B. Ciardi. Constraints on the initial mass function of the first stars. MNRAS, 369(2):825–834, June 2006b. doi:10.1111/j.1365-2966.2006.10331.x.

M. Schwarzschild and L. Spitzer. On the evolution of stars and chemical elements in the early phases of a galaxy. *The Observatory*, 73:77–79, April 1953.

M. Schwarzschild, J. Spitzer, L., and R. Wildt. On the Difference in Chemical Composition Between High- and Low-Velocity Stars. ApJ, 114:398, November 1951. doi:10.1086/145479.

D. W. Schwenke. Opacity of TiO from a coupled electronic state calculation parametrized by AB initio and experimental data. *Faraday Discussions*, 109:321, January 1998. doi:10.1039/a800070k.

D. W. Scott. *Multivariate Density Estimation: Theory, Practice, and Visualization*. John Wiley and Sons, 2015.

P. Sharda and M. R. Krumholz. When did the initial mass function become bottom-heavy? MNRAS, 509(2):1959–1984, January 2022. doi:10.1093/mnras/stab2921.

C. M. Sharp and A. Burrows. Atomic and Molecular Opacities for Brown Dwarf and Giant Planet Atmospheres. ApJS, 168(1):140–166, January 2007. doi:10.1086/508708.

Y. Sibony, B. Liu, C. Simmonds, G. Meynet, and V. Bromm. Impact of Population III homogeneous stellar evolution on early cosmic reionisation. *arXiv e-prints*, art. arXiv:2205.15125, May 2022.

L. Silberstein. Some Spectrum Lines of Neutral Helium derived theoretically. Nature, 110(2755): 247–249, August 1922. doi:10.1038/110247b0.

B. Smalley. Different convection models in ATLAS. *Memorie della Societa Astronomica Italiana Supplementi*, 8:155, Jan 2005.

G. H. Smith and J. Norris. The cyanogen distribution of the red giants in M 5. ApJ, 264:215–222, January 1983. doi:10.1086/160588.

G. H. Smith. The chemical inhomegeneity of globular clusters. PASP, 99:67–90, February 1987. doi:10.1086/131958.

C. Sneden, R. P. Kraft, C. F. Prosser, and G. E. Langer. Oxygen Abundances in Halo Giants. III. Giants in the Mildly Metal-Poor Globular Cluster M5. AJ, 104:2121, December 1992. doi:10.1086/116388.

A. Sokasian, N. Yoshida, T. Abel, L. Hernquist, and V. Springel. Cosmic reionization by stellar sources: population III stars. MNRAS, 350(1):47–65, May 2004. doi:10.1111/j.1365-2966.2004.07636.x.

A. Sollima and H. Baumgardt. The global mass functions of 35 Galactic globular clusters: I. Observational data and correlations with cluster parameters. MNRAS, 471(3):3668–3679, November 2017. doi:10.1093/mnras/stx1856.

A. Sollima, F. R. Ferraro, and M. Bellazzini. The mass function of ω Centauri down to 0.15 M_{solar}. MNRAS, 381(4):1575–1582, November 2007. doi:10.1111/j.1365-2966.2007.12324.x.

J. Soltis, S. Casertano, and A. G. Riess. The Parallax of ω Centauri Measured from Gaia EDR3 and a Direct, Geometric Calibration of the Tip of the Red Giant Branch and the Hubble Constant. ApJ, 908(1):L5, February 2021. doi:10.3847/2041-8213/abdbad.

F. Spada, P. Demarque, Y. C. Kim, T. S. Boyajian, and J. M. Brewer. The Yale-Potsdam Stellar Isochrones. ApJ, 838(2):161, April 2017. doi:10.3847/1538-4357/aa661d.

D. N. Spergel, L. Verde, H. V. Peiris, E. Komatsu, M. R. Nolta, C. L. Bennett, M. Halpern, G. Hinshaw, N. Jarosik, A. Kogut, M. Limon, S. S. Meyer, L. Page, G. S. Tucker, J. L. Weiland, E. Wollack, and E. L. Wright. First-Year Wilkinson Microwave Anisotropy Probe (WMAP) Observations: Determination of Cosmological Parameters. ApJS, 148(1):175–194, September 2003. doi:10.1086/377226.

D. S. Spiegel, A. Burrows, and J. A. Milsom. The Deuterium-burning Mass Limit for Brown Dwarfs and Giant Planets. ApJ, 727(1):57, January 2011. doi:10.1088/0004-637X/727/1/57.

J. Spitzer, Lyman and M. Schwarzschild. The Possible Influence of Interstellar Clouds on Stellar Velocities. ApJ, 114:385, November 1951. doi:10.1086/145478.

L. Spitzer. *Dynamical evolution of globular clusters*. Princeton University Press, 1987.

A. Stacy and V. Bromm. The First Stars: A Low-mass Formation Mode. ApJ, 785(1):73, April 2014. doi:10.1088/0004-637X/785/1/73.

A. Stacy, T. H. Greif, and V. Bromm. The first stars: mass growth under protostellar feedback. MNRAS, 422(1):290–309, May 2012. doi:10.1111/j.1365-2966.2012.20605.x.

A. Stacy, V. Bromm, and A. T. Lee. Building up the Population III initial mass function from cosmological initial conditions. MNRAS, 462(2):1307–1328, October 2016. doi:10.1093/mnras/stw1728.

J. R. Stauffer, G. Schultz, and J. D. Kirkpatrick. Keck Spectra of Pleiades Brown Dwarf Candidates and a Precise Determination of the Lithium Depletion Edge in the Pleiades. ApJ, 499(2):L199–L203, June 1998. doi:10.1086/311379.

J. Strader, J. P. Brodie, and D. A. Forbes. Metal-Poor Globular Clusters and Galaxy Formation. AJ, 127(6):3431–3436, June 2004. doi:10.1086/420995.

A. M. Suliga, S. Shalgar, and G. M. Fuller. A closer look at the *pp*-chain reaction in the Sun: Constraining the coupling of light mediators to protons. *arXiv e-prints*, art. arXiv:2012.11620, December 2020.

H. Susa, K. Hasegawa, and N. Tominaga. The Mass Spectrum of the First Stars. ApJ, 792(1):32, September 2014. doi:10.1088/0004-637X/792/1/32.

Y. Suwa, T. Takiwaki, K. Kotake, and K. Sato. Gravitational Wave Background from Population III Stars. ApJ, 665(1):L43–L46, August 2007. doi:10.1086/521078.

A. V. Sweigart and J. G. Mengel. Meridional circulation and CNO anomalies in red giant stars. ApJ, 229:624–641, April 1979. doi:10.1086/156996.

M. Takada, R. S. Ellis, M. Chiba, J. E. Greene, H. Aihara, N. Arimoto, K. Bundy, J. Cohen, O. Doré, G. Graves, J. E. Gunn, T. Heckman, C. M. Hirata, P. Ho, J.-P. Kneib, O. Le Fèvre, L. Lin, S. More, H. Murayama, T. Nagao, M. Ouchi, M. Seiffert, J. D. Silverman, L. Sodré, D. N. Spergel, M. A. Strauss, H. Sugai, Y. Suto, H. Takami, and R. Wyse. Extragalactic science, cosmology, and Galactic archaeology with the Subaru Prime Focus Spectrograph. PASJ, 66(1): R1, February 2014. doi:10.1093/pasj/pst019.

Y. Takeda, E. Kambe, K. Sadakane, and S. Masada. Oxygen and Neon Abundances of B-Type Stars in Comparison with the Sun. PASJ, 62:1239–1248, October 2010. doi:10.1093/pasj/62.5.1239.

M. Taketani, T. Hatanaka, and S. Obi. Populations and Evolution of Stars. *Progress of Theoretical Physics*, 15(2):89–94, February 1956. doi:10.1143/PTP.15.89.

S. A. Tashkun and V. I. Perevalov. CDSD-4000: High-resolution, high-temperature carbon dioxide spectroscopic databank. J. Quant. Spec. Radiat. Transf., 112:1403–1410, June 2011. doi:10.1016/j.jqsrt.2011.03.005.

M. Tegmark, J. Silk, M. J. Rees, A. Blanchard, T. Abel, and F. Palla. How Small Were the First Cosmological Objects? ApJ, 474:1, January 1997. doi:10.1086/303434.

P. ten Bruggencate. *Sternhaufen: Ihr Bau, Ihre Stellung zum Sternsystem und Ihre Bedeutung für die Kosmogonie*. Springer, 1927.

I. B. Thompson, J. Kaluzny, W. Pych, G. Burley, W. Krzeminski, B. Paczyński, S. E. Persson, and G. W. Preston. Cluster AgeS Experiment: The Age and Distance of the Globular Cluster ω Centauri Determined from Observations of the Eclipsing Binary OGLEGC 17. AJ, 121(6): 3089–3099, June 2001. doi:10.1086/321084.

I. B. Thompson, A. Udalski, A. Dotter, M. Rozyczka, A. Schwarzenberg-Czerny, W. Pych, Y. Beletsky, G. S. Burley, J. L. Marshall, A. McWilliam, N. Morrell, D. Osip, A. Monson, S. E. Persson, M. K. Szymański, I. Soszyński, R. Poleski, K. Ulaczyk, Ł. Wyrzykowski, S. Kozłowski, P. Mróz, P. Pietrukowicz, and J. Skowron. The Cluster AgeS Experiment (CASE)

- VIII. Age and distance of the Globular Cluster 47 Tuc from the analysis of two detached eclipsing binaries. MNRAS, 492(3):4254–4267, March 2020. doi:10.1093/mnras/staa032.

A. O. Thygesen, L. Sbordone, S. Andrievsky, S. Korotin, D. Yong, S. Zaggia, H. G. Ludwig, R. Collet, M. Asplund, P. Ventura, F. D'Antona, J. Meléndez, and A. D'Ercole. The chemical composition of red giants in 47 Tucanae. I. Fundamental parameters and chemical abundance patterns. A&A, 572:A108, December 2014. doi:10.1051/0004-6361/201424533.

F. X. Timmes, S. E. Woosley, and T. A. Weaver. Galactic Chemical Evolution: Hydrogen through Zinc. ApJS, 98:617, June 1995. doi:10.1086/192172.

J. Towns, T. Cockerill, M. Dahan, I. Foster, K. Gaither, A. Grimshaw, V. Hazlewood, S. Lathrop, D. Lifka, G. D. Peterson, R. Roskies, J. R. Scott, and N. Wilkens-Diehr. XSEDE: Accelerating Scientific Discovery. *Computing in Science and Engineering*, 16(5):62–74, September 2014. doi:10.1109/MCSE.2014.80.

M. Trenti and R. van der Marel. No energy equipartition in globular clusters. MNRAS, 435(4): 3272–3282, November 2013. doi:10.1093/mnras/stt1521.

M. Trenti, M. Stiavelli, and J. M. Shull. Metal-free Gas Supply at the Edge of Reionization: Late-epoch Population III Star Formation. ApJ, 700(2):1672–1679, August 2009. doi:10.1088/0004-637X/700/2/1672.

T. Tsuji, K. Ohnaka, and W. Aoki. Dust formation in stellar photospheres: a case of very low mass stars and a possible resolution on the effective temperature scale of M dwarfs. A&A, 305: L1, January 1996.

T. Tsuji and T. Nakajima. Transition from L to T Dwarfs on the Color-Magnitude Diagram. ApJ, 585(2):L151–L154, March 2003. doi:10.1086/374388.

J. Tumlinson, J. M. Shull, and A. Venkatesan. Cosmological Effects of the First Stars: Evolving Spectra of Population III. ApJ, 584(2):608–620, February 2003. doi:10.1086/345737.

D. Tytler, J. M. O'Meara, N. Suzuki, and D. Lubin. Review of Big Bang Nucleosynthesis and Primordial Abundances. *Physica Scripta Volume T*, 85:12, January 2000. doi:10.1238/Physica.Topical.085a00012.

H. Umeda and K. Nomoto. Nucleosynthesis of Zinc and Iron Peak Elements in Population III Type II Supernovae: Comparison with Abundances of Very Metal Poor Halo Stars. ApJ, 565 (1):385–404, January 2002. doi:10.1086/323946.

D. Valcin, J. L. Bernal, R. Jimenez, L. Verde, and B. D. Wandelt. Inferring the age of the universe with globular clusters. J. Cosm. Astropart. Phys., 2020(12):002, December 2020. doi:10.1088/1475-7516/2020/12/002.

D. Valcin, R. Jimenez, L. Verde, J. L. Bernal, and B. D. Wandelt. The age of the Universe with globular clusters: reducing systematic uncertainties. J. Cosm. Astropart. Phys., 2021(8):017, August 2021. doi:10.1088/1475-7516/2021/08/017.

M. Valerdi, A. Peimbert, and M. Peimbert. Chemical abundances in seven metal-poor H II regions and a determination of the primordial helium abundance. MNRAS, 505(3):3624–3634, August 2021. doi:10.1093/mnras/stab1543.

G. van de Ven, R. C. E. van den Bosch, E. K. Verolme, and P. T. de Zeeuw. The dynamical distance and intrinsic structure of the globular cluster ω Centauri. A&A, 445(2):513–543, January 2006. doi:10.1051/0004-6361:20053061.

S. van den Bergh. UBV photometry of globular clusters. AJ, 72:324, April 1967.

D. A. VandenBerg. Models for Old, Metal-Poor Stars with Enhanced α-Element Abundances. II. Their Implications for the Ages of the Galaxy's Globular Clusters and Field Halo Stars. ApJS, 129(1):315–352, July 2000. doi:10.1086/313404.

D. A. VandenBerg, K. Brogaard, R. Leaman, and L. Casagrande. The Ages of 55 Globular Clusters as Determined Using an Improved $\Delta V_{\rm TO}^{\rm HB}$ Method along with Color-Magnitude Diagram Constraints, and Their Implications for Broader Issues. ApJ, 775(2):134, October 2013. doi:10.1088/0004-637X/775/2/134.

E. Vesperini, S. L. W. McMillan, F. D'Antona, and A. D'Ercole. Dynamical evolution and spatial mixing of multiple population globular clusters. MNRAS, 429(3):1913–1921, March 2013. doi:10.1093/mnras/sts434.

E. Visbal, G. L. Bryan, and Z. Haiman. What is the maximum mass of a Population III galaxy? MNRAS, 469(2):1456–1465, August 2017. doi:10.1093/mnras/stx909.

E. T. Vishniac. A necessary condition for equilibrium in stellar systems with a continuous mass spectrum. ApJ, 223:986–990, August 1978. doi:10.1086/156332.

E. Vitral and P. Boldrini. Properties of globular clusters formed in dark matter mini-halos. A&A, 667:A112, November 2022. doi:10.1051/0004-6361/202244530.

R. L. Wagner. Theoretical evolution of extremely metal-poor stars. II. A&A, 62(1-2):9–12, January 1978.

R. V. Wagoner, W. A. Fowler, and F. Hoyle. On the Synthesis of Elements at Very High Temperatures. ApJ, 148:3, April 1967. doi:10.1086/149126.

G. Wallerstein. Atomic Lines in the CH Star HD 209621. ApJ, 158:607, November 1969. doi:10.1086/150222.

G. Wallerstein and J. L. Greenstein. The Chemical Composition of Two CH Stars, HD 26 and HD 201626. ApJ, 139:1163, May 1964. doi:10.1086/147858.

G. Wallerstein, J. L. Greenstein, R. Parker, H. L. Helfer, and L. H. Aller. Red Giants with Extreme Metal Deficiencies. ApJ, 137:280, January 1963. doi:10.1086/147501.

Y.-F. Wang, A. L. Luo, W.-P. Chen, H. R. A. Jones, B. Du, Y.-B. Li, S. Zhang, Z.-R. Bai, X. Kong, and Y.-X. Guo. Ultracool dwarfs identified using spectra in LAMOST DR7. A&A, 660:A38, April 2022. doi:10.1051/0004-6361/202142009.

P. F. Weck, A. Schweitzer, P. C. Stancil, P. H. Hauschildt, and K. Kirby. The Molecular Line Opacity of MgH in Cool Stellar Atmospheres. ApJ, 582(2):1059–1065, January 2003. doi:10.1086/344722.

J.-J. Wei and F. Melia. Exploring the Hubble Tension and Spatial Curvature from the Ages of Old Astrophysical Objects. ApJ, 928(2):165, April 2022. doi:10.3847/1538-4357/ac562c.

B. Welch, D. Coe, J. M. Diego, A. Zitrin, E. Zackrisson, P. Dimauro, Y. Jiménez-Teja, P. Kelly, G. Mahler, M. Oguri, F. X. Timmes, R. Windhorst, M. Florian, S. E. de Mink, R. J. Avila, J. Anderson, L. Bradley, K. Sharon, A. Vikaeus, S. McCandliss, M. Bradač, J. Rigby, B. Frye, S. Toft, V. Strait, M. Trenti, S. Sharma, F. Andrade-Santos, and T. Broadhurst. A highly magnified star at redshift 6.2. Nature, 603(7903):815–818, March 2022a. doi:10.1038/s41586-022-04449-y.

B. Welch, D. Coe, E. Zackrisson, S. E. de Mink, S. Ravindranath, J. Anderson, G. Brammer, L. Bradley, J. Yoon, P. Kelly, J. M. Diego, R. Windhorst, A. Zitrin, P. Dimauro, Y. Jimenez-Teja, Abdurro'uf, M. Nonino, A. Acebron, F. Andrade-Santos, R. J. Avila, M. B. Bayliss, A. Benitez, T. Broadhurst, R. Bhatawdekar, M. Bradac, G. Caminha, W. Chen, J. Eldridge, E. Farag, M. Florian, B. Frye, S. Fujimoto, S. Gomez, A. Henry, T. Y. -Y Hsiao, T. A. Hutchison, B. L. James, M. Joyce, I. Jung, G. Khullar, R. L. Larson, G. Mahler, N. Mandelker, S. McCandliss, T. Morishita, R. Newshore, C. Norman, K. O'Connor, P. A. Oesch, M. Oguri, M. Ouichi, M. Postman, J. R. Rigby, J. Ryan, Russell E., S. Sharma, K. Sharon, V. Strait, L.-G. Strolger, F. X. Timmes, S. Toft, M. Trenti, E. Vanzella, and A. Vikaeus. JWST Imaging of Earendel, the Extremely Magnified Star at Redshift $z = 6.2$. *arXiv e-prints*, art. arXiv:2208.09007, August 2022b.

C. Wenger and J. P. Champion. Spherical Top Data System (STDS) software for the simulation of spherical top spectra. J. Quant. Spec. Radiat. Transf., 59(3-5):471–480, May 1998. doi:10.1016/S0022-4073(97)00106-4.

A. A. West, J. J. Bochanski, B. P. Bowler, A. Dotter, J. A. Johnson, S. Lépine, B. Rojas-Ayala, and A. Schweitzer. Determining the Metallicity of Low-Mass Stars and Brown Dwarfs: Tools for Probing Fundamental Stellar Astrophysics, Tracing Chemical Evolution of the Milky Way and Identifying the Hosts of Extrasolar Planets. In C. Johns-Krull, M. K. Browning, and A. A. West, editors, *16th Cambridge Workshop on Cool Stars, Stellar Systems, and the Sun*, volume 448 of *Astronomical Society of the Pacific Conference Series*, page 531, December 2011.

D. Whalen, B. W. O'Shea, J. Smidt, and M. L. Norman. How the First Stars Regulated Local Star Formation. I. Radiative Feedback. ApJ, 679(2):925–941, June 2008. doi:10.1086/587731.

R. Wielen. The Diffusion of Stellar Orbits Derived from the Observed Age-Dependence of the Velocity Dispersion. A&A, 60(2):263–275, September 1977.

R. A. Windhorst, F. X. Timmes, J. S. B. Wyithe, M. Alpaslan, S. K. Andrews, D. Coe, J. M. Diego, M. Dijkstra, S. P. Driver, P. L. Kelly, and D. Kim. On the Observability of Individual Population III Stars and Their Stellar-mass Black Hole Accretion Disks through Cluster Caustic Transits. ApJS, 234(2):41, February 2018. doi:10.3847/1538-4365/aaa760.

R. F. Wing and J. Stock. Carbon Stars in Omega Centauri. ApJ, 186:979–988, December 1973. doi:10.1086/152561.

A. J. Winter and C. J. Clarke. Accretion of substellar companions as the origin of chemical abundance inhomogeneities in globular clusters. MNRAS, 521(2):1646–1673, May 2023. doi:10.1093/mnras/stad312.

J. H. Wise and T. Abel. Resolving the Formation of Protogalaxies. I. Virialization. ApJ, 665(2): 899–910, August 2007. doi:10.1086/520036.

J. H. Wise, T. Abel, M. J. Turk, M. L. Norman, and B. D. Smith. The birth of a galaxy - II. The role of radiation pressure. MNRAS, 427(1):311–326, November 2012a. doi:10.1111/j.1365-2966.2012.21809.x.

J. H. Wise, M. J. Turk, M. L. Norman, and T. Abel. The Birth of a Galaxy: Primordial Metal Enrichment and Stellar Populations. ApJ, 745(1):50, January 2012b. doi:10.1088/0004-637X/745/1/50.

M. G. Wolfire and J. P. Cassinelli. Conditions for the Formation of Massive Stars. ApJ, 319:850, August 1987. doi:10.1086/165503.

T. E. Woods, S. Patrick, J. S. Elford, D. J. Whalen, and A. Heger. On the Evolution of Supermassive Primordial Stars in Cosmological Flows. ApJ, 915(2):110, July 2021. doi:10.3847/1538-4357/abfaf9.

N. J. Woolf. Observational Aspects of Cosmology. Presented at the conference hosted by S. F. Singer at University of Miami, 1965.

N. J. Woolf. Helium Content of Population II. AJ, 71:187, January 1966. doi:10.1086/110144.

J. S. B. Wyithe and A. Loeb. Reionization of Hydrogen and Helium by Early Stars and Quasars. ApJ, 586(2):693–708, April 2003. doi:10.1086/367721.

H. Xu, J. H. Wise, and M. L. Norman. Population III Stars and Remnants in High-redshift Galaxies. ApJ, 773(2):83, August 2013. doi:10.1088/0004-637X/773/2/83.

D. Yong, J. Meléndez, K. Cunha, A. I. Karakas, J. E. Norris, and V. V. Smith. Chemical Abundances in Giant Stars of the Tidally Disrupted Globular Cluster NGC 6712 from High-Resolution Infrared Spectroscopy. ApJ, 689(2):1020–1030, December 2008. doi:10.1086/592229.

S. C. Yoon, A. Dierks, and N. Langer. Evolution of massive Population III stars with rotation and magnetic fields. A&A, 542:A113, June 2012. doi:10.1051/0004-6361/201117769.

N. Yoshida, K. Omukai, L. Hernquist, and T. Abel. Formation of Primordial Stars in a ΛCDM Universe. ApJ, 652(1):6–25, November 2006. doi:10.1086/507978.

L. Y. A. Yung, R. S. Somerville, S. L. Finkelstein, G. Popping, R. Davé, A. Venkatesan, P. Behroozi, and H. C. Ferguson. Semi-analytic forecasts for JWST - IV. Implications for cosmic reionization and LyC escape fraction. MNRAS, 496(4):4574–4592, August 2020. doi:10.1093/mnras/staa1800.

E. Zackrisson, C.-E. Rydberg, D. Schaerer, G. Östlin, and M. Tuli. The Spectral Evolution of the First Galaxies. I. James Webb Space Telescope Detection Limits and Color Criteria for Population III Galaxies. ApJ, 740(1):13, October 2011. doi:10.1088/0004-637X/740/1/13.

E. Zackrisson, J. González, S. Eriksson, S. Asadi, C. Safranek-Shrader, M. Trenti, and A. K. Inoue. Primordial star clusters at extreme magnification. MNRAS, 449(3):3057–3063, May 2015. doi:10.1093/mnras/stv492.

H. W. Zhang, T. Gehren, and G. Zhao. A non-local thermodynamic equilibrum study of scandium in the Sun. A&A, 481(2):489–497, April 2008. doi:10.1051/0004-6361:20078910.

T. Zhou, A. Whisnant, R. Gerasimov, and A. J. Burgasser. Synthetic Color-Magnitude Diagrams for the Globular Cluster 47 Tucanae. *Research Notes of the American Astronomical Society*, 6 (10):212, October 2022. doi:10.3847/2515-5172/ac9ab6.

T. Ziliotto, A. P. Milone, A. F. Marino, A. L. Dotter, A. Renzini, E. Vesperini, A. I. Karakas, G. Cordoni, E. Dondoglio, M. V. Legnardi, E. P. Lagioia, A. Mohandasan, and S. Baimukhametova. Multiple Stellar Populations in Metal-Poor Globular Clusters with JWST: a NIRCam view of M 92. *arXiv e-prints*, art. arXiv:2304.06026, April 2023. doi:10.48550/arXiv.2304.06026.

R. Zinn. The unusual red giants in M5, M10 and M92. A&A, 25:409–413, June 1973.

A. Zitrin, T. Broadhurst, Y. Rephaeli, and S. Sadeh. The Largest Gravitational Lens: MACS J0717.5+3745 (z = 0.546). ApJ, 707(1):L102–L106, December 2009. doi:10.1088/0004-637X/707/1/L102.